Super Alumina:

Oxide Nanocomposites for Ballistic Armour

Douglas Andrews

St Anne's College



Supervisors:

Professor Richard Todd & Professor Peter Nellist

Department of Materials

University of Oxford

Hillary Term 2024

SUPER ALUMINA: OXIDE NANOCOMPOSITES FOR BALLISTIC ARMOUR

A thesis submitted for the degree of Doctor of Philosophy at the University of Oxford

Douglas Andrews, St Anne's College, Hillary Term 2024

The work described in this thesis aimed to produce alumina-mullite composites with improved mechanical properties relative to undoped alumina. The oxidation of silicon carbide in situ with alumina without other additives was investigated and the resultant composite optimised for density and hardness. This resulted in an alumina-mullite composite with around 5% porosity and a Vickers hardness 14% lower than alumina sintered under the same conditions.

The microstructure of the alumina-mullite composite was modified through the addition of various metal oxides and nitrates. It was found that the addition of yttria resulted in the highest density of material. The resultant microstructure was investigated through SEM and EDX analysis to measure the changes in microstructure and silicon distribution produced due to the addition of yttria. This showed a bimodal microstructure with areas of small grains surrounded by abnormal alumina grains. The abnormal alumina grains contained smaller grains of mullite. TEM-EDS analysis of the grain boundary compositions produced in the alumina-mullite-yttria composite showed equal excesses of silicon on the border of all grains, with segregation of yttria to the borders of abnormal grains exclusively.

Yttria doped alumina-mullite composites resulted in a change in failure mode from intergranular failure, as seen in alumina, to transgranular. This change in failure mode was accompanied by an improvement in mechanical properties compared to the additive-free alumina-mullite composite produced including an increase of 10% in the Vickers hardness over unmodified alumina. The macroscopic properties were finally linked to the performance of the composite under high speed impacts. The yttria doped alumina-mullite composites failed through the formation of a cone crack and a mixture of Hertzian fracture and 'Quasi Plastic' deformation. This resulted in a composite with a higher energy required for failure and that consumed more energy upon failure than alumina.

ACKNOWLEDGEMENTS

The first thanks for this project must go to Professor Richard Todd. His guidance and supervision have proved invaluable for this project and without his assistance this work would not have been possible in any form. Thank you for all you have done during my project here at Oxford. Similarly, I could not have completed this work with the support of my sponsors at the Defence Science and Technology Laboratory. They have provided both funding and feedback throughout my work and this has proved invaluable.

Thanks must also go out to the rest of the RIT group for their help and support. Particularly Dr Jesse Singh for showing me how to manufacture ceramic samples early on, Zonghao Guo for assisting with perfecting cold isostatic pressing techniques, and to Tuoran Chen for assisting with the production of lamellae for transmission electron microscopy imaging.

I am also indebted to the work of other members of the Department of Materials. Dr Gareth Hughes was very helpful in teaching me how to carry out FIB milling and sample preparation, especially as this had to be done remotely due to COVID restrictions. Jennifer Holter was similarly helpful in my training in scanning electron microscopy and EDX mapping at the start of the project. The X-ray tomography work could not have been conducted without the help of Professor James Marrow who was also instrumental in guiding the analysis. I am also very grateful for the assistance of Michael Goode who performed the nanoindentation work throughout this project and whose conversations proved instrumental in helping to guide the work in this area. Finally, the guidance in selection of testing conditions and assistance in performing the testing under high speed conditions offered by Simone Falco allowed for experiments that would not have been possible otherwise. Thank you to everyone in materials who have been supportive over the course of my DPhil.

Many thanks are also owed to my friends and family outside the university without whom I could not possibly have completed my DPhil. These include my friends throughout Oxford who have provided welcome distractions to attempt to alleviate some of my stresses, particularly Laurence who has been the DM for our long running D&D game. Finally, and most importantly, my fiancée, Imogen, has my infinite thanks and appreciation for enabling me to complete this work. She has been a support in all ways I could have possibly asked and many more.

PREFACE

This thesis is an account of the work carried out by the author in the Department of Materials, University of Oxford between September 2019 and January 2024 under the supervision of Professor Richard I. Todd.

No part of this work has been previously submitted for a degree at this or any other university. The work of others has been freely drawn upon and is duly acknowledged and referenced in the relevant points in the text. A full list of references is given at the end of the thesis.

Parts of the work described in the thesis have been presented at the following conferences:

- **D. T. Andrews**, R. I. Todd, *Improvements to the Performance of Alumina-Based Ceramics Through the Reaction Sintering of Alumina-Mullite Nanocomposites*
    - Poster presentation at Ceramics in Europe, Krakow, 10-14th July 2022
- **D. T. Andrews**, R. I. Todd, *Super Alumina: Oxide Nanocomposites for Ballistic Armour*
    - Oral presentation at Defence materials forum, Leicester, 9th November 2022

CONTENTS

Super Alumina: Oxide Nanocomposites for Ballistic Armour 2
Acknowledgements 3
Preface 5
1 Introduction 10
2 Literature Review 13
2.1 Armour Design 13
2.1.1 History of Armour 13
2.1.2 Materials Comparison 14
2.1.3 Current Ceramic Armour 15
2.1.4 Behaviour of Ceramic Armour 16
2.1.5 Mechanical Properties 18
2.1.6 Compressive Strength 18
2.2 Aluminium Oxide 21
2.2.1 Basics 21
2.2.2 Sintering and grain growth 21
2.3 Silicon Carbide 25
2.3.1 General Properties 25
2.3.2 Oxidation profile 26
2.4 Alumina Silicon Carbide Nanocomposites 27
2.4.1 Microstructure 27
2.4.2 Oxidation in Alumina Silicon Carbide Nanocomposites 29
2.4.3 Mechanical and Failure Properties 30
2.5 Complexions in Alumina 33
2.5.1 Nature of Complexions 33
2.5.2 Grain Boundary Tuning 36
2.6 Grain Boundary Facetting 40
2.6.1 Principles of Grain Boundary Faceting 40
2.6.2 Faceting in Alumina 42
2.7 Mechanical Testing 46
2.7.1 Hardness 46
2.7.2 Wear Resistance 48

2.7.3 Fracture Toughness 50
3 Objectives 54
4 Materials and Methods 56
4.1 Materials 56
4.1.1 Alumina 56
4.1.2 Silicon Carbide 56
4.1.3 Dopants 57
4.1.4 Sample Manufacture 58
4.2 In Situ Testing 59
4.2.1 Thermogravimetric Analysis 59
4.2.2 X-Ray Tomography 59
4.3 Characterisation of Materials 60
4.3.1 Particle Size Measurement 60
4.3.2 Grain Size 60
4.3.3 Abnormal Grain Fraction 61
4.3.4 Particle Analysis 62
4.3.5 Density 62
4.3.6 EDX 63
4.3.7 Transmission Electron Microscopy 63
4.3.8 Transmission Electron Microscopy EDX 64
4.4 Mechanical Testing 66
4.4.1 Indentation 66
4.4.2 Nanoindentation 66
4.4.3 Wear Resistance 68
4.4.4 3 Point Bend Testing 69
4.4.5 Fracture Toughness Testing 71
4.4.6 High Speed Impact Testing 73
5 Microstructure of Alumina Matrix Composites 75
5.1 Results 76
5.1.1 In Situ Testing 76
5.1.2 Microstructural analysis 83
5.2 Discussion of Alumina-Mullite Composites Without Any Additives 119
5.3 Microstructure Of Alumina-Silicon Carbide-Yttria Composites 124
5.3.1 Grain Boundary Compositions in Al_2O_3-SiC-Y_2O_3 124
5.3.2 Complexion Formation 126
5.3.3 Abnormal Grain Growth 128

5.3.4 Mullite Distribution 129
5.3.5 Mullite Composition 134
5.3.6 Porosity in Al_2O_3-SiC-Y_2O_3 135
6 Mechanical Properties of Alumina-Silicon Carbide-Yttria 137
6.1 Results 138
6.1.1 Vickers Hardness Testing 138
6.1.2 Nanoindentation 144
6.1.3 Wear Resistance 147
6.1.4 Fracture Toughness 150
6.1.5 Flexural Properties 150
6.2 Discussion 155
6.2.1 Hardness 156
6.2.2 Toughness 158
6.2.3 Strength 159
6.2.4 Weibull Modulus 161
6.2.5 Wear Resistance 161
6.3 High Speed Impact Testing 163
6.3.1 Results 163
6.3.2 Discussion 169
7 Summary 172
8 Conclusions 175
9 Future Work 176
10 Appendix 179
11 Bibliography 181

For Idgey

1 INTRODUCTION

Civilization has used ceramics for millennia. While the very first ceramics were figurative in nature and they were fired around 30,000 years ago [1], over the following years their usage expanded to include pottery vessels, clay bricks and a wide variety of other applications [2] due to their ease of shaping and high temperature properties. More recently these applications have been expanded due to the beneficial properties seen in modern ceramics, such as their high hardness and wear resistance. Among these applications, the one being focused on throughout this work is the use of ceramic materials for ballistic armour.

A wide variety of mechanical properties have been found to be linked to ballistic behaviour, including strength [3], hardness [4] and fracture toughness [5]. While these tests can all be carried out in a laboratory setting, no one of these tests has been found to be solely representative of how ceramics will fail under ballistic conditions. This combination of requirements has led to a variety of ceramics seeing widespread use in ballistic armour and is discussed in greater detail in 2.1.3. However, one material that outwardly appears to have very good properties for ballistic protection has not found any commercial use: alumina with the addition of silicon carbide nanoparticles. While alumina can be sintered to full density at temperatures as low as 1300^{O}C, this is not the case in alumina-silicon carbide nanocomposites. In order to achieve a high density in these composites a far higher temperature and hot pressing sintering under inert gas conditions are required [6]. This has rendered the cost of production of alumina-silicon carbide nanocomposites prohibitive compared to the resultant ballistic properties.

Work has been conducted previously on the effect of dopants on grain boundaries in alumina and how this affects the resultant microstructure. This has shown that significant changes can result from very small dopant concentrations [7]. Through the use of these dopants this work aims to change the microstructure of grain boundaries, and thus the overall microstructure, in alumina-silicon carbide composites under conventional sintering conditions rather than the high temperature hot pressing

previously required. This change in microstructure could allow for the production of composites with a similar resultant microstructure, and potentially ballistic properties, to current hot pressed alumina-silicon carbide nanocomposites.

Following this logic this work progresses in the following fashion. Firstly, an investigation is conducted into the effects of sintering alumina-silicon carbide composites under conventional conditions rather than hot pressing. This is combined with an investigation into the oxidation of silicon carbide with the bulk alumina to attempt to understand any observed differences between in-situ oxidation and that measured in both bulk and powdered silicon carbide. Following on from this work, investigations into the effects of various dopants on the conventionally sintered alumina-silicon carbide composites are investigated. Once the preliminary research into various dopants has been conducted, extensive work is carried out on the optimum additive. This includes investigations into the link between the grain boundary structure and the resultant microstructure. Finally, detailed mechanical investigations are carried out into the properties of the optimum composite. This serves both to attempt to derive the best performing composition and sintering conditions, and to link the microstructure seen in the previous research to the final macroscopic properties. Mechanical research culminates in high speed impact testing to determine the ultimate effects of the dopants in a situation as close to ballistic impact as is attainable under relatively simple laboratory conditions.

Before describing this research, however, a literature review must be carried out. Initially the literature surrounding the requirements of ballistic armour and its mechanical failure are assessed and the current generation of ceramic armours described. The literature on the properties of the primary ceramics being used is considered, particularly in regards to the sintering behaviour of alumina and the oxidation of silicon carbide, alongside the work previously conducted on the formation of alumina-silicon carbide nanocomposites through hot pressing. Thereafter, a study of the literature surrounding the formation of grain boundary “complexions” is undertaken with particular interest being paid to their structure and formation in alumina with dopants and how the grain

boundary structure can affect the macroscopic properties. Work on grain boundary faceting as an alternative explanation for the phenomenon of abnormal grain growth is considered and compared to complexions as an explanation. Finally, a note is made on the mechanical testing techniques used and why the parameters chosen are being used compared to other variants of similar techniques that could be available.

2 LITERATURE REVIEW

2.1 ARMOUR DESIGN

2.1.1 History of Armour

Across history, the materials deployed in warfare have played a key role in determining the results of conflicts. As weapons developed over time, from simple flint axe heads to modern day ballistic weapons, they have been matched by an equal need for protection and armour. Throughout much of history, this armour was formed from metal in the form of plates or other coverings. However, more recently other materials have begun to play a very significant role in armour development.

2.1.1.1 Early Ceramic Usage

The first potential transition from purely metal armours to the use of brittle materials was seen in 1918, when Major Monroe-Hopkins noted the improvements in ballistic performance, against small arms, found when a thin enamel layer was added to the surface of a steel plate [8]. However, it was not until 1966 that monolithic ceramic armour was deployed in combat, when airframe mounted ceramic plates were deployed on Huey helicopters. This resulted in a 53% decrease in the rate of fatalities and a decrease in other injuries by 27% compared to prior to the plates' introduction [9]. Current usage of personal ceramic armour is generally in the form of a ceramic plate, backed by either steel or an ultra-high molecular weight polyethylene, which is slotted into a pocket on the front or back of a vest. Vehicular ceramic armour is generally comprised of similar plates that can be tiled together, and replaced if struck, without needing to replace the entire armour system.

2.1.2 Materials Comparison

2.1.2.1 Metallic Armour

Throughout history, the dominant components used in high performance armour have been manufactured from metals. These still find significant usage. This is largely due to the ease of forming and production metals offer [10]. However, as the kinetic energy of projectiles has increased, a significant increase in armour thickness has been required to maintain performance [11], resulting in a significant weight increase of armour. This is due to the high density of metals, or metallic armour being unable to stop specialist high energy projectiles. However, metallic armour systems offer a significant benefit, which is the potential for multiple impact protection. As the ballistic protection offered by metals is often through methods such as plug formation or petalling [12, 13], the nearby material is broadly unaffected so can offer protection against further impacts.

2.1.2.2 Fibre and Polymer Armour

Fibre-reinforced polymer systems offer very attractive structural properties owing to their comparatively low density and high formability [13]. This has made polymer-based systems very popular for use in armour products such as helmets, where these properties are vital. As reinforced polymer systems tend to withstand ballistic impact primarily through local shearing and delamination [14], the lower compressive strength and fracture toughness of even high performance polymers results in a lower ballistic performance than metal or ceramic alternatives [15]. However, these polymers are exceptionally good at absorbing energy and so offer a good choice for backing materials in compound armour plates [16].

2.1.2.3 Ceramic Armour

Ceramics have found a prominent place in ballistic armour technologies owing to their very high compressive strength [17], high hardness and comparatively low density [12], despite the low tensile strength classically seen in ceramics [18, 19]. This is a result of the brittle attributes of ceramics consuming the kinetic energy of the projectile, while simultaneously eroding it away [13, 20].

2.1.3 Current Ceramic Armour

In current armour applications, 3 main ceramic systems have become established as the dominant options: high-purity alumina, silicon carbide and boron carbide [16].

2.1.3.1 Boron Carbide

Owing to its particularly high hardness and low density, boron carbide appears to offer an ideal set of mechanical properties for armour systems [21, 22] and at most ballistic velocities this is the observed result. However, at high ballistic velocities boron carbide is found to undergo a localised phase transformation [16]. At high shock loads, a series of nanoscale amorphous bands from around the point of impact [22-25]. This causes a significant drop in ballistic performance [26, 27], rendering boron carbide an unsuitable material in situations where this kind of threat is expected.

2.1.3.2 Alumina

Despite offering the lowest ballistic performance of the three ceramic options [27], alumina based armour systems still find some usage. This is primarily due to reasonably good ballistic properties being combined with low material and manufacturing costs, which arise because alumina can be manufactured without the use of protective atmospheres during sintering [18].

2.1.3.3 Silicon Carbide

Conversely, silicon carbide offers a high level of ballistic performance across a wide range of projectile velocities [27] with a lower density, and therefore armour weight, than alumina [18]. However, the manufacturing costs of silicon carbide armour are far higher than the alumina alternative, as the oxidation of silicon carbide requires it to be processed in an inert atmosphere. Reaction bonding offers the potential for net shape manufacture of silicon carbide components [16, 28], however uniaxial pressing followed by pressureless sintering is still the dominant manufacturing technique for personal body armour [29]. This is due to the larger density of flaws present in reaction bonded components compared to components manufactured through conventional pressureless sintering techniques [30].

2.1.4 Behaviour of Ceramic Armour

Ballistic protection in ceramics is primarily formed by a combination of three mechanisms. These are: 'Surface Dwell and Interface Effects', 'Conoidal Fracture' and 'Projectile Erosion' [13, 31]. Each of which are shown in Figure 1.

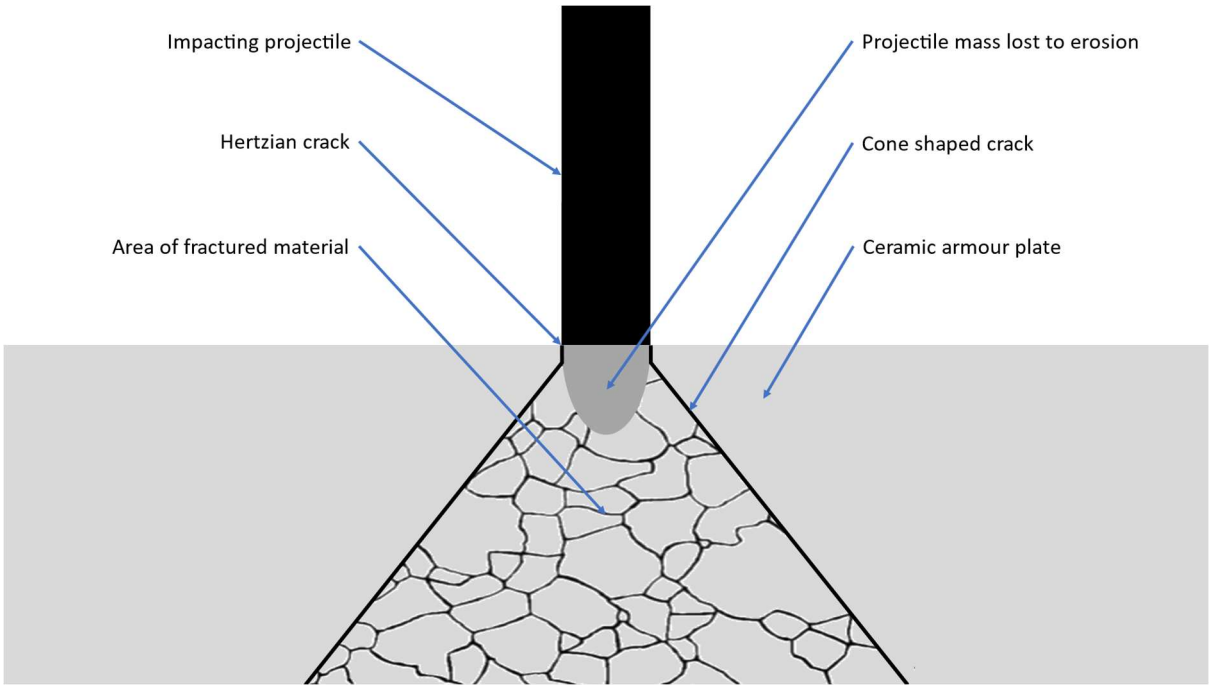


Figure 1: A diagram showing the ballistic protection mechanisms exhibited in ceramic armour systems when struck by a projectile.

2.1.4.1 Ballistic Protection Mechanisms

2.1.4.1.1 Surface Dwell and Interface Effects

If the ceramic plate is harder than the impacting particle, the higher hardness resists the impact load, briefly causing the projectile to lose velocity [32]. Friction between the ceramic plate and the projectile causes the projectile to be ground away as the bullet deforms against the plate. As a result, surface effects reduce the kinetic energy of a ballistic impact through a combination of deceleration and loss of mass due to erosion [33].

2.1.4.1.2 Conoidal Fracture

When the projectile breaches the surface of the ceramic plate, Hertzian cracks form around the point of impact. The formation of these initial cracks is controlled by the activation of flaws surrounding the area of impact, or, failing that, the fracture of the material by the formation of twins and slip nucleating grain boundary cracks [34, 35]. These cracks cause the ceramic plate to fracture along the lines of maximum tensile stress out from the initial failure towards the rear surface of the plate. Therefore, the crack distribution and compressive strength of ceramics used is of vital importance. In brittle materials, this fracture produces a cone shaped crack emanating from the point of impact [13, 20, 36-38]. This serves to redistribute the impact load over a considerably larger area than that of the original impact.

2.1.4.1.3 Projectile Erosion

The core within the conical fracture severely erodes the projectile as it passes through the plate, ejecting material from the plate behind it in the form of spall [13, 38]. Material within the cone crack tends to fracture into multiple pieces and the movement of these fractured pieces creates gaps between them, a process known as bulking. The imperfect packing this produces is responsible for the material ejected from the plate as spall. This process serves to dissipate any remaining energy throughout the ceramic plate and into the backing plate over a significantly larger area than the original impact site [13], thus minimising the risk of total failure. The effectiveness of a ceramic for this role is dependent both on its abrasiveness against the particle passing through it, as well as the amount of bulking the ceramic undergoes during fracture. A greater expansion will cause the ceramic to contract around the projectile, limiting its passage into the armour plate [39].

2.1.4.1.4 Comparative Effectiveness of Mechanisms

While all of these steps absorb the energy of the projectile, some have been shown to have a significantly larger effect than others. Crack formation alone was calculated by *Woodward et al.* [40]

to absorb less than 1% of the total impact energy, while the ejection of material as spall contributed the largest proportion.

2.1.4.2 Component Design

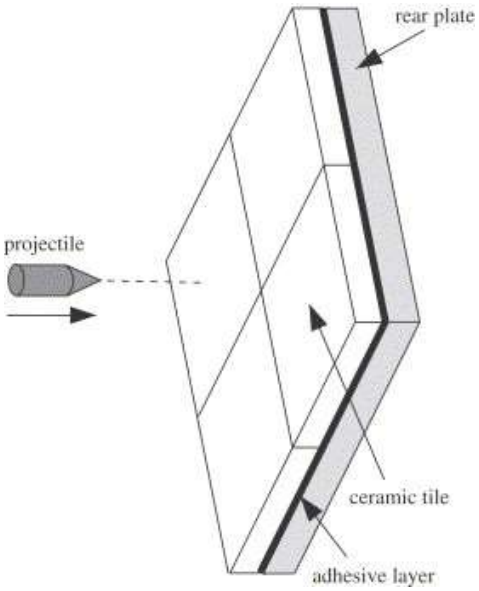


Figure 2: Typical layout of materials in ceramic armour. The projectile is shown prior to striking the protective ceramic tile which has been affixed to the rear plate [44].

In conventional ceramic armour systems, a ceramic plate is stuck to a ductile backing plate formed from either a metal, such as aluminium, or a polymer, such as ultra-high molecular weight polyethylene [16, 41]. This is shown diagrammatically in Figure 2. It is important to note that the formation of axial cracks for reasons other than projectile impact limits the performance of the ceramic front plate. These cracks have the potential to form in the ceramic as the backing plate moves, forcing the ceramic to shift with it [41]. The formation of these cracks could be delayed through the use of a high modulus backing plate to limit the extent of this movement. The performance of ceramic armour can also be improved by pre-stressing the tiles through the use of lateral confinement. This treatment causes a shift in failure mode from complete fragmentation to a more localised failure, as the compressive stress perpendicular to the point of impact causes a reduction in the extent of cracks across the material, resulting in a more localised failure [42, 43].

2.1.5 Mechanical Properties

2.1.6 Compressive Strength

The initial penetration resistance, and therefore the duration of surface dwell, is dominated by the compressive strength of the plate [3]. *Shockey et al.* showed that short projectiles could be entirely defeated if the incoming projectile has a lower strength than the ceramic. This effect is only seen near

the impact end of the projectile however, and therefore the efficacy of a high strength plate as the primary armour is very limited against longer projectiles.

2.1.6.1 Hardness

Woodward et al. showed that a sufficiently hard ceramic will blunt the projectile, causing deceleration and mass loss [4], resulting in a significant improvement in the ballistic properties of the armour. Vickers hardness testing has been shown to display a similar variability in the performance of ceramic plates to the behaviour of the same materials under ballistic testing [45]. This suggests the use of indentation as a possible methodology to identify potential materials for ballistic usage.

2.1.6.2 Fracture Toughness

An increase in fracture toughness results in an increase in the energy absorbed by crack propagation during ballistic impact. This can potentially impart a multi-hit resistance on the ceramic plate [5, 46]. A high fracture toughness also increases the ability of the ceramic to withstand breaking down into a fine spall. This can serve to increases the erosion of the incident particle during penetration, as the ballistic efficiency of the spall is reduced below a critical size [46, 47].

2.1.6.3 Flaw Distribution

The ballistic performance of ceramic plates has been shown to be reduced by up to 9% if the point of impact is directly adjacent to a crack, in comparison to otherwise identical ceramic materials [13]. The static and quasi-static strength of silicon carbide, alumina and boron carbide was shown by *Kaufmann et al.* not to be representative of ballistic performance [27]. They attributed this effect to the very high strain rates present in ballistic impacts activating multiple smaller flaws as they reach a critical stress before a larger flaw further away can fail to relieve them.

In testing, silicon carbide has been shown to possess a far higher density of flaws than alumina [48] despite otherwise similar mechanical properties [49]. The increased flaw density allows a greater number of flaws to be activated by the impacting projectile, thus creating a far greater area of new surface. Similarly, when the ceramic plate is comminuted, the volume the pieces occupy is larger than

the initial volume, as the resultant pieces do not fit perfectly together [39]. The greater distribution of initial cracks present in silicon carbide results in the ceramic fracturing into smaller sections. As a result, the ceramic expands more around the conoidal fracture created by the impact, and subsequently the incident projectile, as it passes through the plate. This causes more erosion of the bullet, and a larger decrease in kinetic energy, than an otherwise equivalent alumina plate [39].

2.2 ALUMINIUM OXIDE

2.2.1 Basics

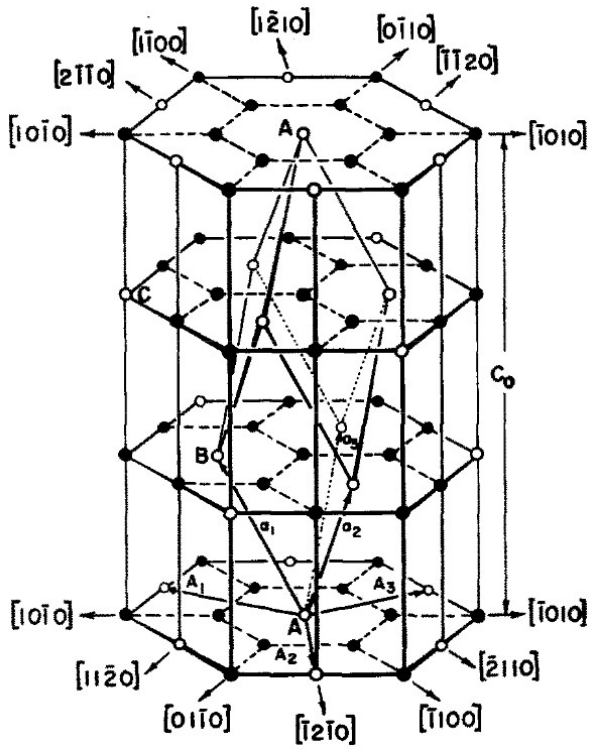


Figure 3: Diagram showing the unit cell of alumina. The rhombohedral unit cell is shown in the centre enclosed by the more convenient hexagonal representation [54].

Aluminium oxide is a widely used engineering ceramic that has found extensive use in applications beyond ballistic protection, such as refractory blocks [50] or street lamps [51]. This is due to the generally favourable properties aluminium oxide displays, such as a good thermal and chemical stability, hardness, and electrical and thermal insulation [50].

The most common polymorph of aluminium oxide, and the one used throughout this project, is α-alumina. It has the corundum structure with a $R\bar{3}c$ space group [52]. While this crystal structure is trigonal [53], it is most convenient to use a hexagonal rather than rhombohedral unit cell as is shown in Figure 3. This crystal structure corresponds to hexagonally close packed oxygen ions with the aluminium ions in two thirds of the octahedral interstitial sites.

2.2.2 Sintering and grain growth

Alumina, without the addition of any additives, has been shown to sinter to densities of 99% at temperatures as low as 1350^{O}C [55]. Most research on the sintering of alumina, however, is performed at temperatures notably higher than this [56-60]. It has been shown that during sintering of alumina up to densities of around 96%, grain growth is observed to be relatively uniform with evenly sized grains throughout the material [55]. At higher densities, abnormal grain growth is observed. This shift can be observed as an increase in the standard deviation of mean grain size, as is shown in Figure 4.

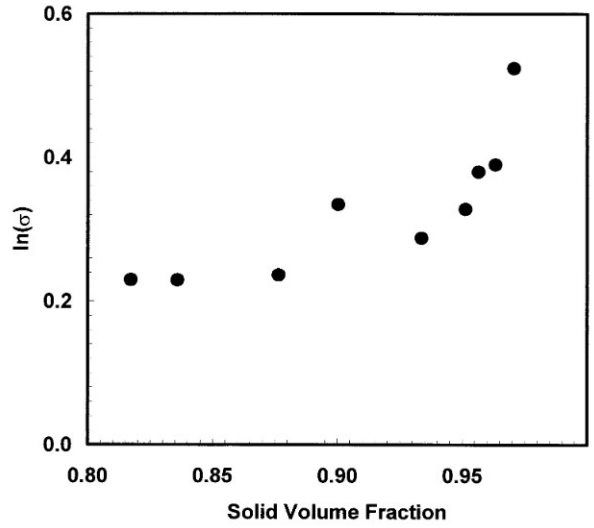


Figure 4: Graph showing the standard deviation in grain size of alumina as a function of density. Standard deviation is plotted logarithmically for clarity [56].

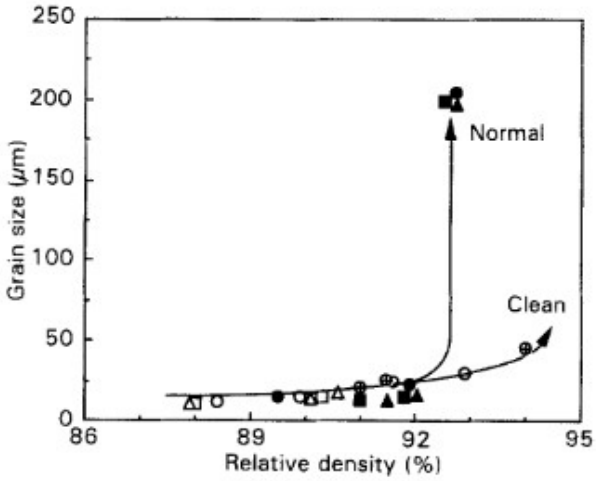


Figure 5: Graph showing mean grain size in alumina sintered at between 1750^{O}C and 1900^{O}C under either normal sintering conditions or ultra clean sintering conditions as a function of relative density [60].

The work of *Nettleship et al [55]*, who carried out this work which demonstrated the development of abnormal grain growth shown in Figure 4, was conducted on alumina with a purity of only 98.8 wt.% alumina. Other work conducted into the effects of additives in alumina has suggested this relatively low purity is the cause of the abnormal grain growth observed at high densities.

Sintering of alumina with an initial purity of 99.999 wt.% has been shown to maintain a consistent microstructure at densities that result in abnormal grain growth in lower purity alumina powders [60]. This work showed that by maintaining an entirely clean sintering environment through the use of a sapphire furnace tube and an argon atmosphere the onset of abnormal grain growth could be delayed to a significantly higher relative density. The difference in mean grain size between alumina sintered under these conditions and alumina sintered in a 99.8 wt.% purity lidded alumina crucible, sintering conditions described as normal, is shown in Figure 5. Therefore, the development of abnormal grains can be attributed to the behaviour of impurities within alumina rather than an intrinsic property of alumina itself.

The effect of many distinct oxide additives in alumina has been investigated and the majority found to inhibit sintering when added intentionally to the powder forming the green body [57]. Notable exceptions to this are the additions of iron oxide, manganese oxide and copper oxide, which all increased measured sintering rate. It was also found, however, that while the addition of any of these three additives promoted sintering, they were also found to promote abnormal grain growth [57] and are likely the cause of the abnormal grain growth seen in otherwise pure alumina [60]. Sintering atmosphere for the processing of alumina has been found to have no effect on the sintering rate up to 98% of theoretical maximum density [56]. Above this density, pore closure limits further densification, as the pressure within the pores exceeds the driving force to remove them. Full theoretical density can be achieved solely in atmospheres of either hydrogen or oxygen [56], however this full densification required sintering for 23 hours at 1900^{O}C. This behaviour was attributed to these gases having a higher solubility in alumina, allowing for the trapped gases to eventually diffuse out of the material after pore closure has occurred.

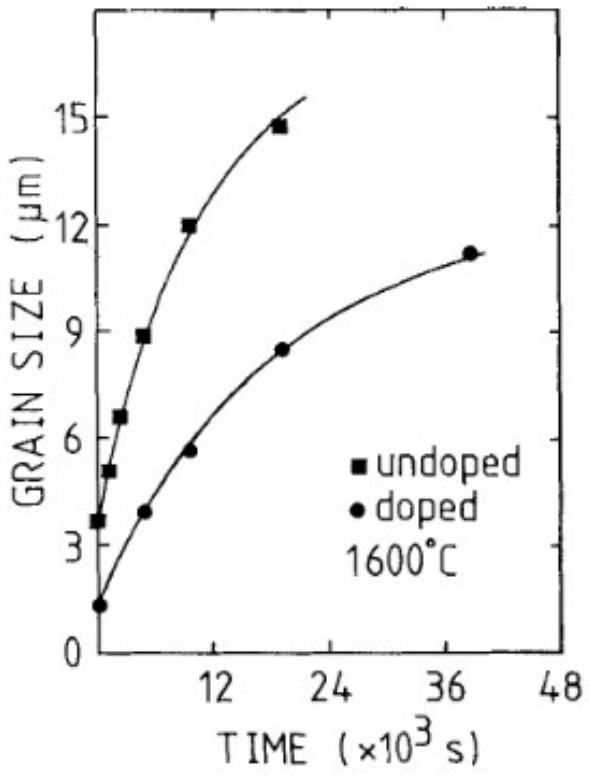


Figure 6: Graph showing the effect of magnesium oxide doping on alumina after sintering at 1660^{O}C for increasing time [62].

A notable additive that has been widely added to alumina is magnesium oxide. The addition of MgO has been shown to retard grain growth in alumina thus preventing the formation of abnormal grains [61-65]. Despite the effects on grain growth seen, MgO-doped alumina has been found to achieve densities of over 95% with additions of only 100 PPM MgO [63]. Further observations of MgO-doped alumina show no liquid phase is formed along the grain boundaries [61, 64]

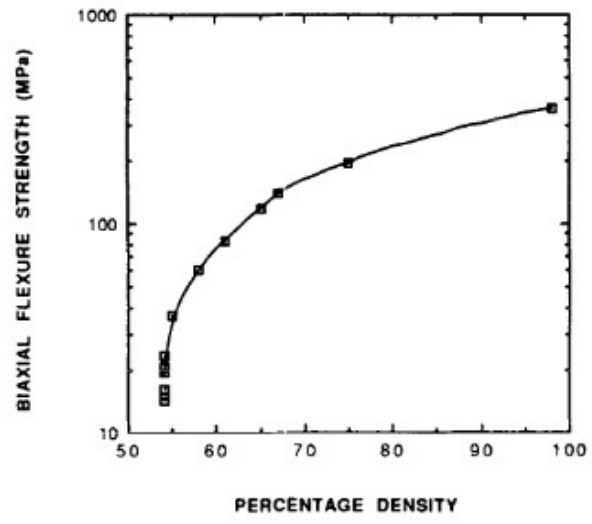


Figure 7: Graph showing the flexural strength of alumina relative to its measured density as a fraction of its theoretical density [66].

The need to achieve high densities in alumina is due to its close links to the measured mechanical properties of alumina. Measurements of fracture toughness, Young's modulus and flexural strength have shown a close dependency on percentage density, with all three measured properties increasing dramatically with increasing density [66]. An example of this correlation, that for flexural strength, is shown in Figure 7. This highlights the importance of achieving a high density in structural alumina. As the majority of additives in alumina hinder sintering [57], this proves a difficult balance in attempting to produce an optimal alumina based ceramic.

2.3 SILICON CARBIDE

2.3.1 General Properties

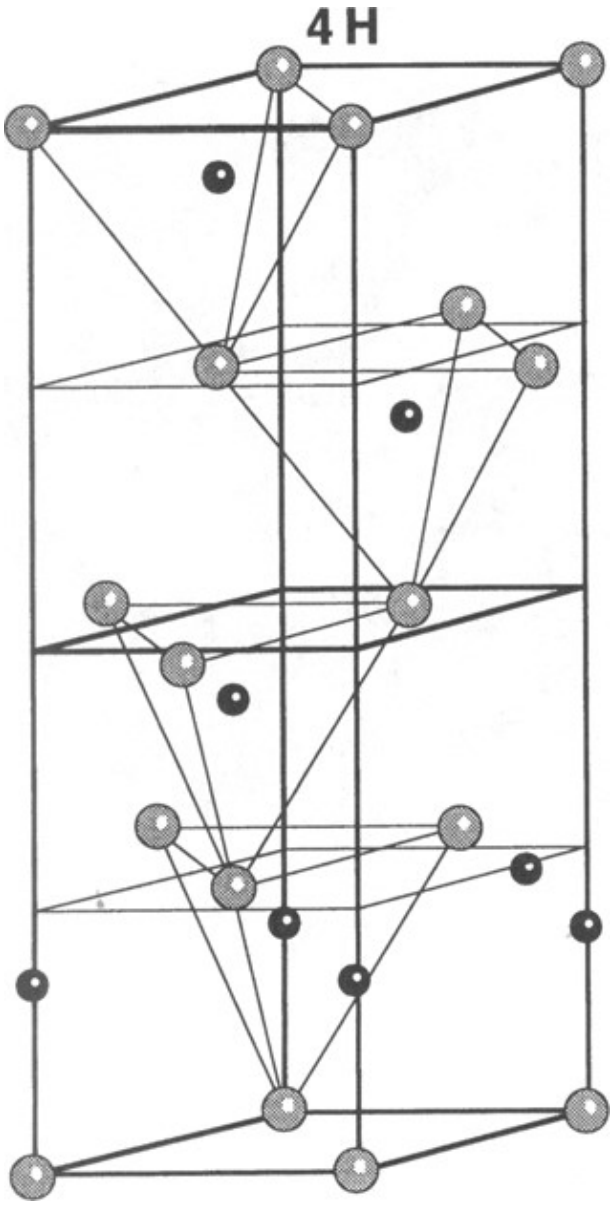


Figure 8: Diagram showing the unit cell of silicon carbide with a 4H lattice structure [71].

Bulk silicon carbide has found uses other than the potential ballistic applications discussed in 2.1.3.3. Owing to its high hardness, silicon carbide has found wide usage in abrasive applications such as grinding or water-jet cutting [67]. Alongside applications due to its mechanical properties, bulk silicon carbide is used widely as a heating element due to its greater stability at higher temperatures than metallic heating elements, and its limited electrical conductivity [68].

The most frequently used series of polymorphs of silicon carbide is α-silicon carbide, which is formed at temperatures above 1700^{O}C [70]. This is the polymorph used throughout this research. It has a hexagonal close packed crystal structure with a P12 space group. Dependent on stacking order present in the alpha silicon carbide the hexagonal phase has a 2H, 4H or 6H lattice structure [71].

2.3.2 Oxidation profile

Dependent on the partial pressure of oxygen in the atmosphere, silicon carbide has been shown to undergo oxidation through two distinct reactions. At low oxygen partial pressures, active oxidation occurs which produces entirely gaseous products. This reaction takes the form of [72]:

$$SiC_{(s)} + O_{2(g)} \rightarrow SiO_{(g)} + CO_{(g)}$$

Conversely, a passive oxidation process occurs at comparatively high oxygen partial pressures. This forms a solid silicon dioxide layer which can inhibit further oxidation. This reaction occurs according to [73]:

$$SiC_{(s)} + 3\ O_{2(g)} \rightarrow 2\ SiO_{2(s)} + 2\ CO_{(g)}$$

It has been shown that at temperatures of 1400^{O}C the transition from passive oxidation to the gaseous products in active oxidation occurs at approximately 3×10^{-4} atm of O_2 [74]. Therefore, under atmospheric conditions the passive oxidation behaviour, described in the second equation, occurs.

These transformations have been shown to commence at temperatures as low as 900^{O}C [75], with the formation of an amorphous silicon carbide layer. As reaction temperature increases, the oxidation rate was seen to increase according to a parabolic Arrhenius equation [73]:

$$w^2 = Ate^{\left(-\frac{E}{RT}\right)}$$

Where *w* is the mass gained during oxidation, *t* is the reaction time, *E* is the activation energy and *T* is the reaction temperature. 900^{O}C is well below the sintering temperature required for silicon carbide containing ceramic components and so this oxidation causes issues in their manufacture. Therefore, in order use silicon carbide as either a ceramic or in a composite, sintering must take place in either a vacuum with a pressure of less than 0.01 Pa or in an inert gas [76].

Investigation of the oxidation of silicon carbide under either atmospheric conditions, or atmospheres with increased oxygen, show the formation of a glassy layer of silicon dioxide on the surface of the

silicon carbide substrate [72, 73, 76-78]. After the formation and growth of the silicon dioxide layer, a significant decrease in oxidation rate was observed [77]. *Costello et al.* attributed this change in sintering rate to the diffusion of oxygen through the silicon dioxide layer as the measured activation energy, 134 kJ/mol in sintered silicon carbide, approached the value for this process [77]. *Singhal et al.,* however, attributed the same effect to the desorption of carbon monoxide from the silicon carbide-silicon dioxide interface [73], while the variations in activation energy seen were due to a high sensitivity in activation energy dependent on temperature. The work of *Singhal et al.* was performed on silicon carbide with the addition of 4wt.% alumina and a variety of other impurities, whereas *Costello et al.* worked in effectively pure silicon carbide. This may explain the discrepancy in results and explanations between the two results. Both works found the formation of silica around the silicon carbide, however, with impurities present, a glassy phase containing the alumina was also found. This phase was shown to affect oxidation rate. Regardless of the underlying cause, it is agreed that the formation of the passivating layer decreases the rate of oxidation considerably. Kinetic modelling of the oxidation of silicon carbide conducted by *Hijikata et al.* found that growth rate of the silicon dioxide passivating layer decreases with thickness [79]. Ultimately a layer of silicon dioxide with a thickness of 0.2 μm was found to be required for the oxidation to be rate limited by diffusion through the passivating layer. This potentially allows for silicon carbide to be retained despite oxidising temperatures and atmospheres, due to the resultant low transformation rates of the diffusion. However, composites with silicon carbide additives rarely contain particles larger in radius than this, so the formation of a passivating silicon dioxide layer offers limited potential for practical use for the preservation of silicon carbide in sintering silicon carbide composites under oxidising conditions.

2.4 Alumina Silicon Carbide Nanocomposites

2.4.1 Microstructure

Generally, alumina silicon carbide nanocomposites are produced by the inclusion of nanosized silicon carbide particles in an alumina matrix. The matrix of alumina has an average grain size of between 2

and 5 microns with the addition of silicon carbide [80-85]. *Chen et al.* found that composites produced with 2.5 vol% silicon carbide in the initial green body, had an average grain size of 4 microns, with 3% of grains having a larger grain size of greater than 8 microns [86]. This work shows the addition of silicon carbide inhibits the growth of abnormal grains in alumina. Comparatively, they found that when hot pressed without the presence of silicon carbide, alumina showed a bimodal microstructure with 13% of grains having a size between 20 and 30 microns.

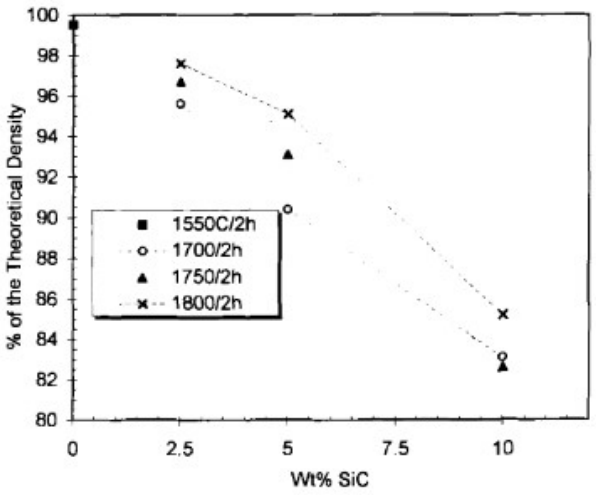


Figure 9: Graph showing the densification behaviour of alumina-silicon carbide nanocomposites with increasing silicon carbide content [6].

Silicon carbide additives in alumina have been shown, however, to hinder sintering in general, rather than exclusively the development of abnormal grains [6, 87]. This is due to the Al_2O_3/SiC interface being inimical to the diffusion process resulting in negligible mobility of the SiC particles. While alumina will sinter to 99% of theoretical density at temperatures as low as 1300^{O}C [87], the addition of silicon carbide renders this level of densification impossible at such low temperatures. In order to counteract this, and produce high density alumina-silicon carbide nanocomposites, hot pressing at temperatures of 1700^{O}C and pressures of 25 MPa has been required [6].

Transmission electron microscopy imaging of alumina-silicon carbide nanocomposites shows silicon carbide grains distinctly within the larger alumina grains [88]. An example of one of these silicon carbide particles is shown in Figure 10. Silicon carbide nanoparticles have also been found along grain boundaries between alumina grains [85, 89]. Measurements of the silicon carbide nanoparticles show that an increase in silicon carbide content results in an increase in the percentage of particles located on grain boundaries. With the addition of 1 vol.% silicon carbide, 23 vol.% of nanoparticles are situated on grain boundaries, and comparatively with the addition of 11 vol.% silicon carbide, 41 vol.% of nanoparticles are located on grain boundaries. This effect was attributed to grain boundaries preferentially taking up sites which pass through silicon carbide particles with increasing frequency with a greater initial silicon carbide addition [85]. The distance between two distinct silicon carbide nanoparticles varies with the initial quantity added. With an addition of 5 wt.% silicon carbide prior to sintering, interparticle spacing is approximately 400 nm on average [89].

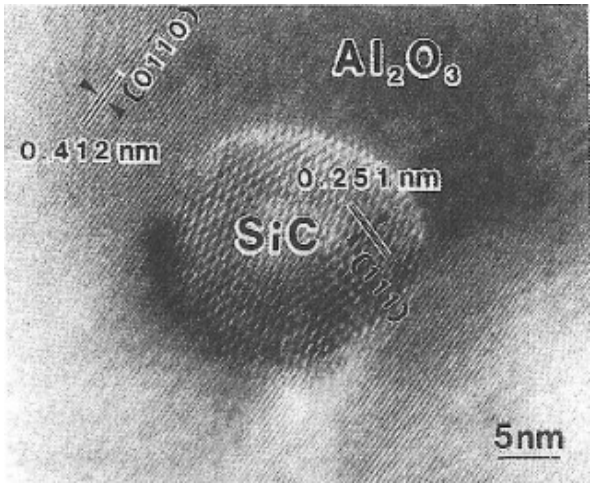


Figure 10: Transmission electron microscopy image showing a nano-sized silicon carbide particle within a larger alumina grain [88].

2.4.2 Oxidation in Alumina Silicon Carbide Nanocomposites

In alumina-SiC composites, another stage of transformation is possible in silicon carbide additions beyond the oxidation in air to silica discussed in 2.3.2. The alumina-silica phase diagram has been widely studied [90-94] and a hybrid phase, named mullite, has been found. Mullite has been determined to be stable at alumina weight percentages of 78 alumina wt.% for temperatures of 1890 ^{O}C [93]. This stability changes at lower temperatures, with mullite being found at percentages between 70 and 75 alumina wt.% at temperatures of 1600 ^{O}C and below [90-92]. This suggests that, during sintering in air, silicon carbide particles will undergo a transformation from silicon carbide to ultimately

result in the formation of mullite; a result reflected in the fact that much of the work studying alumina-mullite composites utilises a silicon carbide precursor [95-99].

When this transformation to mullite has occurred in alumina-silicon carbide composites, a lack of consistent results has been found regarding the distribution of the resultant mullite particles. Researchers, such as *Burgos-Montes et al.* found the observed mullite distributed solely along grain boundaries, with the largest particles being located at triple points within the network [99], while others found a distribution of mullite containing both intra- and inter-granular particles [95-98]. It was noted by *Luo et al.* that the mullite particles found on grain boundaries were considerably larger than those found embedded within the alumina grains [96]. However these intergranular particles have been shown to make up a very small fraction of the total number of particles [95]. This result explains the discrepancy between these works and *Burgos-Montes et al.,* as the finer mullite particles may not have been visible under the scanning electron microscopy techniques used, whereas the larger particles situated on grain boundaries would have been. This mixed intra- and intergranular distribution may be an effect of the initial transformation from silicon carbide to silica, rather than that from silica to mullite, as when silica is used as an initial reactant, mullite nanoparticles were found to decorate grain boundaries exclusively [98].

2.4.3 Mechanical and Failure Properties

2.4.3.1 Mechanical Properties

The earliest reports showing an improvement in the mechanical properties of alumina due to the inclusion of nano-scale particles were by *Niihara* [88]. He reported an improvement after annealing of 430% in strength over pure alumina with the inclusion of 5 vol.% silicon carbide. However, this level of improvement has not been reported in any other paper looking at the same composition [6, 89, 100, 101]. Other groups found that strengths of a similar order to that found by *Niihara* could be found only when nanocomposite samples had been surface ground extensively and then annealed. Instead, strength improvements of around 30% have been more generally found. While *Zhao et al.* believed

this process, and the consequent addition of compressive surface stresses, are exclusively responsible for the improvement in material properties [100], further work found that the increase in strength could be attributed to the shift in failure mode from intergranular to a combination of intergranular and transgranular [6, 89, 102] or the presence, and processing, of the silicon carbide, resulting in a smaller grain and flaw size in the final composite [101]. This conclusion is further supported by the work of *Jiao et al.* [89] who examined alumina-silicon carbide nanocomposites under transmission electron microscopy. They found intragranular silicon carbide particles frequently deflect cracks from grain boundaries into the grain itself, implying crack deflection is a significant toughening mechanism. Work by *Hansson et al.* [103] found that the shift to transgranular failure in an alumina-silicon carbide whisker composite increased fracture toughness by around 58%. While this is not exactly the same material as used by *Jiao et al.* [89], the derivation used does not rely on the silicon carbide structure and so the increased toughness should be generally comparable.

While the strength benefits of nano-scale silicon carbide additions found by *Niihara* have been widely found to be significantly exaggerated, the addition of silicon carbide particles has been found to offer a significant increase in wear resistance [80, 81, 104]. This improvement has been widely attributed to the same shift in failure mode that is seen to improve the strength of these nanocomposites, this being the shift from intergranular to a combination of intergranular and transgranular [6, 102, 104]. In this case, the new failure mode allows far smaller surface pull-outs during wear. It was found during testing that for nanocomposites with a high silicon carbide content, mean pull-out diameters were around 2 microns [81]. In fine grained alumina and alumina nanocomposites, almost all cracks will encounter a grain boundary before completing an arc of this diameter. For pure alumina samples that undergo intergranular fracture, these cracks will often continue along the grain boundary resulting in a far larger volume of sample being removed than would otherwise be the case. As a result of this, the wear rate of alumina has a strong dependence on grain size, with increased grain size leading to an increasing wear rate [80]. Conversely the transgranular nature of fracture in alumina-silicon carbide nanocomposites eliminates the dependence between grain size and wear rate as wear occurs in the

same size pull outs regardless of the size of the grains. This phenomenon is reflected further in the work of *Limpichaipanit and Todd* [80], where they found that in the plastic zone beneath an indentation there was a marked decrease in the quantity and size of pull-out by brittle fracture on subsequent polishing away of the indentation with increasing silicon carbide content. However, they found this effect was due to the silicon carbide nanoparticles preventing dislocation movement and therefore reducing the maximum pile-up length and stress concentration, preventing crack initiation.

This benefit in wear resistance is also seen in alumina-mullite nanocomposites [96, 105]. The improved wear resistance of these composites has been found to be due to the same phenomenon as in alumina-silicon carbide composites, where the reduction of area of pull-out due to the transition of fracture mode. Due to alumina's higher thermal expansion coefficient [106, 107], the areas around the mullite particles will be under compression while the remainder of the matrix will be under tension. This stress field has been shown to increase the fracture toughness [108], as the compressive regions act to close up the tip of the incipient crack. While the model proposed by *Taya et al.* [108] used a matrix in compression, rather than the tension seen in alumina-mullite composites, the principle remains the same. As this strengthening effect increases with mullite fraction, a larger mullite content results in transgranular failure becoming a more dominant failure mechanism. It is likely this is a similar methodology to the improvement in wear resistance seen in the similar alumina-silicon carbide composites, as the same shift in failure mode can be found in alumina-mullite composites as in alumina-silicon carbide composites [99].

2.5 COMPLEXIONS IN ALUMINA

2.5.1 Nature of Complexions

The existence of two dimensional phase transformations along grain boundaries was first proposed over 50 years ago [109] but the development of more modern characterisation techniques was required before their existence could be confirmed. These interfacial phases have become known as complexions [110]. The use of atomic resolution transmission electron microscopy in particular has allowed for the characterisation of distinct complexion phases. In doped alumina, this has resulted in six distinct complexion structures being identified [7, 111-115]. These complexions are typically defined as:

- Type I
    - Dopant cations situate themselves within the largest interstitial sites along the grain boundary creating a sub-monolayer structure.
- Type II
    - No dopant segregation occurs to grain boundaries and a boundary identical to that found in undoped alumina is found.
- Type III
    - Dopant segregation produces a grain boundary with either a single, or double, layer of a distinct phase.
- Type IV
    - The grain boundary contains a disordered layer with a thickness of around 0.6 nm. This is typical of multilayer absorption.
- Type V
    - An intergranular film with a thickness of between 1 and 2 nm is formed along the grain boundary.

- Type VI
    - A complete wetting is observed between the grains producing a film of thickness on the order of 10 nm.

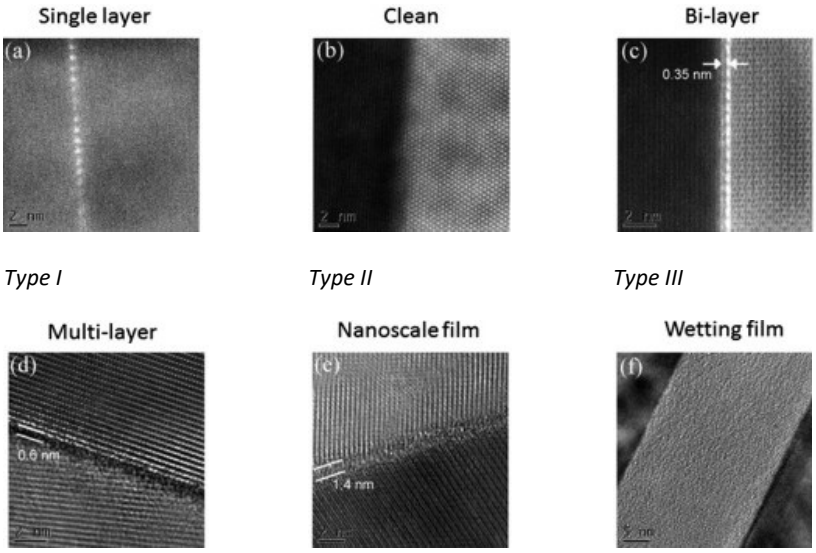


Figure 11: Transmission electron microscopy images showing the 6 types of complexions characterised above. [114]

The transformation between these distinct complexion types has been closely linked to processing temperature [111], along with dopant additions alongside the alumina matrix. This transformation has lead research into attempts to construct phase diagrams for the complexion systems [114, 116]. It has been shown however, that in calcia-doped alumina systems, four distinct grain boundary complexion types can coexist at a single temperature [112]. This suggests that a property beyond merely composition and temperature is affecting the type of complexion formed in this system. However, multiple complexion species are not observed concurrently in silica-doped alumina [113], implying that the nature of dopant additions plays a significant role not just in the type of complexion formed at a given temperature, but also in the interactions between distinct complexions and the kinetics required for the transformation between them.

As the type of complexion found on a grain boundary increases in thickness and complexity, from type I to type IV, the mobility of the grain boundary has been found to similarly increase [111, 114]. This effect has been used to explain the formation of abnormal grains within ceramics, as a higher mobility

in a certain grain boundary leads to a faster expansion in those grains, relative to its neighbours. Therefore, these grains expand out and consume the surrounding grains. The effect of this behaviour can be clearly seen by observing the structure of a grain boundary. The boundaries of abnormal grains in alumina were found by *Cantwell et al.* to have a structure of Type IV, while other grain boundaries had a structure typical of Type III [7], and in the work of *MacLaren et al.* where silicon and yttrium doping of alumina produced a highly disordered boundary around abnormal grains [117]. This effect is also reflected in the relative grain boundary energies, as grain boundaries around abnormal grains have been shown to possess a lower energy than grain boundaries between regular grains [7, 118]. This explanation for abnormal grain growth is reflected in the comparative work of *Dillon and Harmer* [112]. The addition of solely calcia dopants to alumina produced up to 4 distinct types of complexion concurrently and showed clear formation of abnormal grains. Conversely, a similar addition of purely silica dopants produced an identical complexion along all grain boundaries, resulting in a normal distribution of grains [113]. The presence of simultaneous distinct complexions has led to the creation of complexion phase diagrams containing complexion coexistence regions between the other distinct complexions [7].

The addition of multiple dopants simultaneously results in the formation of grain boundaries distinct from those formed through the sole addition of additives such as calcia. *Brydson et al.* showed the addition of calcia and silica to alumina produced a consistent 1.4 nm thick grain boundary throughout the ceramic [119]. This boundary shows a primary segregation of calcium, resulting in a nominal composition of $CaO{\cdot}6Al_2O_3$ along the grain boundaries with silicon segregating to triple points. This effect is seen regardless of the additive percentage, provided the silica and calcia are added in equal quantities. If a larger quantity of silica than calcia is added, the grain boundaries show a similar increase in silicon concentration [120]. When the ratio of added silica to calcia is 10:1, this results in a boundary containing between 0.5 and 2.0 monolayers of silicon and between 0.15 and 0.4 monolayers of calcium as opposed to the nominal composition of $CaO{\cdot}6Al_2O_3$ seen when they are added in approximately equal quantities. This shift in grain boundary structure has also been shown to cause

an improvement in the overall wear resistance of the ceramic over the addition of calcia or silica alone, with the optimum wear resistance being found at the ratio of 10:1 mentioned previously. The structure of grain boundary observed in this high silica ceramic matches the predictions of *Blonski and Garofalini* [121] who found the addition of calcium atoms increased the level of order in alumina grain boundaries that had been wetted by silica. Addition of magnesium nitrate and silica has been shown by *Galusek et al.* to produce a similar reduction in wear rate to the addition of calcia and silica [122]. This effect was attributed to the strengthening of grain boundaries resulting in a shift in failure mode from the intergranular failure of pure alumina to an intragranular wear pattern.

2.5.2 Grain Boundary Tuning

The modification of grain boundaries in ceramics has been shown to significantly alter resultant macroscopic properties. Traditionally, this has involved the formation of glassy phases along grain boundaries as these phases dominate the behaviour of liquid phase sintered ceramics [123]. However, with the development in the understanding of complexions, far greater control over grain boundary properties is possible. The addition of sub-monolayer complexions in ceramics has been shown to offer a significant improvement in fracture toughness over undoped specimens manufactured in the same way [124-127]. This effect is due to a significant increase in grain boundary strength limiting the amount of intergranular fracture in ceramics such as alumina, where this would otherwise be the dominant failure mechanism [124, 125, 127, 128]. Similarly, a multilayer complexion has been shown to weaken grain boundaries and thus to change the macroscopic properties of the resultant ceramics [124, 129, 130]. In the case of alumina this causes a reduction in ceramic toughness as intergranular failure is further promoted [124]. The formation of these multilayer complexions in alumina was found to be promoted by the addition of silica at all processing temperatures [113, 124] but can also be found at elevated temperatures in yttria [124] or calcia [112] doped specimens. If the distribution of grain boundaries can be controlled, an intentionally embrittled grain boundary can cause significant crack deflection away from an ideal crack path. *Daniel et al.* demonstrated that this methodology can produce an increase in fracture toughness of up to 150% without an equivalent loss of hardness [130].

2.5.2.1 Specific additives

2.5.2.1.1 Calcium

The addition of calcium compounds to alumina green bodies has been found to produce 4 distinct complexion phases, as was described in 2.5.1 [112]. Transmission electron microscopy analysis of these grain boundaries allow for the identification of these phases. The boundaries in normal grains were found to contain no intergranular film [112] but thermal grooving measurement showed a variation in energy from the grain boundaries in undoped alumina [131]. This identifies the boundaries in normal grains as type III complexions. Conversely the boundaries in abnormal grains have been seen to display type IV, V and VI complexions in various grains [112]. Modelling of the local environment around the grain boundary shows that these thicker grain boundaries (types IV, V and VI) take the form of a disordered interface with the thickness dependent on local calcium content [120, 121]

2.5.2.1.2 Yttrium

Yttrium compounds have been shown to form type I complexions when added to alumina [128]. This is due to the arrangement of grain boundary structure at certain angles. A tilt angle of 18^{O} about the [0001] axis between the two alumina grains creates a periodic grain boundary structure with a large open seven atom ring unit. This open ring creates a preferential site for yttrium ions to sit along grain boundaries as a sub monolayer type I complexion. A Z-contrast STEM image demonstrating this structure is shown in Figure 12. The very low grain boundary mobility seen in yttrium doped alumina [132, 133] is caused by this grain boundary structure [111]. At other angles, grain boundaries have been shown to form a bilayer, a type III complexion [131]. This grain boundary structure has a higher mobility than the sub-monolayer structure seen in Figure 12, and so leads to the formation of abnormal grains, as the grain boundaries with a type III complexion structure grow significantly faster than those with a type I structure.

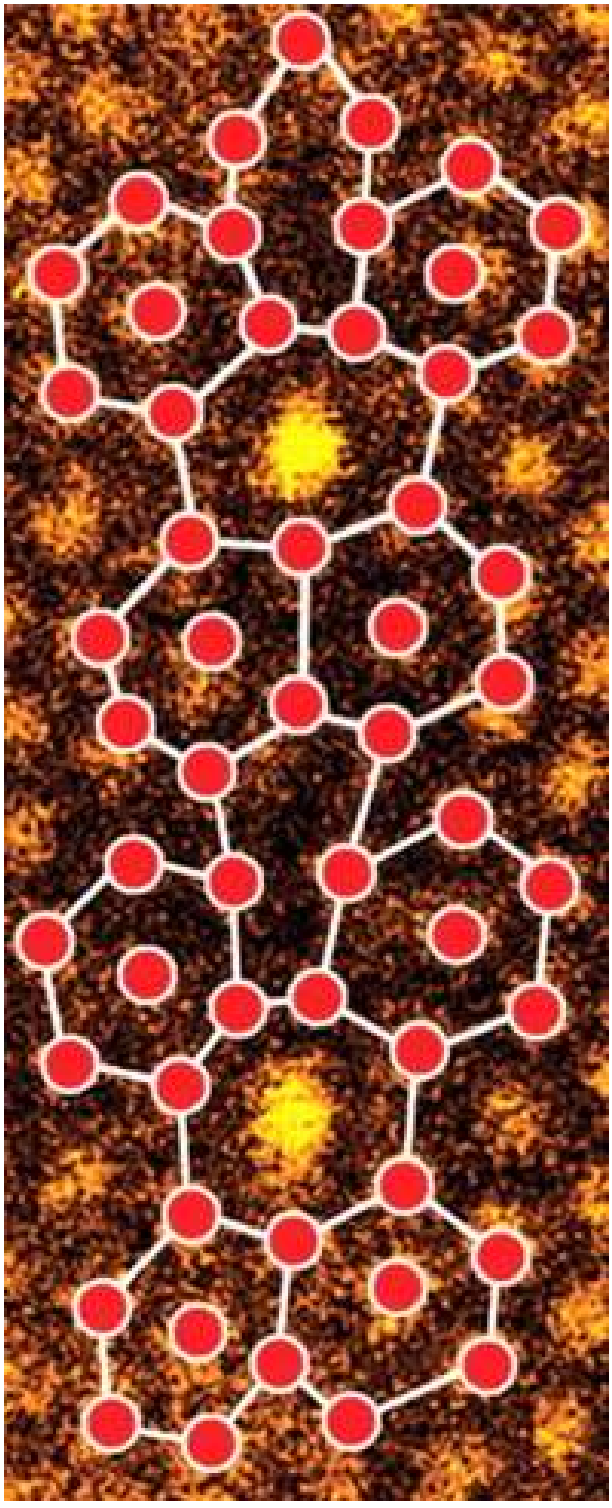


Figure 12: Z-contrast STEM image of yttrium doped alumina along an 18^{O} tilt grain boundary along the [0001] axis. Heavier yttrium ions can be seen in the open seven member rings. The aluminium ion columns are overlayed to allow for more easy identification of the structure [128].

2.5.2.1.3 Neodymium

Complexion structure in alumina with neodymium additions has been shown to form a bimodal microstructure in a similar fashion to the addition of yttrium described in 2.5.2.1.2. A sub-monolayer grain boundary has been identified between normal grains through the use of high angle dark field scanning transmission electron microscopy [114]. While a significant quantity of abnormal grain growth occurs in alumina doped with neodymium, the grain boundary structure surrounding the abnormal grains has 2 distinct forms. At sintering temperatures of 1400^{O}C, the grain boundaries surrounding abnormal grains have a bilayer structure [131]. This takes the form of a type III complexion. Investigations carried out on neodymium doped alumina sintered at 1800^{O}C showed a grain boundary film with a consistent thickness of 0.6 nm [134]. Transmission electron microscopy imaging of this intergranular film shows a multilayer absorption structure of the form of a type IV complexion. This film has been shown to have internal segregation of neodymium ions. The core contains a lower quantity of neodymium ions than the edges of the film, as the dopant ions appear to preferentially segregate to the aluminium sites at the edges of the grains adjacent to the grain boundary.

2.5.2.1.4 Magnesium

Unlike the other dopants considered in 2.5.2.1, the addition of magnesium ions results in the formation of only one distinct complexion at each studied sintering temperature [131]. This effect has been used to explain the role of magnesia in preventing abnormal grain growth in alumina, as magnesium doped alumina samples do not display the abnormal grain growth seen in many doped alumina compositions [114]. Without a higher mobility grain boundary created by a higher order complexion, there is far less ability for initial movement of a grain boundary required for the formation of abnormal grains to occur. At sintering temperatures of 1400^{O}C, the addition of magnesium results in the formation of a sub-monolayer type I complexion [131]. Comparatively, after sintering at 1700^{O}C magnesium ions form a type III bilayer complexion along the grain boundaries.

2.6 Grain Boundary Faceting

While complexions have offered an explanation for the formation of abnormal grain growth- the creation of a different grain boundary structure leading to higher grain boundary mobility in certain grains- an additional explanation has been proposed that does not rely on the chemical structure of grain boundaries.

2.6.1 Principles of Grain Boundary Faceting

If grain boundary energy is uniform across all the grains prior to grain growth, it has been shown that abnormal grains do not grow at a rate higher than their normal neighbours and so cannot form [135]. Notably this effect is still seen if some initial grains are larger than others prior to grain growth, as the increased growth rate will not outstrip that of the smaller grains sufficiently to lead to abnormal grain growth. Therefore, an explanation other than purely grain boundary energy must be the cause of abnormal grain growth.

In many metals, some grain boundary misorientation angles have a preferential arrangement which result in a lower grain boundary energy. The most obvious of these preferential arrangements is a low angle grain boundary as a deviation of 0^{O} a direct continuation of the atomic structure. When a grain boundary possesses one of these lower energy structures it tends to maintain this misorientation angle to keep the low energy structure [136, 137]. As a result, the grain boundary remains straight with facets inclined to the primary direction of the grain boundary, as opposed to the smooth curved grain boundary that would be otherwise seen. In aluminium, the transition of grain boundaries from straight to curved has been shown to occur at misorientation angles of 15^{O} [136].

Through the comparison of nickel samples annealed at varying temperatures, the presence of faceted grain boundaries was required to observe abnormal grain growth [138]. If all grain boundaries possessed a rough curved structure, normal isotropic growth occurred. Conversely if a fraction of grain

boundaries are faceted, abnormal grain growth is observed. The same effect can be seen in samples of stainless steel [139] or barium titanate [140], with faceted grain boundaries seen only in samples containing abnormal grain growth. Faceted grain boundaries in metals progress by transferring atoms to the steps of the growing grains, moving the facet along the grain boundary and the grain boundary forwards [141]. This growth mechanism has a lower required driving force for growth than in equivalent non-faceted grain boundaries [142] and increases velocity non-linearly with driving energy. The increased velocity of these faceted grain boundaries has been used to explain the formation of abnormal grains. An example of this logic is provided by *Fisher et al.* [143] who used it to explain the effect of alumina doping on barium titanate. The segregation of dopant atoms to the dislocation component of the faceted grain boundary reduces the free energy of the dislocation and thus the grain boundary as a whole. This results in an increase in growth rate in the barium titanate grains and the formation of abnormal grains.

It should be noted, however, that the correlation between abnormal grains and grain boundary faceting may not be causal. Instead, both effects may be caused by grain boundary segregation independently. This explanation would support a complexion-based theory of abnormal grain growth, particularly in the case of a large increase in grain boundary mobility above a certain driving force, as the grain boundary breaks away from the ions pinning it in place due to segregation. This has been observed to be the case in grain boundaries in both sodium chloride [144] and in iron doped with silicon, nitrogen or boron [145], however not in the case of alumina.

2.6.2 Faceting in Alumina

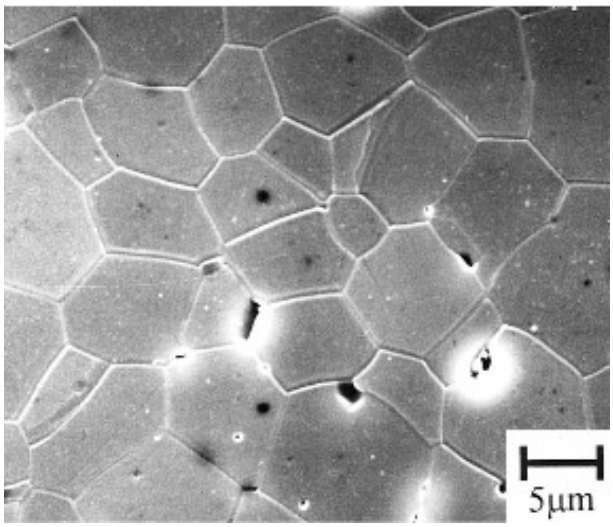


Figure 13: SEM micrograph of pure alumina sintered at 1620^{O}C for 12 h [61].

When sintered at temperatures of 1200^{O}C or higher, pure alumina has been found to form a grain structure of approximately uniformly sized equiaxed grains [61, 146] as can be seen in Figure 13. Transmission electron microscopy observations of these grain boundaries in pure alumina have shown that these grain boundaries curve smoothly without faceting [61]. This curvature suggests grain boundaries in alumina are atomically rough under these conditions. After heat treatments at lower temperatures, 900^{O}C, around 30% of grain boundaries between the basal plain of an alumina grain and a neighbouring grain were shown under transmission electron microscopy analysis to be kinked with flat boundary segments between them [146]. An example of an alumina grain boundary formed in this way is shown in Figure 14*. Kim et al*. note that the formation of these kinks is reversible through further heat treatment, as heat treatment at 1400^{O}C returns the grain boundaries to their original curved state [146]. The formation of these facets and their positions are controlled by the lowest energy planes in alumina. The Wulff shape gives the orientation of the lowest energy grain boundaries; in alumina this construction shows a significant preference for grain boundaries along the basal plane [147]. This preference is the cause of faceting seen in low angle alumina grain boundaries across the basal plain, such as those seen by *Carter et al.* [148]. Particular higher angle grain boundaries can also be seen to facet; however, this occurs only at certain special angles. Most notably two misorientation angles, other than slight



Figure 14: Transmission electron microscopy image showing a faceted grain boundary in alumina after sintering at 1400^{O}C for 3h and heat treating at 1000^{O}C for 4 days [148].

misorientation across the basal plane, were seen to create faceted grain boundaries in pure alumina [149]. A rhombohedral twin grain boundary in alumina occurs parallel to the $[1\bar{2}10]$ direction with a displacement of the $[0001]$ axis by 65^{O} [150, 151]. In this case the major facet lies along the common $(1\bar{1}02)$ plane in both grains, while the smaller facet lies parallel to the (0001) plane [149]. The other high angle grain boundary found by *Morrisey and Carter* to form facets corresponds to a misorientation of 27.8^{O} between the two grains [149]. This has the effect of bringing the $[11\bar{2}0]$ of one grain into coincidence with the $[01\bar{1}0]$ direction of the other grain. In a similar fashion to the previous boundary discussed, this grain boundary also tends to facet along the (0001) plane.

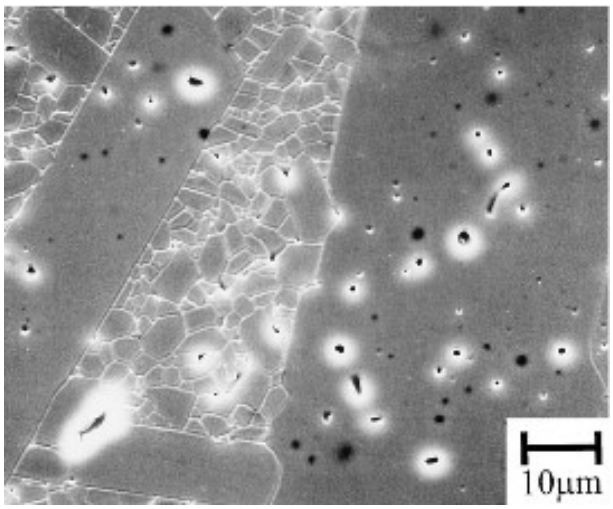


Figure 15: Scanning electron microscopy image of the abnormal grain growth seen in alumina with the addition of 100 PPM silicon dioxide and 50 PPM calcium oxide after sintering for 12 h at 1620^{O}C [61].

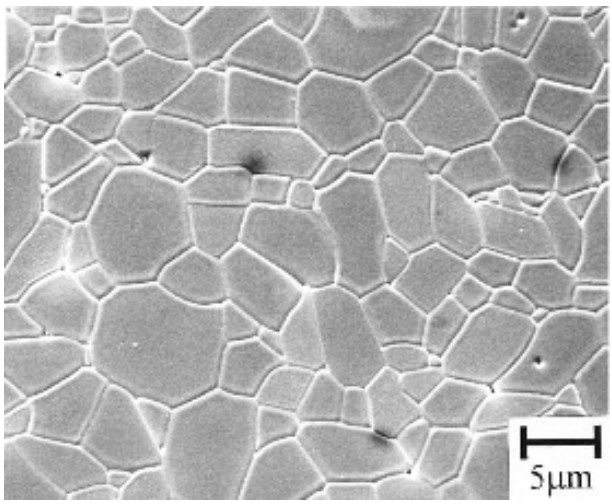


Figure 16: Scanning electron microscopy image of the grain growth seen in alumina with the addition of 100 PPM silicon dioxide, 50 PPM calcium oxide, and 600 PPM magnesium oxide after sintering for 12 h at 1620^{O}C [61].

While the doping of alumina has been shown to affect grain boundary structure and the resultant microstructure, as described in 2.5.2.1; the doping of alumina has also been shown to modify the faceting behaviour. Most of this work has focussed on the behaviour of alumina with the addition of silicon dioxide to the green body. Sintering at around 1600^{O}C with the addition of either 100 PPM silicon dioxide [61] or 800 PPM silicon dioxide [152] resulted in abnormal grain growth in the alumina. This took the form of large, elongated grains surrounded by straight grain boundaries, as can be clearly seen in Figure 15. Transmission electron microscopy of this

microstructure shows the long straight grain boundaries coincide with the (0001) planes of the abnormal grains [61]. A closer examination of the grain boundaries in the fine matrix grains shows that approximately 10% of these grain boundaries appear straight and are faceted when examined through transmission electron microscopy. The addition of magnesium oxide alongside silicon dioxide, however, was seen to entirely negate the growth of these abnormal grains. Instead, a microstructure very similar to that of pure alumina under the same sintering conditions was produced, with evenly sized equiaxed grains as can be seen in Figure 16. Microscopy of the grain boundaries in this material showed no faceting with the boundaries appearing to be uniformly curved regardless of magnification [61]. This change was attributed to the addition of magnesium oxide decreasing the free energy of the facet, and therefore reducing the driving force for the formation of faceted grain boundaries. Measurements of excess concentration of dopants was conducted on grain boundaries produced by the doping of alumina with both silica and magnesia. Calculation of the density of aluminium atoms along the $(11\bar{2}0)$ plane gives a base line atomic density of approximately 10 atoms/nm^2 [152] and therefore this is the density considered a monolayer coverage. Silicon coverage in samples doped with silica and calcia was measured as 22.5 atoms/nm^2, which suggests the formation of a bilayer similar to that seen by *Brydson et al*. [120] in a similar composition. Comparatively, samples doped with magnesia showed a magnesium concentration of 2.8 atoms/nm^2, significantly less than required to form a full monolayer. This analysis was not conducted, however, on grain boundaries in samples co-doped with silica and magnesia that produced the uniaxed microstructure seen in Figure 16.

The doping of alumina with 500 PPM hafnium has also been shown to promote the formation of faceted grain boundaries. While multiple different facetted grain boundaries have been observed in pure alumina, the only observed facet found in hafnium doped alumina lies along the (0001) plane with the smaller facets lying parallel to the $(\bar{2}110)$ plane [153]. This faceting was observed at hot pressing temperatures of 1400^{O}C, a temperature which would prevent the formation of facets in pure alumina [146]. Alumina with the addition of 1000 PPM yttrium was also found by *Gülgün et al.* to form faceted grain boundaries despite hot pressing at temperatures of 1475 ^{O}C [154]. Notably in addition

to the more commonly seen low angle basal grain boundaries seen in both alumina and hafnium doped alumina, a rhombohedral twin grain boundary was identified. In this case while all grain boundaries were found to be decorated with yttrium, the excess concentration of yttrium was measured to be 3.3 ± 0.9 atoms/nm^2 [154]. This corresponds to, at most, a half monolayer, which reflects the work discussed in 2.5.2.1.2, as the presence of yttrium leads to the formation of type I complexions.

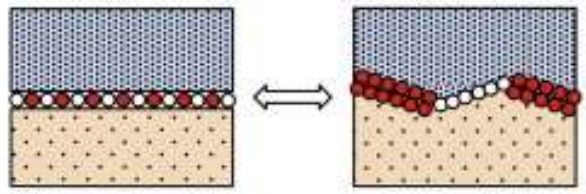


Figure 17: Schematic representation of the formation of distinct facets from a single complexion without a change in overall misorientation [7].

The formation of facetted grain boundaries discussed above has been attempted to be explained through complexions. A single complexion grain boundary is considered to decompose into two distinct compositions [7]. Each new complexion has a different inclination and forms one of the facets used to explain the changes in grain boundary mobility seen. This transformation is shown in Figure 17. The faceting transformation has been demonstrated in this form in Bi-doped Cu [155]. This work found that of the two facets comprising the faceted grain boundary, one had a Bi-rich bilayer complexion while the other possessed a clean complexion. As different complexion structures posses different grain boundary energies this would promote the same growth of one facet over the other discussed above through a purely faceting based approach.

2.7 MECHANICAL TESTING

2.7.1 Hardness

Indentation hardness measurements are performed across a wide range of weight scales. Macroindentation testing is usually used to describe testing loads of around 1 kgf or greater. This results in an indentation large enough to measure the macroscopic hardness of materials. The size of these indents is sufficient that the primary diagonals can be measured easily using optical microscopy without a significant error in the calculated hardness measurement [156]. Measurements can be limited, however, due to cracking and spalling. Under the lowest testing loads, a crack free impression can be created even in ceramics; though at loads capable of producing indentations that can be measured accurately under optical microscopy, a crack free indentation is very unlikely to be formed. Initial crack formation originates from the 4 corners of the indentation, with subsequent lateral cracks causing sections of the surface around the impression to pull away from the surface as spalling [157]. These effects can render measurement of the impression left behind after indentation difficult or even impossible depending on the severity of the cracking, as is shown in Figure 18.

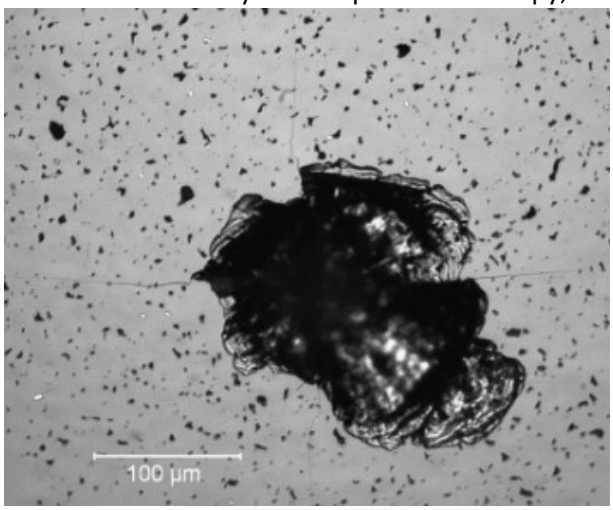


Figure 18: Optical microscopy image of a Vickers indentation in boron carbide showing severe spalling and cracking around the indentation [157].

Additional complications in the measurement of the ceramic hardness arise from indentation size effects. A comparison between measured hardness and indentation size shows a significant increase in hardness with decreasing indentation size, as is demonstrated in Figure 19. This effect has been

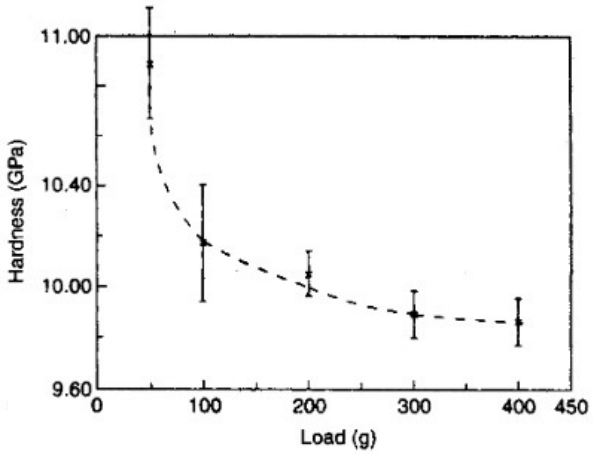


Figure 19: Graph showing the variation in measured hardness of Al-Cu-Co polycrystals demonstrating the indentation size effect [167].

observed in a variety of ceramics, including alumina [158], silicon carbide [158], boron carbide [159] and silicon nitride [160]. These phenomena can be described empirically through Meyer's law [161]:

$$P_{max} = Ah_c{}^n$$

where P_{max} is the peak indentation load and h_c is the contact depth for the same indent. A and n are constants derived from curve fitting experimental data. Indentation size effects are often attributed to the shift from exclusively elastic deformation at the lowest loads to plastic deformation at higher loads [158, 159] and the subsequent formation of radial and lateral cracks at higher loads [162]. The deformation seen in nanoindentations has been shown to occur in discrete bands of plastic deformation with any intermediate deformation forming from recoverable elastic deformation [158] and this forms the basis of the elastic recovery model suggested by *Tarkanian et al.* [163]. The elastic recovery model suggests the true hardness, H_0, can be found using the formula:

$$H_0 = kPd + d_0{}^2$$

where d_0 is the correction in indentation size, d, due to the elastic recovery once the indenter is removed, P is the indentation load and k is a constant dependent on the indenter geometry being used. Testing of this model, however, has shown it results in unrealistic values of d_0 [160]. Therefore, the indentation size effect cannot be fully explained through elastic recovery alone, and a more complex explanation must be derived to fully explain the phenomenon.

The elastic recovery discussed above, under unloading of the indenter, has the largest effect on nanoindentations as the recovery forms a larger fraction of the overall indentation size. In order to

attempt to negate this effect, *Oliver and Pharr* measured the unloading curves after indentations [165]. These curves were found to be described by the power law relation:

$$P = A\left(h - h_f\right)^m$$

where P is the load, h is the true depth of the indent under the load, h_f is the depth of the observed indent after the indenters removal and A and m are material constants. The resultant methodology allows for the prediction of contact area under the maximum load by extrapolation from the measurements of the final indentation size. This has become widely used in nanoindentation analysis [166, 167]. This method does require accurate knowledge of several key apparatus quantities such as load frame compliance and the area function of the diamond indenter. These parameters do not vary between measurements, however, so the Oliver-Pharr method offers an attractive means of measuring nanoindentations in materials.

2.7.2 Wear Resistance

The measurement of wear resistance is carried out using an exceptionally wide variety of different methods. A meta-analysis by *Owen-Jones and Gee* [168] identified 21 distinct methodologies used in different papers to calculate the wear resistance of samples. Stylistic grouping of these techniques shows three categories of test: eroding the sample through blasting the sample with a powder, grinding the sample against a solid abrasive surface, and eroding the sample through a wet slurry.

2.7.2.1 Powder Slurry Blasting Tests

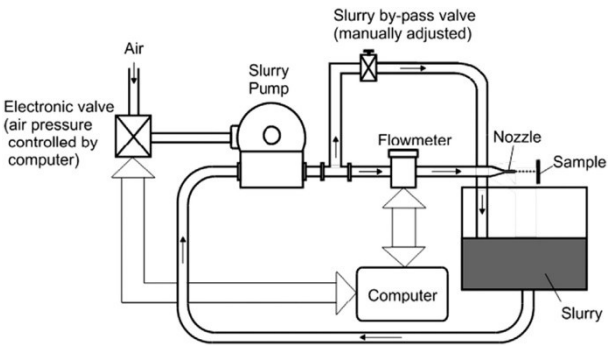


Figure 20: Schematic diagram showing a jet erosion setup [171].

Blasting samples with a powder slurry, using an apparatus such as the one shown in Figure 20, provides a particularly good model for erosion in situations where the component is constantly under a liquid flow, but does also allow modelling of other erosion conditions [168]. Testing of this style under a variety of parameters, such as nozzle geometry and slurry concentration, has shown

significant variation in erosion rate across multiple tests [169]. As a result, the measured hardness values calculated from this methodology can show significant deviation from the results seen in field tests under what would be expected to be similar conditions [170].

2.7.2.2 Solid Abrasive Grinding Tests

Wear resistance testing through solid based methodologies takes on a wide variety of geometries. The simplest of these geometries is a Taber abrasion test [172], which consists of a pair of abrading wheels that rotate across the surface of the sample for a defined number of rotations, but other methodologies include a tri-pin-on-disc methodology [86, 173], where 3 wear pins were loaded and rotated on the surface of the sample, and a ball-on-plate configuration [174], which drives a ball bearing into the same area of the surface of the sample repeatedly. As the same material is used for the entire erosion in each of these methods, the erosion of the wear mechanism can reduce the reproducibility and reliability of testing methods based on solid abrasive materials.

2.7.2.3 Wet Slurry Tests

Wet slurry tests act as a hybrid between the solid abrasive tests and the powder blasting tests. A rotating ball bearing acts to transfer a grinding powder slurry onto the sample continually during testing, either through a drip feed onto the sphere [175-177] or by immersing the lower half of the rotating sphere in the slurry [178]. This prevents the variations seen in solid testing, as the sphere is not abrading the sample, and so remains more consistent throughout testing. To maintain a consistent slurry, the mixture is stirred constantly throughout and recirculated through the system. Due to the recirculation described, it is possible for abraded material to enter circulation and change the composition of the slurry [168], however this issue can be easily negated through the use of a sufficiently large reservoir. Due to the reliability and comparability of wet slurry testing, alongside the relative simplicity of the method, this technique has been chosen for use in this research.

2.7.3 Fracture Toughness

Macroscopic fracture toughness testing of ceramics is performed through the bend testing to failure of ceramics with a known initial flaw size and shape that can be measured either before or after fracture. Traditionally this has taken the form of one of 4 primary testing geometries [179, 180]. These distinct geometries are shown schematically in Figure 21.

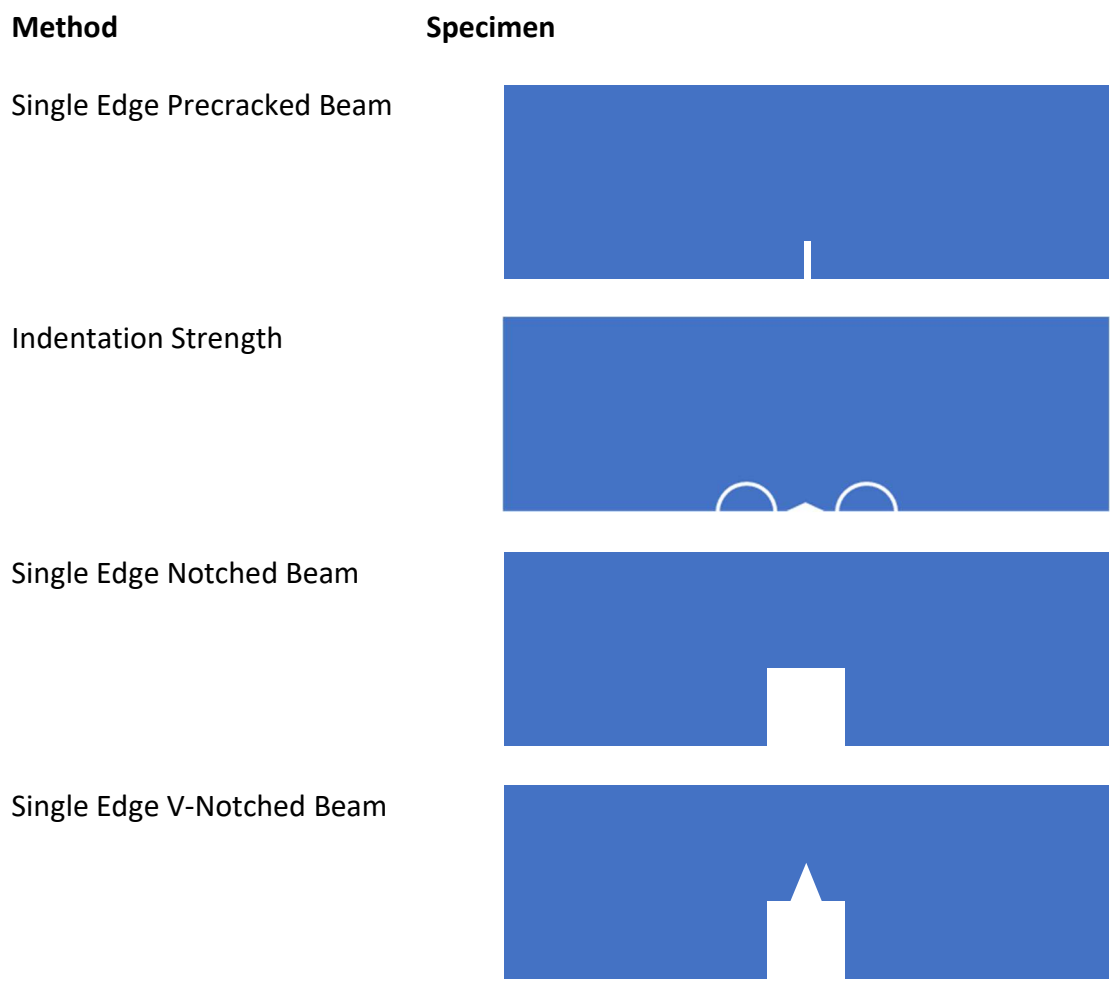


Figure 21: schematic diagrams showing the 4 conventional fracture toughness testing geometries.

2.7.3.1 Single Edge Precracked Beams

Single edge precracked beams have been shown to produce the sharpest pre-failure tip among the methodologies regularly used [181]. This is known to be important for the accurate determination of fracture toughness [182], as crack radius increases the stress intensity factor and so the measured fracture toughness is above the true value [183]. A pre-crack is generated by the bridge-indentation

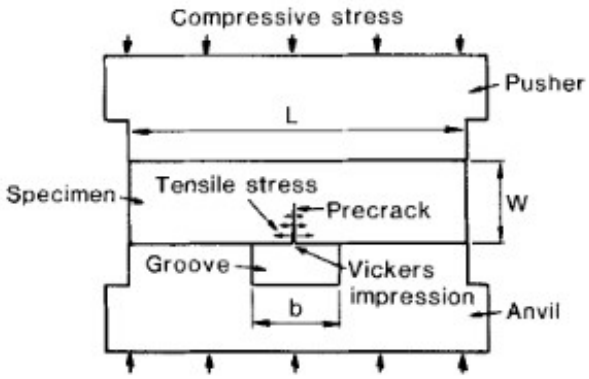


Figure 22: Schematic representation of the bridge-indentation method showing the sample sandwiched between a flat pusher and the bridge shaped anvil [185].

method [184, 185]; the sample is loaded on either side of a trigger such as a scratch. This geometry is shown in Figure 22. Loading in this format creates a tensile stress around the inciting scratch until the crack pops-in. The comparison of multiple tests conducted using this method shows limited variation in fracture toughness due to the length of the precrack generated [185], and this is reflected in an excellent reproducibility of results carried out in this fashion across multiple laboratories [181]. Difficulties have been reported in this methodology, however, and this has prevented its universal usage. Most notably among these flaws are, a high failure rate in the formation of precracks due to factors such as unwanted changes in the precrack path causing growth in different planes and the frequent growth of excessively long precracks [186].

2.7.3.2 Indentation Strength

Indentation strength tests rely on the formation of surface flaws due to the indentation of the sample's surface. Once the residual stress area around the indentation has been removed, bend testing can be conducted with the cracks generated around the indent acting as the initial flaw. This methodology has a tendency to produce precracks with a very small size, rendering the test unsuitable for materials with a coarse microstructure or a high porosity [187]. Difficulty in measurement of the fracture toughness by this method also stems from difficulty in performing fractographic analysis. Variations in measurements of the size and shape of the precrack were responsible for the high variability of results, with *Quinn and Lloyd* finding in some case multiple different fracture toughness values had been found from the same sample due to differing initial precrack size measurements [182].

2.7.3.3 Single Edge Notched Beams

Compared to the notches produced in the other methodologies shown in Figure 21, single edged notched beams form a significantly wider crack tip, as the crack is produced through the use of a saw disk [188]. While this does result in a more reliable and consistent measurement of fracture toughness [189], the crack tip radius has a significant effect on the measured fracture toughness, with a larger crack tip resulting in a higher measured fracture toughness [190]. This resulted in a measured fracture toughness between 11% and 67% higher than the value found through other methods dependent on the ceramic being studied [180].

2.7.3.4 Single Edged V-Notched Beams

Single edge V-notched beams offer a compromise between the reliability of single edged notched beams while offering a significantly narrower crack tip. Despite the simple production method, a razor blade oscillating in the crack sharpened with diamond paste, crack tip radii as low as 10 µm can be generated [191]. This is a very reliable production method with multiple studies finding a very small spread of measured results across multiple laboratories and testing apparatus [180, 192-194]. Due to the combination of the simplicity of manufacture, limited chance of failure and reliability in results, this is the geometry used in this research.

2.7.3.4.1 Notch Bluntness

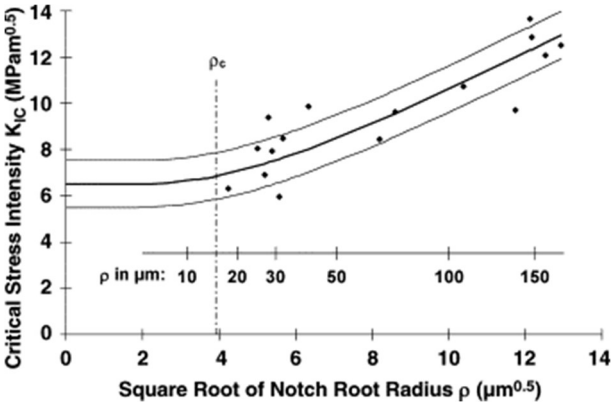


Figure 23: Graph showing the calculated fracture toughness of zirconia samples fractured after notching with cracks with varying radii [195].

The effect of crack tip radius on the final calculated fracture toughness in single edged V-notched beams can be clearly seen by the production of specimens with varying notch radii. While a narrower crack tip has been shown to result in a lower measured fracture toughness, there exists a critical value below which the measured value is consistent [195]. This effect

can be seen in a wide variety of ceramics such as alumina, silicon carbide, silicon nitride, and zirconia [196]. This correlation follows that predicted by *Fett* [197] and allows for the calculation of a critical notch size regardless of the presence of cracks with a radius smaller than this critical value. If cracks are produced with a sufficiently sharp tip, such that is below the critical value, the measured fracture toughness is very similar to that measured in single edge precracked beams. Experimentally, this critical notch root radius is approximately the same as the size of the major microstructural feature in the bulk of the sample [195, 196], often found to be the size of the largest grains within the sample.

3 OBJECTIVES

Extensive work has been carried out previously into alumina-silicon carbide composites that have been hot pressed in an inert atmosphere to prevent oxidation. Particular interest has been paid to the beneficial properties these composites display compared to pure alumina. However, far less work has been conducted into the mechanical effects of these composites if oxidation has been allowed to occur during conventional sintering techniques. In a similar fashion, a considerable body of work has been conducted into the effects on the modification of grain boundary structures due to doping by various metal oxides. However, the effects of combining alumina with silicon carbide particles and subsequent doping by a metal oxide have not been well studied. As a result of this the primary objectives of this project are:

1. Investigation into alumina-silicon carbide composites
    - Both the macroscopic and microscopic properties of alumina-silicon carbide composites are investigated when sintered in air under conventional conditions. This is used to attempt to optimise the sintering conditions and level of dopants required to achieve the optimum mechanical properties.
2. Investigation into alumina-silicon carbide-metal oxide composites
    - The effects on macroscopic properties, such as Vickers hardness and relative density, between alumina-silicon carbide composites and equivalent alumina-silicon carbide-metal oxide composites are studied. This is linked to the grain structure for each additive considered.
3. Optimisation of the best performing alumina-silicon carbide-metal oxide composite
    - After preliminary investigations into the effects of various metal oxides the best performing metal oxide additive is chosen for further study. The effects of variations in sintering conditions and additive quantities are investigated in this composite to determine the best performing overall composition.

4. Study of the grain boundaries in the alumina-silicon carbide-metal oxide composite
    - Through the use of transmission electron microscopy and nanoindentations the structure of the grain boundaries in the best performing composite discovered above are investigated. This structure is linked to the resultant microstructure and ultimately the macroscopic properties.
5. High speed projectile testing for comparison
    - High speed testing of alumina, alumina-silicon carbide, and the best performing alumina-silicon carbide-metal oxide composite is conducted using a gas gun to determine how the changes in bulk properties and microstructure have affected the behaviour of the materials under catastrophic failure due to a projectile. This is as close to a true ballistic test as can be conducted within our laboratory.

4 MATERIALS AND METHODS

4.1 MATERIALS

4.1.1 Alumina

Taimicron TM-DAR powder (Taimei Chemicals Co. Ltd., Tokyo, Japan) was used throughout the project to produce alumina samples. The mean particle size was 230±5 nm and the powder purity was >99.99% with the maximum potential impurities being as follows [198]:

Ca:	0.003%
Cr:	0.002%
Fe:	0.008%
K:	0.004%
Mg:	0.003%
Na:	0.008%
Si:	0.010%

This material was chosen due to its small particle size and high purity. Thus, investigations into the effects of very small quantities of additives could be conducted as was carried out in this work.

4.1.2 Silicon Carbide

UF25 silicon carbide powder (Logitech Ltd., Glasgow, United Kingdom) was added to alumina powders during manufacture. The mean particle size was 293±5 nm and the powder purity was 97.60% with the maximum potential impurities being as follows [199]:

Al:	0.30%
C:	0.50%
Fe:	0.24%
Si:	0.80%
SiO_2:	0.60%

This SiC powder was chosen as it possesses a similar particle size to the alumina powder with very little particle agglomeration seen during the measurement of particle size. This helps aid mixing and prevents the clumping of SiC during powder processing.

4.1.3 Dopants

Various dopants were used to modify alumina samples during manufacture throughout this work. The details of these dopants are tabulated below in Figure 24 [200-203]. These powders were chosen in an effort to correspond to those used in other work investigating the effects of low concentration additives on grain boundary structures in alumina, alongside their relatively high purity ensuring the modifications seen in the resultant microstructures arose from the effects of the chosen additives rather than any other impurities.

Dopant	Calcium Nitrate	Neodymium Nitrate	Magnesium Nitrate	Yttrium Oxide
Source	Alfa Aesar, Tewksbury, United States	Alfa Aesar, Tewksbury, United States	Sigma-Aldrich, St. Louis, United States	Alfa Aesar, Tewksbury, United States
Purity / %	>99.98	>99.99	>99.0	>99.995
Maximum Potential Impurities / %	Sr 0.050 Rb 0.010 Na 0.005 $CaCl_2$ 0.020 $CaSO_4$ 0.020 $Ca_3(PO_4)_2$ 0.010	Rare Earth Oxides 0.100	Ca 0.500 K 0.010 Na 0.010 $MgCl_2$ 0.005 $MgSO_4$ 0.005	CaO 0.010 Dy_2O_3 0.005 Er_2O_3 0.010 Ho_2O_3 0.050 K_2O 0.010 Na_2O 0.010 SiO_2 0.010

Figure 24: table showing the purity and the maximum potential impurities in the dopants used throughout this thesis.

4.1.4 Sample Manufacture

Samples of Al_2O_3 were produced with combinations of various quantities of SiC and transition metal compounds. Powders were ball milled for 24 hours using alumina milling media, with a diameter of approximately 5 mm, and a slurry of ethanol and the powder mixture. Ball milling was conducted in a polyethylene bottle filled to 20 % of the height of the bottle with powder slurry (without the milling media) and 30 % of the height of the bottle with milling media. The resultant slurry was dried through rotary evaporation, for a period of around 45 minutes, to completely remove the ethanol and leave a dry powder, which was then sieved to produce a usable powder consistency.

To manufacture ceramic sample disks, 5 g of powder was uniaxially cold pressed at a pressure of 50 MPa for 5 minutes in a 32 mm diameter steel die. The uniaxially pressed disks were then cold

isostatically pressed at 200 MPa for 5 minutes to finish production of the green body. Green bodies were then sintered in a tube furnace in air. The sintering was conducted in an open alumina crucible to minimise interactions between the green body and the furnace tube and allow for the sample to be easily removed following sintering. All samples were sintered with a heating rate of 10 ^{O}C/min and a cooling rate of 25 ^{O}C/min regardless of sintering temperature and time.

4.2 In Situ Testing

4.2.1 Thermogravimetric Analysis

The changes in mass of samples during sintering was analysed through the use of thermogravimetric analysis through the use of a Netzsch Jupiter STA 449 F3. Green body disks were prepared in the same fashion as described in 4.1.4. Due to the size limitations of the crucibles used in thermogravimetric analysis, segments of the green body approximately 0.3 cm in diameter were fractured off the larger green body for testing. These segments were weighed and sintered in air at 1550 ^{O}C in the TGA for 4 hours following the heating profile outlined in 4.1.4.

Changes in weight observed during this sintering were normalised against a blank profile created under the same heating schedule using an empty crucible to ensure any observed changes originated purely from the measured sample. Weights were normalised as a percentage of the starting mass of each sample, as fracturing the green body results in irregular shaped specimens with distinct masses between samples.

4.2.2 X-Ray Tomography

In order to determine if any variations in density are present in the green body prior to sintering, X-ray tomography of the pressed green body was performed by Professor James Marrow. Samples were manufactured using the method described in 4.1.4 without sintering to produce pressed green bodies. Limitations of the testing methodology prevented full green bodies from being tested. Therefore, in a

similar fashion to 4.2.1, the green body was fractured to produce samples with a diameter of around 1 mm.

As the voxel size in the X-ray tomography is approximately 1 µm and resolution of a pore requires it to be present in at least 8 voxels, pores are unlikely to be individually resolvable. Therefore, a histogram of voxel brightness across all slices was taken. The spread of brightness in the resultant histogram corresponds to the spread of density observed. A larger fraction of the tomography data with a lower-than-average brightness would correspond to increased porosity not individually resolvable. If individual pores are not resolvable, the distribution of X-ray intensity across the entirety of the measured sample can be plotted as a histogram of pixel brightness across the entire series of slices. This allows for variations in density to be observed without individual particles being identifiable.

4.3 Characterisation of Materials

4.3.1 Particle Size Measurement

Particle size was measured through the use of a Malvern Zetasizer Lab. 0.1 g of powder was mixed with 0.002 g of Dispex A40 and diluted with 50 ml of distilled water to create a suspension of powder. 1 ml of powder suspension was transferred to the Zetasizer vessel before being scanned to measure both volume and diameter particle size distributions.

4.3.2 Grain Size

Average grain size was determined through the use of the mean-linear-intercept method. Samples manufactured using the method described in 4.1.4 were sectioned to expose an internal surface close to the centre of the disc. The exposed surface was polished to a finish of 1 µm and thermally etched for 15 minutes at a temperature 50 ^{O}C below the original sintering temperature with the same heating and cooling profile. After etching, the polished surfaces were coated in a 5 µm layer of gold to ensure electrical conductivity and micrographed in a scanning electron microscope. Lines covering the width

of the SEM images were drawn at random angles and the number of intercepts counted. The average grain size along this line was then calculated by dividing the total length of the line by the number of intercepts observed. For samples containing a large number of abnormal grains, additional steps were taken to give separate grain sizes for both abnormal and regular grain sizes. For the measurement of normal grains, only the segments of the lines drawn passing through normal grains were considered for the number of intercepts and length of the line. The 3-dimensional grain size was then determined using a multiplication factor of 1.57 [204]. Abnormal grain sizes were calculated by measuring the size of grains intercepted by the randomly generated lines. The longest dimension of the abnormal grain and its perpendicular dimension were measured to produce an average dimension for the abnormal grain. 5 different random lines were drawn for each sample and the average grain size and error were calculated using the mean and standard deviation across the 5 calculated grain sizes taken from these lines. This typically resulted in between 25 and 40 intercepts per line taken across the micrographs.

4.3.3 Abnormal Grain Fraction

The fraction of grains displaying abnormal growth was determined by overlaying a grid of 150 points evenly distributed over the images produced in 4.3.2. This grid consisted of an array of 15 points across by 10 points tall offset by a random amount in both the x and y dimensions. An example of this is shown in Figure 25. Each point was determined visually to be within either an abnormal grain or a regularly sized grain and the respective fraction of each calculated.

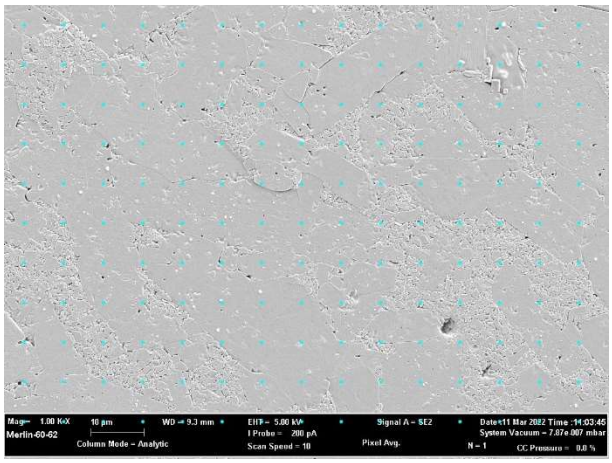


Figure 25: SEM image showing the microstructure of Al_2O_3-1wt%SiC-500PPMY_2O_3 overlayed with a grid of points for the determination of the abnormal grain fraction.

4.3.4 Particle Analysis

In order to analyse 2nd phase particles, the SEM images taken in 4.3.2 were again used. A random distribution of 25 particles were taken from across the image and the diameter of each was measured. This was used to calculate the mean diameter using a multiplication factor of 1.27. This is derived in 10. Total particle area was then found by counting the number of subgranular grains within a typical area of microstructure and multiplying by the mean cross sectional area. This results in a volume fraction of subgranular particles calculated from the ratio between the total particle area and the total area scanned.

4.3.5 Density



Figure 26: Photograph of the scales used for Archimedes testing with a sample submerged in the beneath the scales in the cage to be weighed

Sample density was measured using the Archimedes method. Following sample manufacture and sintering, as described in 4.1.4, the dry mass, m_{dry}, of samples was measured 5 times before being submerged in boiling water to ensure stable infiltration of water throughout all the porosity of the samples. The saturated samples were submerged in a cage beneath the scales, Figure 26, and the weight of the submerged sample was recorded, m_{wet}. The sample was then removed from the cage. The saturated mass, m_{sat}, was finally measured by placing both sides of the sample on tissue paper to dry the surface of any excess water, then recording the weight in air. Repeating the submerged and saturated measurements 5 times allows for mean values of all masses to be found.

Density of samples could then be calculated using the following equation:

$$\rho_{sample} = \frac{m_{dry}}{m_{sat} - m_{wet}} \times \rho_{H_2O} \; [g\ cm^{-3}]$$

4.3.6 EDX

EDX in scanning electron microscopy was carried out on the samples produced during 4.3.2 using a Zeiss Merlin at 5 kV and a probe current of 200 pA. Resultant spectra were analysed using AZTEC software to produce maps of elemental distribution within samples.

4.3.7 Transmission Electron Microscopy

Transmission electron microscopy samples were produced using Focussed Ion Beam milling using a Zeiss Nvision FIB-SEM. Samples were produced in the same fashion as 4.3.2. A layer of carbon was deposited on the surface of the sample in a rectangle 20 µm by 2 µm to a depth of around 2 µm. The deposition was deliberately centred on an area of interest to be investigated, such as the grain boundary of an abnormal grain. Material was removed on either side of the carbon out to a distance of 20 µm and a depth of 10 µm, with a milling current of 6 nA. After milling, both newly created surfaces were polished with a milling current of 1.5 nA to remove any defects created during material removal by the higher current used. The sample was tilted to $54^{O,}$ and a section etched away in a column on one side and along the bottom of the sample to allow for later removal. This process is shown in Figure 27.

Lift-out was then performed to place the sample on a copper grid for TEM. A needle was inserted into the microscope and positioned against the surface of the sample, before being welded to the sample using a 2 µm x 2 µm square of carbon. The final side of the sample was milled away to entirely separate it from the original material.

After removing the sample from its original location, it was welded into place on the copper grid using carbon and the needle removed from the other end of the sample. In order to achieve electron

transparency, the sample was then thinned using a current from 300 pA to 80 pA until the sample had a thickness of around 1 µm.

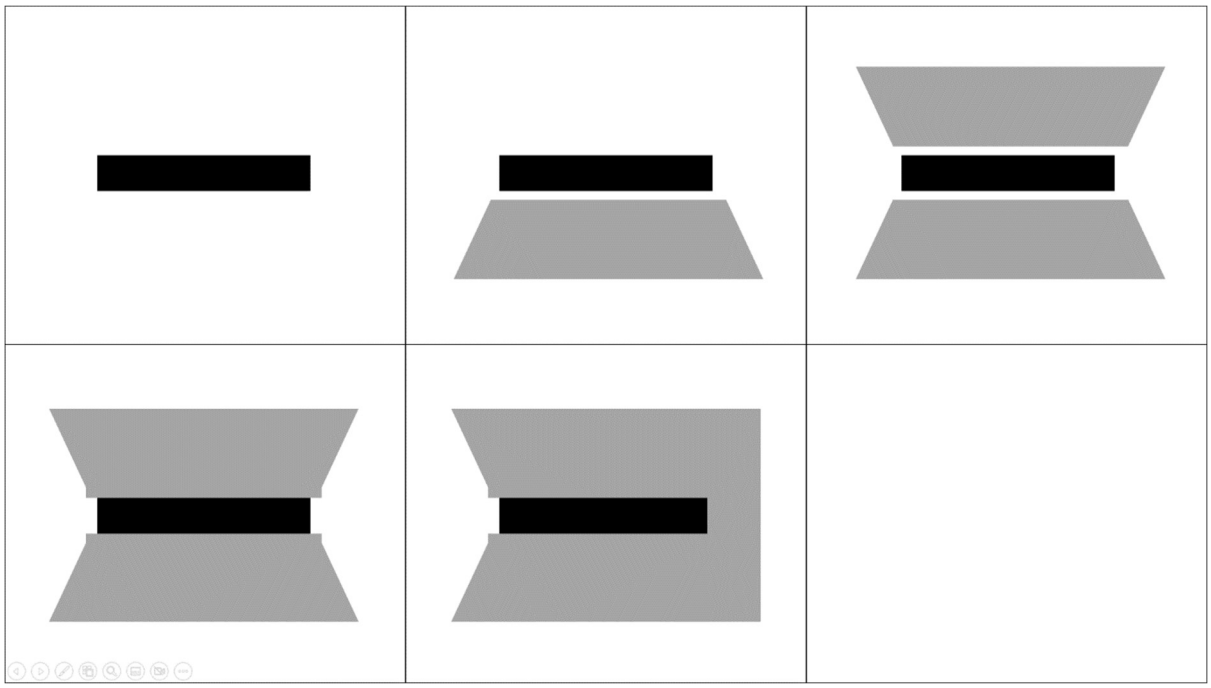


Figure 27: Schematic diagrams showing the FIB milling process. Carbon deposition is shown in black and material etched away into the samples surface is shown in grey.

4.3.8 Transmission Electron Microscopy EDX

The composition of grain boundaries within the TEM lamellae was found using STEM-EDX. Line scans were taken perpendicular to the grain boundary being investigated and within the bulk away from any grain boundaries to provide a bulk reference value. The planar concentration of elements could be calculated from the resultant line spectra using the equation [152]:

$$\Gamma_x = \rho_{at}\omega_{eff}\frac{M_y}{M_x}\left(\frac{C_x}{C_y}\right)$$

where the planar coverage, Γ, of dopant x is found dependent on the atomic density of the bulk material, ρ_{at}, the effective scan width of the line, ω_{eff}, the atomic weight ratio of ions M_x and M_y, and the weight fractions of the same ions C_x and C_y. For the investigation of dopants in alumina being considered here, the atomic density of alumina is used for ρ_{at} alongside aluminium being used for element y.

The ratio of weight fractions, $\left(\frac{C_x}{C_{Al}}\right)$, is linked to the measured intensity through the Cliff-Lorimer factor [205] which gives the ratio between the measured experimental EDX counts and the weight fractions required for calculations. This factor can be calculated as follows:

$$k_{ab} = \frac{M_a \omega_b Q_b}{M_b \omega_a Q_a}$$

where *M* is the atomic weight, *ω* is the fluorescent yield, and *Q* is the ionization cross section of the respective elements *a* and *b*.

The effective width of the line scan is limited by the spatial resolution of the TEM and so this must be considered. The spatial resolution, *R*, is given by the formula [206]:

$$R = \frac{d+(b^2+d^2)^{\frac{1}{2}}}{2}$$

where *d* is the beam diameter and *b* is the beam spreading. Beam spreading, *b*, can be found using the formula [207]:

$$b = 7.21 \times 10^5 \frac{Z}{E_0}\left(\frac{\rho}{A}\right)^{\frac{1}{2}} t^{\frac{3}{2}}$$

where *t* is the foil thickness in cm, E_0 is the beam energy in eV, *ρ* is the density in gcm^{-3}, *A* is the atomic weight, and *Z* is the atomic number. The beam diameter on the JEOL 2100 used for STEM-EDX was between 1 and 25 nm dependent on spot size chosen. This results in a spatial resolution of between 15 and 32 nm when the constants for alumina and the dimensions of samples tested are added to the equation for beam spreading. These limits of spatial resolution become the effective width of the line scan used.

Excess grain boundary coverage was therefore calculated by subtracting the measured planar coverage along grain boundaries from the value found in the bulk material.

4.4 MECHANICAL TESTING

4.4.1 Indentation

Alumina samples, manufactured in the fashion described in 4.1.4, were ground and polished to a finish of 1 µm. The polished surface was tested under a Vickers hardness test loads of 20 kg and 5 kg (Future-Tech FV-110). 5 indentations were made, sufficiently spread across the surface of the sample to ensure no interaction between indentations was observed. This ensured that differences in the measured hardness were resultant of the effects of the area of the specimen tested rather than the effects of other testing indentations made in the sample.

Each indentation was imaged under optical microscopy and the dimensions of the principal diagonals measured from the micrographs for each indent. Vickers hardness for that indentation could then be calculated using the formula:

$$HV = \frac{2F\sin(68)}{d_1 d_2}\ [kgf\ mm^{-2}]$$

The 5 different hardness measurements allowed for the calculation of a mean and standard deviation of hardness values to be calculated for each sample.

4.4.2 Nanoindentation

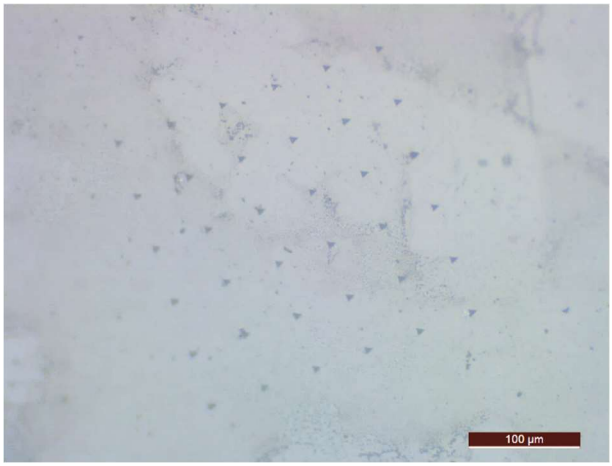
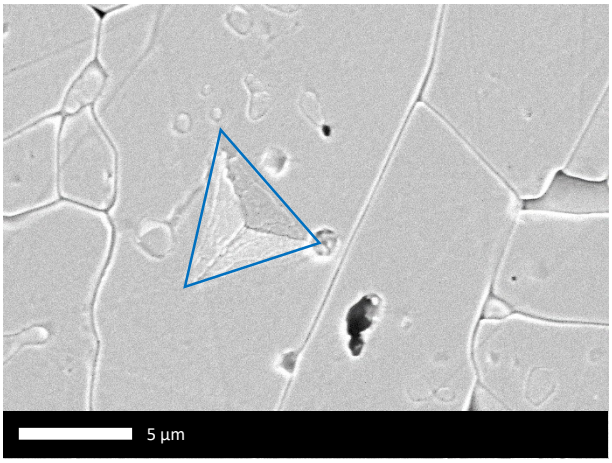


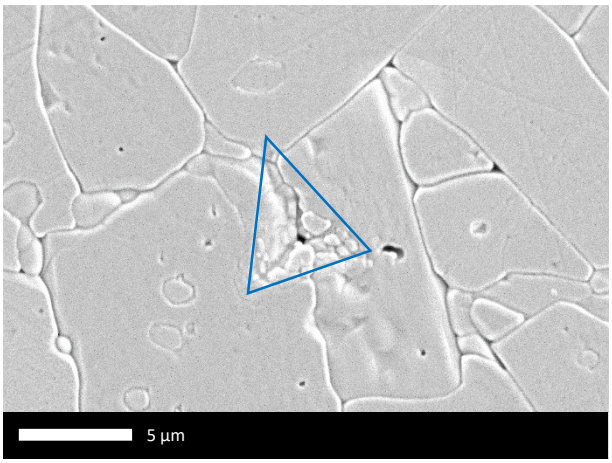
Figure 28: Optical microscopy image of a set of 36 nanoindents in the surface of alumina.

Samples for nanoindentation were prepared in the fashion described in 4.1.4. The surface was ground and polished to a finish of 1 µm in preparation for nanoindentation. The polished surface was then tested under a Berkovich indenter tip to produce indents with a width of 3.5 µm, 7 µm and 14 µm. These indentations were performed by Michael Goode. A set of 36 indentations of each width was performed to create a grid, an example of an indentation grid made

a)



b)



c)

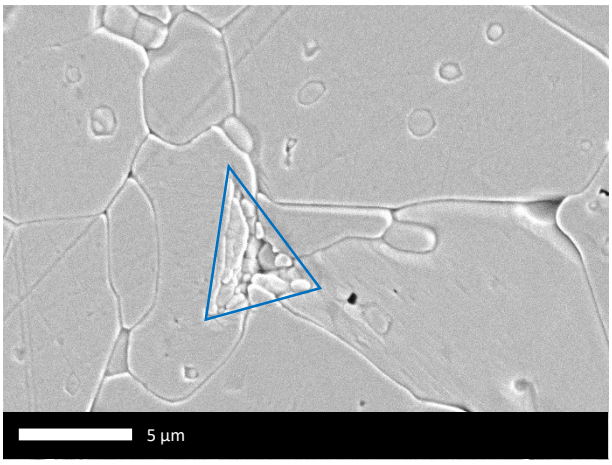


Figure 29: SEM micrographs of nanoindentations showing an indent within a) 1 large grain, b) across a single grain boundary between 2 grains, c) across several grains. The indentations have been outlined in blue for clarity.

in this fashion is shown in Figure 28. The indentations were spaced 50 µm apart with a gap of 100 µm between sets of distinct depths. This allows for the identification of individual indentations with respect to the measured load used in their production.

The location of the indentation grids was determined through optical microscopy owing to its higher contrast compared to scanning electron microscopy and a mark made nearby to allow for location of the indentations under electron microscopy. Scanning electron microscopy images of each indentation were taken to determine if each indentation was successful and data from failed indentations was discounted. The gold coating was removed from the surface of the sample using a soft cloth and the sample thermally etched for 15 minutes at a temperature 50 ^{O}C below the original sintering temperature with the same heating and cooling profile. Scanning electron microscopy on the

thermally etched, indented surface was carried out to micrograph the area immediately around each indentation in the same fashion as prior to thermal etching.

As the grain boundary microstructure within the indentation cannot be readily identified despite the thermal etch, local microstructure was determined using the grain boundaries surrounding the indent. Indentations were categorised based on the number of grain boundaries passing into the indentation triangle. This categorisation resulted in 3 primary groups: indentations containing no grain boundaries, indentations situated along a single grain boundary, and indentations containing multiple grain boundaries. An example of each of these categories is shown in Figure 29. A comparison between the resultant mechanical properties could then be obtained relative to the local microstructure of the nanoindentation.

4.4.3 Wear Resistance



Figure 30: Photograph showing the tribology appartus with the sample holder held above the veiwing lense.

Samples, manufactured in the fashion described in 4.1.4, were ground and polished to a finish of 1 µm before wear resistance testing under a load of 2.5 N (Phoenix Tribology Ltd. TE66). The polished alumina samples were mounted on the cantilever beam and loaded to be held against a steel ball bearing, as shown in Figure 30. A slurry of 0.35 g cm^{-3} SiC in water with 0.37 wt.% Dispex A40 added as a dispersant was produced and pumped over the ball bearing during testing. The bearing was rotated at 100 rpm for 1 minute and the absolute size of the resultant indentation measured using the attached optical

microscope. The test was repeated in the same location in increments of 1 minute until the resultant wear scar was of the maximum size that could be accurately measured on the attached optical microscope without repositioning the sample. This resulted in a wear scar in the form of a circular cap of removed material. The final dimensions of the wear scar were measured by coating the worn sample in a 5 µm layer of gold and imaging under a scanning electron microscope. The final diameter, d, was calculated by measuring the width at 5 different angles spaced throughout the entire circumference of the wear scar and calculating the mean diameter. This methodology is based on the method described by *Rutherford and Hutchings* [208] and is described in more detail in that work.

The dimensions of the wear scar are modelled as a circular cap with the shape of the cap conforming to the shape of the ball. Following this model, the volume of the wear scar was calculated using the following formula [175]:

$$V = \frac{\pi b^4}{64R}$$

where *b* is the crater diameter and *R* is the radius of the ball. Following the Archard wear law that states the wear volume follows the equation:

$$V = kSP$$

where *k* is the wear coefficient, *S* is the total distance travelled along the surface by the ball, and *P* is the applied load. Therefore, combining the two equations above:

$$k = \frac{\pi b^4}{64SPR}$$

4.4.4 3 Point Bend Testing

Alumina discs were manufactured by sintering for 4 hours at 1550 ^{O}C according to the method described in 4.1.4. The resultant disks were sectioned into beams with a cross section of 3 mm x 3 mm across the width of the sintered disk. Each beam was polished on 3 of the longer sides to a finish of 1

µm ensuring all surfaces remained perpendicular to each other throughout. The beams were then measured in all 3 primary dimensions using a set of Vernier callipers and a micrometer.

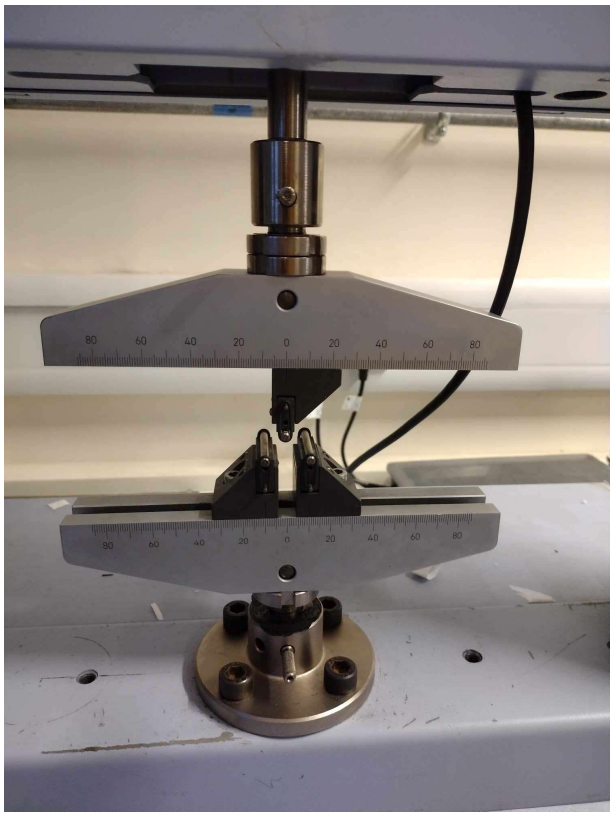


Figure 31: Photograph showing a pair of supports and the indenter prior to 3 point bend testing.

The beams were individually broken using a Shimadzu AGS-X across a pair of supports positioned 20 mm apart with a single loading beam positioned midway between them. This configuration is shown in Figure 31. The beams were positioned with the unpolished face orientated upwards towards the loading beam. Loading was conducted at a rate of 5 mm/min with measurements of load and displacement taken at 0.01 second intervals throughout. Testing was displacement controlled and continued until stopped by the detection of a sudden drop in load required due to failure of the test specimen.

4.4.4.1 Data Analysis

Flexural strength was calculated using the formulas:

$$\sigma_f = \frac{3FL}{2wh^2}$$

where *F* is the load applied at failure, *L* is the span between the support beams, *w* is the width of the beam, *h* is the height of the beam.

4.4.4.1.1 Weibull Analysis

The failure of the polished beams in 3-point bending was fitted to a Weibull distribution. The failure probability therefore follows the formula:

$$F = 1 - e^{\left(\frac{-\sigma_f}{\sigma_0}\right)^m}$$

Where m is the Weibull modulus, σ_f is the flexural strength and σ_0 is the characteristic scale parameter.

By plotting a graph of:

$$ln\left(ln\left(\frac{1}{1-F}\right)\right) = m\ ln(\sigma_f) - m\ ln(\sigma_0)$$

for each composition, the Weibull modulus and scale parameter can be determined from the gradient and intercept of the straight line.

4.4.5 Fracture Toughness Testing



Figure 32: Photograph showing the homemade notching equipment.

Alumina disks were manufactured at 1550 ^{O}C with 4 hours sintering hold according to the method described in 4.1.4. The resultant disks were sectioned into beams with a cross section of 3 mm x 3 mm across the width of the sintered disk similar to 4.4.4. The beams were then each measured using a micrometer in all 3 dimensions. Each beam had a 0.5 mm notch cut into the centre of one side using a razor blade sharpened with a 6 µm diamond paste. The notch was made using a homemade apparatus to oscillate the sample across the blade consistently. This is shown in Figure 32. The produced notches were then sharpened in the same apparatus through the use of a new razor blade and a 1 µm diamond paste. This resulted in a notch with a crack tip radius of approximately 10 µm. An

example of a notch created in this manner is shown in Figure 33. The notch was then micrographed under an optical microscope to accurately determine its depth. This was repeated on the opposite side of the notch to allow an average depth across the crack to be measured.

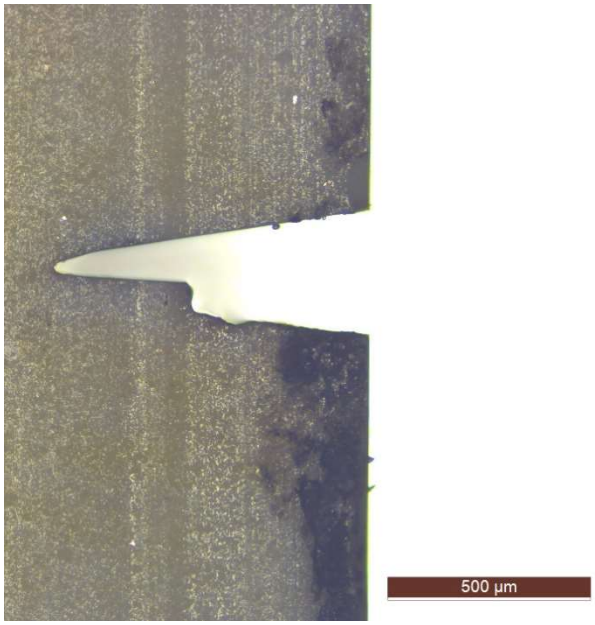


Figure 33: Optical micrograph showing the sharpened notch tip produced in a composite of 99 wt.% Al_2O_3 1 wt.% SiC by notching with 6 µm diamond paste and sharpening with 1 µm diamond paste.

The beams were individually broken using a Shimadzu AGS-X on a pair of loading supports 20 mm apart. Each beam was positioned with the notch situated centrally facing away from the loading beam. Testing was conducted at a loading rate of 5 mm/min with measurements of load and displacement taken at 0.01 second intervals throughout. Failure testing was carried out under displacement control until failure was detected by the rapid decrease in measured force.

4.4.5.1 Data Analysis

Fracture toughness values were calculated using the formulas:

$$\beta = \frac{a}{h} \qquad F(\beta) = 1.106 - 1.552\beta + 7.71\beta^2 - 13.53\beta^3 + 14.23\beta^4$$

$$K_{1C} = \frac{3LP\sqrt{\pi a}}{2wh^2} F(\beta)$$

where *a* is the average notch length, *h* is the height of the beam, *w* is the width of the beam and *L* is the span between the support beams, and *P* is the applied load at sample failure [209, 210].

4.4.6 High Speed Impact Testing

Impact testing at elevated speeds was conducted through the use of a gas gun. Alumina disks were manufactured using the method described in 4.1.4 with a sintering hold of either 1550 ^{O}C for 4 hours or 1400 ^{O}C for 1 hour. The resultant disks had one surface polished to a finish of 1 µm to minimise the effects of differing surface texture during testing.

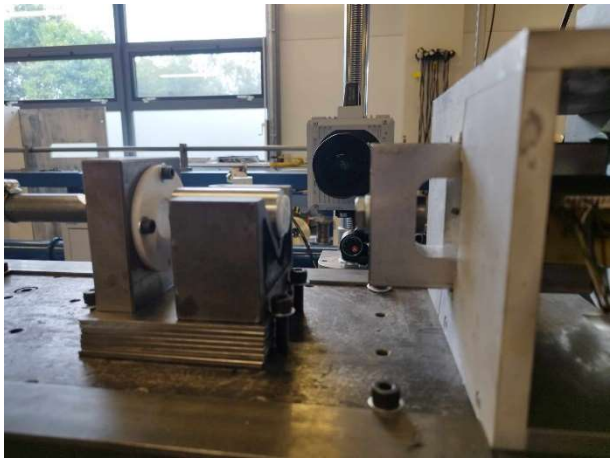


Figure 34: Photograph showing an alumina sample mounted at the end of the gas gun prior to being shot.

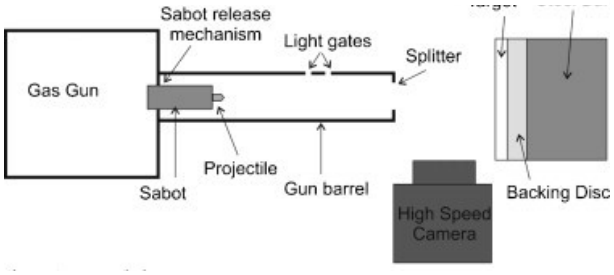


Figure 35: Schematic diagram showing the gas gun set up used in high speed impact testing [211].

The polished disks were mounted on an aluminium rod using silicon grease to ensure it remained in position at the end of the gun without significant mechanical interaction between the rod and the sample. This is shown in Figure 34. 304 stainless steel ball bearings were fired at the centre of the alumina disks using a 12 mm diameter bore gas gun at speeds of between 100 and 200 ms^{-1}. The impact speed of the ball bearings was measured using a light gate near the end of the barrel of the gas gun. A high-speed camera was used to observe the impact between the alumina specimen and the ball bearing. This set up is shown in Figure 35. The ultimate energy of impact samples could withstand before failure was found by testing multiple samples of material. Tests were conducted at decreasing velocities until samples survived impact. Owing to the minimum viable velocity of the gas gun used, projectiles of both 3 mm and 2 mm in diameter were used in different tests.

By counting the frames between the ball bearing entering the image, its impact with the sample and the ball bearing exiting the frame, along with any changes in distance travelled due to deflection from

the entry direction, the change in speed, and therefore kinetic energy, on impact can be calculated as follows:

$$v_f = \frac{v_i f_i}{f_f}$$

$$\Delta E_k = \frac{m}{2}\left({v_i}^2 - {v_f}^2\right)$$

Where vi is the initial speed of the ball bearing, vf is the final speed of the ball bearing, fi is the number frames of video prior to impact, ff is the number of frames following the impact and m is the mass of the ball bearing. This calculation assumes limited deflection perpendicular to the plane of the image; however, given the very small deflection that occurs in the plane of the image a similarly small deflection in the perpendicular direction can be assumed and largely discounted.

5 MICROSTRUCTURE OF ALUMINA MATRIX COMPOSITES

Following the key objectives of this project outlined in chapter 5, this chapter is structured into 3 distinct sections as follows:

1. Firstly, the results of research conducted into the development of the microstructure in alumina, alumina matrix composites, and alumina matrix composites with the addition of metal oxide and nitrate after sintering in air are described.
2. A discussion of the behaviour of alumina with the addition of silicon carbide, and without any other additions, when sintered in air. This includes consideration of both the microstructure and mechanical properties of the resultant nanocomposites.
3. An explanation of the microstructure of alumina-silicon carbide-yttria nanocomposites. Special attention will be paid to the link between grain boundary composition and the resultant microstructure.

5.1 RESULTS

5.1.1 In Situ Testing

5.1.1.1 Thermogravimetric Analysis

Thermogravimetric analysis (TGA) was conducted on unsintered samples of pure silicon carbide, pure alumina, and alumina with the addition of combinations of 1 wt.% silicon carbide and 500 ppm yttrium oxide.

5.1.1.1.1 Oxidation of Silicon Carbide

TGA was conducted on both silicon carbide pressed in the same fashion as 4.2.1 and loose silicon carbide, by heating the samples to 1550 ^{O}C and holding at that elevated temperature for 4 hours under the same conditions as sintered samples. The resultant weight changes in these materials can been seen in Figure 36.

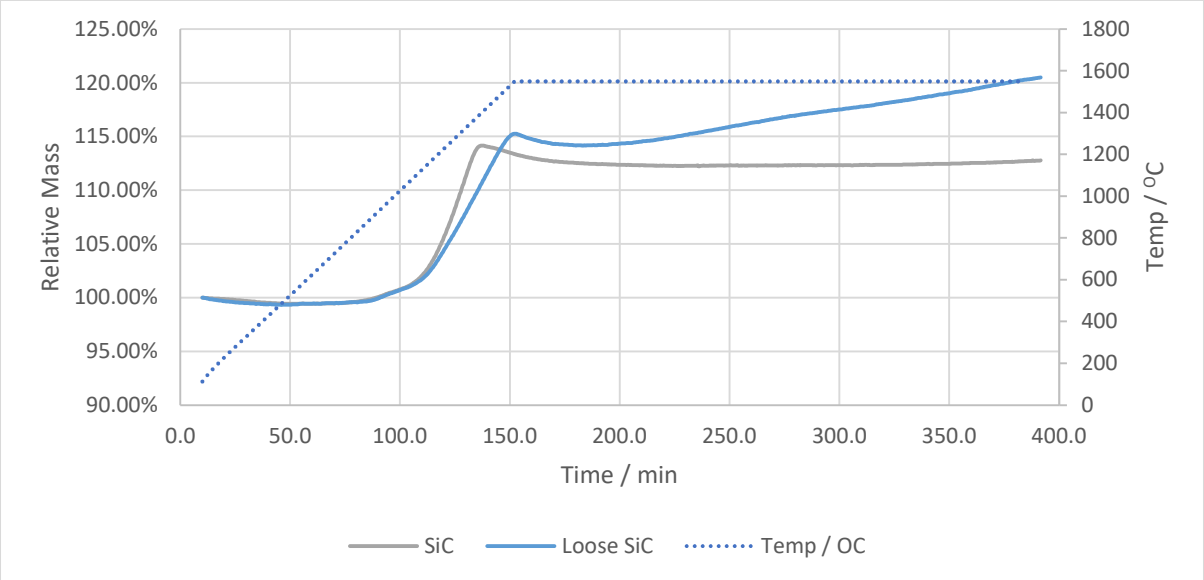


Figure 36: Graph showing the mass change of loose silicon carbide and silicon carbide uniaxially and coaxially pressed after heating to 1550 ^{O}C and holding for 4 hours according to the heating profile shown.

Loose silicon carbide had a maximum measured increase in mass of 21 % over unsintered silicon carbide, whereas the maximum increase seen in processed silicon carbide was 15 %. The increase in mass seen in both samples measured in Figure 36 commences at temperatures around 900 ^{O}C before increasing in rate at 1100 ^{O}C. This mirrors the oxidation behaviour of silicon carbide seen in other work [75, 212], confirming this is the reaction observed.

5.1.1.1.2 Alumina-Silicon Carbide

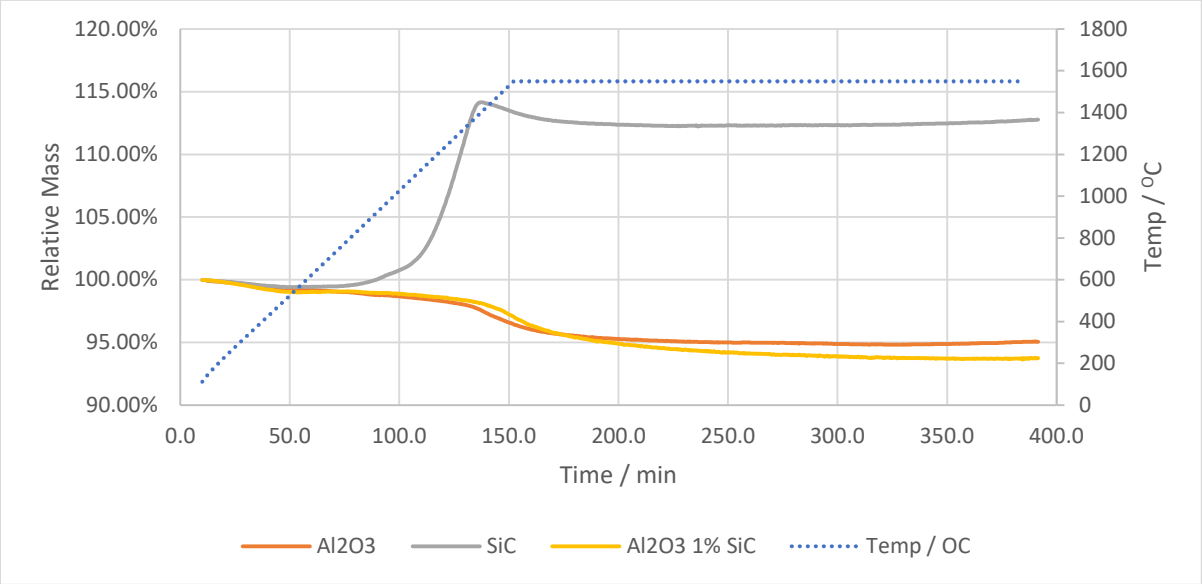


Figure 37: Graph showing the change in mass of processed alumina, silicon carbide, and alumina with the addition of 1 wt.% silicon carbide with sintering at 1550 ^{O}C for 4 hours.

The addition of 1 wt.% silicon carbide to alumina was compared, using thermogravimetric analysis, to the behaviour of alumina and silicon carbide individually, after processing in the same fashion as 4.2.1. Weight changes seen in these 3 compositions after sintering for 4 hours at 1550 ^{O}C are shown in Figure 37. Al_2O_3-1wt.%SiC showed an increase in mass which was comparable to the period in which silicon carbide increased in mass. The maximum discrepancy between pure alumina and Al_2O_3-1wt.%SiC during this period was found to be a 0.75 % increase in measured weight. While the samples were held at 1550 ^{O}C, both alumina and silicon carbide remained a reasonably consistent mass throughout measurement. Al_2O_3-1wt.%SiC, however, displayed a decrease in mass during the period of constant temperature suggesting a further reaction was taking place. This result was found to occur across

multiple tests on the same composition and the apparatus had a maximum balance drift of 0.02% across the duration of the test. Other investigations [213, 214] into this system have found high temperature reactions between alumina and silicon carbide such as:

$$4Al_2O_3 + 3SiC \rightarrow 2Al_4O_4C + 3SiO_{(g)} + CO_{(g)}$$

$$3Al_2O_3 + 3SiC \rightarrow Al_4O_4C + Al_2OC + 3SiO_{(g)} + CO_{(g)}$$

$$2Al_2O_3 + 3SiC \rightarrow 2Al_2OC + 3SiO_{(g)} + CO_{(g)}$$

and a reaction between mullite and silicon carbide:

$$3Al_2O_3 \cdot 2SiO_2 + SiC = 3Al_2O_3 + 3SiO_{(g)} + CO_{(g)}$$

These reactions result in gaseous products so may offer an explanation for the decrease in mass observed during the high temperature hold in this experiment. At the conclusion of sintering, after the full 4 hours hold, Al_2O_3-1wt.%SiC had a measured mass 1.41 % lower than pure alumina at the same point.

Comparison between the measured value of the mass of Al_2O_3-1wt.%SiC and the sum of the equivalent masses in alumina and silicon carbide in the fraction of 0.99 times the mass of alumina and 0.01 times the mass of compacted silicon carbide is shown in Figure 38. During the period of increase in the mass of silicon carbide seen in Figure 36, Al_2O_3-1wt.%SiC showed a maximum difference in mass of 0.58 % from the calculated values. At the conclusion of sintering, however, the summation of values calculated had a mass 1.59 % higher than Al_2O_3-1wt.%SiC.

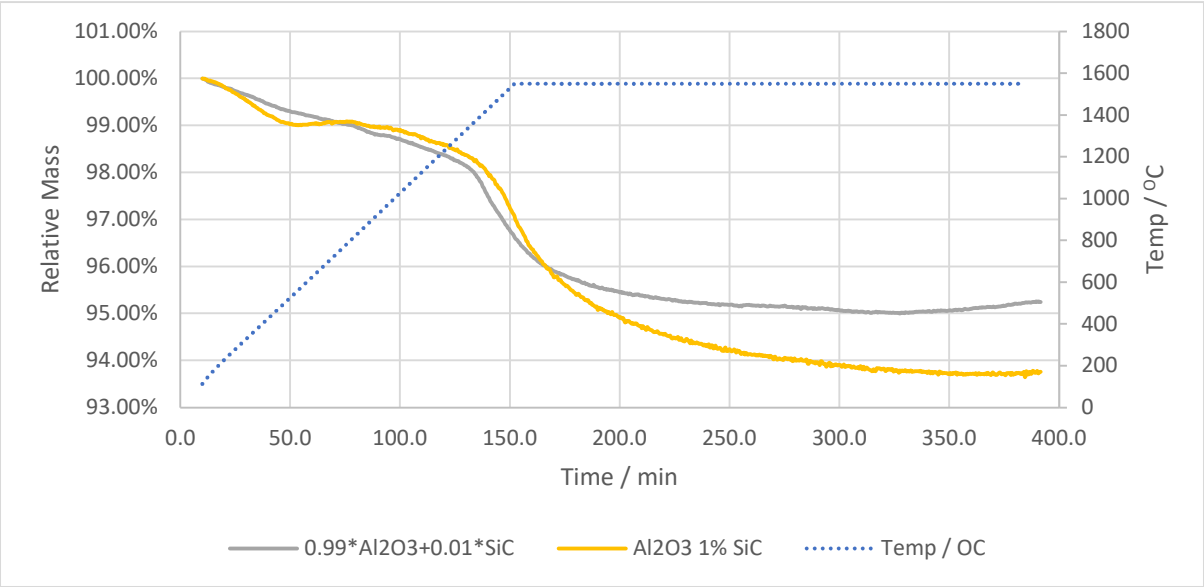


Figure 38: Graph showing the change in mass of alumina with the addition of 1 wt.% silicon carbide after sintering for 4 hours at 1550 ^{O}C and the calculated summation of 0.99 times alumina and 0.01 times silicon carbide each individually sintered in the same fashion.

5.1.1.1.3 Alumina-Silicon Carbide-Yttrium Oxide

The addition of both silicon carbide and yttrium oxide to alumina was also studied through thermogravimetric analysis. Al_2O_3-1wt.%SiC was investigated in 5.1.1.1.2 and showed a total decrease of around 6 % in mass over the course of heating. This behaviour, along with the changes in mass measured in Al_2O_3-500ppmY_2O_3 and in Al_2O_3-1wt.%SiC-500ppmY_2O_3, are shown in Figure 39.

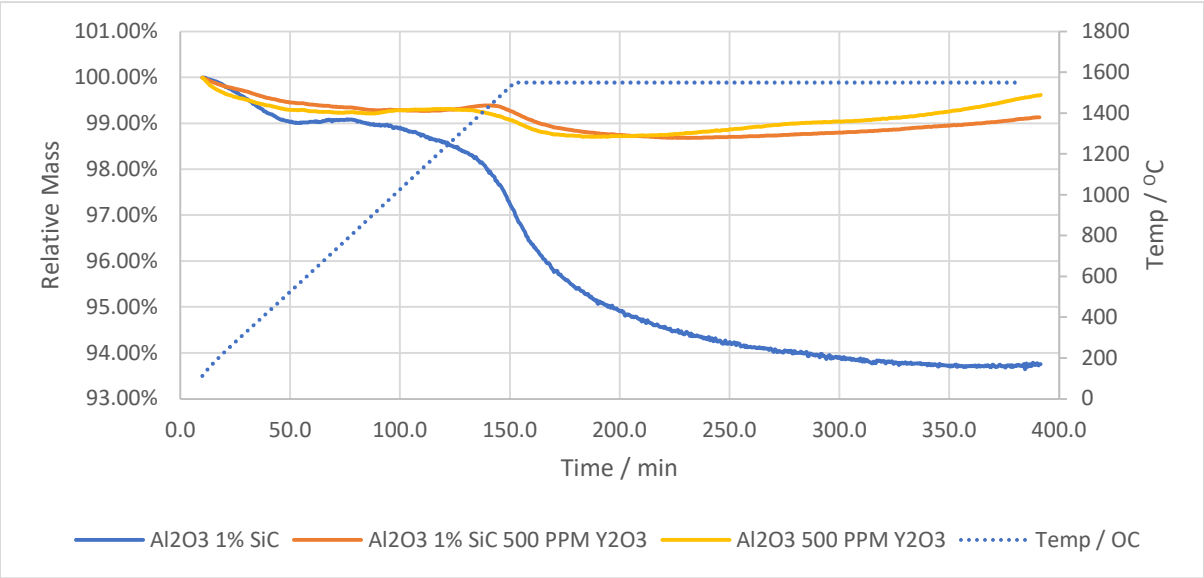


Figure 39: Graph showing the change in mass of alumina with the addition of 1 wt.% silicon carbide, alumina with the addition 500 ppm yttrium oxide, and alumina with the addition of 1 wt.% silicon carbide and 500 ppm yttrium oxide sintered for 4 hours at 1550 ^{O}C.

As is shown in Figure 39, sintered pure alumina had a decrease in mass of 5 % during sintering at 1550 ^{O}C for 4 hours. This effect is significantly reduced with the addition of yttrium oxide. Alumina with the addition of 500 ppm yttrium oxide has a decrease in mass of only 0.4% over the course of the sintering profile. Al_2O_3-1wt.%SiC-500ppmY_2O_3 follows the behaviour of Al_2O_3-500ppmY_2O_3 closely with a maximum discrepancy in mass change of 0.21 %.

5.1.1.2 X-Ray Tomography

The x-ray tomography sample slices show very limited variation in measured x-ray intensity across the sample regardless of composition. An example slice from a green body manufactured from Al_2O_3-1wt.%SiC-500ppmY_2O_3 using the process described in 4.2.2 is shown in Figure 40. This slice is representative of what is observed throughout the sample. Areas of lower density would show as darker areas within the resultant circle. In extreme cases, such as pores, a value of 0 density would result in an area of black within the measurement. The slices observed from Al_2O_3-1wt.%SiC-500ppmY_2O_3 composite green bodies do not show any of these dark areas so cannot contain any

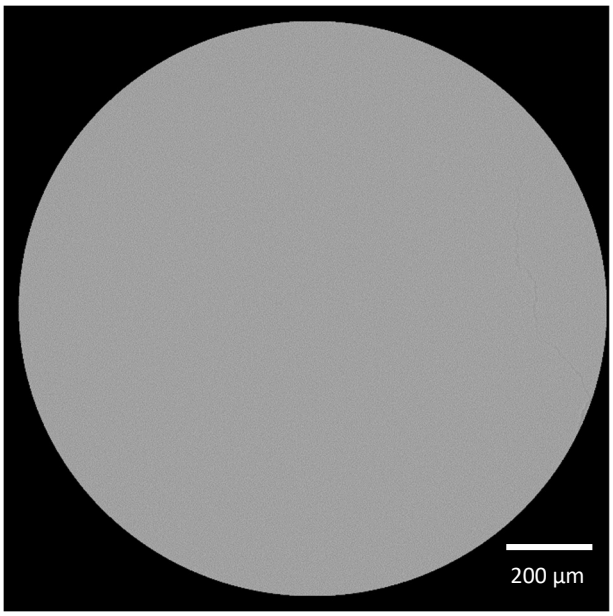


Figure 40: X-ray tomography slice of an aluminium oxide green body with the addition of 1 wt.% silicon carbide and 500 ppm yttrium oxide

porosity on the scale observable using X-ray tomography despite such porosity being visible in the final sintered composite, Figure 51.

As is described in 4.2.2, the distribution of X-ray intensity can be plotted as a histogram due to its lack of individually resolvable pores. This data is shown in the form of histograms in Figure 41. Each sample shows a clear singular peak at a certain brightness level. This confirms a consistent density throughout the sample without any distinct pores. The full width at half maximum of the measured intensity peaks is shown in Figure 42. All 4 peaks have a full width at half maximum within a range of 20 percent between the highest and lowest values. Both samples tested containing yttria showed a visible tail of higher pixel brightness in Figure 41. This corresponds to areas of higher density within the green body and is indicative of the yttria.

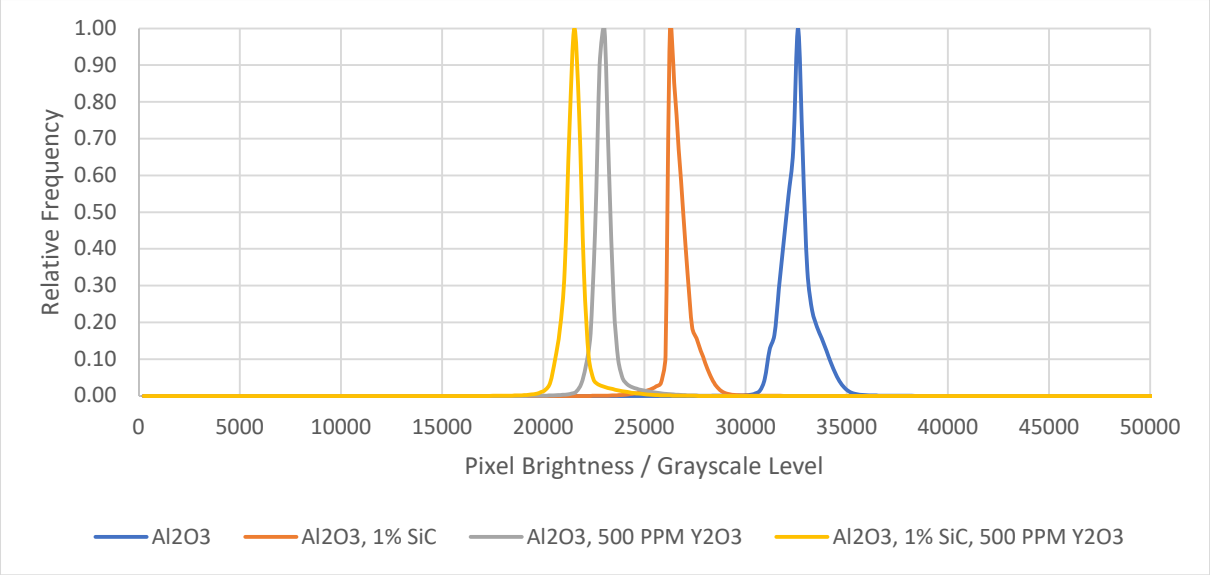


Figure 41: Histogram showing the relative intensity of pixel brightness in x-ray tomography of green bodies manufactured from: aluminium oxide, aluminium oxide with the addition of 1 wt.% silicon carbide, aluminium oxide with the addition of 500 ppm yttrium oxide, and aluminium oxide with the addition of both 1 wt.% silicon carbide and 500 ppm yttrium oxide.

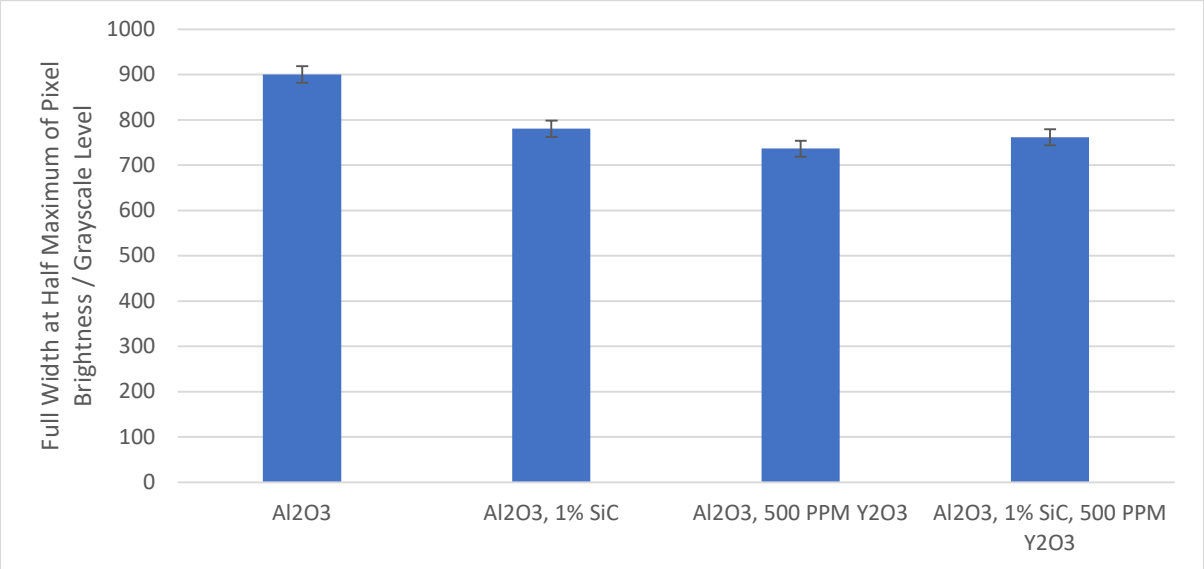


Figure 42: Graph showing the full width at half maximum of the peaks shown in Figure 41. Errors were calculated according to the formula derived by Valentine et al. [215]

5.1.2 Microstructural analysis

5.1.2.1 Density

Following the Archimedes method described in 4.3.5, the density of samples produced could be measured from entire sintered disks without any further processing.

5.1.2.1.1 Pure Alumina

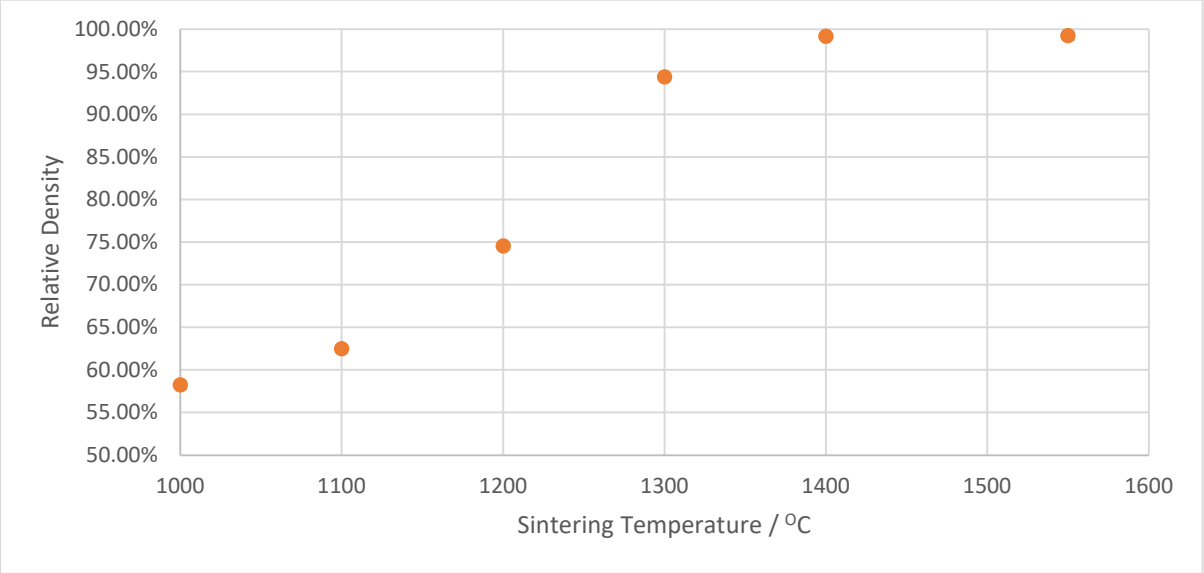


Figure 43: Graph showing the change in relative density of pure alumina after sintering for 1 hour at various temperatures.

Alumina was found to reach over 99% density after sintering for 1 hour at 1400 ^{O}C. The increase in density with sintering temperature can be clearly seen in Figure 43. For reference, the relative density of a green body was measured using a geometric method by finding the volume of the sample and weighing the same sample, as the green bodies would break apart during immersion in water prior to sintering. This measurement found a resultant green body density of 56 %.

5.1.2.1.2 Alumina-Silicon Carbide

The addition of silicon carbide to alumina prior to sintering was shown to dramatically decrease the resultant density of the final composite. Regardless of silicon carbide quantity initially added, final relative density was not found to be higher than 95.5 %. With additions of 1 wt.% silicon carbide or lower, density remained consistently over 95 % regardless of sintering time, as can be seen in Figure

44. However, with quantities of silicon carbide higher than this, a lower resultant density was seen after shorter sintering times.

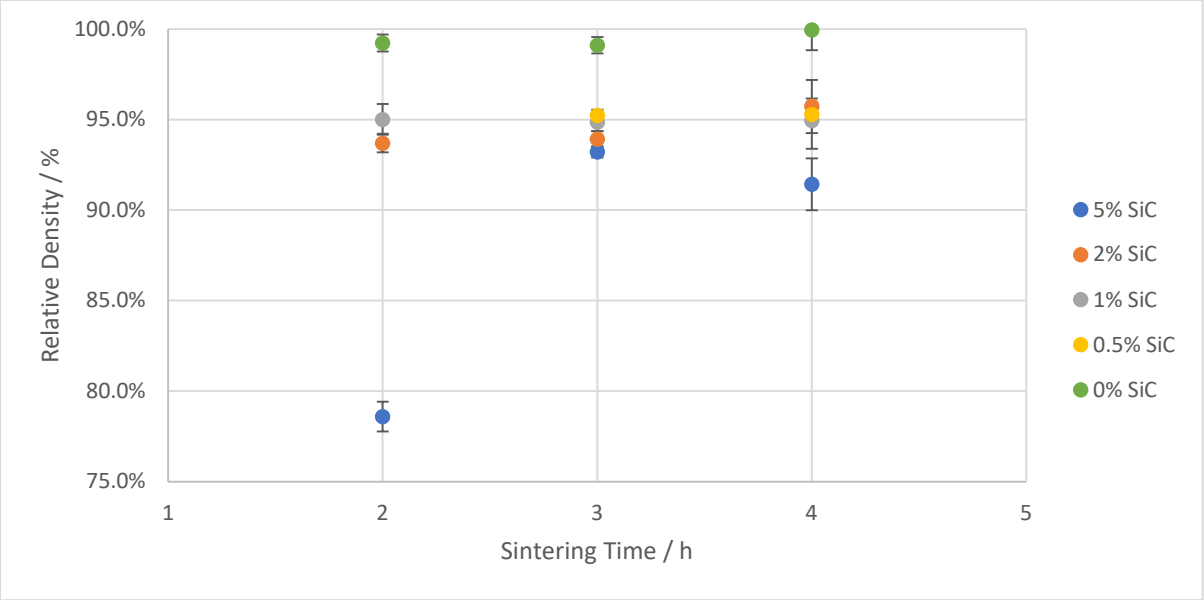


Figure 44: Graph showing the change in relative density of alumina samples sintered at 1550 ^{O}C for between 2 and 4 hours with varying initial quantities of silicon carbide added.

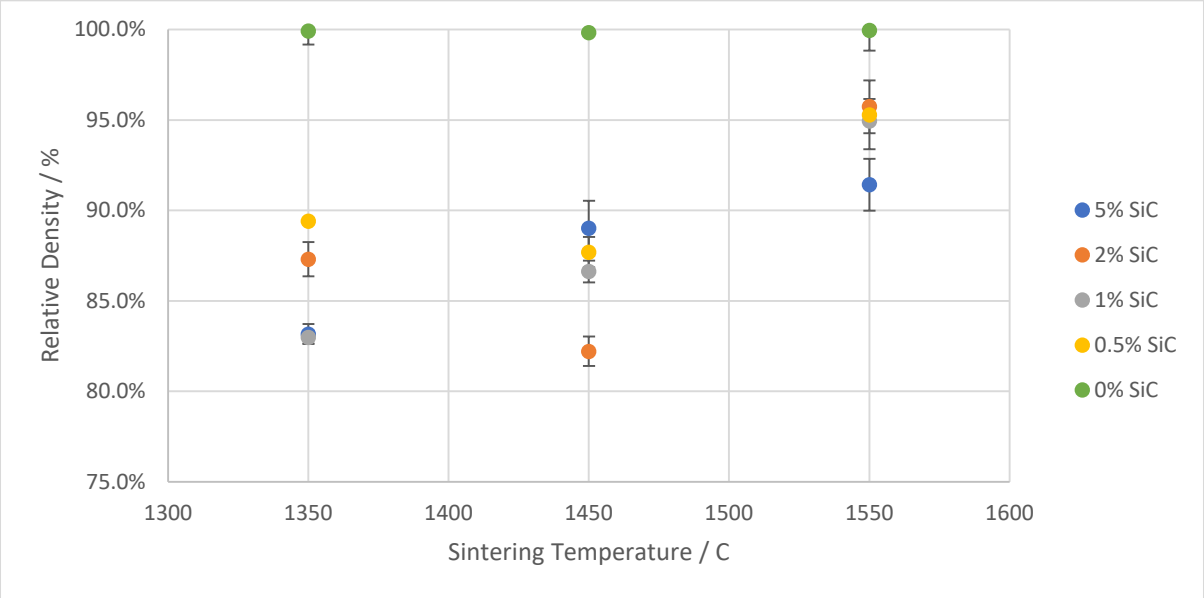


Figure 45: Graph showing the change in relative density of alumina samples sintered for 4 hours at between 1350 ^{O}C and 1550 ^{O}C with varying initial quantities of silicon carbide added.

The reduction in density with the addition of silicon carbide was found to be more prevalent at lower sintering temperatures. As can be seen in Figure 45, pure alumina remained above 99 % density after 4 hours sintering even at sintering temperatures as low as 1350 ^{O}C. Conversely, the addition of any silicon carbide reduced final density below 90 % when sintered at temperatures of 1450 ^{O}C or below.

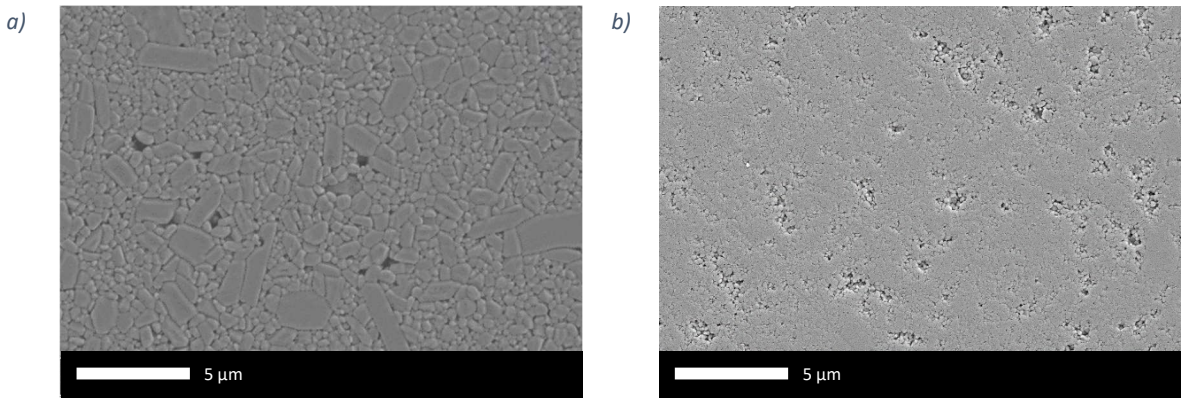


Figure 46: SEM images of alumina with 1 wt.% silicon carbide sintered for 4 hours at a) 1550 ^{O}C b) 1450 ^{O}C.

Scanning electron microscopy of the microstructures produced in these samples support these measurements as can be seen in Figure 46. The microstructure produced at a sintering temperature of 1450 ^{O}C showed a visibly higher quantity of pores than the otherwise equivalent sample sintered at 1550 ^{O}C. This is commensurate with the change in density measured in Figure 45.

5.1.2.1.3 Alumina-Silicon Carbide-Metal Compounds

The loss of density caused by the addition of silicon carbide can be partially mitigated by the addition of metal nitrates or oxides. The effects of these additives can be seen in Figure 47. A density of over 98.2 ± 0.3 % was achieved after 4 hours sintering time at 1550 ^{O}C Al_2O_3-1wt.%SiC-500ppmY_2O_3. This is a significant improvement in density over the same sintering conditions in Al_2O_3-1wt.%SiC, which had a relative density 95 ± 0.7 %.

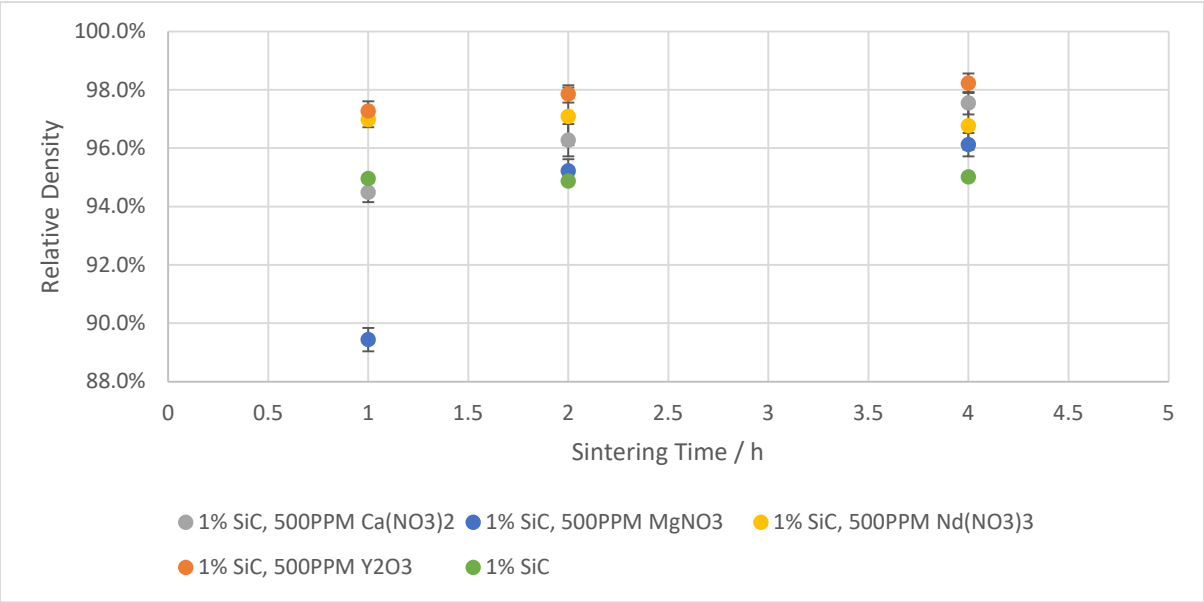


Figure 47: Graph showing the change in relative density of alumina samples with 1 wt.% silicon carbide and 500 ppm of calcium nitrate, magnesium nitrate, neodymium nitrate or yttrium oxide sintered at 1550 ^{O}C for between 1 and 4 hours.

The relative density of Al_2O_3-1wt.%SiC-500ppmY_2O_3 after 4 hours sintering at 1550 ^{O}C was found to be higher than the highest measured density of Al_2O_3-1wt.%SiC-500ppm$Ca(NO_3)_2$, Al_2O_3-1wt.%SiC-500ppm$MgNO_3$ or Al_2O_3-1wt.%SiC-500ppm$Nd(NO_3)_3$ regardless of sintering time. These composites had a maximum relative density of 97.3 ± 0.4 %, 96.1 ± 0.4 %, and 97.1 ± 0.7 % respectively.

5.1.2.1.4 Alumina-Silicon Carbide-Yttrium oxide

The increase in density due to the addition of yttrium oxide seen in Figure 47 was not repeated at lower sintering temperatures. Below 1550 ^{O}C, the addition of yttrium oxide offered no benefits in density over Al_2O_3-1wt.%SiC sintered under the same conditions. After 4 hours sintering at 1450 ^{O}C, Al_2O_3-1wt.%SiC results in a relative density of 86.6 ± 0.6 % and the addition of 500 ppm yttrium oxide under the same conditions results in a relative density of 86.0 ± 1.4 %. This difference is shown graphically in Figure 48.

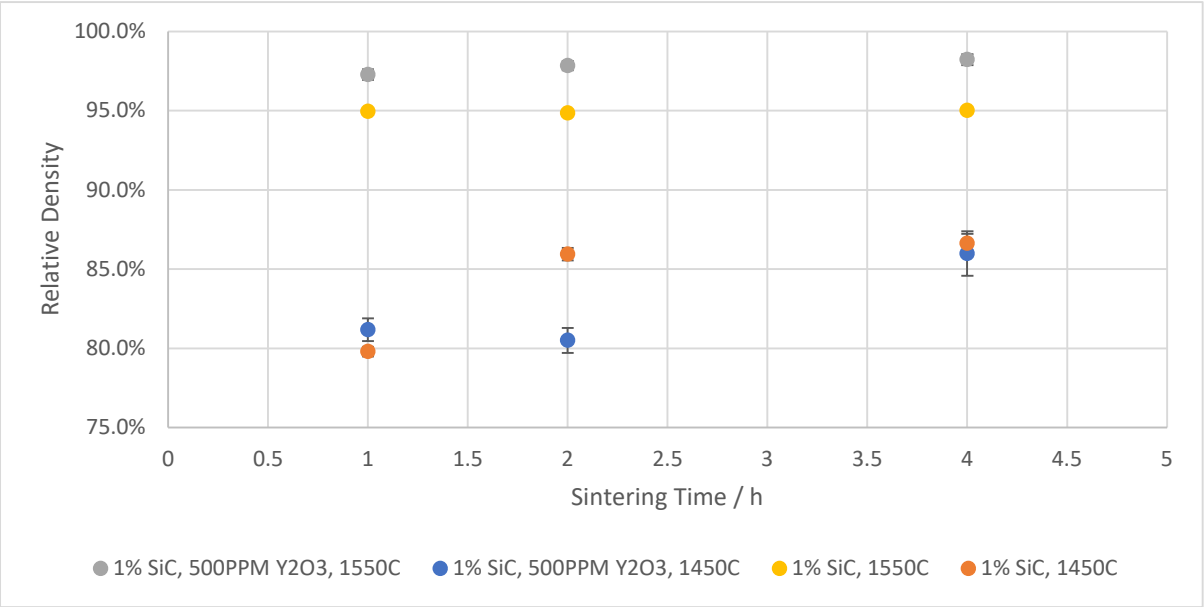


Figure 48: Graph showing the relative density of alumina with 1 wt.% silicon carbide and alumina with 1 wt.% silicon carbide and 500 ppm yttrium oxide sintered at 1550 ^{O}C or 1450 ^{O}C for between 1 and 4 hours.

The addition of varying quantities of yttrium oxide shows that after sintering at 1550 ^{O}C the addition of any quantity of yttrium oxide results in an increase in relative density over Al_2O_3-1wt.%SiC sintered under the same conditions. This is clearly shown in Figure 49. A comparison between the effects of yttria additives to alumina with both 1 wt.% silicon carbide and 0.5 wt.% silicon carbide is also shown in Figure 50.

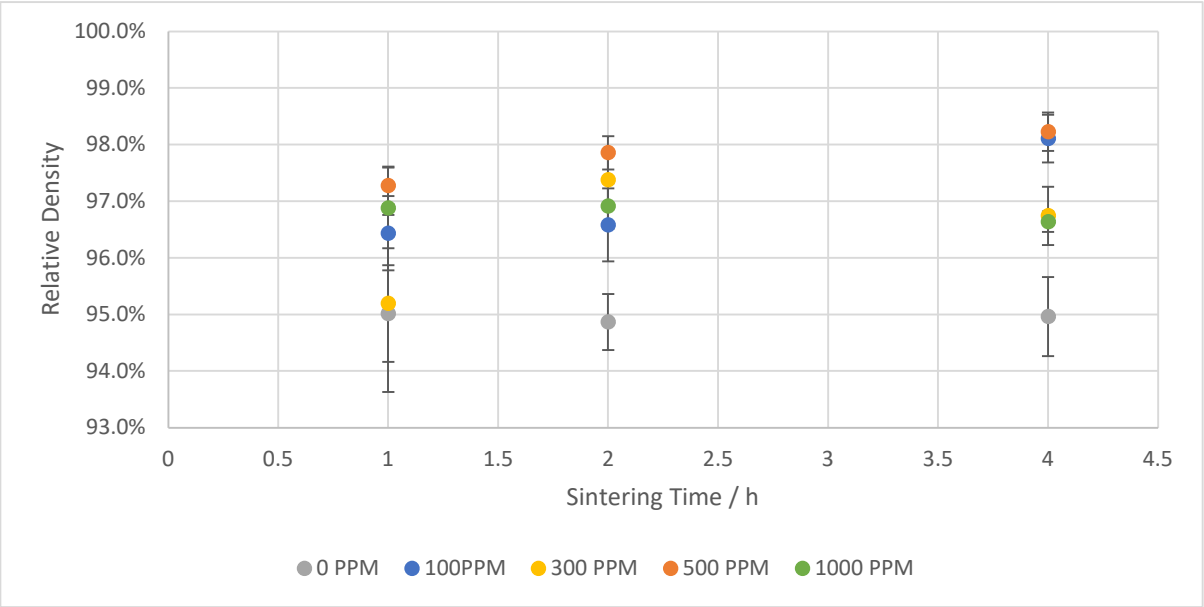


Figure 49: Graph showing the relative density of alumina with 1 wt.% silicon carbide and various quantities of yttrium oxide sintered at 1550 ^{O}C for between 1 and 4 hours.

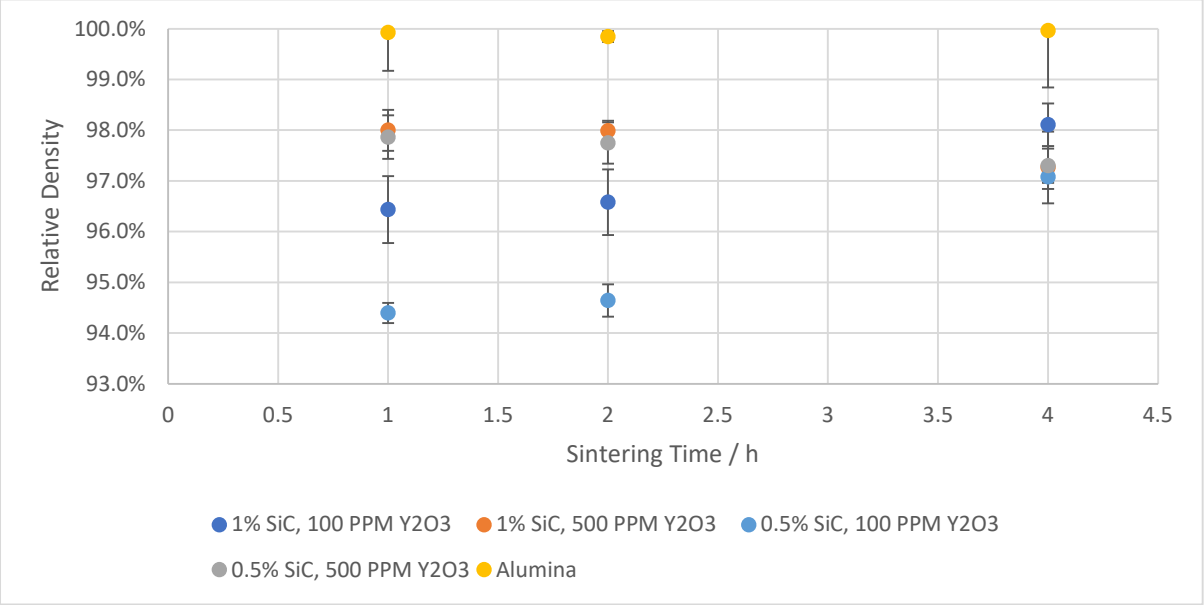


Figure 50: Graph showing the relative density of alumina with various quantities of silicon carbide and yttrium oxide sintered at 1550 ^{O}C for between 1 and 4 hours.

5.1.2.1.4.1 Large Scale Porosity

Porosity in samples made using Al_2O_3-1wt.%SiC with the addition of yttria tended to be in the form of pores with a large diameter. Examples of the resultant microstructure are shown in Figure 51.

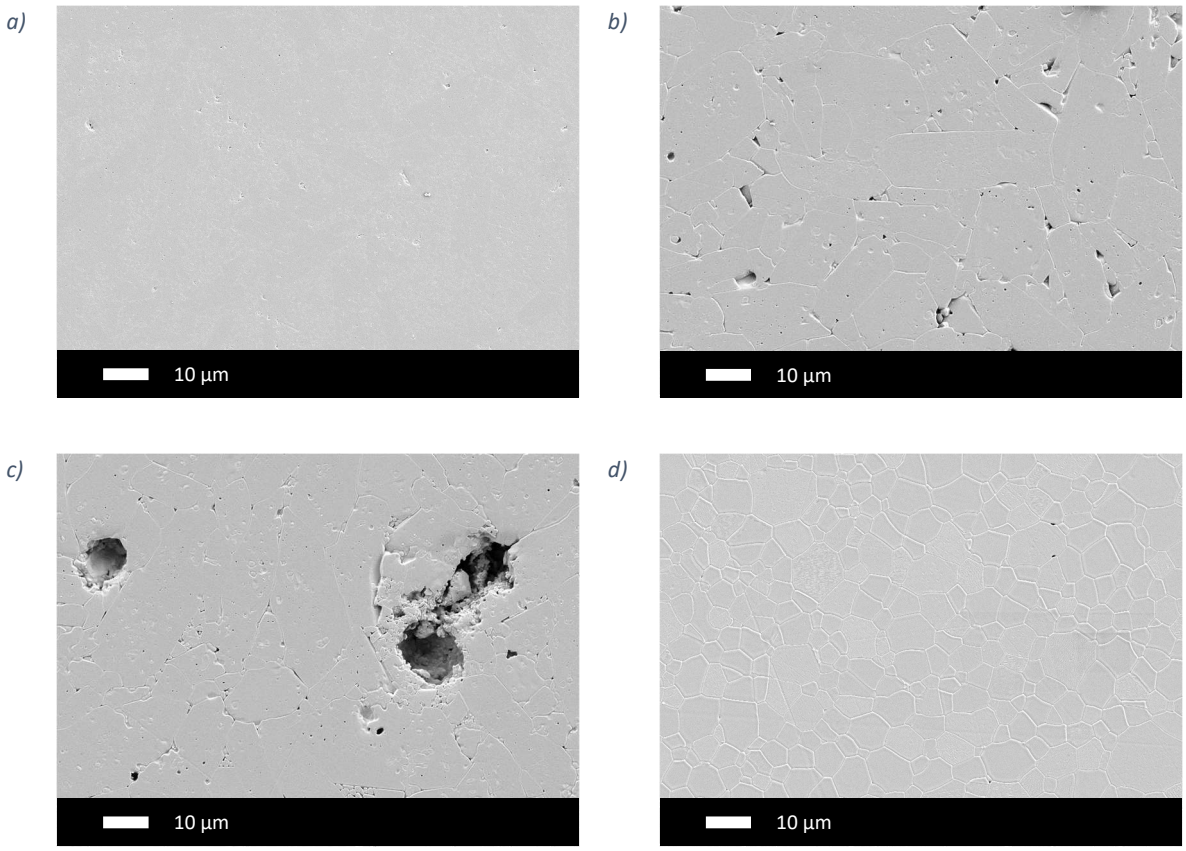


Figure 51: SEM images showing the porosity in alumina with 1 wt.% silicon carbide after sintering for 4 hours at 1550^{O}C with the addition of a) 100 PPM Y_2O_3 b) 500 PPM Y_2O_3 c) 1000 PPM Y_2O_3. An SEM image of alumina sintered under the same conditions is included for comparison, d.

The changes in measured pore size with yttria content are shown in Figure 52. These show an increase in pore size with yttria content from 0.63 ± 0.06 µm with the addition of 100 PPM yttria up to 11.98 ± 2.51 µm with the addition of 1000 PPM yttria.

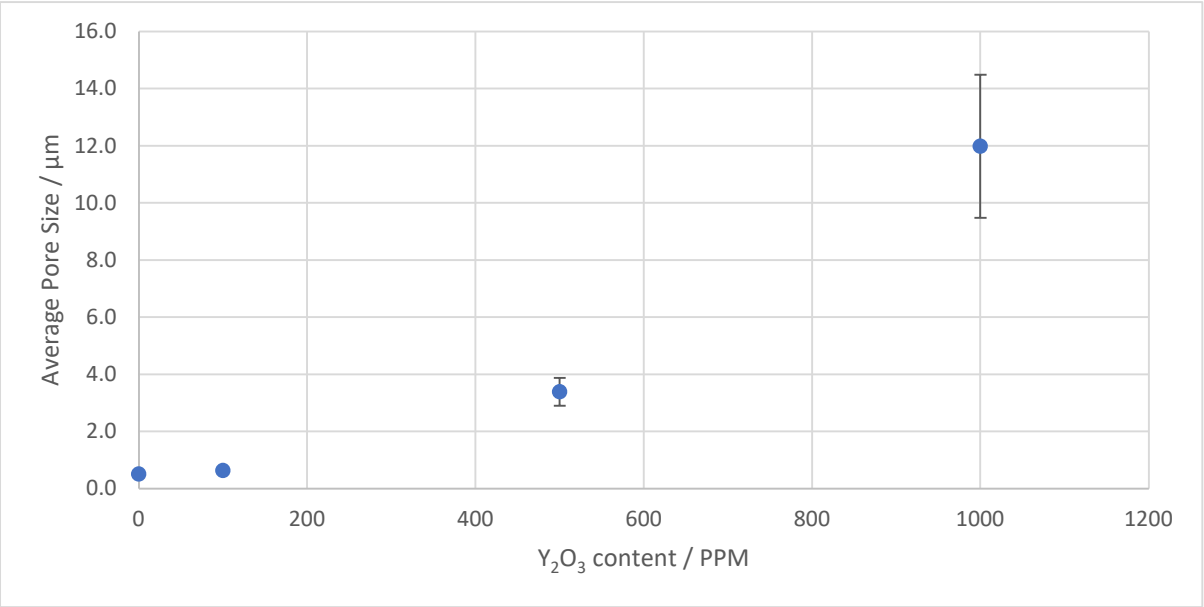


Figure 52: Graph showing the average pore size in alumina with the addition of 1 wt.% silicon carbide and varying quantities of yttria after sintering for 1550^{O}C for 4 hours.

5.1.2.2 Grain Size

Following the mean-linear-intercept method described in section 4.3.2, the mean grain size was determined from images taken using scanning electron microscopy. Similarly, using the calculation of abnormal grain fraction detailed in section 4.3.3, the proportion of abnormal grains was measured from the same scanning electron images where anomalous grains were present.

5.1.2.2.1 Pure Alumina

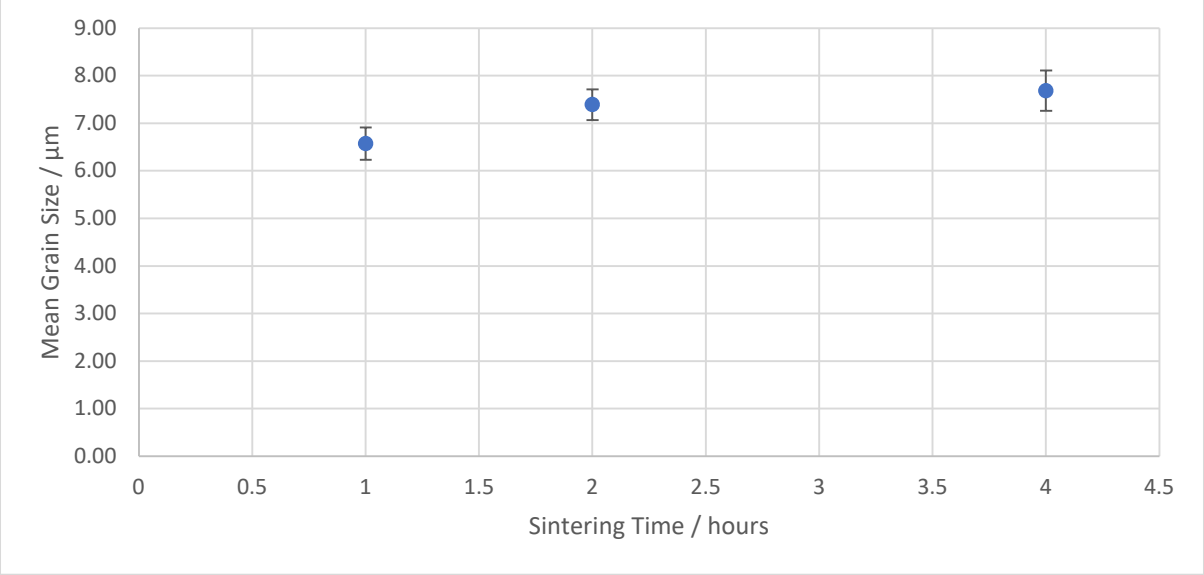
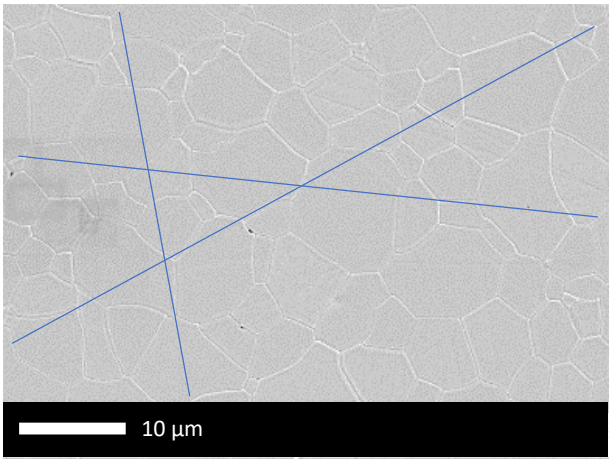


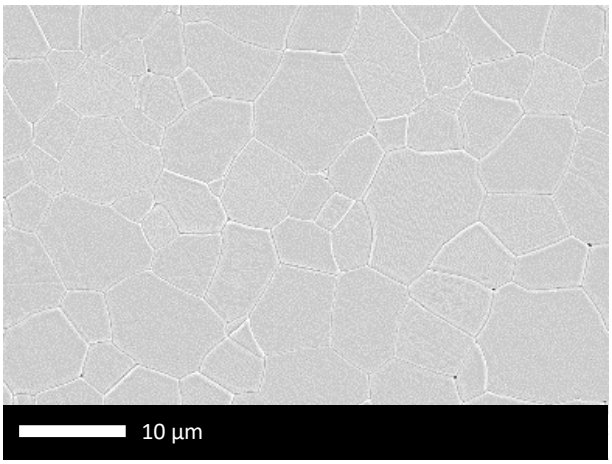
Figure 53: Graph showing the mean grain size of alumina sintered at 1550 ^{O}C against sintering time.

Alumina processed and sintered in the same fashion as described in 4.1.4 resulted in a mean calculated grain size of 7.69 ± 0.43 µm when sintered for 4 hours at 1550 ^{O}C. The growth of these grains with time can be seen in Figure 53. SEM images of the microstructures seen in the samples measured in Figure 53 showed a range of grain sizes regardless of sintering time, as can be seen in Figure 54.

a)



b)



c)

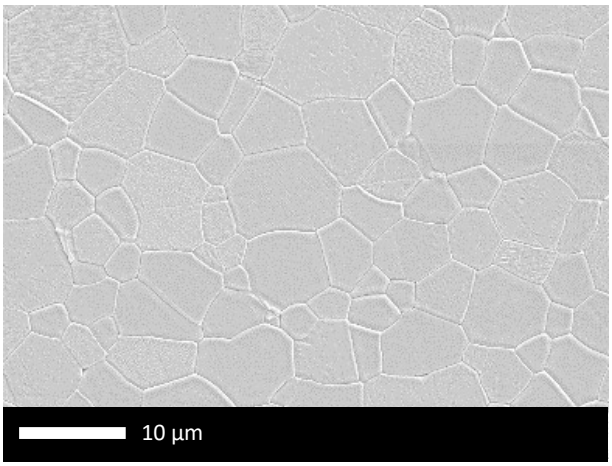


Figure 54: SEM images of alumina sintered at 1550 ^{O}C for a) 1h b) 2h c) 4h. Examples of lines from which the mean linear intercept is calculated are shown overlayed on a.

5.1.2.2.2 Alumina-Silicon Carbide

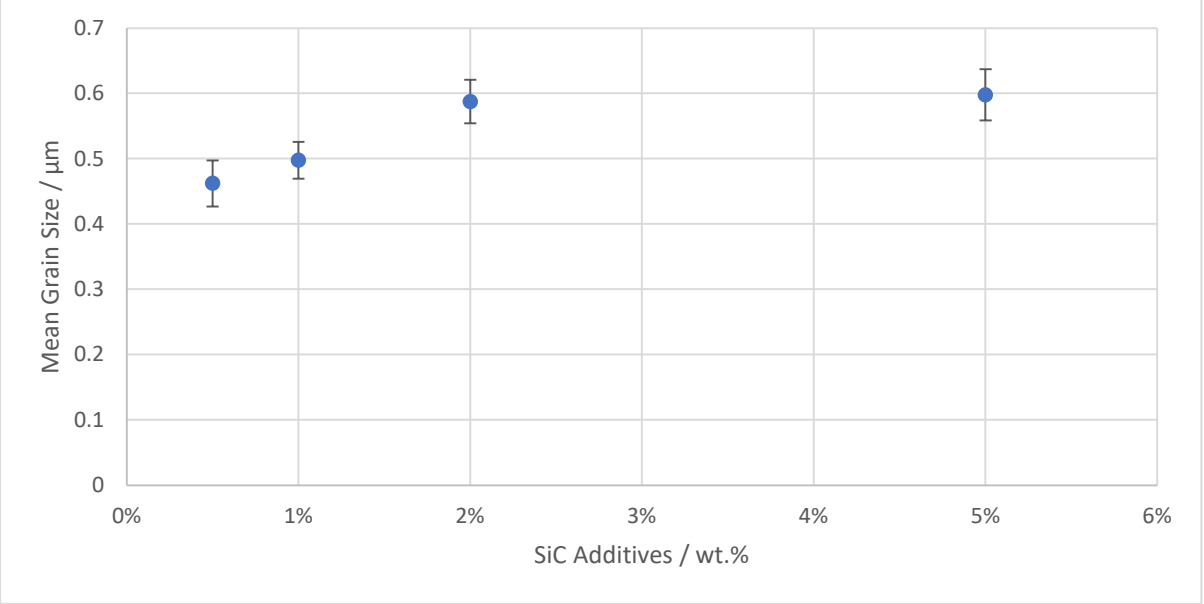
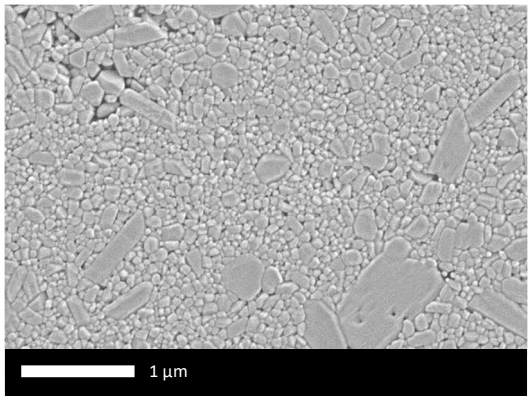


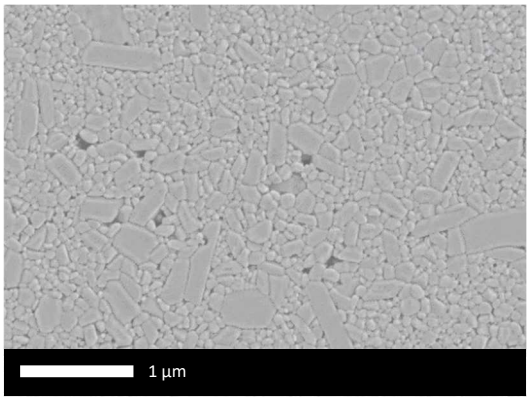
Figure 55: Graph showing change in mean grain size, with standard deviation, of alumina with varying silicon carbide additions after sintering for 4 hours at 1550 ^{O}C.

The mean grain size of alumina with silicon carbide additives sintered at 1550 ^{O}C for 4 hours was between 0.45 µm and 0.60 µm dependent on the percentage of silicon carbide additives. This is a significant decrease in mean grain size from pure alumina, however increased grain size was found to positively correlate with increased silicon carbide additions at 0.5 wt.% SiC and above. This increase in mean grain size is shown in Figure 55.

a)



b)



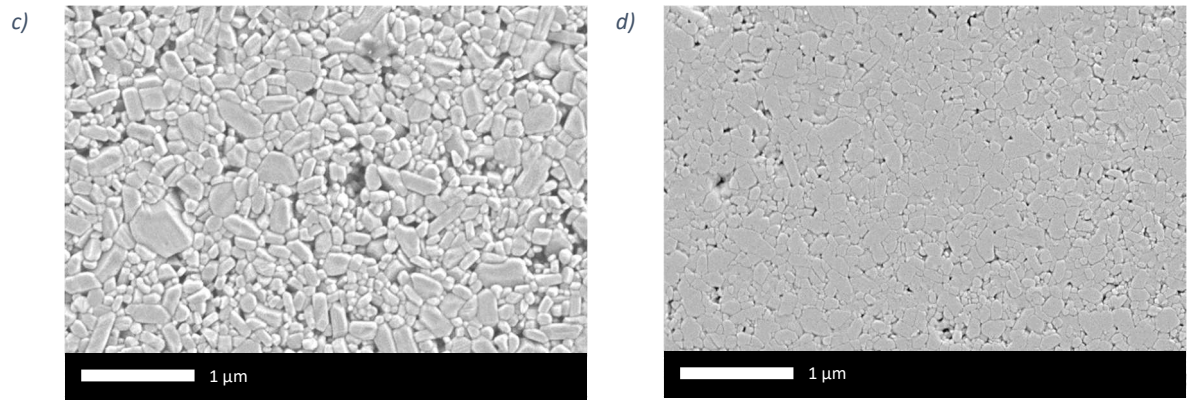


Figure 56: SEM images of alumina sintered at 1550 ^{O}C for 4 hours with a) 0.5 wt.% silicon carbide b) 1 wt.% silicon carbide c) 2 wt.% silicon carbide d) 5 wt.% silicon carbide.

The addition of silicon carbide resulted in the growth of abnormal grains, as can be seen in Figure 56. The measured quantity of abnormal grains decreases with increasing silicon carbide content, from 33 % of the cross-sectional area being taken up by abnormal grains with the addition of 0.5 wt.% silicon carbide to 0 % abnormal grains with the addition of 5 wt.% silicon carbide. This decrease in abnormal grains can be seen in Figure 57.

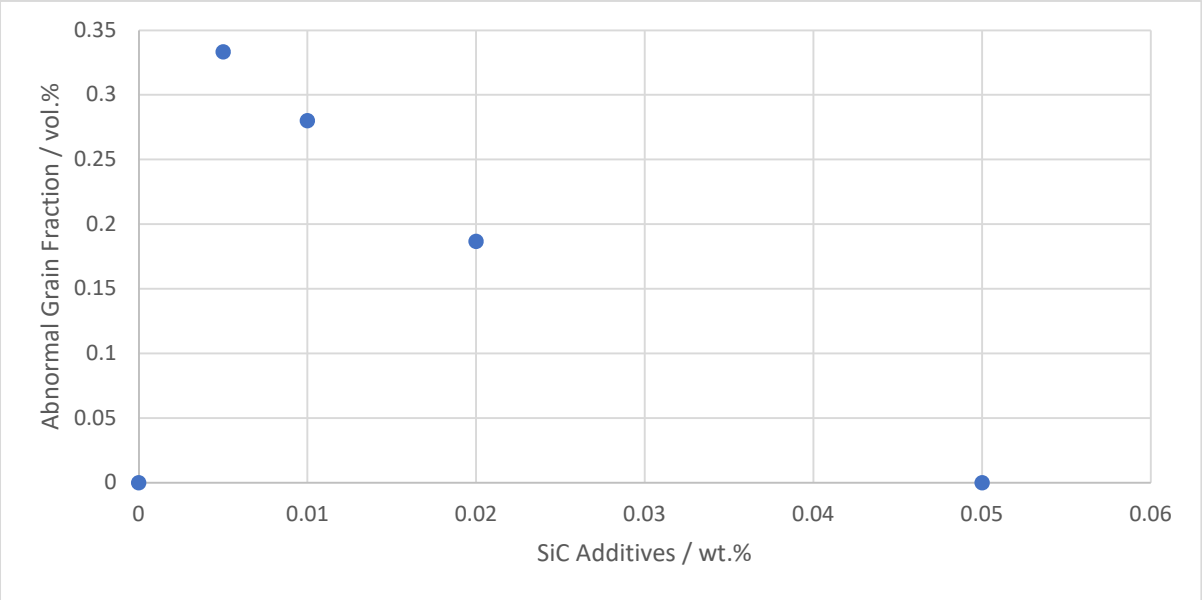


Figure 57: Graph showing decrease in abnormal grain fraction of alumina with varying silicon carbide additions after sintering for 4 hours at 1550 ^{O}C.

Al_2O_3-1wt.%SiC was sintered at 1450 ^{O}C and 1550 ^{O}C for between 1 and 4 hours. A significant increase in mean grain size was seen after 2h or longer sintering at 1550 ^{O}C. This growth in grain size was not seen after sintering at 1450 ^{O}C regardless of sintering time, as is shown in Figure 58. The increase in mean grain size can be seen micrographically in Figure 59. This shows the formation of the abnormal grains coinciding with the increase in normal grain size measured.

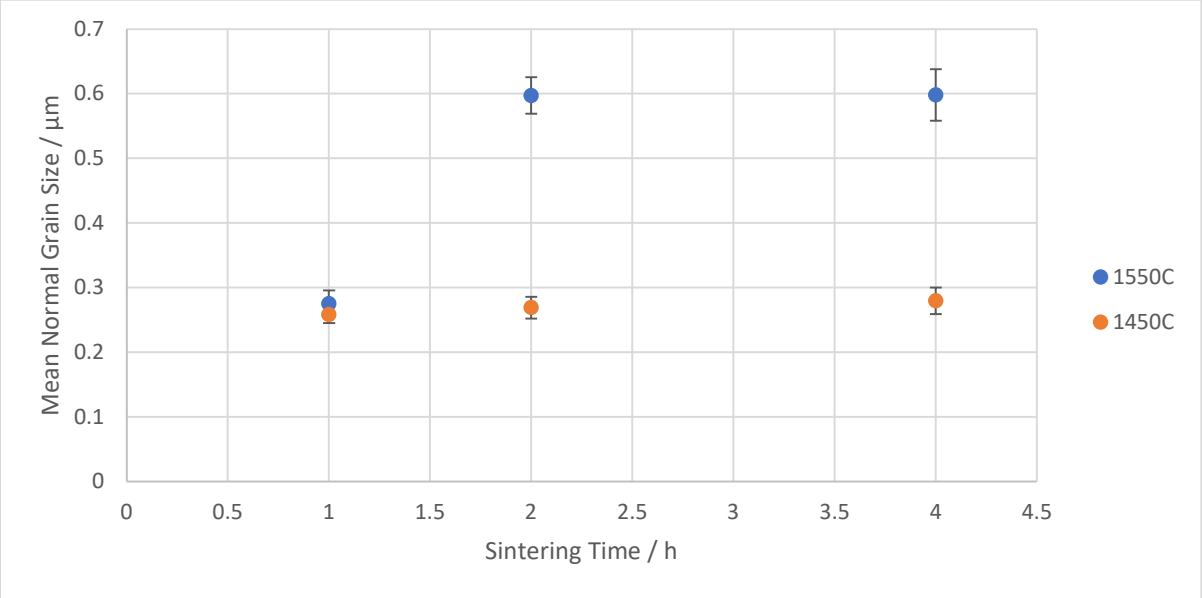
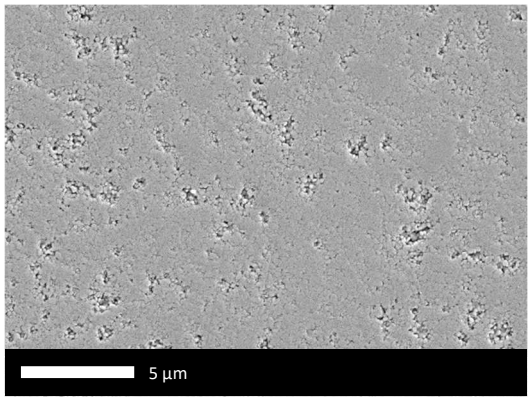
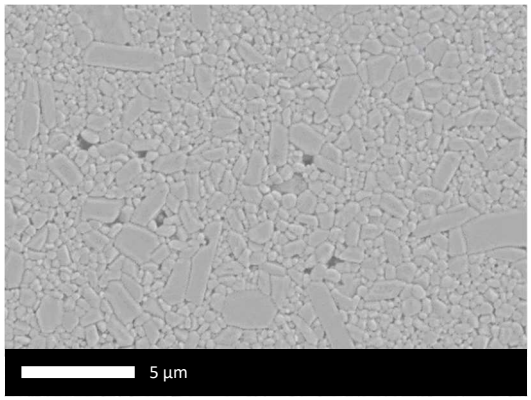


Figure 58: Graph showing change in mean grain size of alumina with 1 wt.% silicon carbide after sintering at 1550 ^{O}C and 1450 ^{O}C for between 1 and 4 hours.

a)



b)



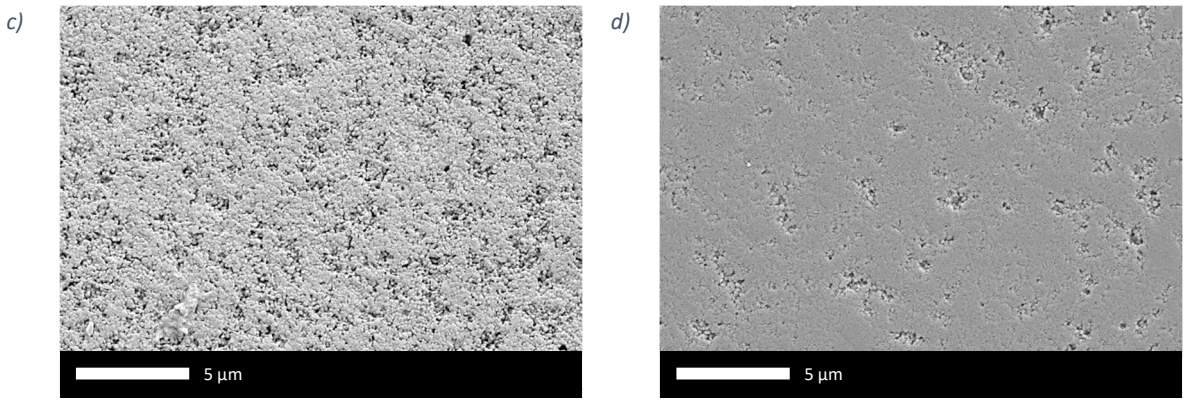


Figure 59: SEM Images of alumina with 1 wt.% silicon carbide sintered at a) 1550 ^{O}C for 1 hour b) 1550 ^{O}C for 4 hours c) 1450 ^{O}C for 1 hour d) 1450 ^{O}C for 4 hours.

5.1.2.2.3 Alumina-Silicon Carbide-Additives

The mean grain size of alumina with 1 wt.% SiC sintered at 1550 ^{O}C increased with a 500 ppm addition of calcium nitrate, magnesium nitrate, neodymium nitrate or yttrium oxide. This increase can be clearly seen in Figure 60; the addition of yttrium oxide results in the largest mean grain size after 4 hours sintering.

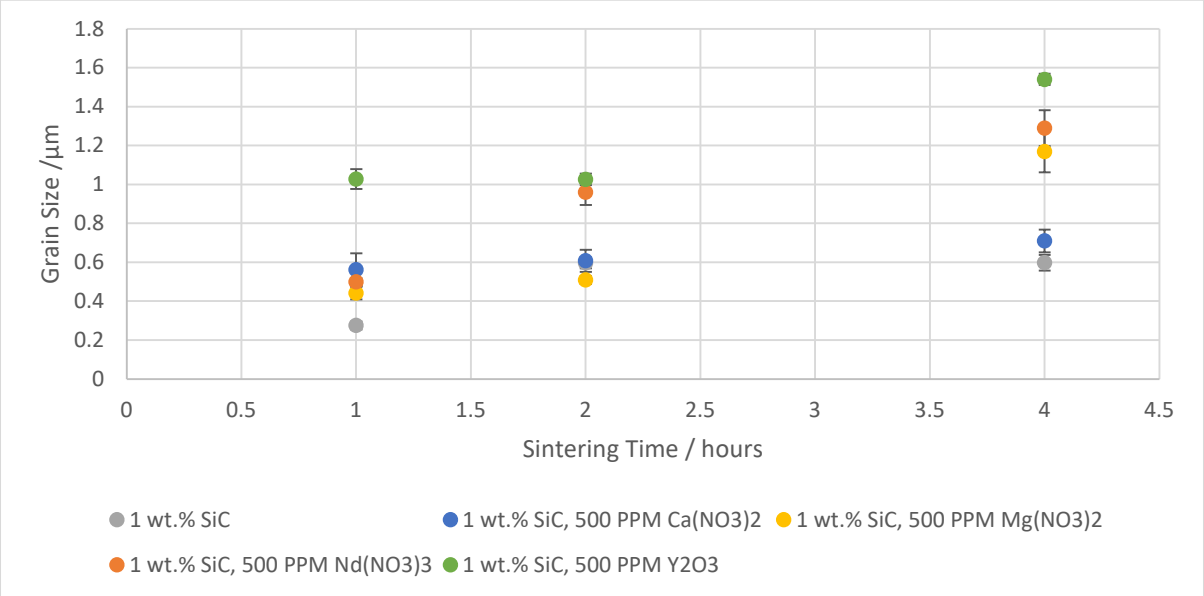


Figure 60: Graph showing the mean normal grain size of alumina with 1 wt.% silicon carbide after sintering at 1550 ^{O}C for between 1 and 4 hours with the addition of 500 ppm of calcium nitrate, magnesium nitrate, neodymium nitrate or yttrium oxide.

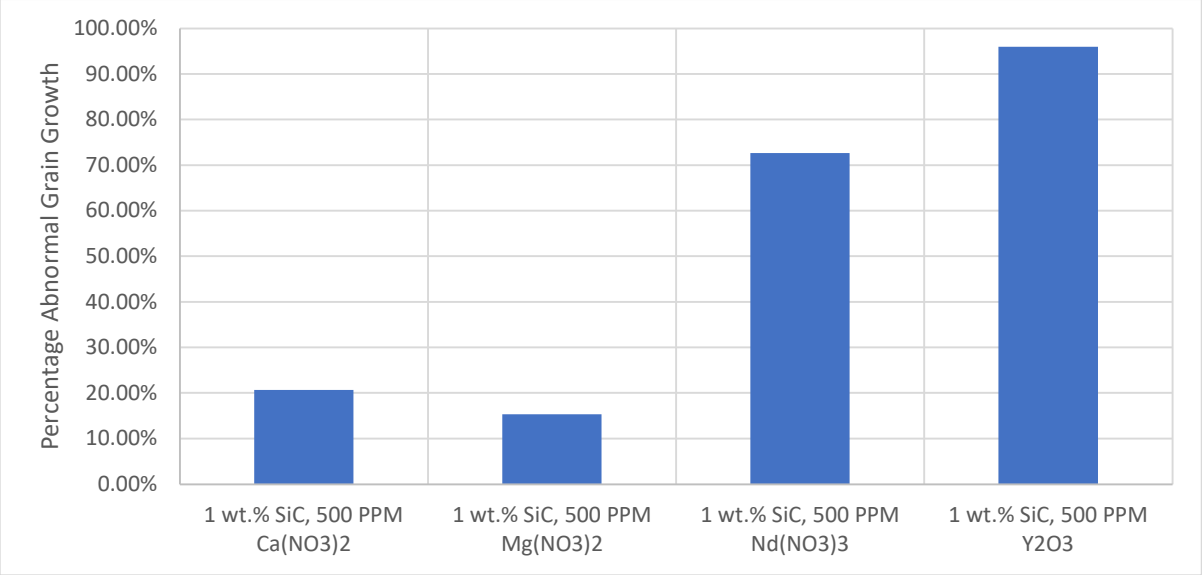
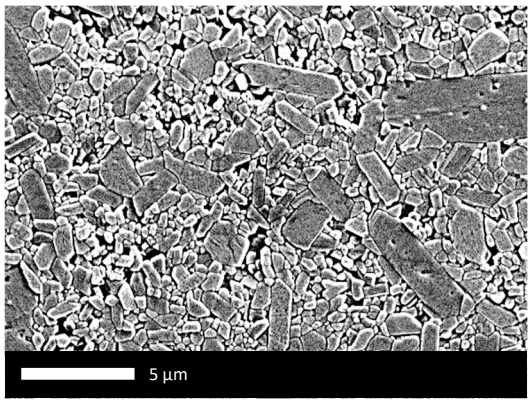


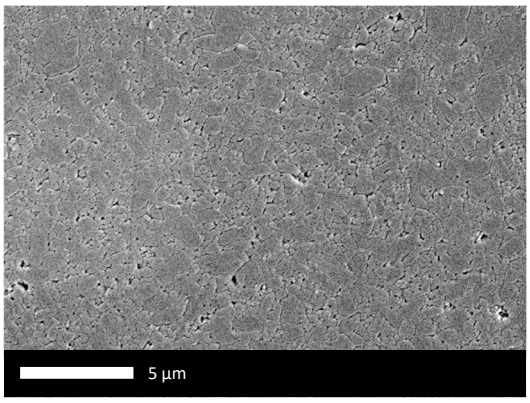
Figure 61: Graph showing the volume fraction of abnormal grains of alumina with 1 wt.% silicon carbide and 500 ppm additions of calcium nitrate, magnesium nitrate, neodymium nitrate or yttrium oxide after sintering at 1550 OC for 4 hours.

Scanning electron microscopy images of the resultant microstructures in the samples studied in Figure 60 show the neodymium nitrate and yttrium oxide additives each promoted significant quantities of abnormal grain growth as well as the larger mean grain size measured. These additives resulted in a volume percentage of abnormal grains of 73 % and 96 % in each sample respectively. While calcium nitrate and magnesium nitrate had a smaller effect on grain size, both additives did produce some abnormal grain growth within the resultant microstructure. The comparison between the quantities abnormal grains seen with the additions of these 4 additives are shown in Figure 61 and the respective microstructures are shown in Figure 62.

a)



b)



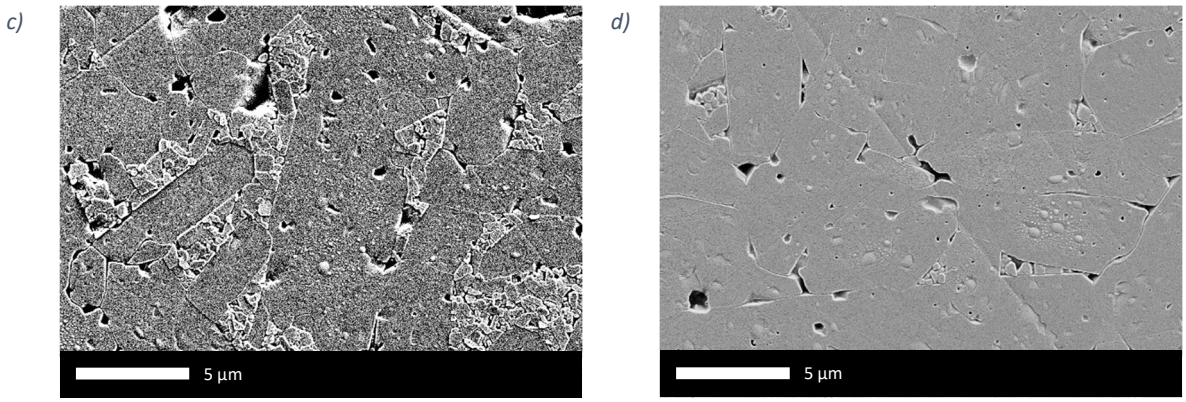


Figure 62: SEM Images of alumina with 1 wt.% silicon carbide sintered at 1550 ^{O}C for 4 hours with 500 ppm additives of a) calcium nitrate b) magnesium nitrate c) neodymium nitrate d) yttrium oxide.

Measurements of the size of abnormal grains in the samples imaged in Figure 62 are shown in Figure 63. This shows a significantly larger mean abnormal grain size in Al_2O_3-1wt.% SiC with the addition of neodymium nitrate or yttrium oxide than the equivalent additions in calcium nitrate or magnesium nitrate. The micrographs in Figure 62.c and d both show particles within the abnormal grains and these are investigated further in later chapters.

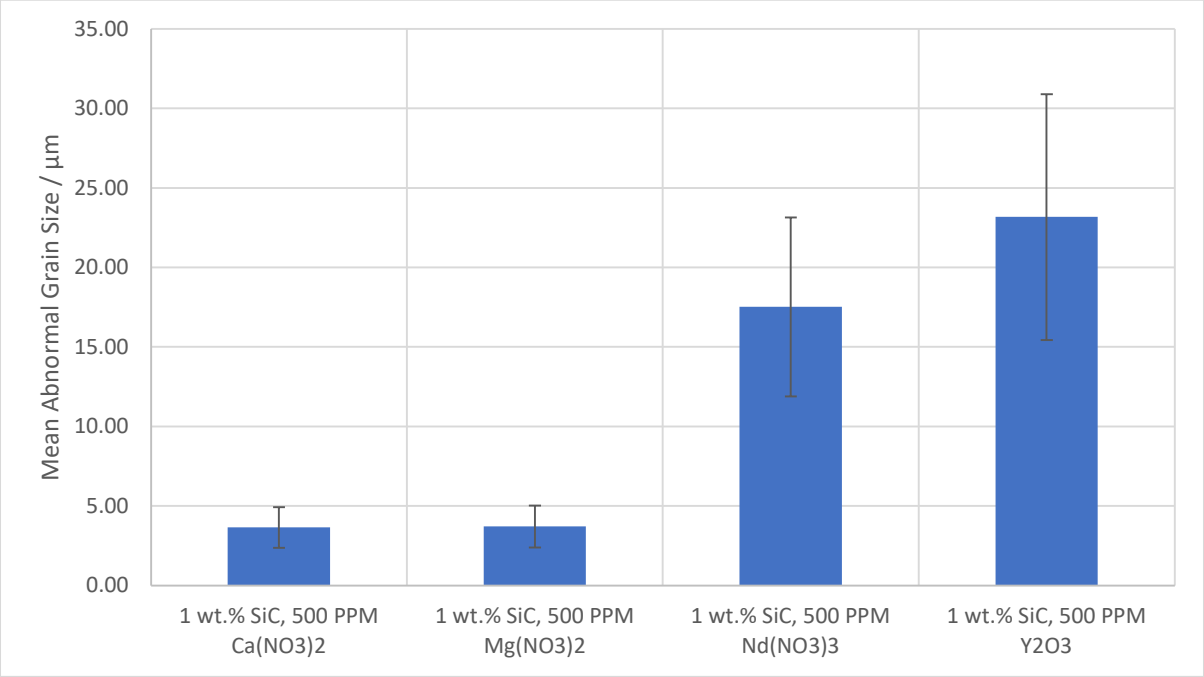


Figure 63: Graph showing the mean grain size of abnormal grains of alumina with 1 wt.% silicon carbide and 500 ppm additions of calcium nitrate, magnesium nitrate, neodymium nitrate or yttrium oxide after sintering at 1550 ^{O}C for 4 hours.

5.1.2.2.4 Alumina-Silicon Carbide-Yttria

The work following the composites created in 5.1.2.2.3 focused on the development of the microstructure in the alumina-silicon carbide-yttria composite as it possessed the highest density among the additives tested. A significant increase in grain size is seen in this composite at sintering temperatures of 1550 ^{O}C, with an average normal grain size of 1.54 ± 0.04 µm after 4 hours sintering. Below this temperature, mean grain size remains below 0.4 µm regardless of sintering time. This distinction in grain size can clearly be seen in Figure 64.

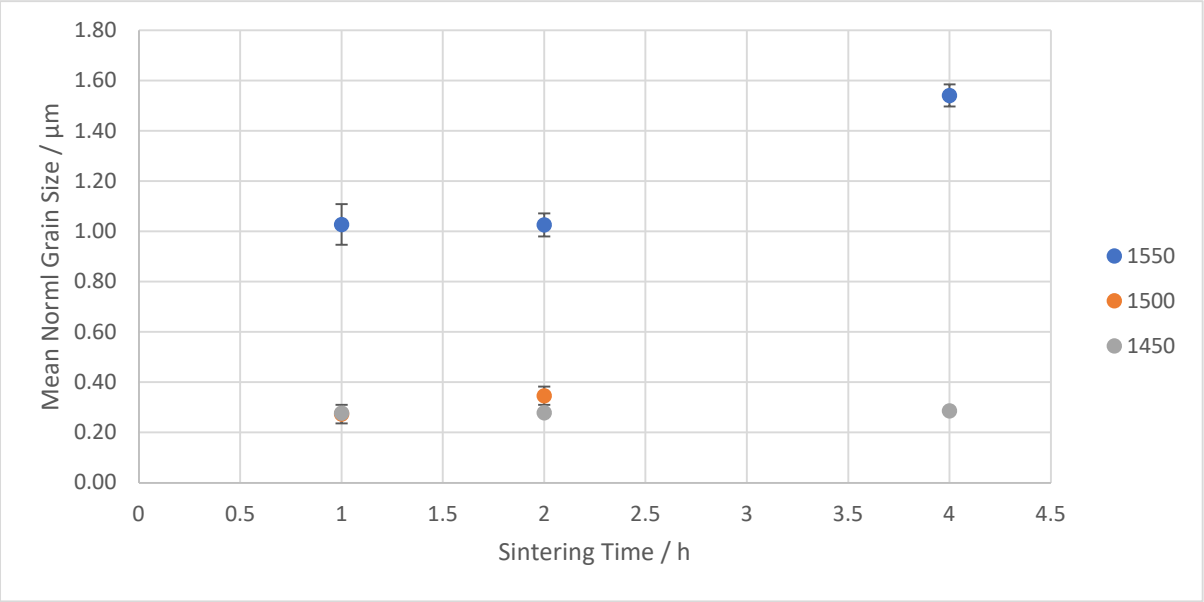


Figure 64: Graph showing the change in mean grain size of alumina with 1 wt.% silicon carbide and 500 ppm Y_2O_3 after sintering for between 1 and 4 hours at 1450 ^{O}C, 1500 ^{O}C and 1550 ^{O}C.

Similar, to what can be seen in Figure 62, the formation of the larger normal grain size coincides with the growth of abnormal grains. Below 1550 ^{O}C, abnormal grain growth does not occur, but after sintering at this temperature abnormal grain growth can be clearly seen. SEM micrographs plainly show this difference in microstructure in Figure 65.

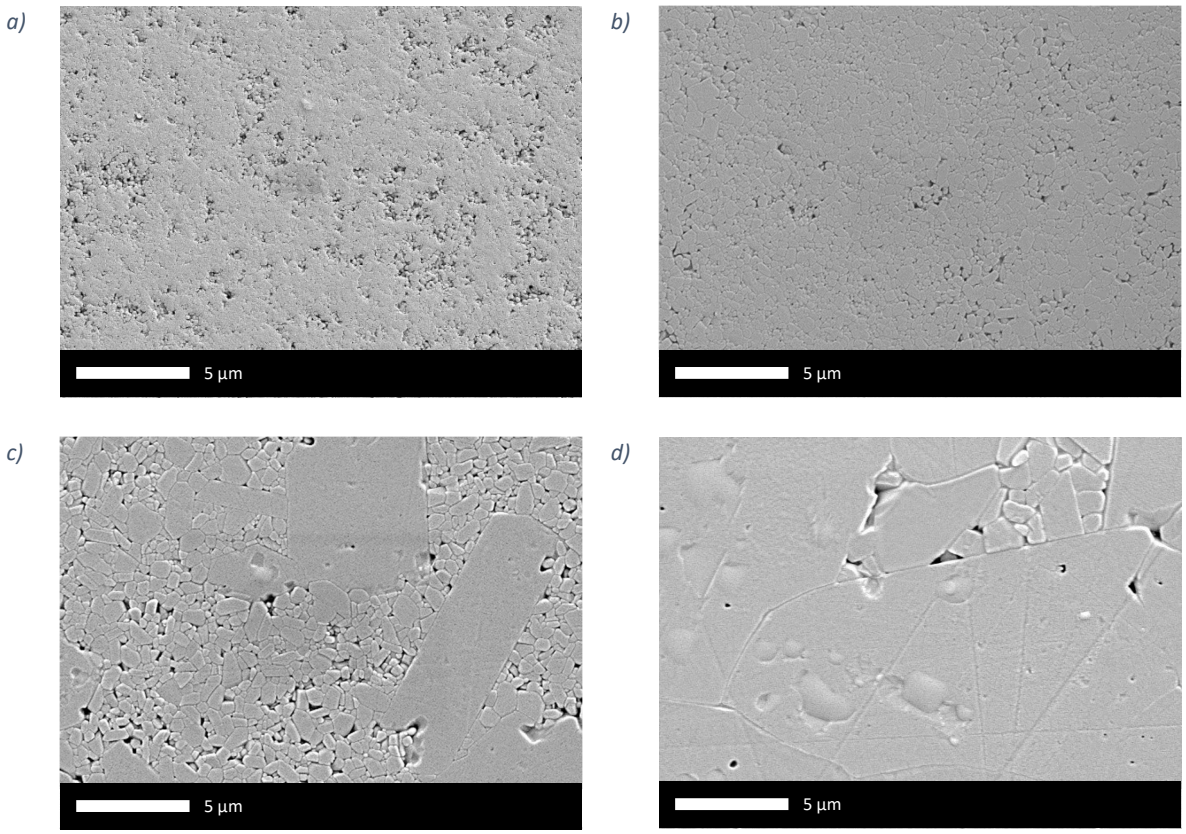


Figure 65: SEM Images of alumina with 1 wt.% silicon carbide and 500 ppm yttria sintered for a) 4h at 1450 ^{O}C b) 4h at 1500 ^{O}C c) 1h at 1550 ^{O}C d) 4h at 1550 ^{O}C.

5.1.2.2.4.1 Variations in yttria content

The effect of changes in yttrium oxide additive content were investigated by producing samples with 1 wt.% silicon carbide and varying yttrium oxide contents. A 1000ppm Y_2O_3 addition was found to result in the largest mean grain size across samples manufactured with varying yttrium oxide content after 4 hours sintering, with a calculated mean grain size of 2.89 ± 0.65 µm. Generally, a lower quantity of yttrium oxide resulted in a smaller mean grain size, as can be seen in Figure 66.

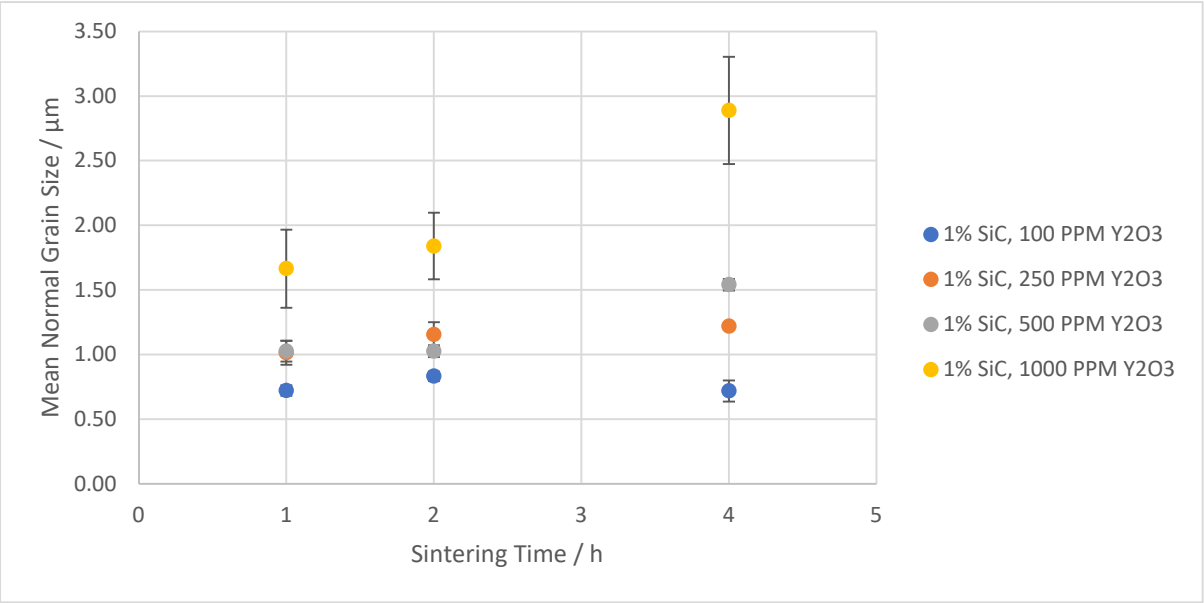


Figure 66: Graph showing the change in mean normal grain size of alumina with 1 wt.% silicon carbide and varying quantities of yttria after sintering for between 1 and 4 hours at 1550 ^{O}C.

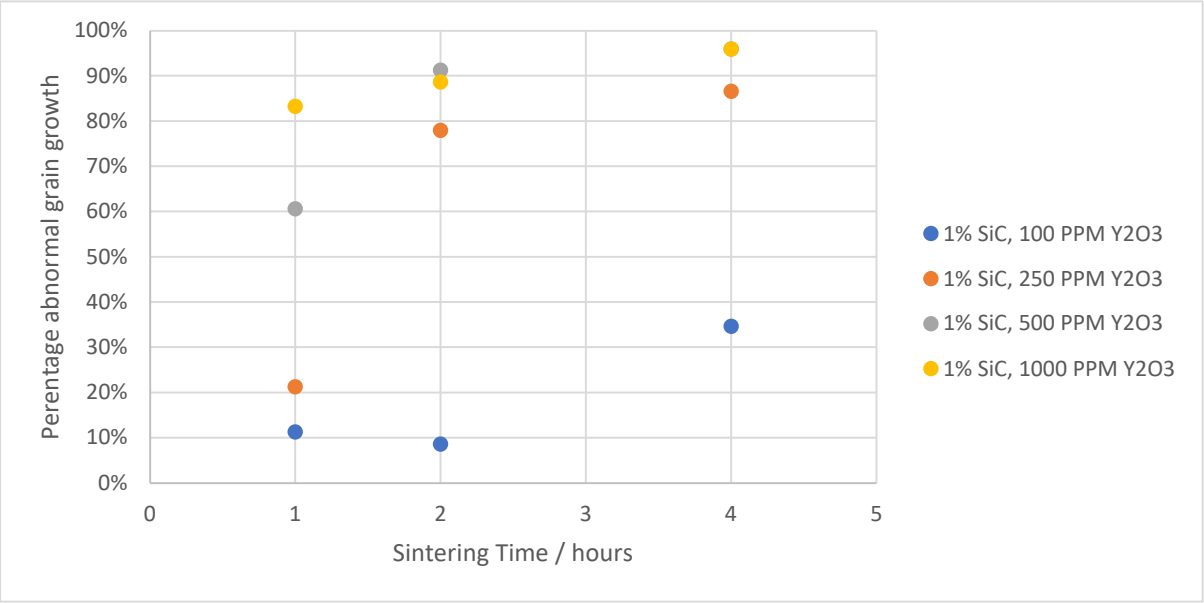


Figure 67: Graph showing the volume fraction of abnormal grains of alumina with 1 wt.% silicon carbide and varying quantities of yttria after sintering for between 1 and 4 hours at 1550 ^{O}C.

A similar effect was seen in the growth of abnormal grains. A larger quantity of yttrium oxide additives resulted in a higher fraction of abnormal grain growth, as is shown in Figure 67. This change can also be clearly seen in the resultant microstructure as in Figure 68. The abnormal grains observed in Figure 68 showed the same trend in grain size as seen in Figure 66. A smaller quantity of Y_2O_3 additives

resulted in a smaller mean abnormal grain size with samples of Al_2O_3-1wt.%SiC-100ppmY_2O_3 having an abnormal grain size 35% of the abnormal grains seen in Al_2O_3-1wt.%SiC-1000ppmY_2O_3.

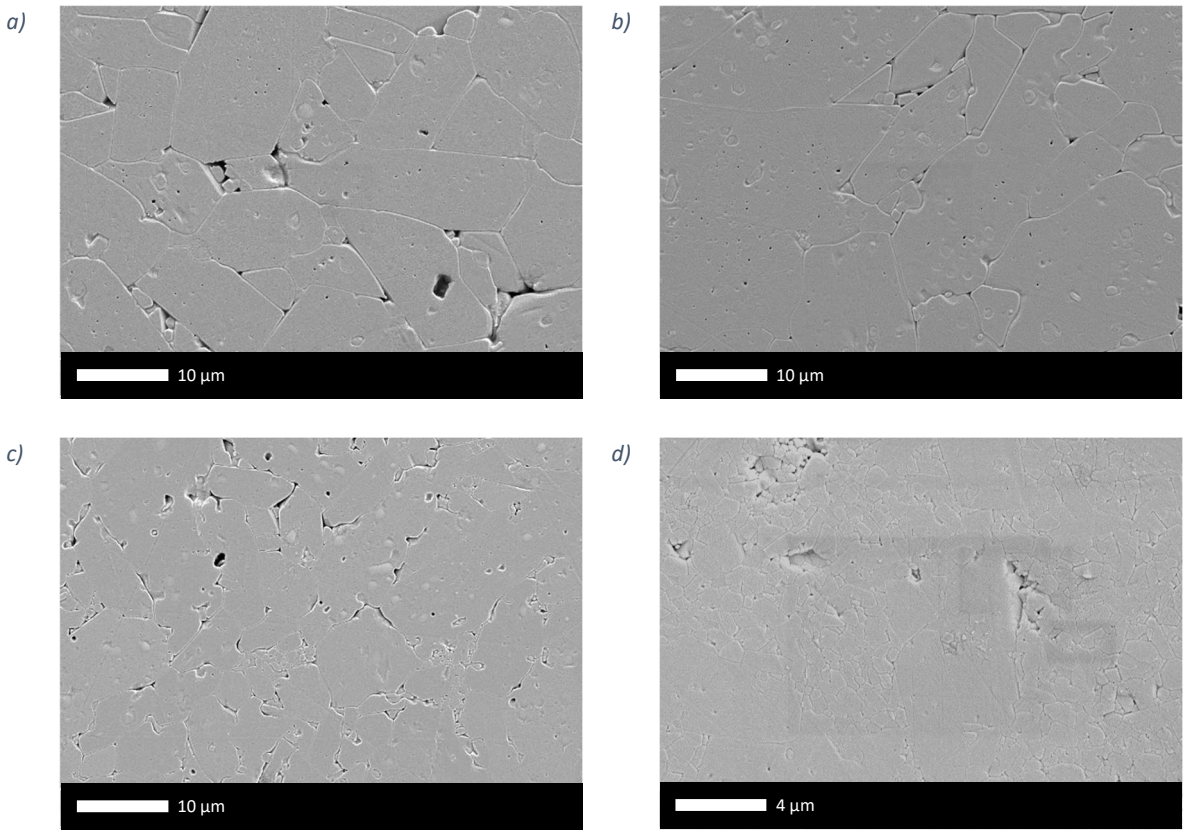


Figure 68: SEM Images of alumina with 1 wt.% silicon carbide sintered for 4 hours at 1550 ^{O}C with a) 1000 ppm Y_2O_3 b) 500 ppm Y_2O_3 c) 250 ppm Y_2O_3 d) 100 ppm Y_2O_3.

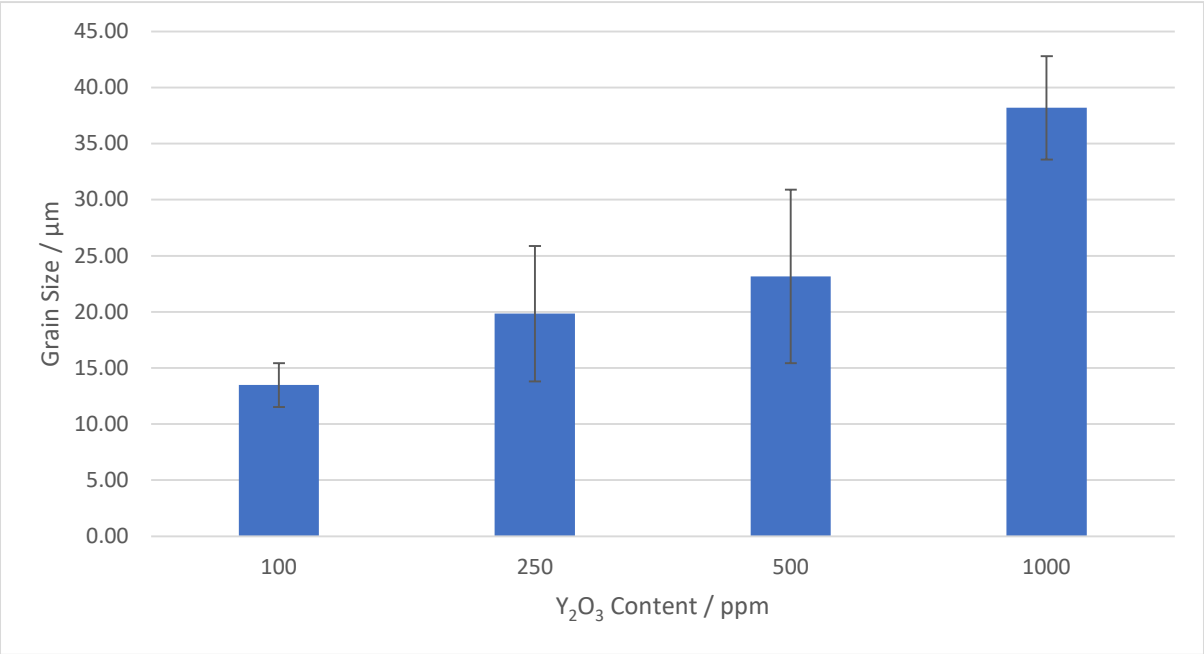


Figure 69: Graph showing the mean grain size of abnormal grains of alumina with the addition of 1 wt.% silicon carbide and various quantities of yttrium oxide after sintering for 4 hours at 1550 ^{O}C.

5.1.2.3 Chemical composition

Following the method described in section 4.3.6, the distribution of elements within samples was determined from energy dispersive X-ray spectroscopy data taken using a Zeiss Merlin scanning electron microscope.

5.1.2.3.1 Alumina Mullite Composites

Energy dispersive x-ray spectroscopy mapping of silicon in Al_2O_3-SiC composites sintered for 4 hours at 1550 ^{O}C showed a clear trend in distribution dependent on the initial percentage of silicon carbide added. This change can be seen in the maps showing the distribution of silicon shown in Figure 70. Alumina and silica show negligible solid solubility with each other. This was demonstrated by Klug et al. [93], as is shown in Figure 71 through the alumina-silica phase diagram. Therefore, the distribution seen in silicon carbide additions of up to 1 wt.%, is likely mullite particles that are too small to individually resolve using the SEM-EDX technique employed. Above this percentage, the silicon groups into areas of higher silicon density that are individually distinguishable and at 5 wt.% silicon carbide these take the form of silicon-containing grains of similar size to the surrounding alumina grains.

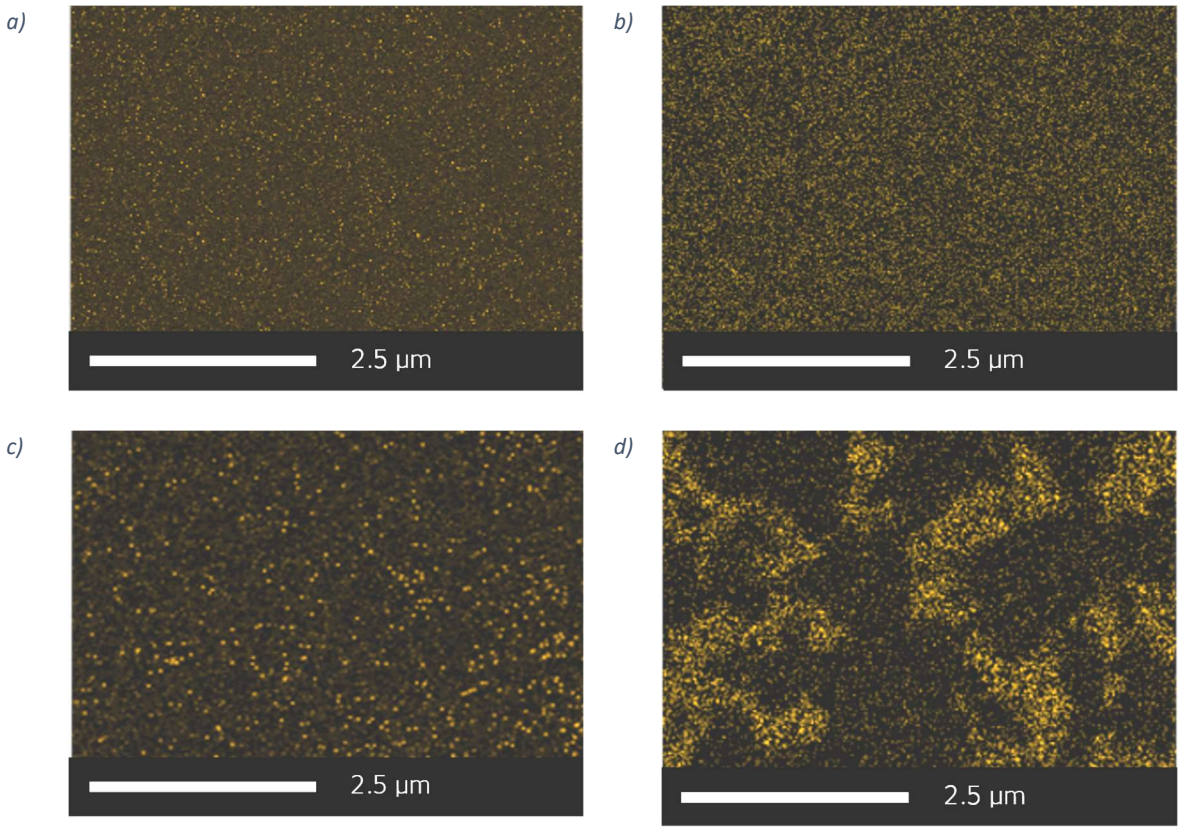


Figure 70: EDX maps showing the distribution of silicon in alumina samples sintered at 1550^{O}C for 4 hours containing a) 0.5 wt.% silicon carbide b) 1 wt.% silicon carbide c) 2 wt.% silicon carbide d) 5 wt.% silicon carbide.

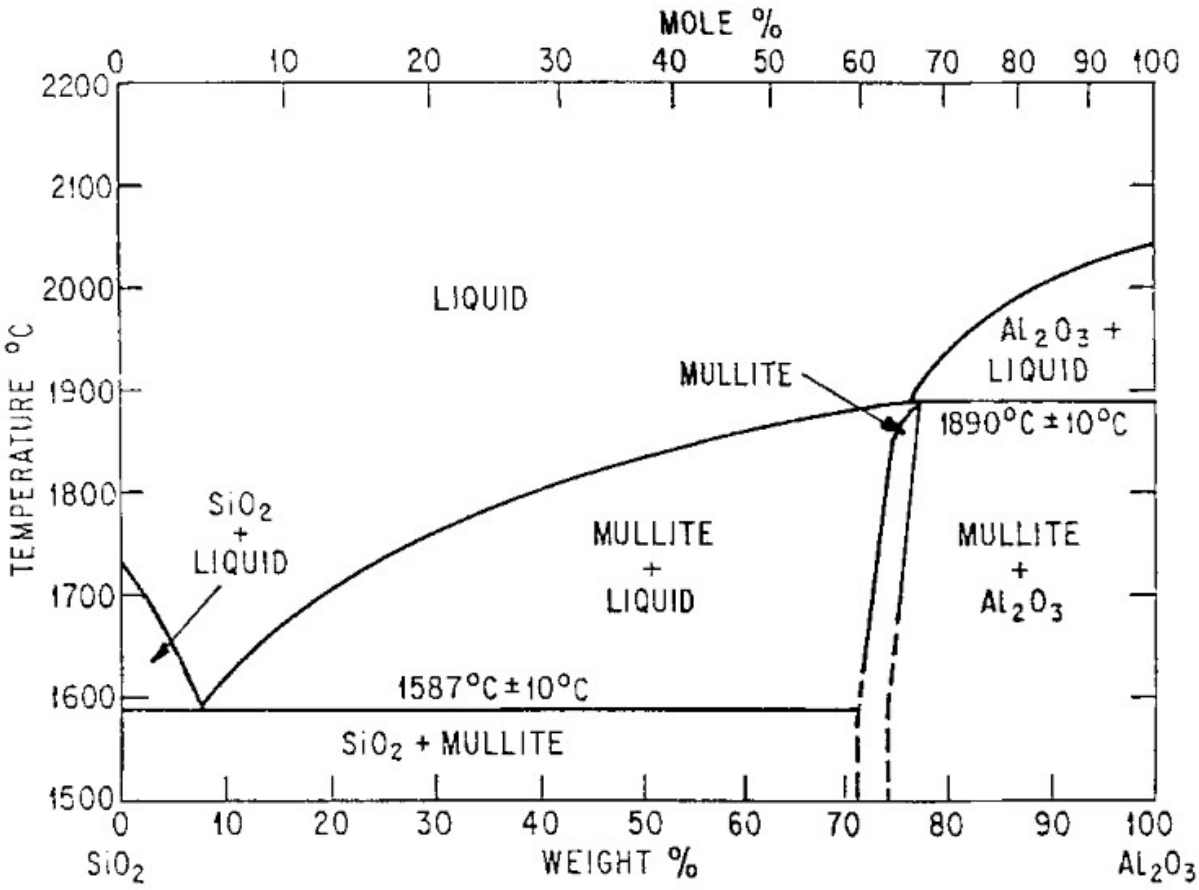


Figure 71: Alumina-silica phase diagram, reproduced from Klug et al. [93].

5.1.2.3.2 Alumina-Silicon Carbide-Yttrium Oxide

As shown in Figure 68, the addition of both silicon carbide and yttrium oxide to alumina created a significant quantity of abnormal grain growth with smaller grains contained within the larger abnormal grains when sintered at 1550 ^{O}C. EDX spectroscopy mapping of this microstructure shows silicon predominantly within the small grains contained within the abnormal alumina grains. These silicon containing particles can be clearly seen in Figure 72. This can be seen regardless of yttrium oxide additive content. However, it was found to be most prevalent with higher quantities of yttrium oxide additions. In samples containing lower yttrium oxide quantities, and consequently a smaller percentage abnormal grains, the areas of normal grains show a mixture of grain types. Some of the grains contain silicon and some are pure alumina in a similar fashion to the grains seen in Figure 70.d.

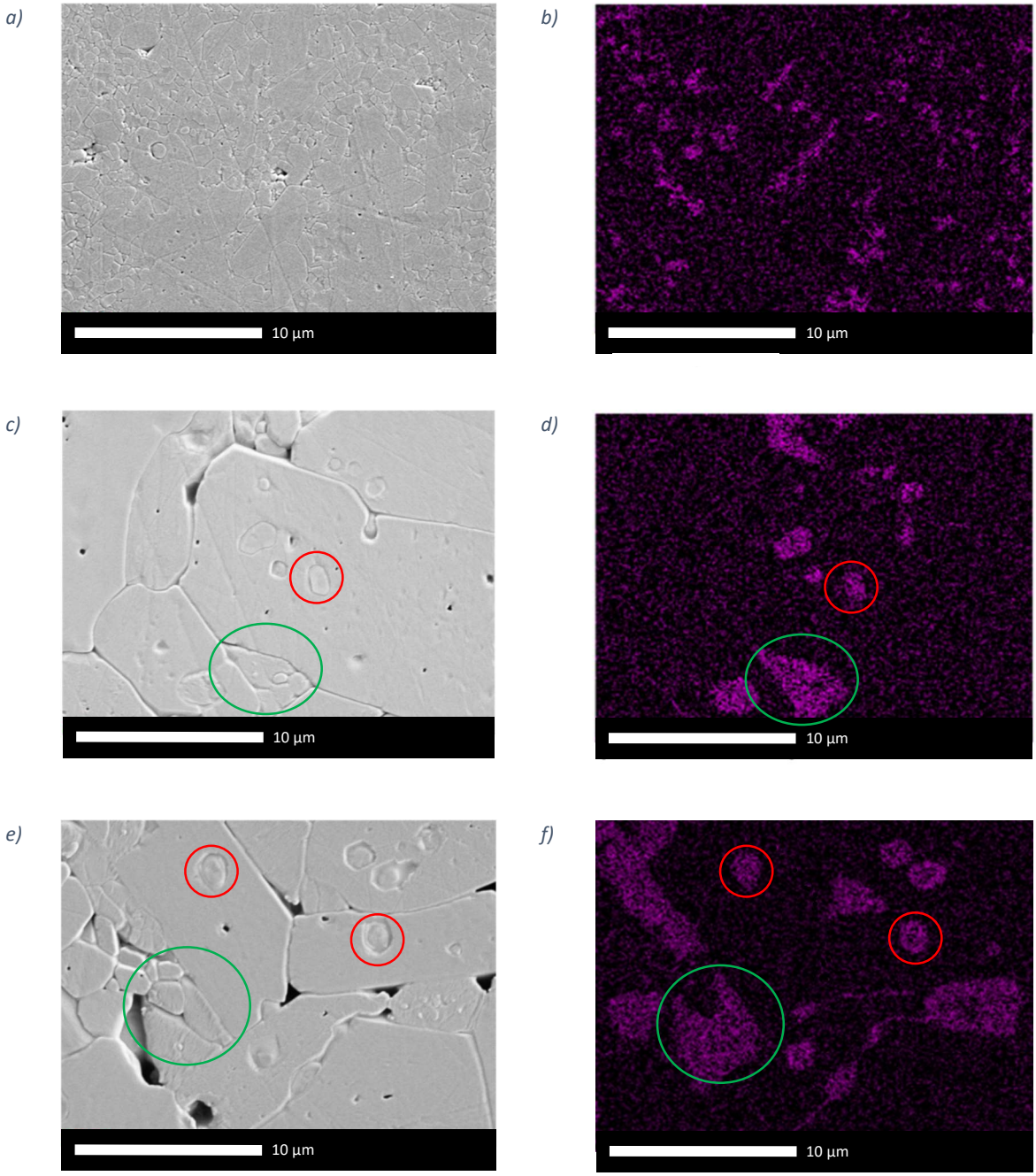


Figure 72: SEM images of alumina with 1 wt.% silicon carbide sintered at 1550 ^{O}C for 4 hours alongside EDX maps of silicon taken of the same area of microstructure. The samples were each doped with a-b) 100 ppm yttrium oxide c-d) 500 ppm yttrium oxide e-f) 1000 ppm yttrium oxide. Some examples of intragranular mullite grains are circled in red and regions of polycrystalline mullite are circled in green.

Figure 72.f appears to show a silicon rich film along some of the observed grain boundaries separating two abnormal grains. These grain boundaries in the equivalent SEM image, Figure 72.e, do not show any different structure to other grain boundaries bordering abnormal grains, however. This suggests

the presence of the silicon seen here is an artifact owing to the angle between the sample and the detector created by thermal etching [216]. As all the grain boundaries which show this observed silicon layer lie approximately from left to right, and therefore show a consistent angle away from the detector not seen in grain boundaries that run from the bottom to the top of micrograph.

5.1.2.4 Mullite Distribution

Using the methodology described in 4.3.4, the average mullite particle size can be measured across Al_2O_3-1wt.%SiC-Y_2O_3 with a variety of yttrium contents as is shown in Figure 73. This shows an increase in mullite grain size with added yttrium oxide content.

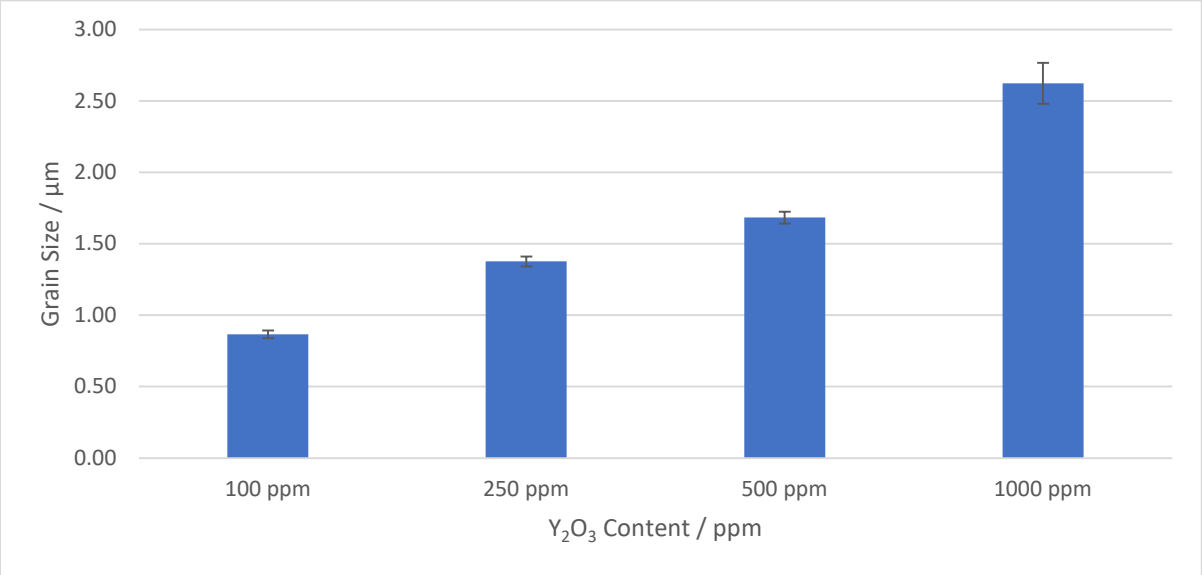


Figure 73: Graph showing the mean grain size of intragranular mullite grains within the abnormal grains of Al_2O_3-1wt.%SiC-Y_2O_3 with varying quantities of Y_2O_3 after sintering at 1550 ^{O}C for 4 hours in air.

However, the lower levels of yttrium oxide additives resulted in a larger number of intragranular mullite grains found within the micrograph as a whole. Therefore, the volume percentage of mullite is not proportional to the grain size measured and so the resultant volume percentage mullite is plotted in Figure 74. This methodology is only capable of measuring the mullite grains within the abnormal alumina grains as the mullite and alumina grains are indistinguishable under scanning electron microscopy within the sections of normal grains as they display no distinct contrast between grains of the 2 materials. As a result, the significant changes in quantity of abnormal grains with

changes in yttrium oxide content affects the resultant measurements. For comparison a plot of the proportion of abnormal grains filled with mullite particles is shown in Figure 75 and shows a significantly smaller variation in vol.% than that seen in Figure 74.

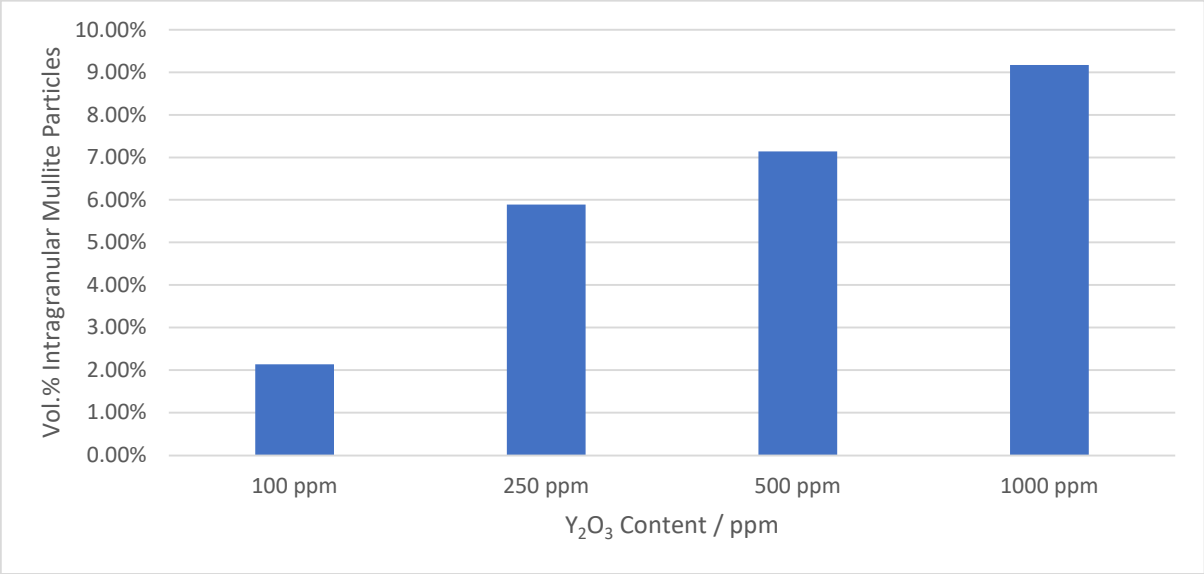


Figure 74: Graph showing the volume percentage of mullite grains within Al_2O_3-1wt.%SiC-Y_2O_3 with varying quantities of Y_2O_3 after sintering at 1550 ^{O}C for 4 hours in air.

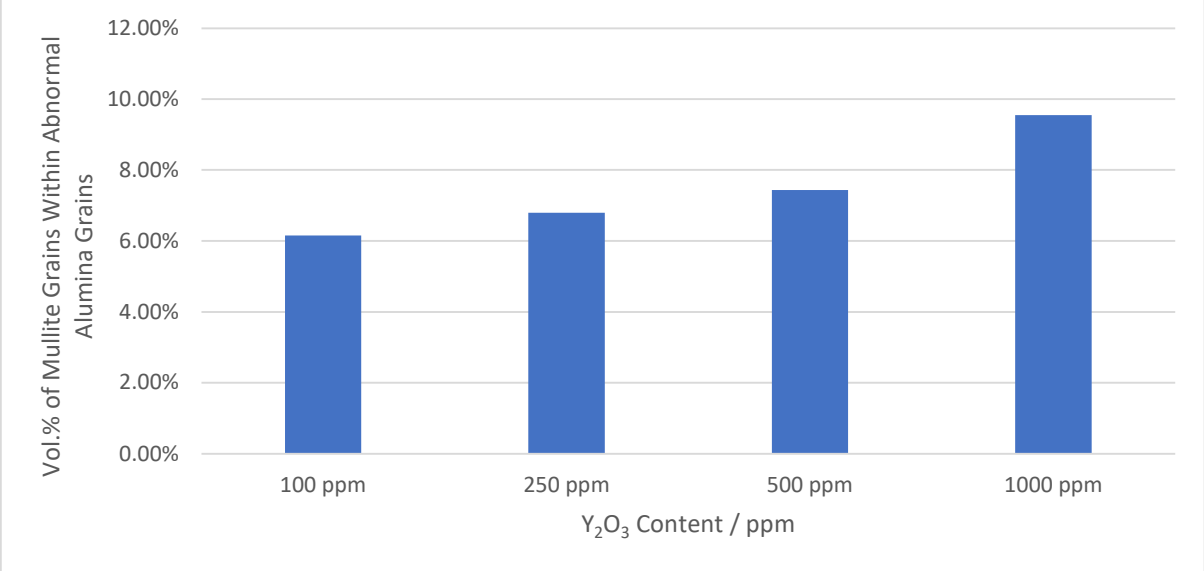


Figure 75: Graph showing the volume percentage of mullite grains within the abnormal grains of Al_2O_3-1wt.%SiC-Y_2O_3 with varying quantities of Y_2O_3 after sintering at 1550 ^{O}C for 4 hours in air.

The fraction of mullite grains on the boundary of abnormal grains can be measured by simply counting the number of grains in each site. This is shown in Figure 76. Conversely to the graphs shown in Figure 74 and Figure 75, an increasing quantity of yttrium oxide results in a lower percentage of mullite grains lying along grain boundaries.

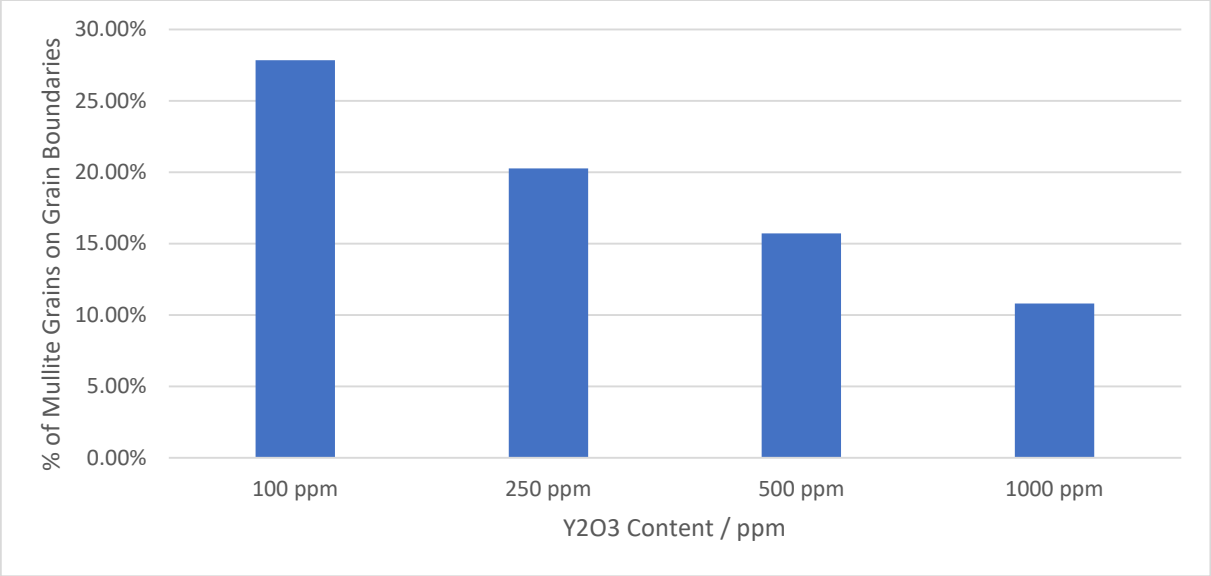


Figure 76: Graph showing the percentage of mullite grains which lie along the grain boundaries of Al_2O_3-1wt.%SiC-Y_2O_3 with varying quantities of Y_2O_3 after sintering at 1550 ^{O}C for 4 hours in air.

5.1.2.5 Transmission Electron Microscopy

While scanning electron microscopy allows for the analysis of grain size and distribution, transmission electron microscopy allows for the analysis of the sub granular structures and other key features. Following the process described in 4.3.7, transmission electron microscopy samples of alumina with the addition of both silicon carbide and yttrium oxide were produced.

Example TEM images showing the observed microstructure are shown in Figure 77. These clearly show grain boundaries between differing alumina grains and the presence of smaller grains within the larger alumina matrix.

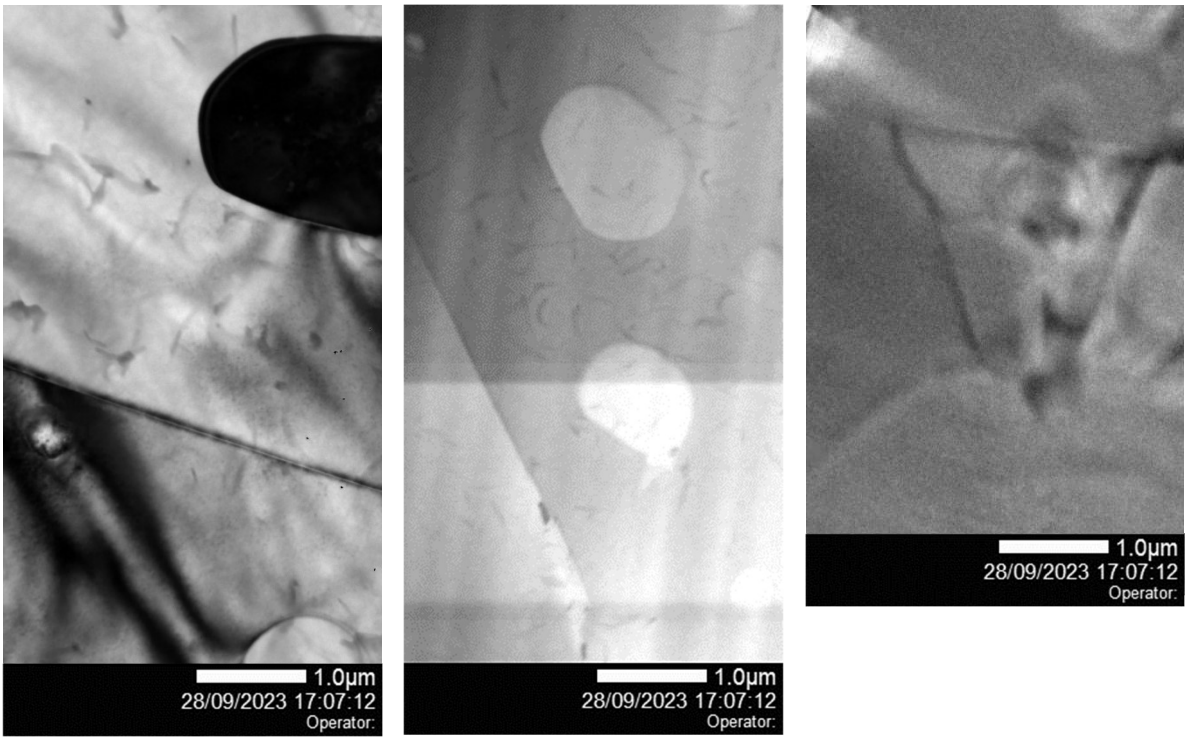


Figure 77: TEM images showing sections of grain boundaries, particles within the larger alumina grains and an area of normal grain growth in Al_2O_3-1wt.%SiC-500ppmY_2O_3.

5.1.2.5.1 Silicon Containing Grains

Transmission electron microscopy of thin films produced from Al_2O_3-1wt.%SiC-500ppmY_2O_3 show clear bend contours throughout the large alumina grains. These can be seen as black lines throughout the micrographs shown in Figure 78. The bend contours originate from the silicon containing particles and do not pass through them when they originate from a different location. This suggests a discontinuity in the lattice structure along the edge of the silicon containing particles, therefore the particles are distinct grains within the larger alumina grain.

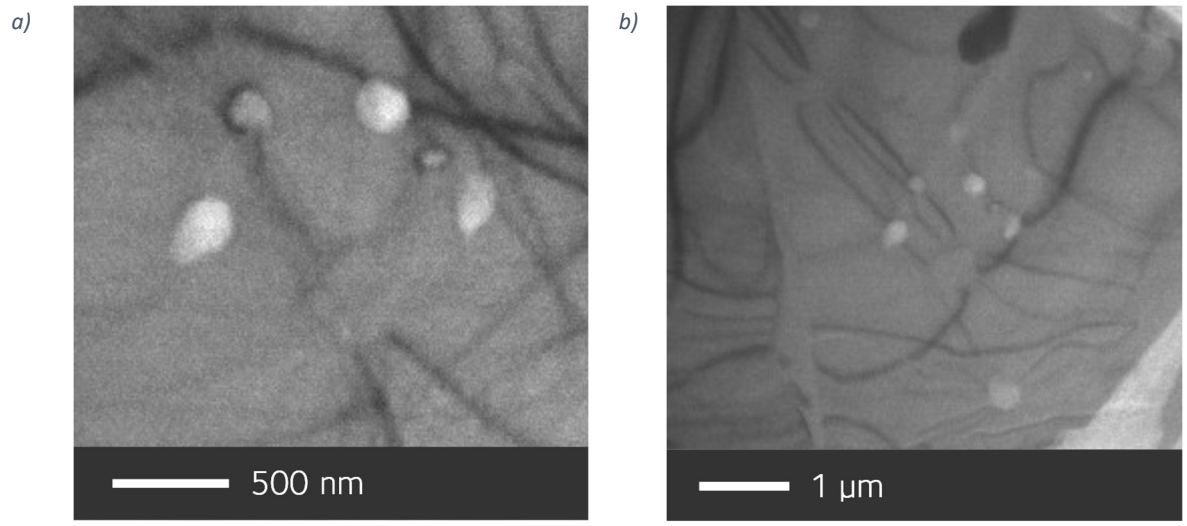


Figure 78: TEM images of alumina with 1 wt.% silicon carbide and 500 ppm yttrium oxide sintered for 4 hours at 1550 ^{O}C; showing in detail a) silicon-containing grains within a larger alumina grain b) a grain boundary between 2 abnormal grains.

5.1.2.5.1.1 Diffraction Patterns

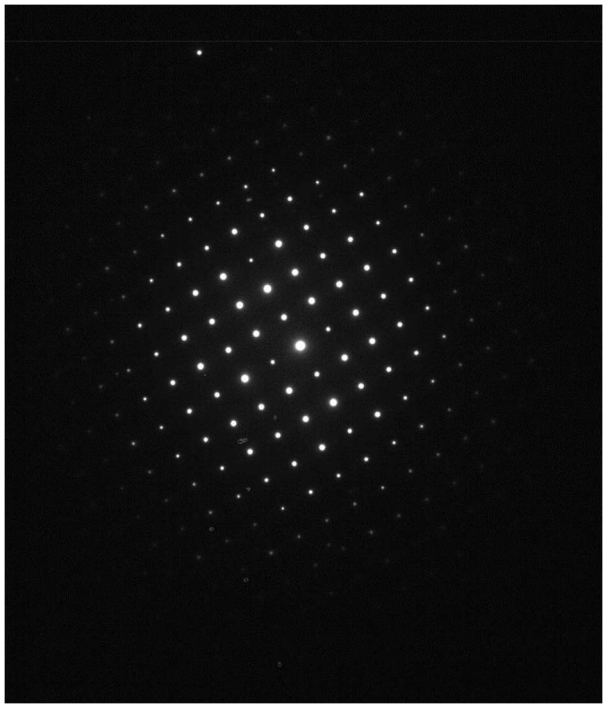


Figure 79: Diffraction pattern taken from a silicon containing grain along the [001] direction in a sample of Al_2O_3-1wt.%SiC-500ppmY_2O_3.

Diffraction patterns produced through a silicon-containing grain allow for the measurement of the lattice parameters and crystal structure. This diffraction pattern is shown in Figure 79. Indexing of this pattern shows that it was taken along the [001] direction of an orthorhombic crystal structure. This indexing is shown in Figure 80. Measurement of the lattice parameters gives a unit cell with basal dimensions of:

a / Å	7.68 ± 0.01
b / Å	7.58 ± 0.01

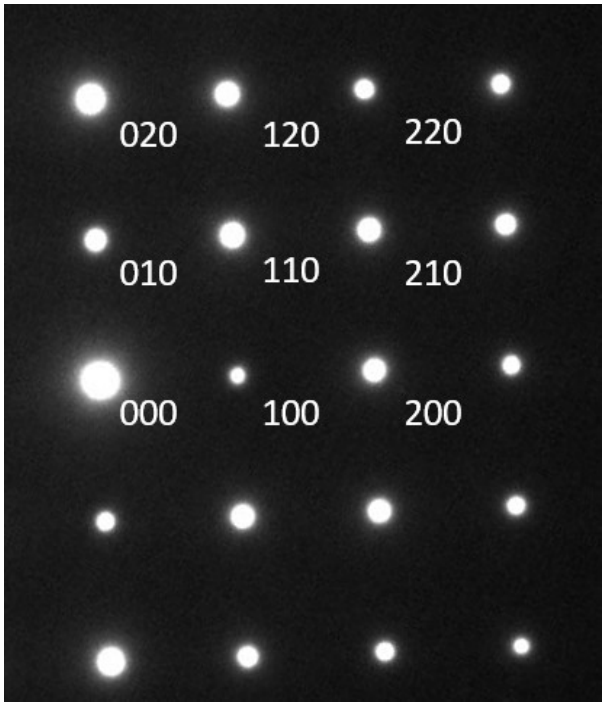


Figure 80: Indexing of the diffraction pattern produced in Figure 79.

This closely matches the unit cell dimensions of known samples of mullite measured by *Angel and Prewitt* [217] who found the unit cell had basal dimensions of:

a / Å	7.6812
b / Å	7.5786

5.1.2.6 Transmission Electron Microscopy EDX

EDX Line scans across grain boundaries in transmission electron microscopy allow for the identification of any segregated atoms that lie along these grain boundaries. Grain boundaries separate into three distinct categories based on the type of grains they separate.

5.1.2.6.1 Silicon-Containing Grains

Mapping of both the matrix material and the small particles seen in Figure 78 can be used to determine the composition of the material in these 2 distinct areas of the microstructure. A typical line scan across one of these particles is shown in Figure 81. The width of the particle can be clearly seen from the rise in silicon content and mirrored decrease in aluminium concentration across the width of the grain. Averaging the measured concentration of each present element across this period allows for the composition of the particle to be measured.

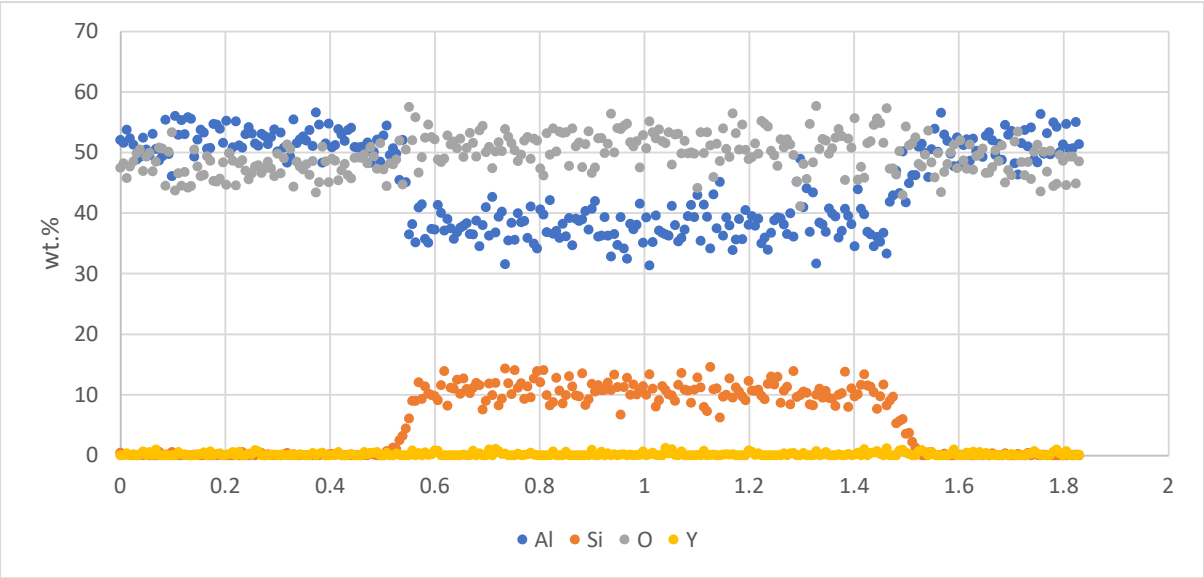


Figure 81: Graph of the weight percentage of aluminium, silicon, oxygen, and yttrium across a sub grain taken from a STEM-EDX line scan.

Across multiple particles this averages to a measured composition of:

	at.%		
Al	27.9	±	0.2
Si	7.6	±	0.01
O	64.4	±	0.2
Y	0.0	±	0.01

Table 1

Assuming a mullite type structure for the intragranular particle this results in a composition of $1.84Al_2O_3{\cdot}SiO_2$. This composition is within the mullite composition range described in Figure 71 and Figure 95 and so it is likely that this is the material that forms the intragranular particles.

A similar analysis of the matrix material not at grain boundaries or within the mullite grains results in a measured composition of:

	at.%		
Al	38.8	±	0.3
Si	0.1	±	0.00
O	61.2	±	0.3
Y	0.0	±	0.01

Table 2

This composition is the expected Al_2O_3 that forms the matrix of the composite without any significant presence of either silicon or yttrium.

5.1.2.6.2 Abnormal-Abnormal Grain Boundaries

Line scans of the boundary between two large grains show a reasonably constant quantity of aluminium across the entirety of the scan. An example of one of these line scans is shown in Figure 82. Silicon and yttrium traces are present, but any changes in measured count increase cannot be easily seen. In order to counter this, a plot of counts was made without displaying the aluminium trace,

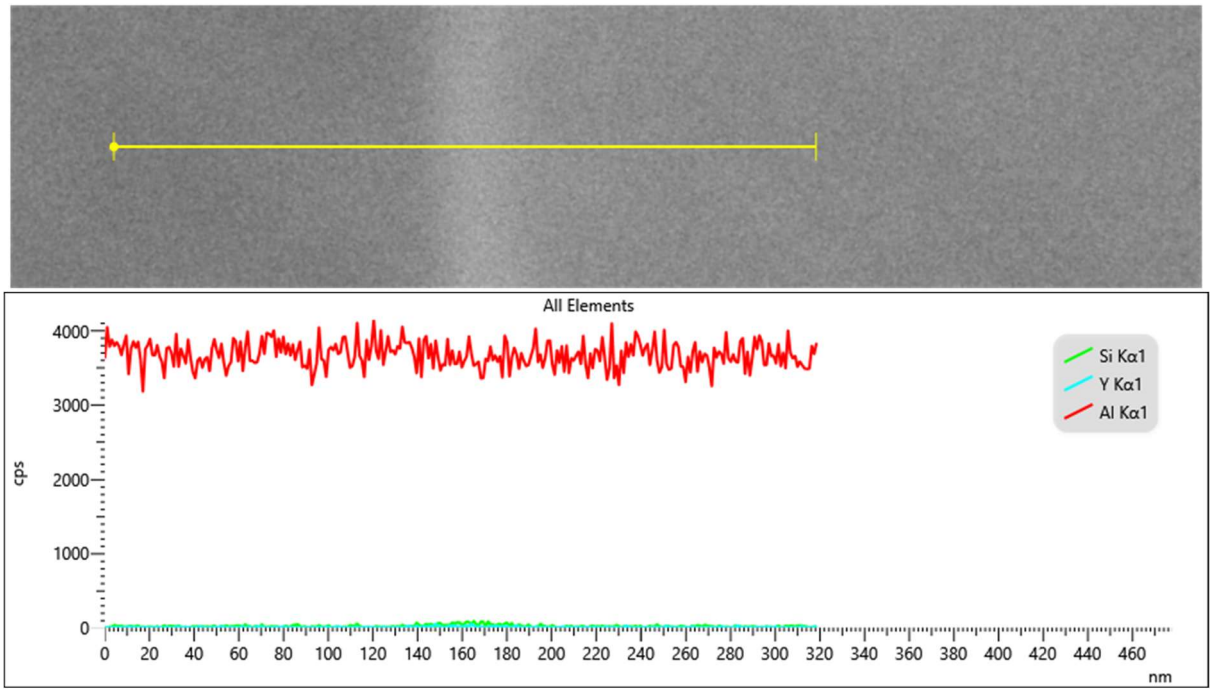


Figure 82: TEM image showing the line scan taken across a grain boundary between two abnormal grains matched to the corresponding EDX trace of counts per second seen for aluminium, silicon, and yttrium at that location.

as is shown in Figure 83. This shows a peak in both silicon and yttrium across the grain boundary. The peak seen in both these elements is wider than the extent of the grain boundary seen in the TEM image. This is likely due to the spatial resolution of the microscope as described in 4.3.8.

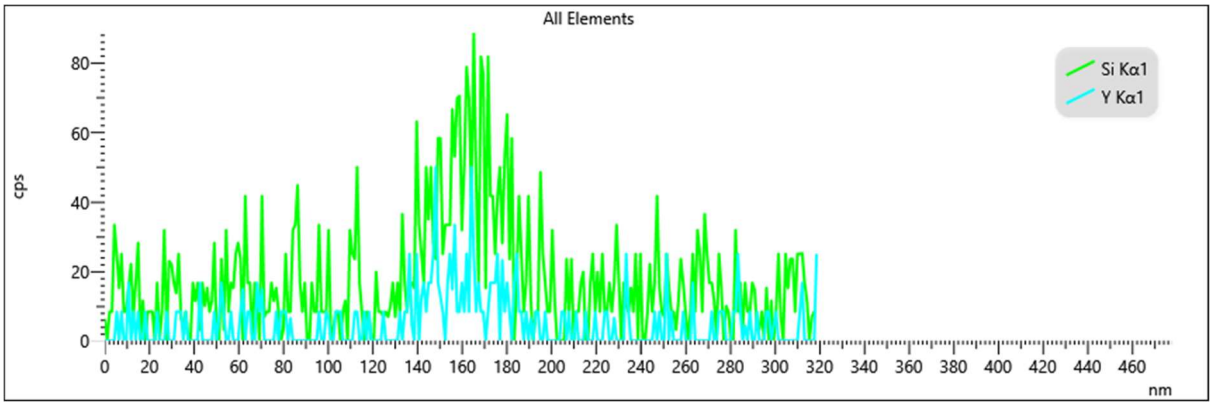


Figure 83: EDX line scan of the same line shown in Figure 82 scaled with the aluminium trace removed and scaled to the remaining data.

Similar scans of other grain boundaries between abnormal grains show the same peak in both silicon and yttrium suggesting this segregation occurs around all abnormal grains. Analysis of the peaks using the method described in 4.3.8 allows for the excess silicon and yttrium along the grain boundary to be measured. This results in an average yttrium excess of 0.92 ± 0.12 atoms nm^{-2} and an average silicon excess of 139 ± 16 atoms nm^{-2}.

5.1.2.6.3 Normal-Normal Grain Boundaries

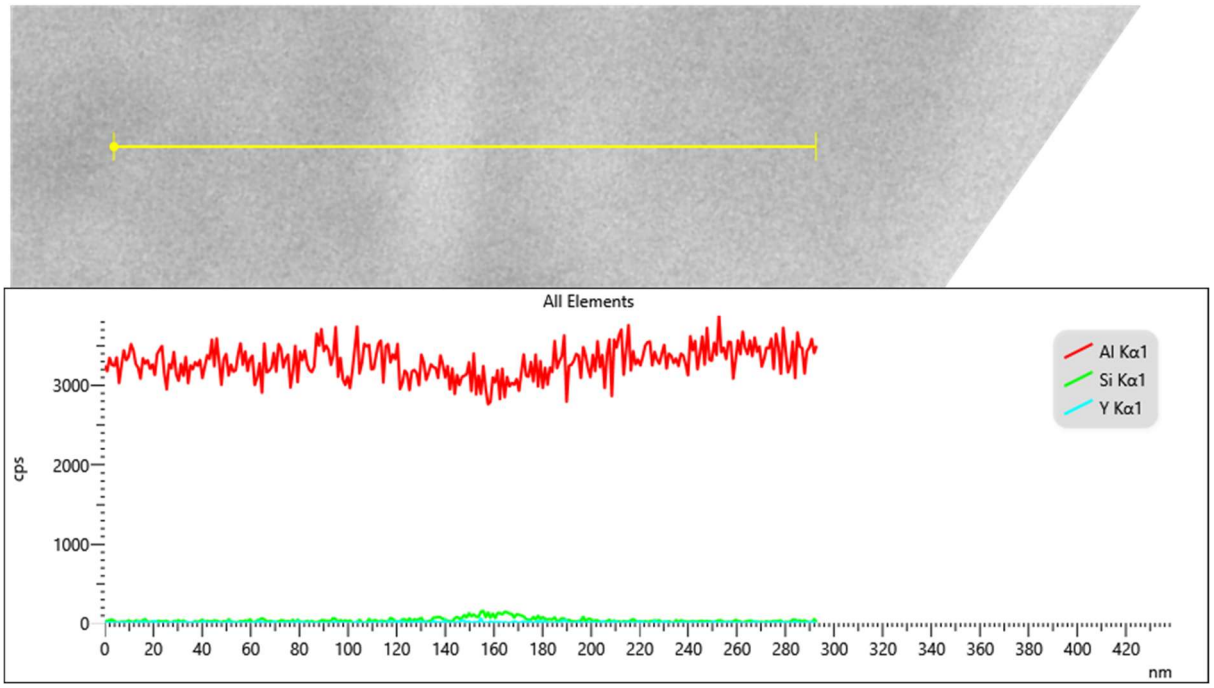


Figure 84: TEM image showing the line scan taken across a grain boundary between two normal alumina grains matched to the corresponding EDX trace of counts per second seen for aluminium, silicon, and yttrium at that location.

A similar plot to Figure 82 but across the grain boundary between 2 normal grains is shown in Figure 84 containing the same aluminium, silicon, and yttrium traces. Aluminium traces across grain boundaries between small grains show the same reasonably constant value as seen in Figure 82. The same plot with aluminium excluded is shown in Figure 85. This shows a peak in silicon similar to that

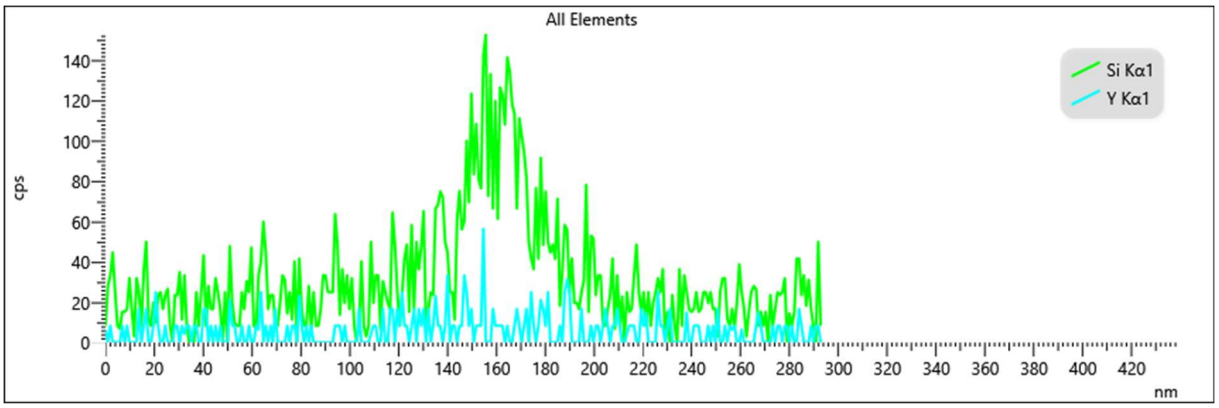


Figure 85: EDX line scan of the same line shown in Figure 84: TEM image showing the line scan taken across a grain boundary between two normal alumina grains matched to the corresponding EDX trace of counts per second seen for aluminium, silicon, and yttrium at that location. Figure 84 scaled with the aluminium trace removed and scaled to the remaining data.

seen between abnormal grains, with a notable spike in silicon content as the scan passes across the grain boundary, in Figure 83 but lacks the peak in yttrium. Similar results were seen when other normal-normal grain boundaries were examined. Similarly, to the analysis conducted in 5.1.2.6.2 the excess concentration of elements along the grain boundaries of the normal grains can also be measured. Across these grain boundaries this results in an average yttrium excess of 0.08 ± 0.01 atoms nm^{-2} and an average silicon excess of 139 ± 13 atoms nm^{-2}.

Some grain boundaries between what were otherwise seen to be normal alumina grains proved under EDX examination to be boundaries between a mullite grain and an alumina grain. This formation resulted in an EDX trace with a significant change in aluminium content across the grain boundary. An inverse change in silicon content was seen, with the negligible quantity of silicon seen in the alumina grain increasing significantly in the mullite grain. Because of this change, the segregation of silicon to the grain boundary is impossible to measure. Due to the lack of yttrium in either grain it can be readily

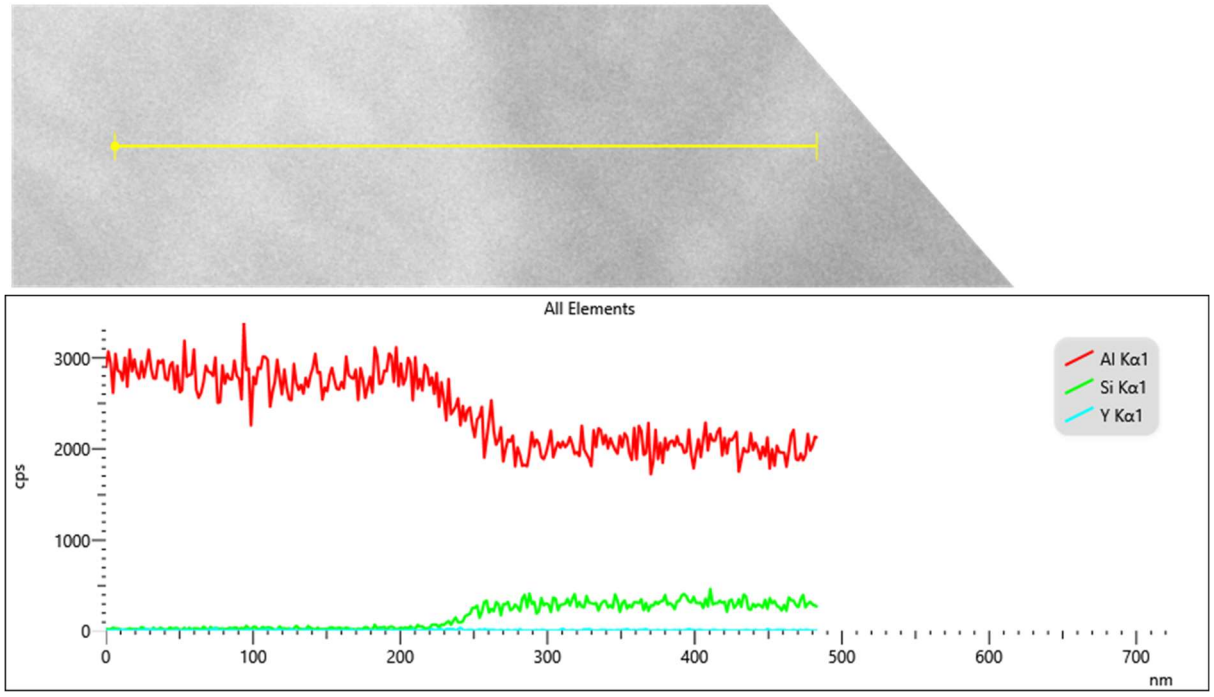


Figure 86: TEM image showing the line scan taken across a grain boundary between a normal alumina grain, on the left, and a mullite grain, on the right, matched to the corresponding EDX trace of counts per second seen for aluminium, silicon, and yttrium at that location.

shown, however, that no yttrium segregation is present along these boundaries, as can be seen in Figure 87.

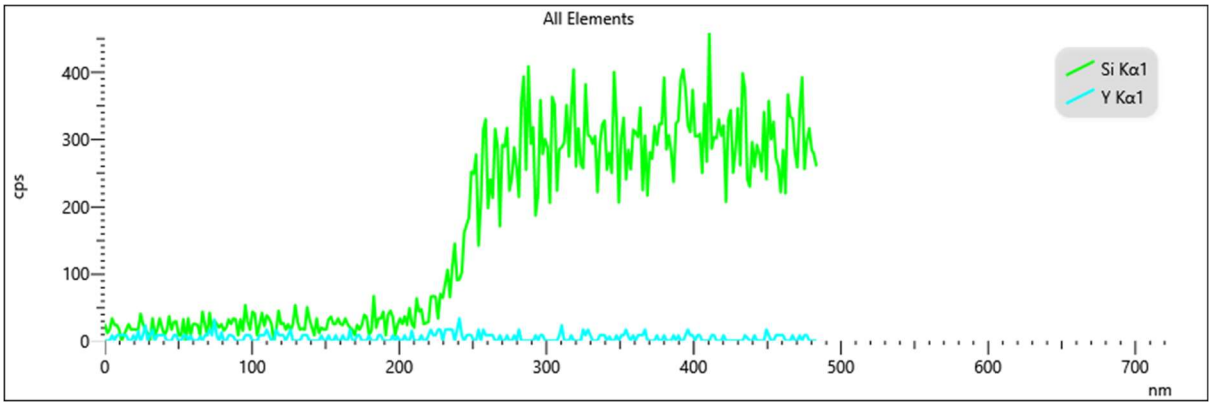


Figure 87: EDX line scan of the same line shown in Figure 84: TEM image showing the line scan taken across a grain boundary between two normal alumina grains matched to the corresponding EDX trace of counts per second seen for aluminium, silicon, and yttrium at that location. Figure 86 scaled with the aluminium trace removed and scaled to the remaining data.

The measurement of the compositions of the mullite grains at one end of this form of spectrum showed a mean composition of:

	at.%		
Al	37.4	±	0.2
Si	6.2	±	0.5
O	56.4	±	0.5
Y	0.0	±	0.01

Table 3

Assuming a mullite structure, the results in Table 3 give a chemical composition of $3Al_2O_3{\cdot}SiO_2$. This composition is not within the mullite regime shown in Figure 71.

5.2 Discussion of Alumina-Mullite Composites Without Any Additives

The effect of the addition of silicon carbide to alumina prior to sintering has been shown to be almost universally negative, in the absence of other additions, regardless of the quantity of silicon carbide initially added or the sintering conditions used. The addition of quantities of silicon carbide as low as 0.5wt.% resulted in a significant decrease in relative density compared to pure Al_2O_3. In pure alumina, densities of greater than 99% could be achieved at sintering temperatures of 1350^{O}C and sintering times of only 2 hours. For comparison, the addition of silicon carbide resulted in a decrease of around 5% relative density with the best performing sintering conditions (1550^{O}C for 4 hours with only 0.5wt.% SiC) with some samples possessing relative densities as low as 78.6% (1550^{O}C for 2 hours with 5wt.%SiC). This difference in porosity can be clearly seen through the comparison of internal surfaces under microscopy, with the Al_2O_3-SiC, Figure 56.b, possessing significant visible porosity not seen in pure Al_2O_3, Figure 54.c, sintered under the same conditions. Mechanical properties have been shown to be closely linked to the density of the resultant ceramic, as discussed by *Hardy and Green* [66]. Therefore, the decrease in density due to the addition of silicon carbide results in a significant decrease in mechanical properties, as is discussed in chapter 6. It is possible the difference in density could be overcome through a significantly longer sintering period, but Figure 44 shows that densification has almost plateaued by 4 hours sintering time so the efficacy of this method of achieving complete, or near complete, densification may be low. Other work has achieved higher densities in alumina-silicon carbide composites without an applied pressure [218, 219], however this has required a significantly higher temperature to achieve, and measured densities peaked at around 98%. Research conducted at a similar temperature to this work only achieved a density of 88% in alumina-silicon carbide [218].

Comparisons between the mean grain size in alumina with and without the addition of silicon carbide show a similar trend to the lower density seen in the composite. The addition of silicon carbide results

in a far smaller mean grain size regardless of sintering time, as is shown in Figure 88. In this case the addition of 1wt.% SiC resulted in a mean grain size 6.5% of the size seen in pure Al_2O_3 without any dopants.

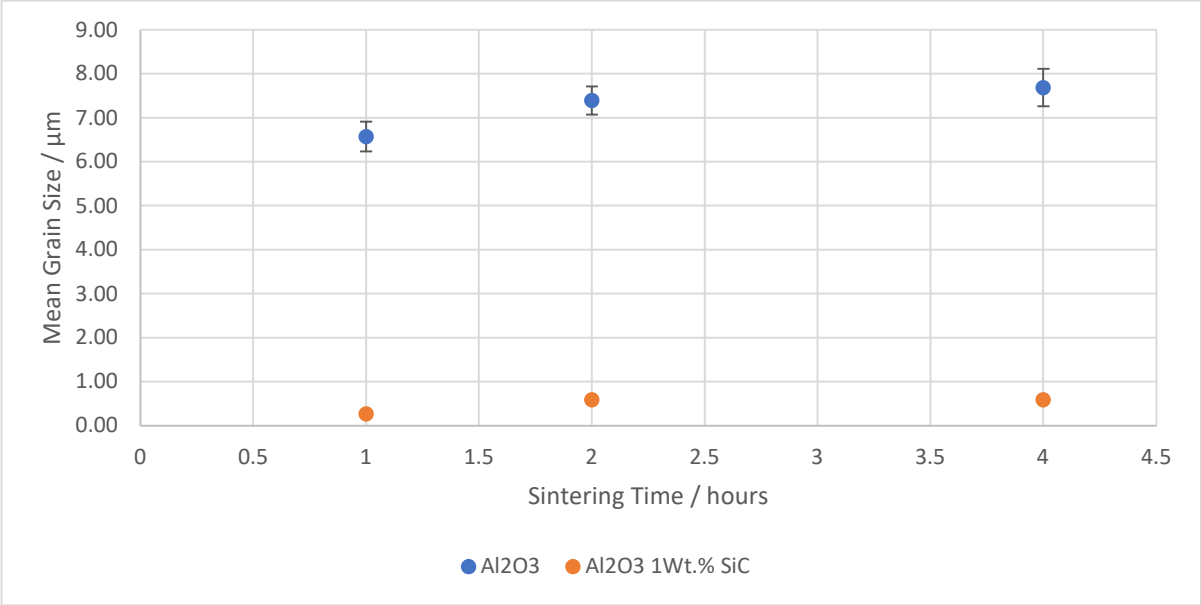


Figure 88: Graph showing the ratio between the mean grain size in alumina and Al_2O_3-1wt%SiC after sintering at 1550 ^{O}C for between 1 and 4 hours.

This phenomenon is well understood in alumina silicon carbide nanocomposites that have been hot pressed in an inert gas atmosphere at temperatures of around 2000K [6, 87]. These samples showed close agreement with the Zener model of grain growth inhibition. This correlation shows the silicon carbide particles displayed almost zero mobility within the alumina matrix during sintering. Further support for the immobility of the silicon carbide particles is provided by the even distribution of the particles seen by *Borsa et al.* [6] after sintering is completed, confirming very limited movement from the initial distribution of SiC. Both these observations demonstrate the properties of the Al_2O_3-SiC interface as inimical to diffusion, a property that also results in the inhibition of sintering in these materials.

However, samples produced throughout this work were not sintered under the inert atmosphere conditions described above. Instead, they were all sintered under atmospheric pressure in air. TGA

analysis of the silicon carbide used in the manufacture of the composites in this work showed that oxidation began at temperatures of around 900^{O}C before a significant increasing in the rate of mass gain was observed at temperatures of 1100^{O}C. This is in line with oxidation of bulk silicon carbide measured by *Jorgensen et al.* [75]. If silicon carbide were to fully oxidise, an increase in mass of 50% would be expected for the complete transformation from silicon carbide to silicon dioxide. As neither pressed nor loose silicon carbide powder achieved an increase in mass close to this level, this suggests that the formation of a layer of silicon dioxide around each silicon carbide particle prevented the oxidation of further interior material. Owing to their increased spacing and larger effective surface area, the loose silicon carbide particles allowed for more oxidation before complete passivation occurred but could not achieve complete transformation within the 4 hours at 1550^{O}C tested. Despite the incomplete transformation, a surface transformation could be sufficient to remove the inimical Al_2O_3-SiC interface seen by *Borsa et al.* [6]. Oxidation of silicon carbide when mixed with alumina showed an increase mass during the oxidation phase of silicon carbide commencing at around 900^{O}C. This suggests that despite being enclosed within the alumina matrix, the oxidation of SiC commences at the same temperature as in bulk SiC [75]. Owing to the lack of contrast seen between the differing compositions under scanning electron microscopy, such as in Figure 56.d, it is impossible to determine if a core of SiC is present within the mullite grains in the final sintered alumina-mullite composites. This structure would be suggested by the formation of a passivating layer as suggested by other work on the oxidation of SiC [75]. EDX mapping may offer a potential solution to this issue, however due to the resolution limitations discussed below it is not possible in this material.

The TGA testing conducted on samples containing alumina, Figure 37, all displayed a loss of mass during heating. This is present in the testing of pure alumina alongside similar experiments containing composites of alumina-silicon carbide, Figure 38. The initial loss on ignition seen in this period is likely due to the evaporation of water [220], however the cause of the continued decrease in mass at higher temperatures has not been identified. The decrease in mass did not hinder the sintering behaviour of

pure alumina and densities of over 99% were achieved in pure alumina at sintering temperatures from 1400 ^{O}C.

The EDX mapping of silicon seen in Figure 70 shows an apparently even distribution of silicon at the lower percentages of silicon carbide (0.5 and 1 wt.%). As demonstrated by *Klug et al.* [93], this distribution cannot be due to solubility of silica within the alumina as the two compounds possess negligible solid solubility. Therefore, this distribution is likely due to silica or mullite particles too small to be resolved in SEM-EDX. The maximum resolution achievable in SEM-EDX is closely linked to the accelerating voltage and consequently the interaction volume. For the 5 kV accelerating voltage used in this work, an interaction diameter of around 200 nm has been simulated [221]. Therefore, if the mullite particles were smaller than this, resolution of individual particles would not be achievable and an apparently even distribution would be seen. As the mullite particles have not been able to migrate and coalesce when low percentage quantities of silicon carbide have been added, they must possess a degree of immobility in a similar fashion to that seen in silicon carbide particles within an alumina matrix. Unfortunately, SEM imaging has not been able to confirm the dimensions of the mullite particles as they have not been identifiable within the SEM images taken of Al_2O_3-1wt.%SiC, Figure 56.b. This immobility suggests that the alumina-mullite boundary is inimical to diffusion in a similar fashion to the alumina-silicon carbide equivalent. This inimical diffusion pathway is responsible for the low density measured in all the alumina-mullite composites manufactured during this work. In order to close the pores and increase density, material must be removed from the grain boundary to the pores. This requires the movement of material from the alumina-mullite interface alongside the material moved from the alumina-alumina grain boundary. Therefore, the hindering of diffusion along the alumina-mullite grain boundary slows the densification of the composite.

At higher initial silicon carbide percentages, the silicon tends to be present primarily within certain grains while leaving others with a significantly lower overall silicon content, as can be seen in Figure 70.d. This shows close alignment with the grain size seen in Al_2O_3-5wt%SiC seen in Figure 56.d,

suggesting the transformation of entire grains to mullite has occurred. The volume consumed by the higher silicon density areas was measured to be around 36% of the total volume of Al_2O_3-5wt%SiC from the EDX image taken in Figure 70.d. This is likely a small systematic overestimation due to an imperfect mask of the image. Under complete transformation of silicon carbide to mullite, a 5 wt.% SiC addition prior to sintering would theoretically result in a final composition of 30 vol% mullite. Therefore, this suggests the silicon carbide present with the Al_2O_3-5wt%SiC has undergone a complete transformation to mullite, as the partial oxidation to silica would have resulted in a smaller volume fraction of material consumed.

The higher concentrations of initial silicon carbide, such as the 5 wt.% SiC additives discussed above, may allow sufficient diffusion to be present at these concentrations resulting in the observed distribution with an even initial distribution of silicon carbide. This explanation implies the Al_2O_3-mullite boundary is not as slow a diffusion path as its equivalent in Al_2O_3-SiC, allowing for the coalescence of mullite into larger grains due to its higher mobility; while still being slow enough to severely hinder sintering as is seen by the lower final densities seen in all Al_2O_3-SiC composites tested. This is reflective of the higher stability observed in silicon carbide compared to mullite.

5.3 Microstructure Of Alumina-Silicon Carbide-Yttria Composites

5.3.1 Grain Boundary Compositions in Al_2O_3-SiC-Y_2O_3

The grain boundary excesses of yttrium and silicon seen in the interfaces between abnormal grains and between normal grains in Al_2O_3-SiC-Y_2O_3, as shown in Figure 83, allows for some comparison with the complexions present in the resultant material. Grain boundaries consistently show a silicon excess of around 140 atoms nm^{-2} regardless of environment. However, the borders of abnormal grains show an yttrium excess of around 0.9 atoms nm^{-2} compared to the 0.08 atoms nm^{-2} seen on the borders of normal grains. The standard planar density of alumina varies between 5 atoms nm^{-2} along the basal (0001) plane and 10 atoms nm^{-2} on the $(11\bar{2}0)$ plane [152]. Therefore, abnormal grains contain the equivalent of a sub-monolayer of yttrium along the grain boundary with a quantity equivalent to between 10 and 20% of a full monolayer in the absence of any other grain boundary segregation. The true distribution of yttrium in this material cannot be readily determined in the fashion of the complexion types described by *Dillon et al.* [114] from this measurement however due to the presence of silicon along the same grain boundaries. Comparatively, silicon displays a consistent measured quantity across all the measured grain boundaries with a thickness of multiple monolayers, between 14 and 28 monolayers depending on the angle of the grain boundary relative to its neighbouring grains. TEM images of grain boundaries, such as those shown in Figure 77, does not show a significant increase in grain boundary width across the observed length of the grain boundary. This suggests that all the grain boundaries in Al_2O_3-SiC-Y_2O_3 are type IV or higher, as described in 2.5.1, with the key distinction between the structure of the boundaries of the abnormal grains and the boundaries of the normal grains being the presence of 0.9 atoms nm^{-2} of yttrium in the interfaces of the abnormal grains. Type IV grain boundaries have been seen in alumina grain boundaries by *Cantwell et al.* [7], however the work of *Cantwell et al.* found the normal grain boundaries had a type III structure rather than what was present in the alumina-mullite-yttria composite produced in this work.

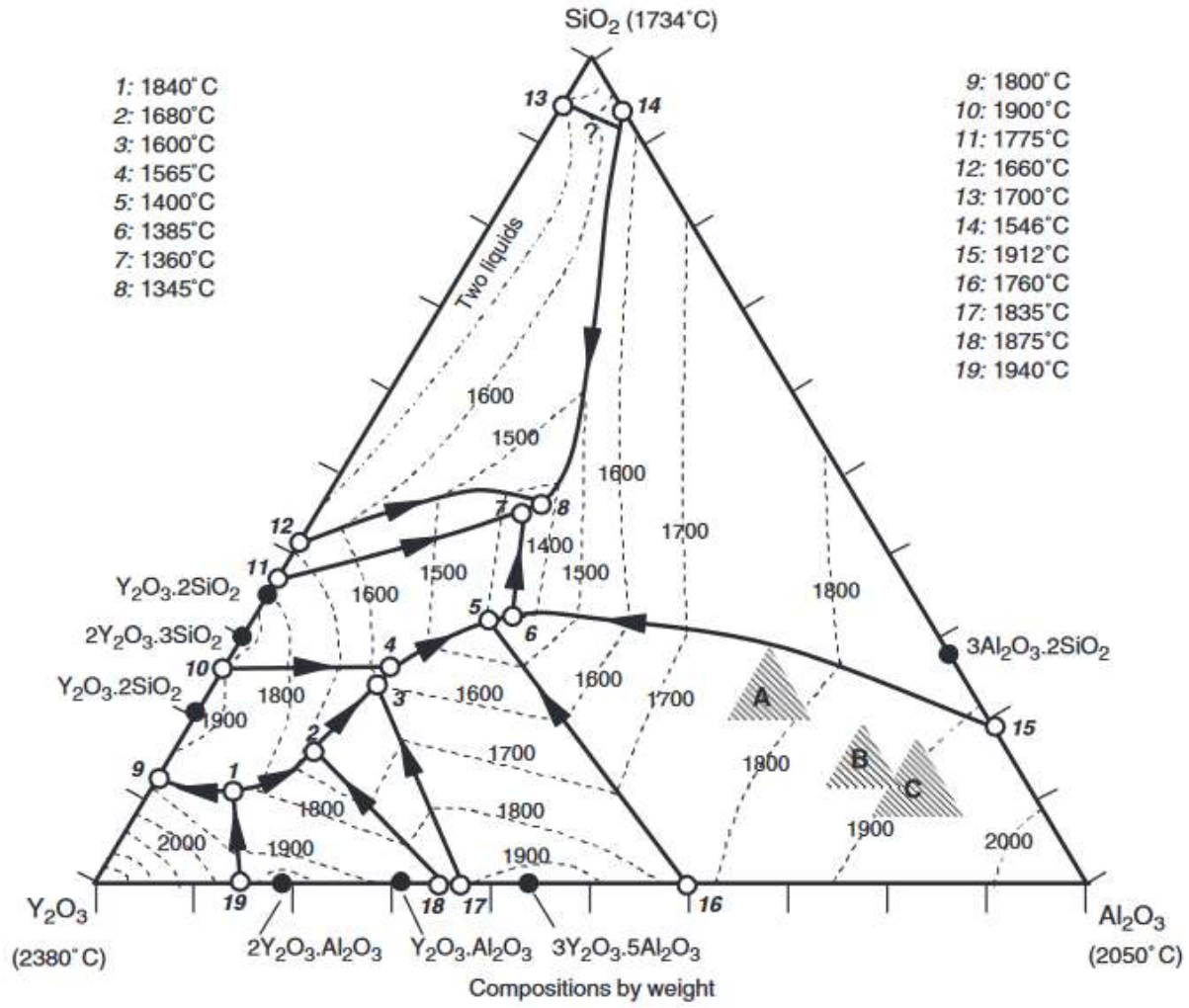


Figure 89: Ternary phase diagram showing the Y_2O_3-SiO_2-Al_2O_3 system. Reproduced from Cock et al. [222].

The liquidus surface of the Y_2O_3-Al_2O_3-SiO_2 system was presented by *Cock et al.* [222]. This work showed a liquid phase potentially forming at temperatures significantly below the sintering temperature of the materials studied in this work, with the lowest liquid temperature being found to be 1345 ^{O}C. This composition however contained 22 wt.% Al_2O_3 and 32 wt.% Y_2O_3. The STEM-EDX analysis conducted on the grain boundaries in the Al_2O_3-1wt.%SiC-500PPMY_2O_3 samples produced in this work showed that, while the alumina content of the grain boundary could not be differentiated from the background, the yttria content along the grain boundary is 2.1 wt.% assuming the remainder of the material along the grain boundary is silica. A notable minimum for this work is point 14 in Figure 89. In the complete absence of yttria, the liquidus is at a temperature of around 1546 ^{O}C with a decrease in temperature as yttria content increases. Therefore, the type IV grain boundaries formed

can be associated with the creation of a liquid phase during sintering both on the borders of abnormal and normal grains. The exact temperature of this liquidus has not been conclusively identified. While the work of *Cock et al.* [222] places the transformation below the sintering temperature of 1550^{O}C, other research conducted into the alumina-silica system has identified a higher temperature for the liquidus. Temperatures of either 1595^{O}C [93, 223-225] or 1587^{O}C [226] have been measured for the minimum liquid temperature in the alumina-silica system. As the sintering temperatures used in this work did not reach either of these temperatures, the formation of a liquid phase may not have occurred. This would mean the significant increase in grain growth had occurred without the aid of a liquid phase and the segregation of silicon and yttrium would have needed to take place without its formation.

5.3.2 Complexion Formation

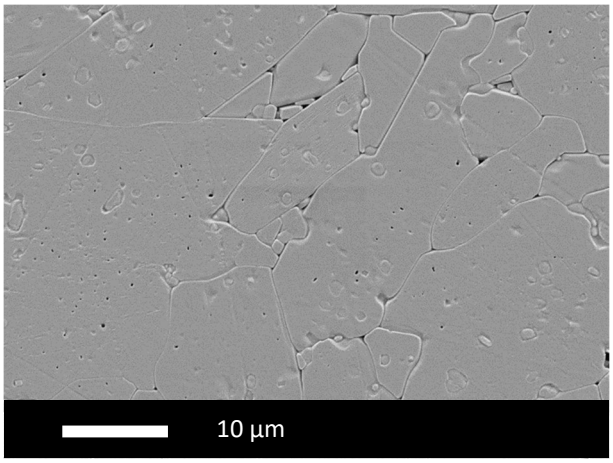


Figure 90: SEM image of alumina with 1 wt.% silicon carbide and 500 ppm yttria after sintering for 4 hours at 1550 ^{O}C.

A complexion based explanation for the abnormal grain growth has been conducted here, rather than the interface faceting based explanation discussed in 2.6.2. This is due to the interface faceting explanation being typically identified by long straight grain boundaries along the borders which were found to be coincident with the (0001) planes [61]. The abnormal grains in Al_2O_3-1wt%SiC-Y_2O_3 did not typically follow these straight grain boundaries and instead were generally curved, Figure 90. The complexion type formed along the boundaries to abnormal grains described above results in these grain boundaries possessing a higher mobility and therefore progressing far faster through the material during sintering than the grain boundaries that formed without this complexion. This results in the growth of abnormal grains, as once one grain grows larger than its surroundings it will continue growing due to the increased driving force present from its size advantage over the neighbouring grains. Unfortunately, this effect renders determination of the

original environment that caused the formation of the yttrium and silicon co-doped grain boundaries impossible as the abnormal grains grow far beyond their original environment consuming any neighbouring grains that would have produced the relevant conditions for the formation of the type IV complexion with the addition of yttrium. Complexions are sometimes considered analogous to 2 dimensional phases in equilibrium conditions. This has led to the creation of phase diagrams for some complexions such as Bi-doped Ni [227] or W based composites [228]. This reasoning allows for an equilibrium between two complexions to be formed without the need for any initial specific variations in local conditions to form them.

Changes in sintering temperature provide a key insight into the development of complexions within the alumina-mullite-yttria system. While the increase in both density, Figure 48, and grain size, Figure 60, is clearly visible compared to alumina with addition of solely silicon carbide at sintering temperatures of 1550^{O}C, the effect is almost entirely absent at any lower sintering temperatures, as can be seen in Figure 91. The marked change in sintering behaviour seen between temperatures of 1500^{O}C and 1550^{O}C, Figure 64 and Figure 65, suggests that the complexion formed by co-segregation of Si and Y results in abnormal grain growth at a temperature between these two conditions. The

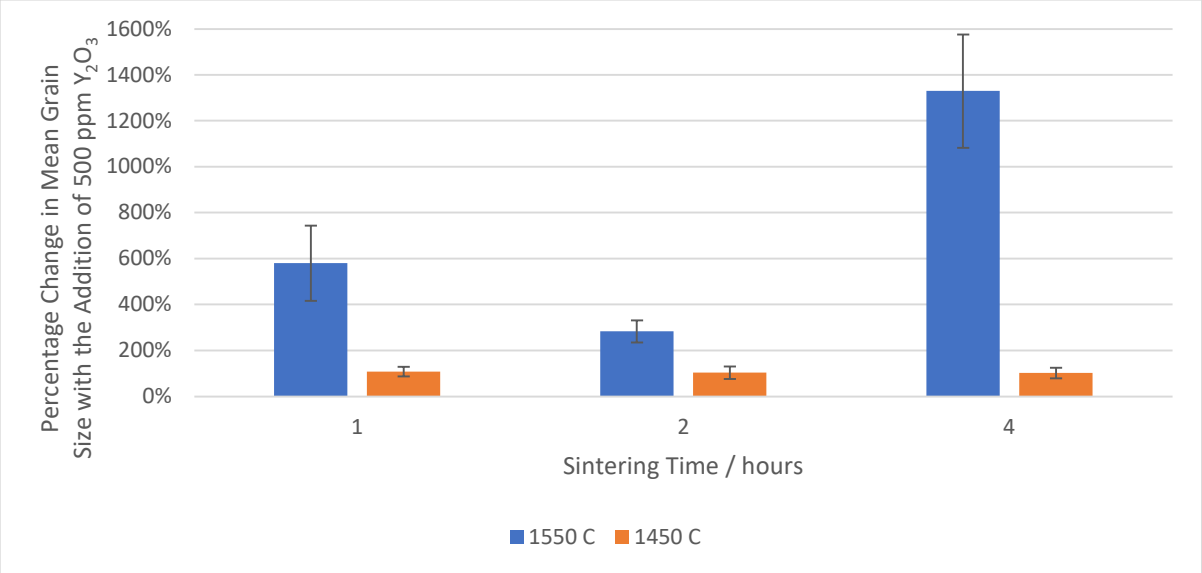


Figure 91: Graph showing the ratio of mean normal grain sizes between Al_2O_3-1wt.%SiC-500ppmY_2O_3 and Al_2O_3-1wt.%SiC after sintering at either 1550 ^{O}C or 1450 ^{O}C for between 1 and 4 hours.

liquidus described above in relation to point 14 in Figure 89 occurs in this region and it is potentially this transition that is the cause of the dramatic increase in grain growth. The curvature of the line away from the purely alumina-silica system due to the effects of the addition of yttrium to the system changing the minimum temperature at which the liquid phase can form, along with the disagreements in the actual temperature of the liquidus measured prevents this from being confirmed through the phase diagram. However, the significant change in behaviour at this temperature suggests that this liquidus is the cause of the measured changes in microstructure as it allows the grain composition to readily form.

5.3.3 Abnormal Grain Growth

The rapid growth of grains bordered by the co-doped complexions results in the changes in microstructure seen due to the addition of yttria. Most obvious among these changes is the effects on grain size and abnormal grain growth. The presence of yttria, and consequently the particular complexions formed along abnormal grain boundaries, resulted in increased abnormal grain growth throughout the sample as higher mobility allows for faster grain growth. Similarly, increases in initial yttria content promoted additional abnormal grain growth, with Al_2O_3-1wt.%SiC-1000ppmY_2O_3 resulting in abnormal grains consuming 96% of the volume of the sample after sintering for 4 hours at 1550^{O}C. Comparatively, the addition of 100ppm Y_2O_3 resulted in only 35% of the overall volume being consumed by abnormal grain growth, as can be seen in Figure 67. Electron microscopy of the grain boundaries in any of these samples does not show the presence of any visible grain boundary wetting or glassy phase with a wider grain boundary thickness as can be seen in Figure 77. Therefore, the additional abnormal grain growth is due to a larger fraction of initial grain boundaries being doped with both silicon and yttrium in the composition found above rather than the formation of a more mobile glassy phase from the new composition, as this would be visible along grain boundaries following sintering. Additionally, the increase in quantity of Y_2O_3-containing grain boundaries, rather than an increase in level of segregation, implies that the complexion formed along the boundaries of abnormal grains possessed a specific chemistry, rather than merely being a product of local

environment. This result is reflected in the consistency of the silicon and yttrium contents seen in the STEM-EDX measurements across multiple different grain boundaries within the Al_2O_3-1wt.%SiC-500ppmY_2O_3 system. However, this has not been tested across samples containing differing quantities of Y_2O_3.

5.3.4 Mullite Distribution

While the quantities of yttria added throughout this work are too small to allow for their detection through SEM-EDX, the silicon can be readily located. As discussed in 5.1.2.3.1 and 5.1.2.4, Al_2O_3-SiC with higher percentage additions of SiC result in grains of mullite dispersed among grains of alumina. With the addition of Y_2O_3 and the accompanying rapid growth of abnormal alumina grains, a different structure develops. The addition of yttria causes grouping of mullite into individually resolvable grains with a lower percentage addition of silicon carbide than in the presence of silicon carbide alone, as can be seen in the comparison shown in Figure 92. This suggests that the grain boundaries formed along the borders of abnormal grains in Al_2O_3-1wt.%SiC-500ppmY_2O_3 are not as inimical to diffusion as those formed in the Al_2O_3-1wt.%SiC equivalent. At additions of 1wt.% SiC, the diffusion distance required to form the larger grains of mullite could be obtained in the presence of yttria, a behaviour not seen with SiC as the sole additive.

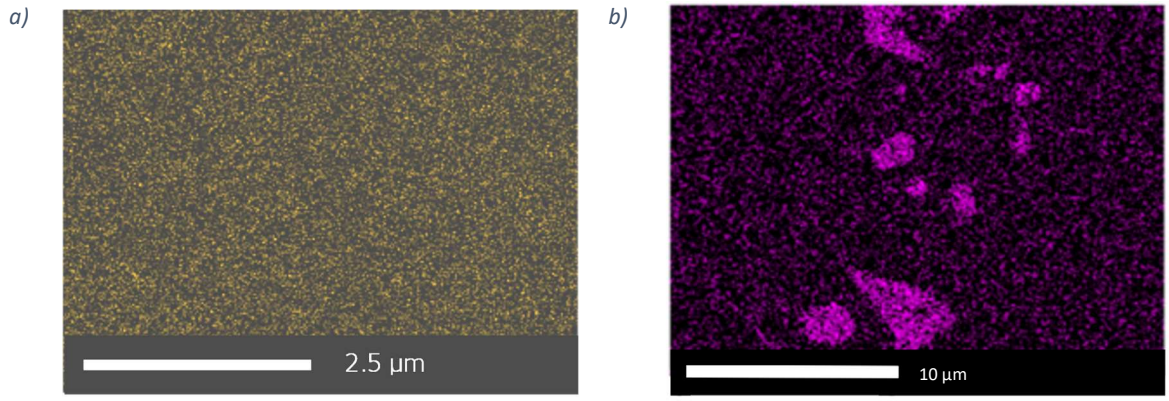


Figure 92: EDX maps showing the distribution of silicon in alumina samples sintered for 4 hours at 1550^{O}C containing a) 1wt.% SiC and b) 1wt.% SiC and 500ppm Y_2O_3.

These faster diffusion pathways allow for the abnormal grain growth of alumina, as the grains possessing the higher mobility yttria and silicon containing grain boundaries are able to grow larger than those bordered purely by the silicon containing grain boundaries. This growth allows the grains to fully encircle some of the mullite particles, leading to the mullite grains within the larger alumina grains, such as those seen in Figure 68.b. The growth of abnormal alumina grains in this fashion also explains the coalescence of mullite particles within the regions of normal grains. The growth of the abnormal alumina grains consumes alumina from the grains separating the mullite. This results in the mullite grains being brought together during grain growth to form a polycrystalline mullite region in the final microstructure. EDX mapping of silicon along with the matching SEM images of the same area, Figure 72.c-f, shows these regions of polycrystalline mullite.

5.3.4.1 Zener Pinning

A substantial quantity of the mullite grains seen in microscopy lie along grain boundaries as was shown in Figure 76. This suggests an element of grain boundary pinning by the mullite grains has occurred. According to the Zener pinning model [229], the maximum grain boundary pinning force occurs at an angle of 45^{O} between the original line of the grain boundary and the grain boundary at the point of connection with the particle, as is shown diagrammatically in Figure 93, and has been found to be:

$$f = \pi r \sigma$$

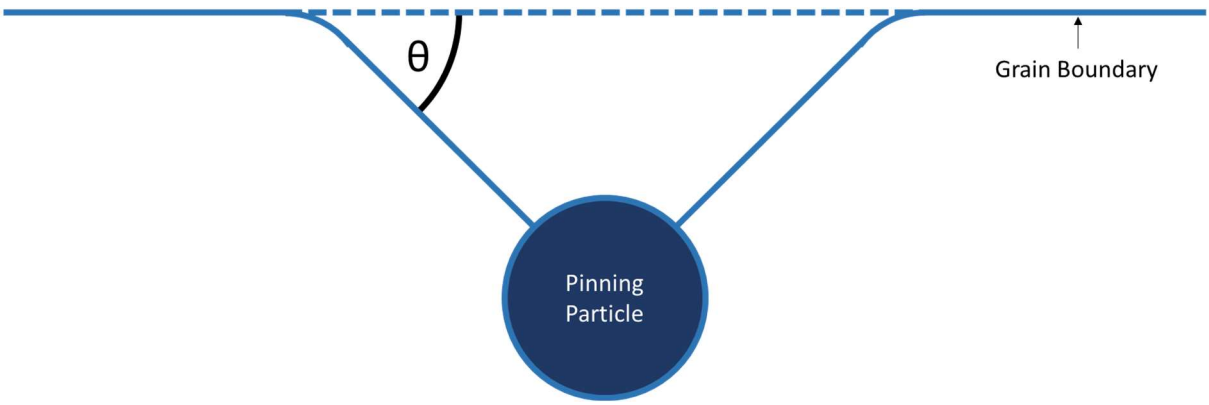


Figure 93: Diagram showing the angle at which the maximum grain boundary pinning force occurs in the Zener pinning model.

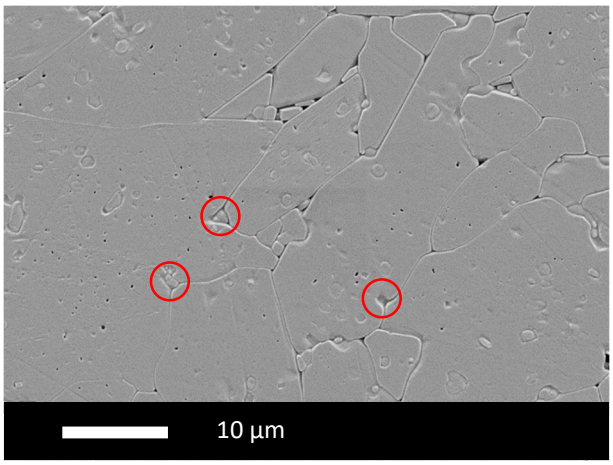


Figure 94: SEM image of alumina with 1 wt.% silicon carbide and 500 ppm yttria after sintering for 4 hours at 1550 ^{O}C. Some examples of particles pinning grain boundaries are circled.

where r is the particle radius, σ is the tension in the grain boundary intersected by the mullite particle and π is the constant pi. Structures similar to that shown in Figure 93 have been seen in Al_2O_3-SiC-Y_2O_3 and some examples are circled in red in Figure 94. As the compositions across a range of abnormal grain boundaries are consistent the grain boundary tension must be constant. This results in the pinning force being directly proportional to the radius of the mullite grain. As the measured mullite grain radius was seen to increase with increasing yttria content this implies the pinning force increases similarly. However, as was shown in Figure 76, the percentage of mullite particles on alumina grain boundaries decreases with increasing yttria content. This implies less pinning is occurring and so suggests grain boundary pinning is not occurring to a level that significantly affects the resultant microstructure.

The Zener pinning model also allows for the prediction of an ultimate grain size by balancing the driving force for grain growth against the pinning force calculated above. This results in a formula for the ultimate grain size of:

$$R = \frac{4r}{3\zeta}$$

where R is the radius of the bulk grain, r is the mean radius of the inclusions and ζ is the volume fraction of the inclusions. The resultant predicted grain sizes given by this method are shown in Table 4. The volume fraction of the inclusions, ζ, has been modelled using both the volume fraction of mullite grains across the entirety of the material and the volume fraction of mullite grains within the regions of abnormal grains. This may have been an underestimation as the mullite grains within the areas of normal grains are difficult to separate from the alumina grains.

Yttria Additive / PPM	Predicted Abnormal Grain Size / µm		Measured Abnormal Grain Size / µm
	All Material	Only Abnormal Grains	
100	54.1 ± 1.7	18.8 ± 0.6	13.5 ± 2.0
250	31.2 ± 1.1	27.0 ± 0.7	19.8 ± 6.0
500	31.4 ± 0.8	30.2 ± 0.7	23.2 ± 7.7
1000	38.2 ± 2.1	36.6 ± 2.0	38.2 ± 4.6

Table 4: Table showing the predicted grain size assuming Zener pinning has occurred in Al_2O_3-1wt.%SiC-Y_2O_3 compared to the actual grain size measured in the same material.

Regardless of the method of calculating the volume fraction used, the Zener model generally overpredicted the grain size compared to the actual measured value. There are two potential explanations. Firstly, the Zener model calculation gives a limiting grain size after growth has reached its final value. Despite the high density that is successfully achieved with the addition of only 100 PPM Y_2O_3, abnormal grain growth has not consumed the entirety of the material. The addition of higher quantities of yttria results in more abnormal grain growth as is shown in Figure 67. The samples containing a higher percentage yttria with shorter sintering times possess a similar microstructure to those with less yttria but longer sintering times; abnormal grains have formed but have not yet grown to consume a significant majority of the material. This suggests that after longer sintering times more abnormal grain growth will occur regardless of yttria content. Therefore, the Al_2O_3-1wt.%SiC-Y_2O_3 with lower yttria contents have not achieved the limiting conditions calculated by the Zener model, resulting in the lower measured grain size observed. This explanation, however, does not explain all the results. As the Zener pinning model assumes the particles are completely immobile, it would be impossible for the mullite particles to coalesce into the regions of normal grains as described in 5.3.4. Therefore, some level of particle mobility must be present.

5.3.4.2 Mullite Particle Mobility

This leads to the second explanation for the final observed distribution of mullite particles: particle mobility and the consequent particle drag. The movement of particles due to diffusion has long been seen across a variety of materials [230-232] and it has been shown that the drag of these particles with grain boundaries acts to slow grain boundary migration [233]. Dependent on the relative velocities of mullite and the grain boundaries in alumina, the mullite particles are either dragged along with the grain boundary or bypassed in a similar fashion to the Zener model discussed above. This generally results in a smaller grain size than is predicted by the Zener model [233], and so explains the results seen in Table 4. This is due to mobile particles allowing for particles to accumulate on the grain boundaries as the growth slows, further decreasing the grain boundaries mobility. The movement of particles in this fashion also allows for the diffusion of material to change the size of the formed mullite grains through Ostwald ripening. This is seen in the changes in mullite particle size measured in Figure 73. This shows the larger number of yttrium-containing grain boundaries allows for more grain growth of mullite. Potentially the combination of multiple mullite grains to form a larger particle through coalescence could occur however the observed microstructures, such as that seen in Figure 72 e-f, does not show this coalescence and instead forms a region of distinct mullite grains.

5.3.5 Mullite Composition

5.3.5.1 EDX Analysis

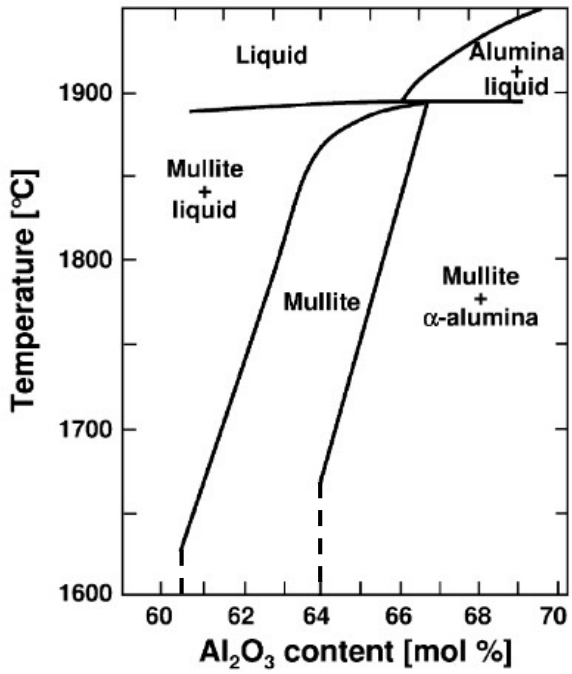


Figure 95: A section of the Al_2O_3-SiO_2 system phase diagram showing the mullite region in detail. Reproduced from Schneider et al. [234].

There is a notable difference in the measured composition of the mullite grains between those measured inside the grains and those outside. Mullite grains within abnormal alumina grains had a composition of $1.8Al_2O_3{\cdot}SiO_2$ (64 mol.% Al_2O_3), as is shown in Table 1. This is within the range of mullite compositions found to be valid in the phase diagram produced in the work of *Klug et al*. [93], Figure 95. Comparatively however, the mullite grains within the areas of normal grains show a very different composition. These grains show an average composition of $3Al_2O_3{\cdot}SiO_2$ (75 mol.% Al_2O_3), as is shown in Table 3, assuming all material scanned is of a mullite type structure. This composition is not within the mullite regime of the phase diagram regardless of temperature considered. [234] This effect is due to the mullite grains not being exclusively scanned during STEM-EDX analysis of these mullite grains. Comparison between the primarily observed side of the lamellae and the reverse shows a different layout of grain boundaries. Therefore, the EDX line scan samples both the primarily chosen mullite grain and the alumina grain. This results in a measured composition with a higher alumina content than is actually present in the mullite grain that is attempting to be measured.

5.3.5.2 Unit Cell Dimensions

As described in 5.1.2.5.1.1, the measured unit cell in the mullite grains has basal dimensions of 0.768 ± 0.001 nm and 0.758 ± 0.001 nm. The ratio between these basal dimensions is 1.013 ± 0.004. The measurement of the basal dimensions of the unit cell of known compositions of mullite range between 0.769 nm by 0.755 nm, for a ratio in the basal dimensions of 1.018, in 3/2-mullite [235] and 0.768 nm by 0.758 nm, for a ratio of basal dimensions of 1.013, in 2/1-mullite [236]. This places the unit cell measured within the mullite subgrains in this work within the range of mullite grain sizes measured by others providing further evidence for the transformation of silicon carbide within these grains. The close agreement between the basal dimensions themselves, the ratio between the basal dimensions and the composition of the particles measured to known mullite values confirms the grains are mullite within the alumina matrix. The measured unit cell dimensions match closely to the dimensions measured in 2/1-mullite, indicating a composition comprising 66 mol.% Al_2O_3. This matches closely the compositional results shown in Table 1 suggesting the mullite formed is primarily 2/1 mullite.

5.3.6 Porosity in Al_2O_3-SiC-Y_2O_3

While Al_2O_3-SiC-Y_2O_3 nanocomposites have achieved a high relative density, they show a distinctive porosity distribution. Both Al_2O_3 and Al_2O_3-SiC show an even distribution of porosity regardless of the total porosity present, however this is not the case within Al_2O_3-SiC-Y_2O_3 regardless of quantity of Y_2O_3 present. Al_2O_3-SiC-Y_2O_3 results in porosity dominated by large pores with the remainder of the material showing limited porosity. An example of the difference between the structure of Al_2O_3 and the pores in Al_2O_3-SiC-Y_2O_3 is shown in Figure 51. This porosity appears more prevalent with the addition of more Y_2O_3, with the addition of 100ppm Y_2O_3 resulting in pores with diameters of on average 0.6 µm and 1000ppm Y_2O_3 resulting in pores of on average 12 µm in diameter as is shown in Figure 52.

Porosity of this kind could be due to variations in green body density due to the yttria additives interfering with processing, however the X-ray tomography analysis described in 5.1.1.2 suggests this is not the root cause of the porosity. The pores seen in micrographs, such as the one shown in Figure

51, are of sufficient size that their presence would be visible under X-ray tomography as areas of lower density or even potentially voids. As these lower density regions are not seen either optically or through statistical analysis of the X-ray tomography data, the large-scale porosity must be formed during sintering. These pores could initially form through a similar mechanism to the coarsening of grains, as a greater quantity of abnormal grain growth, and its accompanying increase in grain boundary mobility, could allow for the significant diffusion and coalescence of porosity required to form these pores. The effect of these methods to produce large pores is somewhat limited however [237], and so cannot explain the final size of the pores seen with the addition of 1000ppm Y_2O_3. The limited quantity of smaller pores surrounding the large pores in Al_2O_3-1wt.%SiC-1000ppmY_2O_3 suggests that Ostwald ripening of the pores has occurred [238] and this has produced the large pores seen in Figure 51.

6 MECHANICAL PROPERTIES OF ALUMINA-SILICON CARBIDE-YTTRIA

The key objectives of the project are outlined in Chapter 5. These objectives are considered, and, in this chapter, the following sections are presented:

1. The results of mechanical testing including hardness, wear resistance, and fracture properties. This had the aim of optimising the composition of the resultant alumina-silicon carbide-yttria for ballistic performance.
2. A discussion of the link between the measured bulk macroscopic properties and the microstructure and grain boundary structure described in 5.3.1.
3. Finally, the behaviour of alumina-silicon carbide-yttria nanocomposites will be compared to alumina in the case of high-speed impacts and consideration will be given to how this may correspond to potential ballistic resistance behaviour.

6.1 RESULTS

6.1.1 Vickers Hardness Testing

6.1.1.1 Alumina

Vickers hardness testing was carried out with a load of 20 kg on samples of alumina sintered for up to 4 hours, the results of which can be seen in Figure 96. This showed an overall trend in hardness with sintering temperature although the effect of sintering time was limited. Hardness showed a peak after sintering at 1450^{O}C regardless of sintering time. Due to significant flaking this data possesses a large error, and the improvement in overall hardness is not statistically significant as is discussed below in 6.1.1.2.

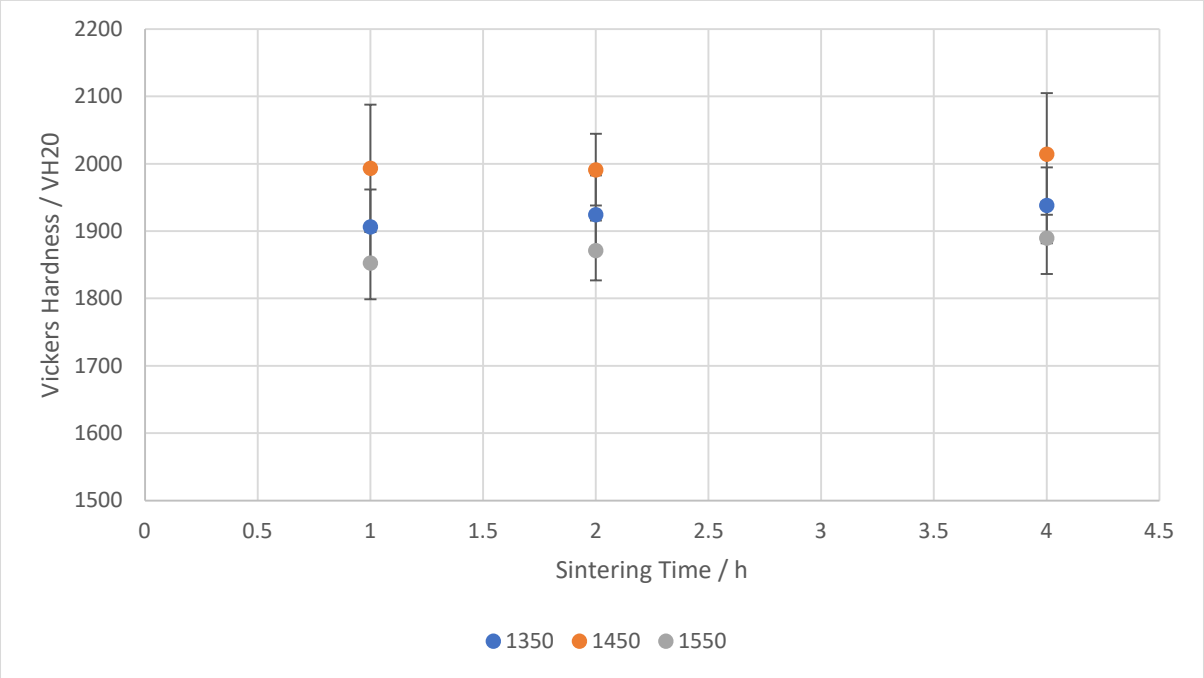


Figure 96: Graph showing the Vickers hardness of Al_2O_3 under a 20kg load after sintering for up to 4 hours at temperatures between 1350 and 1550 ^{O}C.

6.1.1.2 *Alumina-Silicon Carbide*

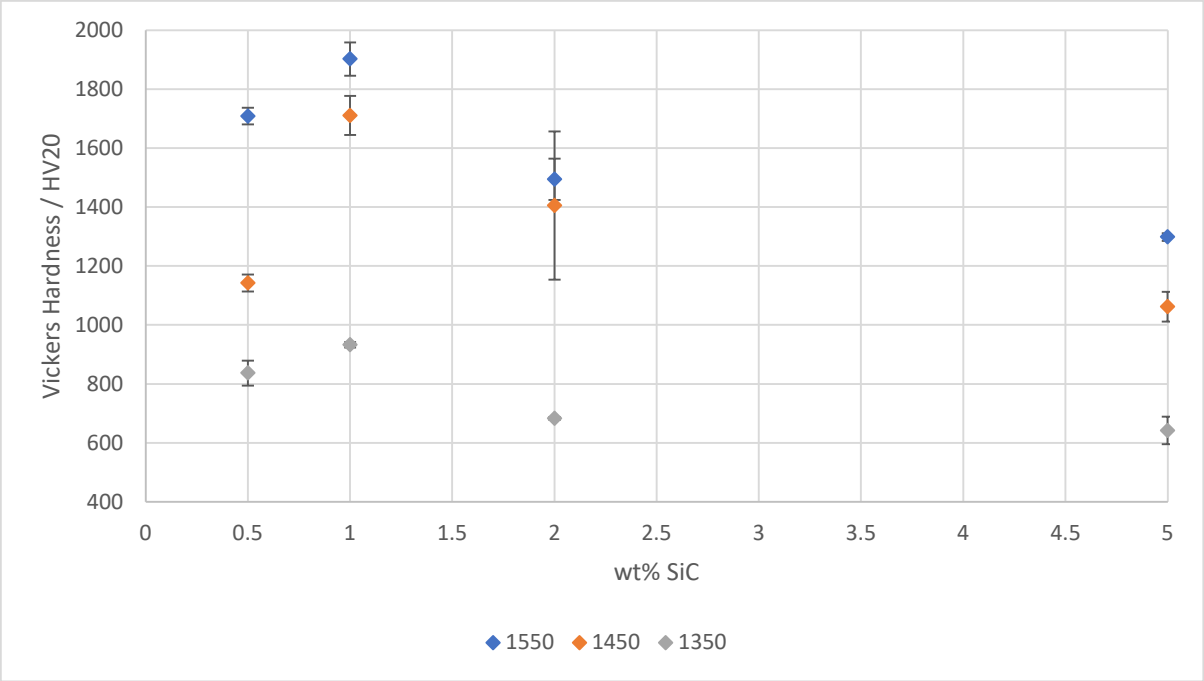


Figure 97: Graph showing the Vickers hardness values of alumina under a 20 kg load with varying quantities of silicon carbide after sintering for 4 hours at temperatures between 1350 and 1550 ^{O}C.

Vickers hardness testing was carried out with a load of 20 kg on samples of alumina with the addition of silicon carbide additives sintered for 4 hours as described in 4.4.1. This showed a clear trend in Vickers hardness, Figure 97. A peak hardness was seen with the addition of 1 wt.% silicon carbide regardless of sintering temperature. The highest measured hardness values were found with higher sintering temperatures, with a peak hardness of 1900 ± 56 HV20.

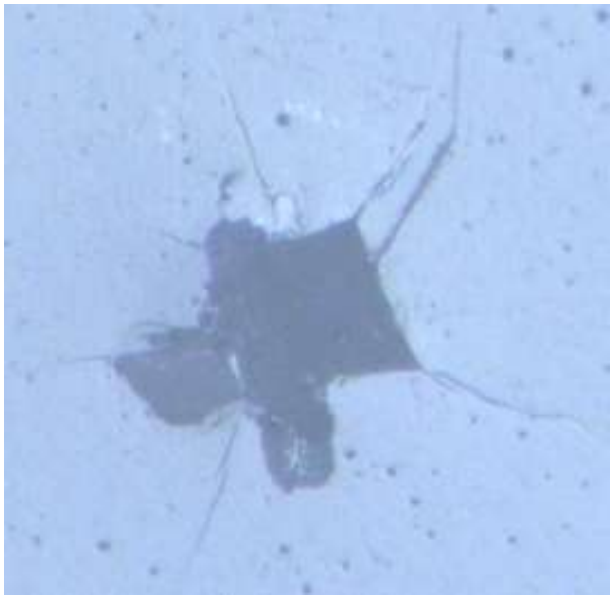


Figure 98: Optical micrograph showing the surface flaking in a 20 kg Vickers hardness test.

Further testing was conducted at the lower load of 5 kg, as the load of 20 kg was resulting in significant surface chipping around the indentation site. An example of this chipping can

be seen in Figure 98. This flaking can render accurate measurement of the size of the primary diagonals impossible, as the exact location of the corner is lost. Reduction of the load minimised the quantity of surface cracking allowing for more accurate measurements of the dimensions of the impact site and consequently more accurate calculation of Vickers hardness.

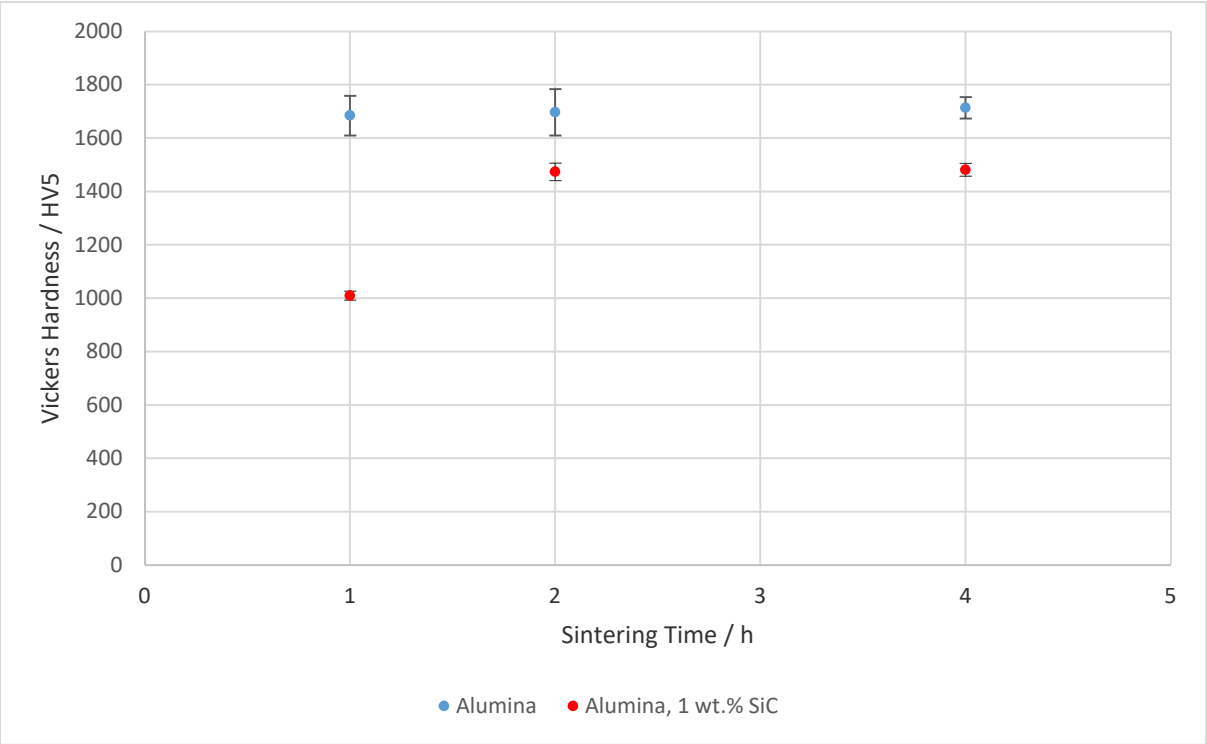


Figure 99: Graph showing the Vickers hardness values of alumina and alumina with 1 wt.% silicon carbide sintered at 1550 ^{O}C for between 1 and 4 hours under a 5kg load.

A comparison between the hardness of the best performing alumina silicon carbide composite, 1 wt.% silicon carbide sintered for 4 hours, against unmodified alumina sintered under the same conditions results in a performance reduction of 14 % in Vickers hardness. This difference is seen to be even greater at lower sintering times as can be seen in Figure 99.

6.1.1.3 Alumina-Silicon Carbide-Metal Compounds

The addition of 500 ppm of the metal oxides and nitrates described in 4.1.3 offered an improvement in hardness over the comparable composites with the addition of solely 1 wt.% silicon carbide. Most notably, the addition of 500 ppm of calcium nitrate, neodymium nitrate or yttria offered a significant

benefit in Vickers hardness after only 1 hour sintering, but the effect continued to be observed at higher sintering times to a lesser effect. This improvement is shown in Figure 100.

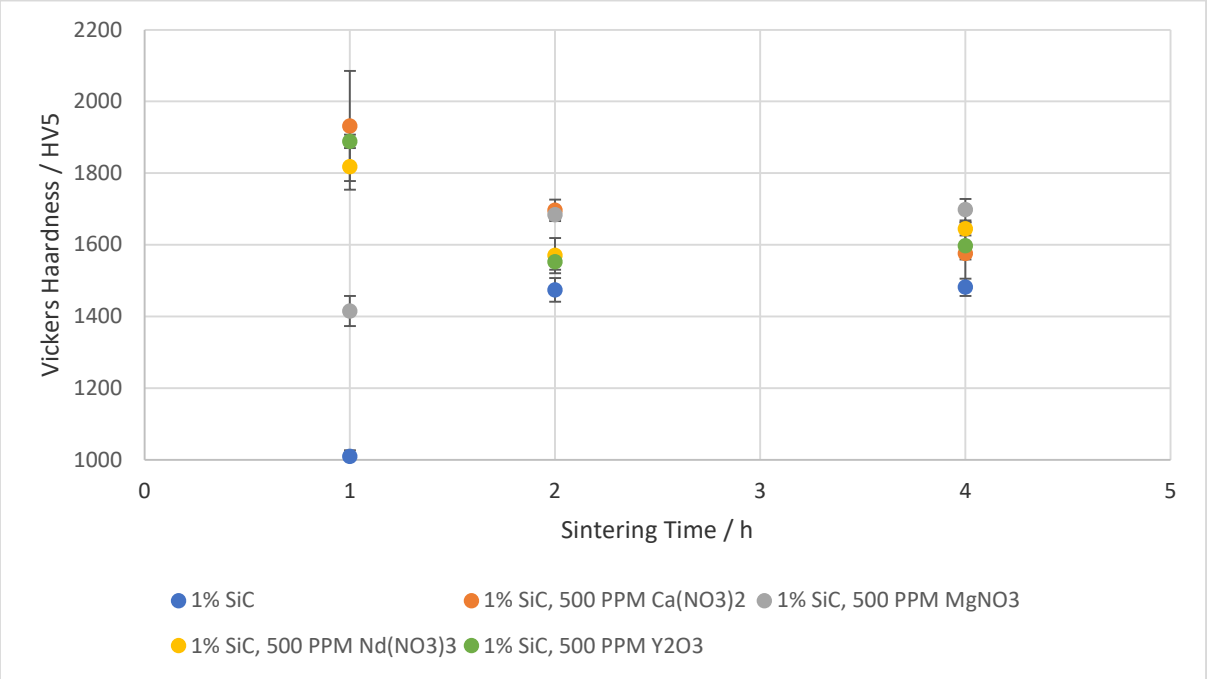


Figure 100: Graph showing the Vickers hardness values after a 5 kg load for alumina samples with 1 wt.% silicon carbide and 500 ppm of calcium nitrate, magnesium nitrate, neodymium nitrate or yttrium oxide sintered at 1550 ^{O}C for between 1 and 4 hours.

6.1.1.4 Alumina-Silicon Carbide-Yttria

The effects of variations in yttrium oxide content were investigated, as is shown in Figure 101. It was found that the lower the quantity of yttrium oxide added to Al_2O_3-1wt.%SiC, the larger an improvement in Vickers hardness was measured. This effect is most pronounced after longer sintering times; larger quantities of yttrium oxide, such as 500 ppm or 1000 ppm, resulted in a decrease in Vickers hardness compared to the same composition after lower sintering time. Conversely, an addition of 100 ppm yttrium oxide resulted in an increase in measured Vickers hardness with sintering time. After 4 hours sintering at 1550 ^{O}C, Al_2O_3-1wt.%SiC-100ppmY_2O_3 showed an improvement in Vickers hardness of 9% over alumina sintered under the same conditions and 5% over alumina sintered to result in a fine grain size with a high density, 1400 ^{O}C.

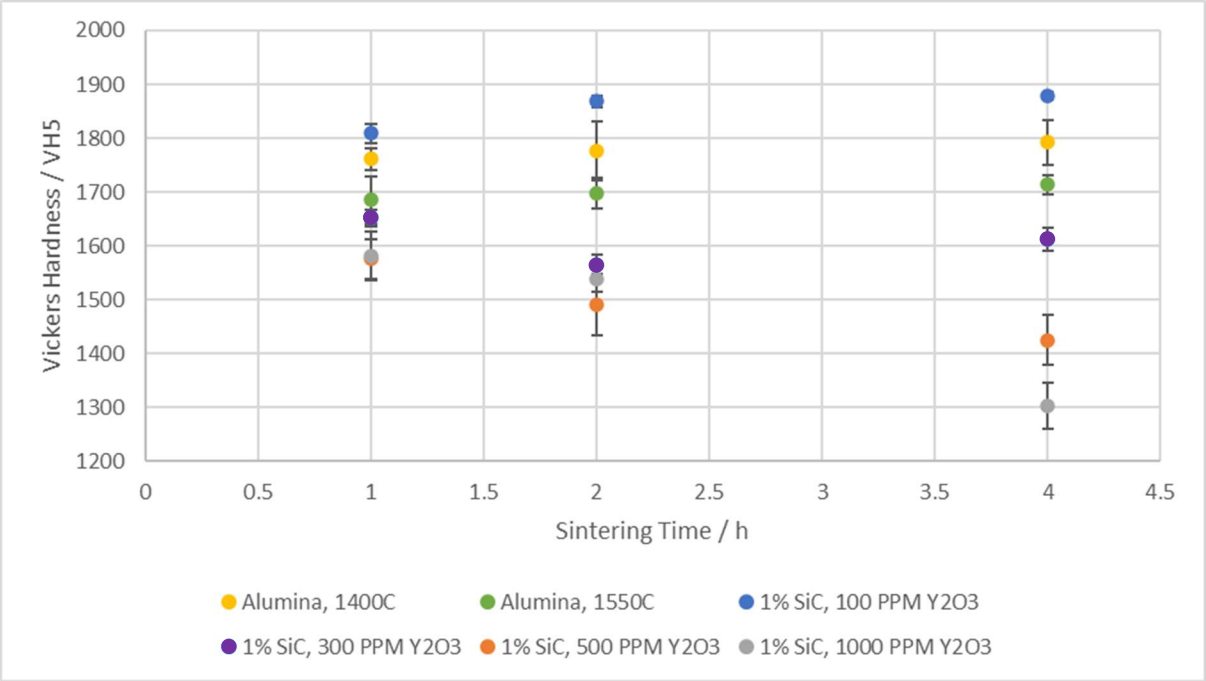


Figure 101: Graph showing the Vickers hardness after a 5 kg load for alumina samples with 1 wt.% silicon carbide and various quantities of yttrium oxide sintered at 1550 ^{O}C for between 1 and 4 hours. Undoped alumina sintered under the same conditions and sintered at 1400 ^{O}C is included for comparison.

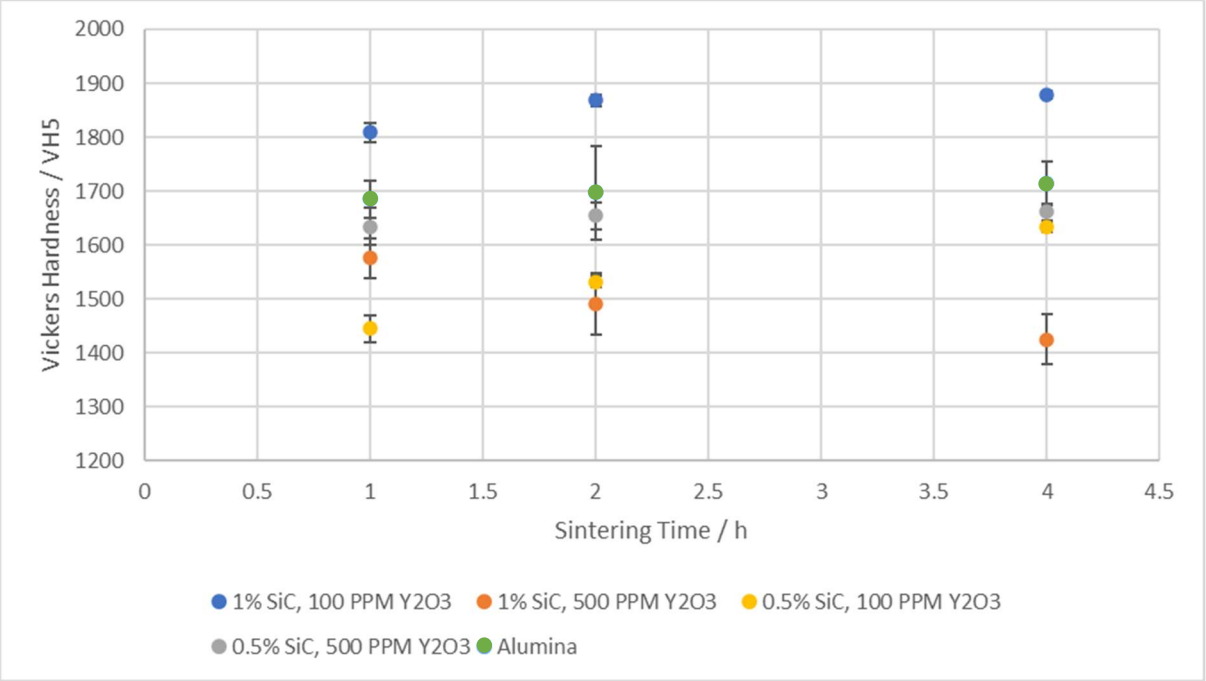


Figure 102: Graph showing the Vickers hardness after a 5 kg load for alumina samples with various quantities of silicon carbide and yttrium oxide sintered at 1550 ^{O}C for between 1 and 4 hours. Undoped alumina sintered under the same conditions is included for comparison.

6.1.1.4.1 Vickers Hardness Crack Behaviour

Microscopy of the cracks generated from the corners of the Vickers hardness indentations showed the difference between the crack paths seen in the presence of yttrium oxide and in its absence. Scanning electron microscopy images of these crack paths are shown in Figure 103. With the addition of solely 1 wt.% silicon carbide to alumina, the crack path shows clear deflection along grain boundaries as it progresses. The presence of yttrium oxide, however, resulted in significantly different crack behaviour; the crack path progressed straight across grains with very limited deflection at grain boundaries.

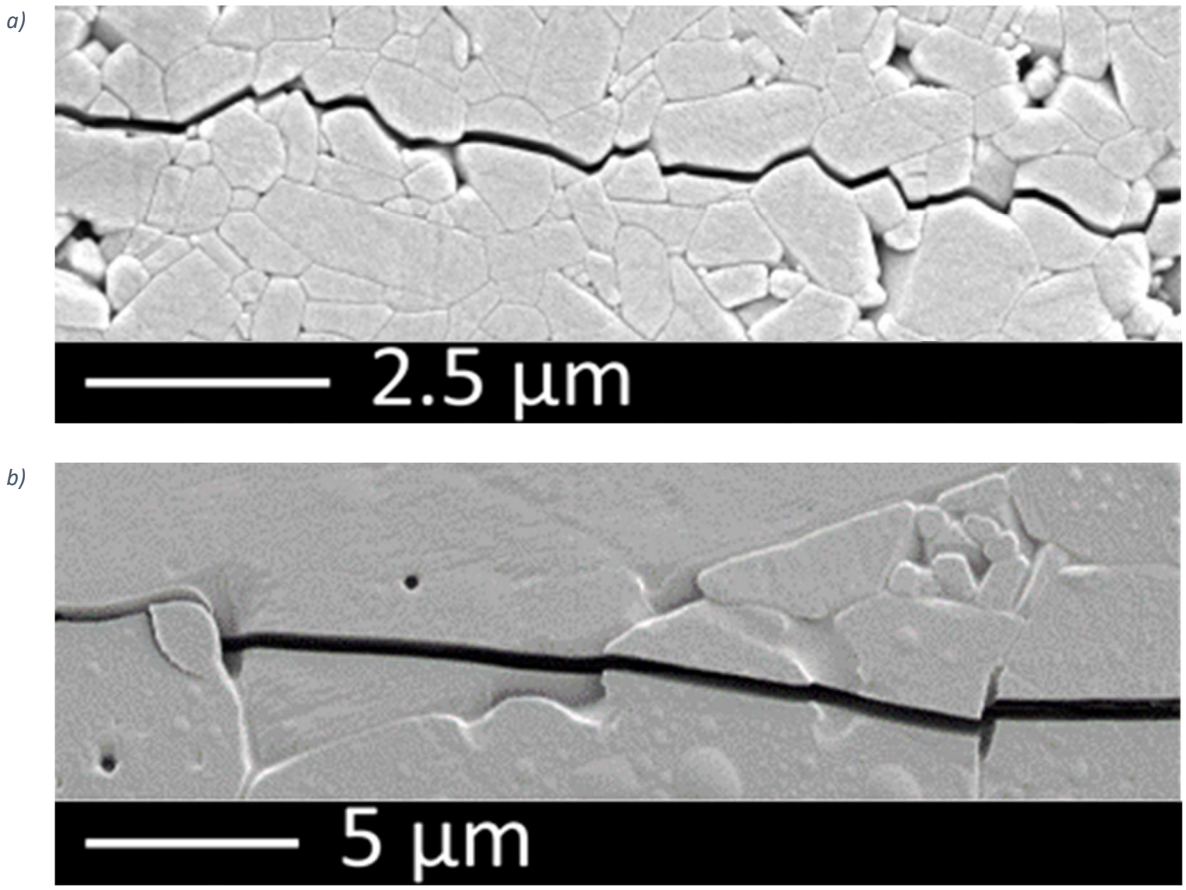


Figure 103: SEM images of the cracks surrounding Vickers hardness indentations in a) alumina with 1 wt.% silicon carbide sintered for 4 hours at 1550 ^{O}C b) alumina with 1 wt.% silicon carbide and 500 ppm yttrium oxide sintered for 4 hours at 1550 ^{O}C.

6.1.2 Nanoindentation

Micrographs of the 1 µm indents after thermal etching were used to identify the number of grains within the indentation triangle. A comparison between the number of grains within the indentation and the measured modulus, Figure 104, or hardness, Figure 106, of the material, shows no correlation in Al_2O_3 sintered at 1550 ^{O}C for 4 hours with either property. Comparatively, Al_2O_3-1wt.%SiC-500ppmY_2O_3 shows a decrease in both modulus and hardness with the number of grains intercepted by the indentation.

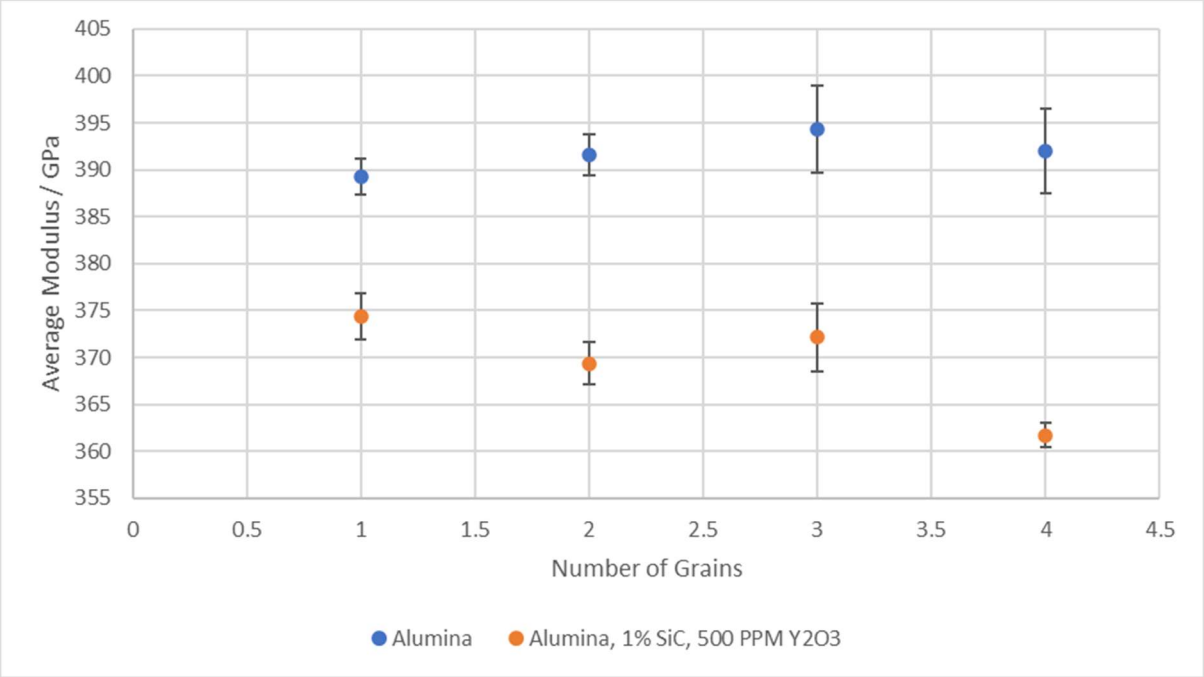


Figure 104: Graph showing the mean average modulus measured in nanoindentations in alumina and alumina with the addition of 1 wt.% silicon carbide and 500 ppm Y_2O_3 that had been sintered at 1550 ^{O}C for 4 hours compared to the number of grains within the indentation.

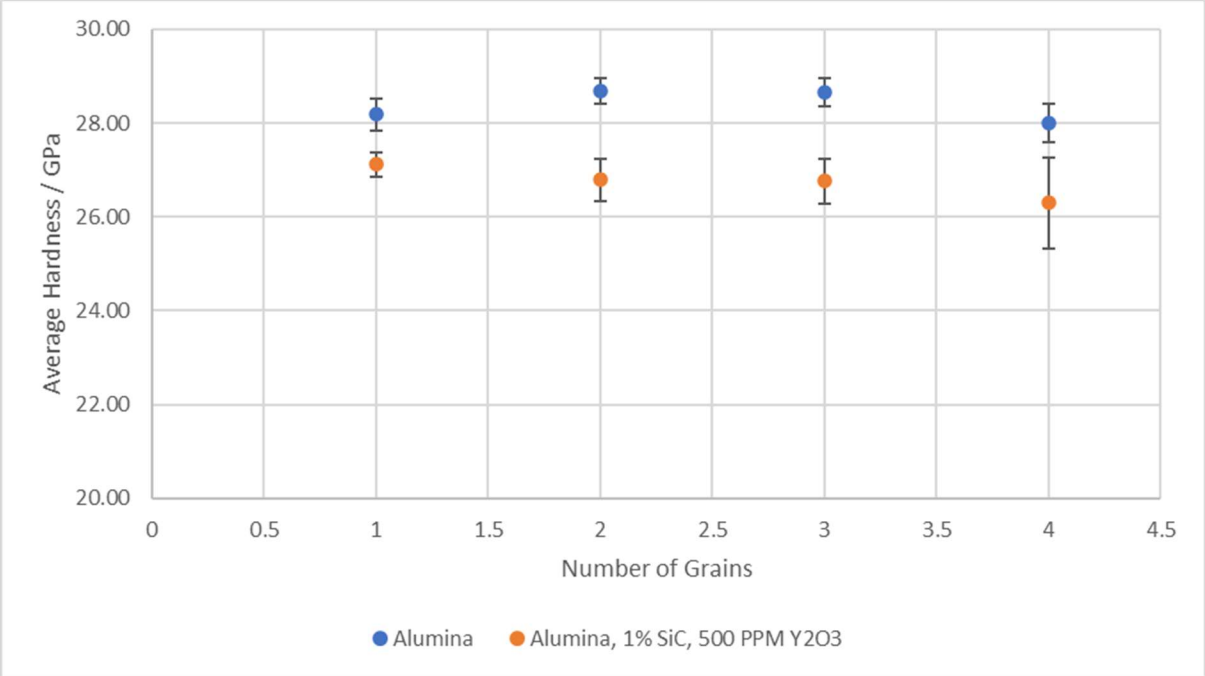


Figure 106: Graph showing the mean average hardness measured in nanoindentations in alumina and alumina with the addition of 1 wt.% silicon carbide and 500 ppm Y2O3 that had been sintered at 1550 OC for 4 hours compared to the number of grains within the indentation.

Al_2O_3-1wt.%SiC-100ppmY_2O_3 resulted in grains that were regularly significantly smaller than the indentations created. Therefore, the number of grains within the indentation could not be accurately measured from the resultant micrographs. As a result, indentations were categorised by the type of environment surrounding the indent. This showed the indentations which were partially within an abnormal grain, and partially within an area of smaller grains as shown in Figure 105, showed a higher modulus than the modulus measured in indentations entirely within one type of grains. This comparison is shown in Figure 107. Regardless of indentation environment, samples of Al_2O_3-1wt.%SiC-100ppmY_2O_3 possessed a higher measured hardness and modulus than

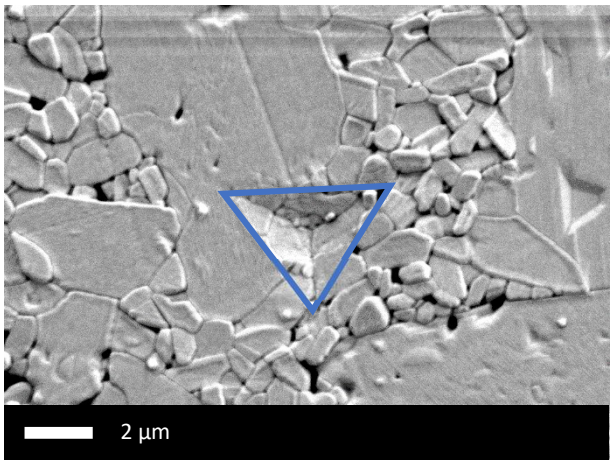


Figure 105: Micrograph showing an indentation in Al_2O_3-1wt.%SiC-100ppmY_2O_3 including an indentation crossing the border between abnormal grains and smaller grains. The indentation has been outlined for clarity.

the same environment in samples of Al_2O_3-1wt.%SiC-500ppmY_2O_3.

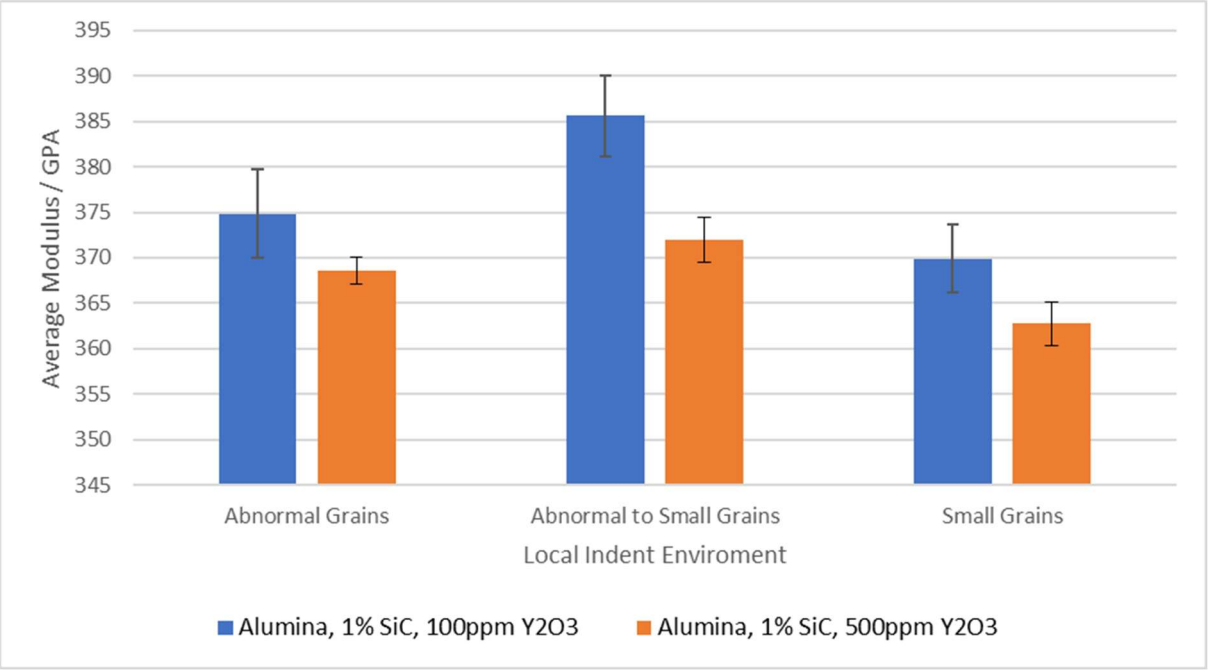


Figure 107: Graph showing the mean average modulus measured in nanoindentations in alumina with the addition of 1 wt.% silicon carbide and either 100 or 500 ppm Y_2O_3 that had been sintered at 1550 ^{O}C for 4 hours compared to the local environment.

6.1.3 Wear Resistance

Wear resistance of alumina samples was measured with loads of both 3.5 N and 2 N by the method described in 4.4.3. This resulted in a scar such as the one shown in Figure 108; a complete circular cap of removed material.

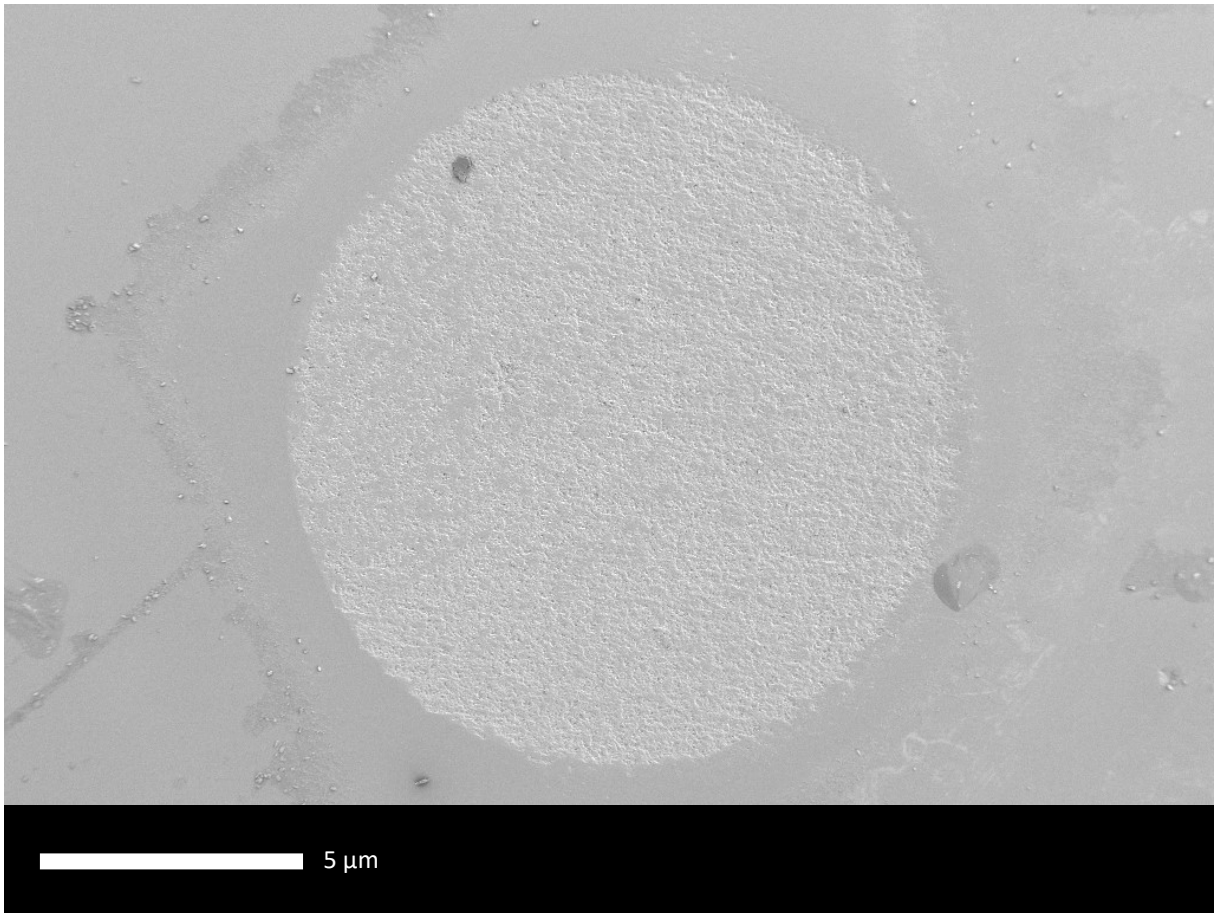


Figure 108: SEM image showing the resultant wear scar created in alumina with a load of 3.5 N.

Measurement of material removed allowed for the comparison of wear resistance between Al_2O_3, Al_2O_3-1wt.%SiC, and Al_2O_3-1wt.%SiC-500ppmY_2O_3. This data is shown in Figure 109 and Figure 110, for loads of 2 N and 3.5 N respectively. An average improvement of over 400% was measured due to the addition of 500 ppm yttrium oxide compared to the equivalent sample with only the addition of 1 wt.% silicon carbide after sintering at 1550 ^{O}C for between 1 and 4 hours. The composite of Al_2O_3-1wt.%SiC-500ppmY_2O_3 displayed a lower measured wear resistance than alumina under the same conditions regardless of the sintering time or load used.

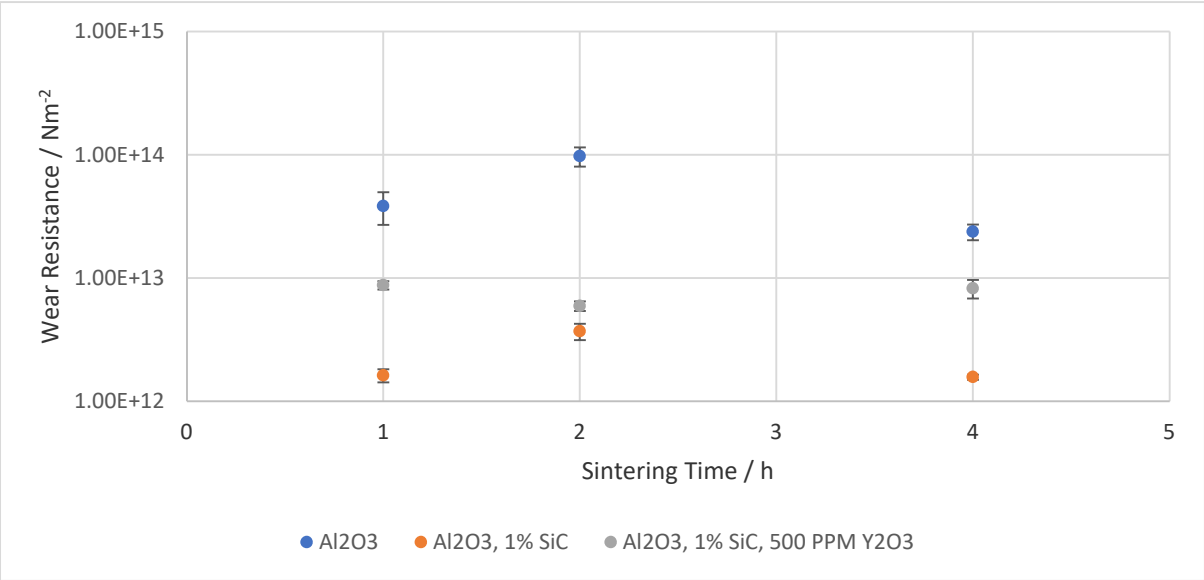


Figure 109: Graph showing the calculated wear resistance under a load of 2 N in Al_2O_3, Al_2O_3-1wt.%SiC, and Al_2O_3-1wt.%SiC-500ppmY_2O_3 after sintering at 1550 ^{O}C for between 1 and 4 hours.

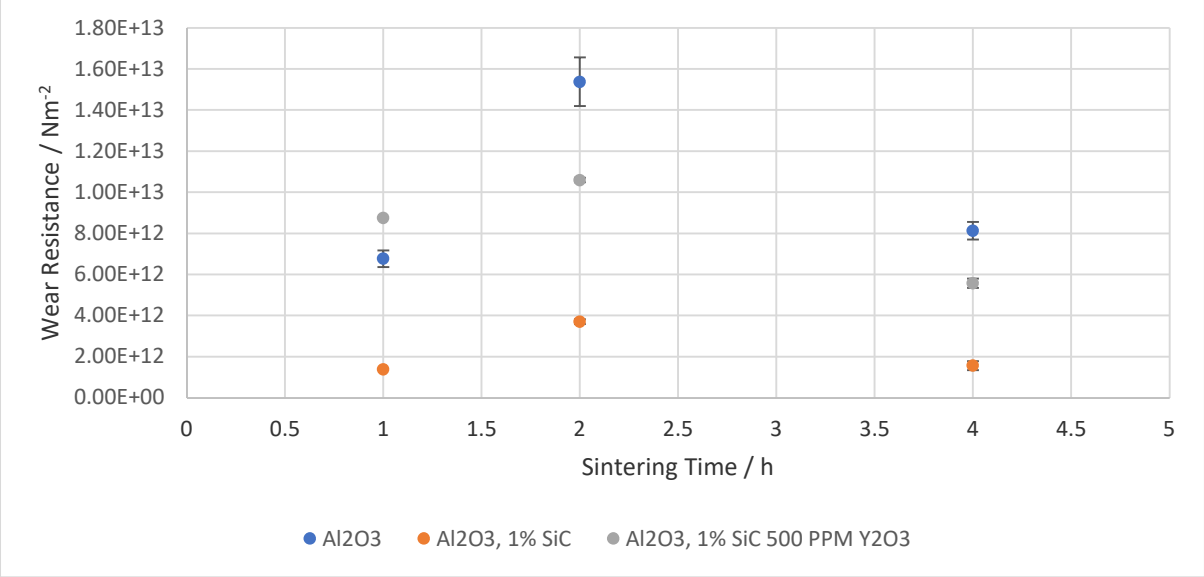


Figure 110: Graph showing the calculated wear resistance under a load of 3.5 N in Al_2O_3, Al_2O_3-1wt.%SiC, and Al_2O_3-1wt.%SiC-500ppmY_2O_3 after sintering at 1550 ^{O}C for between 1 and 4 hours.

Microscopy of the wear scars produced in Figure 110 showed a difference in failure behaviour. With the addition of only silicon carbide to alumina, a finer structure than in the wear scar seen in pure alumina. Conversely the addition of 500 ppm yttrium oxide alongside silicon carbide to alumina results in a microstructure with larger sections of smooth material with limited pull-out between them than the wear scar seen in pure alumina. These respective structures can be clearly seen in Figure 111. The

discrepancy in scar structures seen here mirrors the crack behaviour shown in Figure 103, with the addition of yttria resulting in large lengths of intragranular cracks and similarly large areas of smooth wear surfaces where pull out does not occur. Conversely, the crack deflection seen without the presence of yttrium oxide mirrors the larger proportion of pull-out seen in the wear scar.

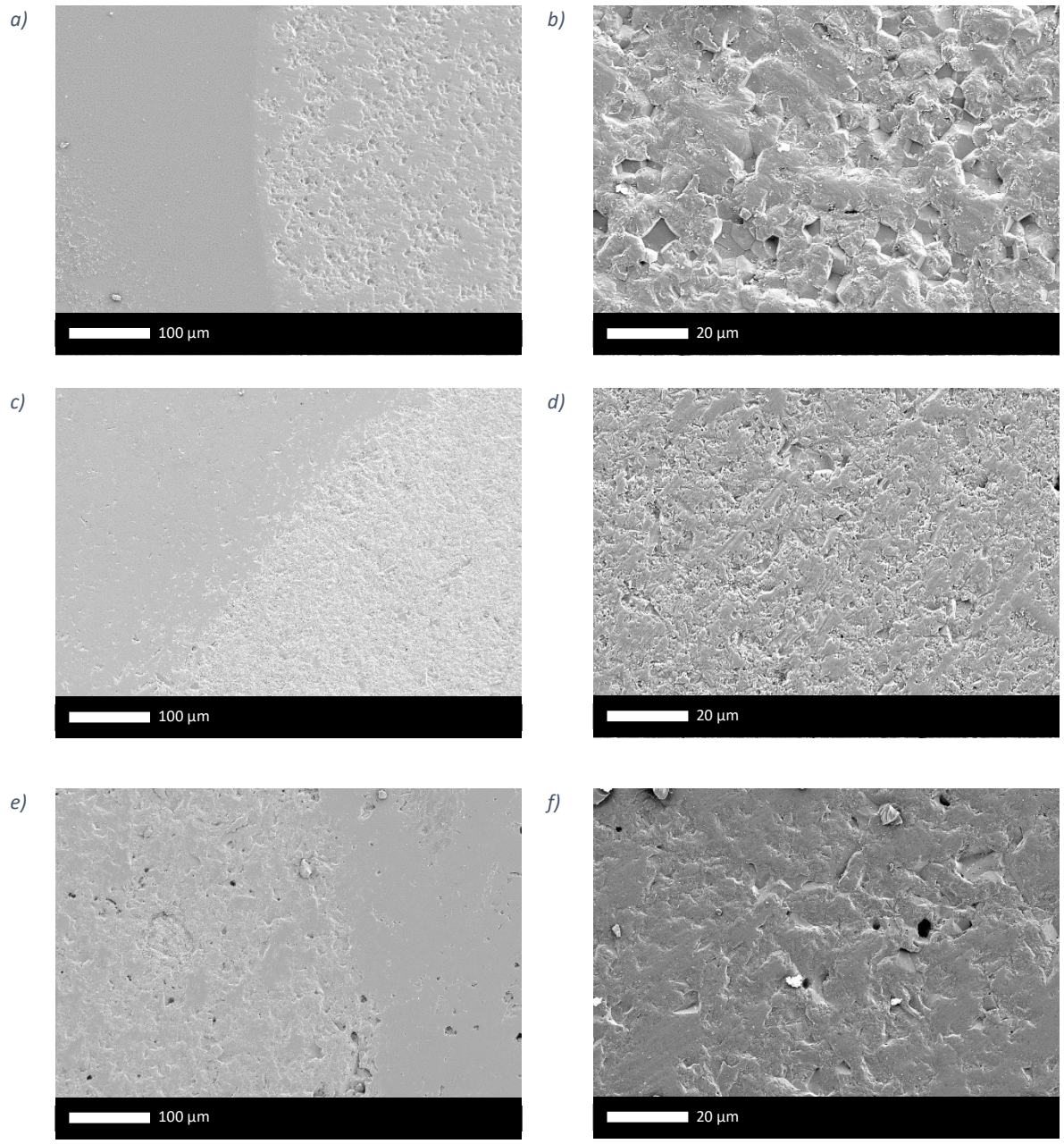


Figure 111: SEM images of more detailed sections of the wear scar created by a 3.5 N load in samples sintered for 4 hours at 1550 ^{O}C in a-b) Al_2O_3 c-d) Al_2O_3-1wt.%SiC e-f) Al_2O_3-1wt.%SiC-500ppmY_2O_3.

6.1.4 Fracture Toughness

The fracture toughness of samples was measured using the maximum load recorded prior to the sample fracturing and the equation detailed in 4.4.5. Al_2O_3-1wt.%SiC-100ppmY_2O_3 resulted in a higher fracture toughness than either Al_2O_3 or Al_2O_3-1wt.%SiC after sintering for 4 hours at 1550 ^{O}C, although this improvement is within the experimental error of the data. This can be seen in Figure 112, and shows a nominal improvement of 7 % and 6 % over Al_2O_3 and Al_2O_3-1wt.%SiC added respectively.

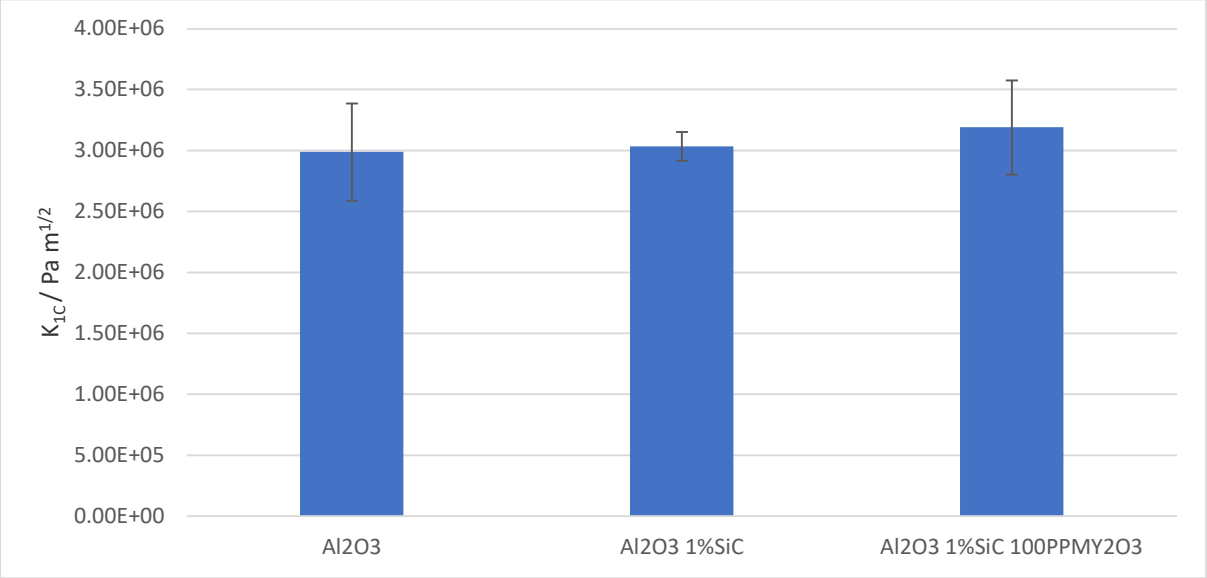


Figure 112: Graph showing the fracture toughness of notched beams Al_2O_3, Al_2O_3-1wt.%SiC, and Al_2O_3-1wt.%SiC-100ppmY_2O_3 after sintering for 4 hours at 1550 ^{O}C.

6.1.5 Flexural Properties

By analysing the bend data resulting from the fracture of polished unnotched beams, as described in 4.4.4.1, both flexural strength and Weibull modulus can be determined.

6.1.5.1 Flexural Strength

The flexural strength of samples was found using the maximum load measured during testing and the formula described in 4.4.4.1 Al_2O_3-1wt.%SiC-100ppmY_2O_3 showed a higher flexural strength than alumina with the addition of either silicon carbide or yttrium oxide individually after sintering for 4 hours at 1550 ^{O}C. This change can be seen in Figure 113, and had a calculated improvement of 26%

and 65% for the addition of silicon carbide and yttrium oxide respectively. Al_2O_3-1wt.%SiC-500ppmY_2O_3 displayed a mean flexural strength of only 92 % of the value measured for alumina sintered under the same conditions and 82% of alumina sintered at 1400 ^{O}C for 4 hours.

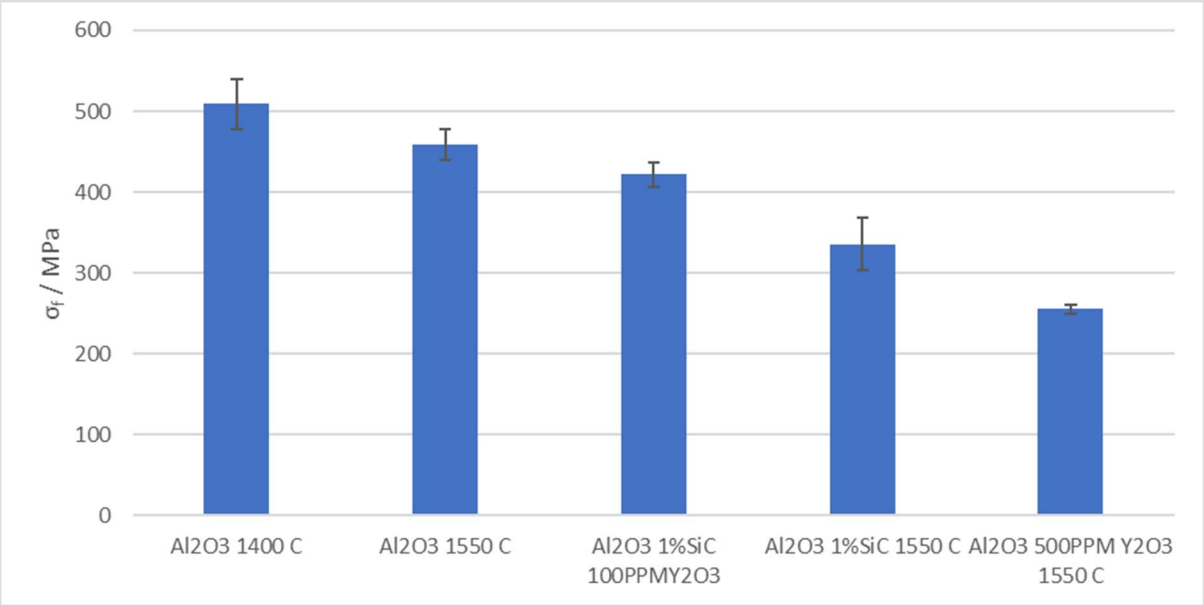


Figure 113: Graph showing the mean flexural strength of alumina, alumina with 1 wt.% silicon carbide, alumina, with 500 ppm yttrium oxide, and alumina with both 1 wt.% silicon carbide and 100 ppm yttrium oxide after sintering for 4 hours at 1550 ^{O}C.

6.1.5.2 Weibull Analysis

Weibull statistical analysis of the flexural strength values calculated from samples in 6.1.5.1 was conducted as described in 4.4.4.1.1. The respective Weibull moduli found from the samples in 6.1.5.1 are shown in Figure 114. The highest Weibull modulus found after 4 hours sintering at 1550 ^{O}C was measured in Al_2O_3-500ppmY_2O_3. Al_2O_3-1wt.%SiC-100ppmY_2O_3 was found to have a slightly higher Weibull modulus than alumina sintered under the same conditions. Therefore, despite the higher mean ultimate flexural strength found in pure alumina, at a certain failure load both alumina and the composite Al_2O_3-1wt.%SiC-100ppmY_2O_3 tested have an equal probability of failure. In this case, at a failure probability of 0.33% both materials have an equal mean maximum load before failure.

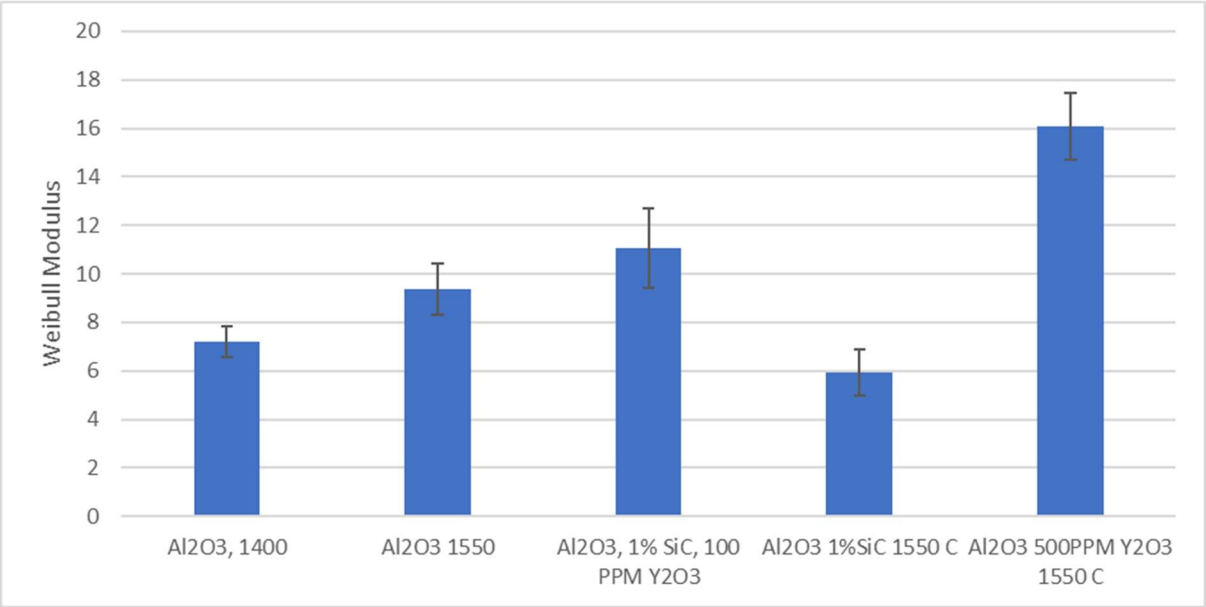
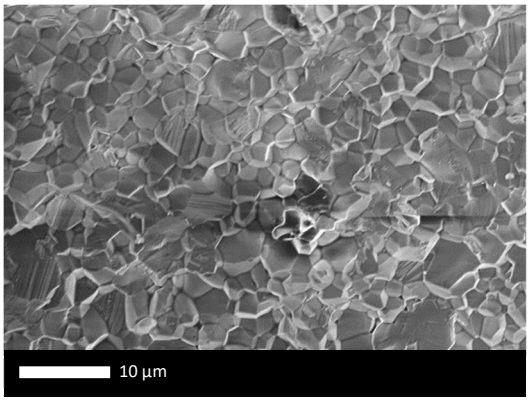


Figure 114: Graph showing the Weibull modulus of the flexural strength of alumina, alumina with 1 wt.% silicon carbide, alumina, with 500 ppm yttrium oxide, and alumina with both 1 wt.% silicon carbide and 100 ppm yttrium oxide after sintering for 4 hours at 1550 ^{O}C.

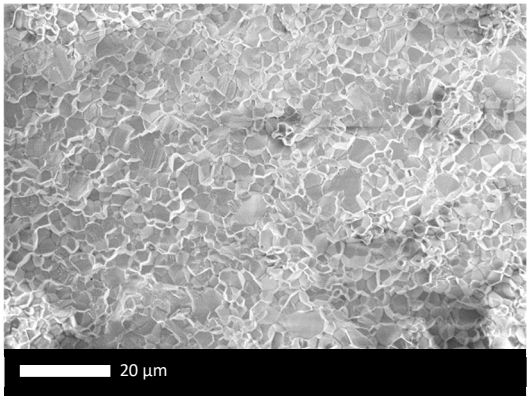
6.1.5.3 Fractography

After fracturing samples, as described in 6.1.5, the resultant fracture surfaces were examined using scanning electron microscopy. These micrographs are shown in Figure 115. A clear difference can be seen between the surfaces created in the differing samples studied. Samples of pure alumina, and alumina with the sole addition of 500 ppm yttrium oxide sintered for 4 hours at 1550 ^{O}C both show clear intergranular fracture on a large scale, as can be seen from the angular features remaining in the fracture surface in Figure 115.a, Figure 115.c and Figure 115.g. The addition of 1 wt.% silicon carbide to alumina resulted in a fracture surface where the higher porosity in this sample is also evident in the resultant structure within the fracture surface.

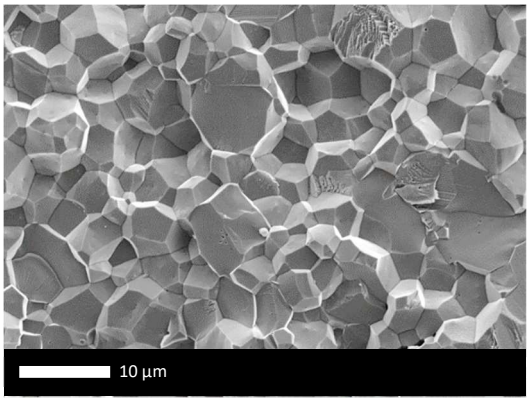
a)



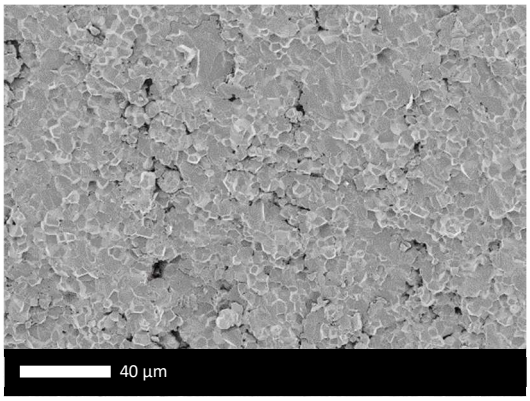
b)



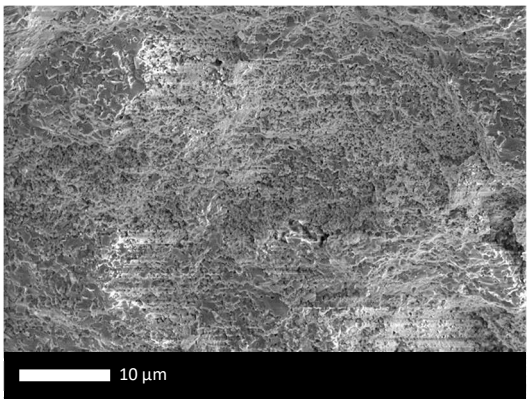
c)



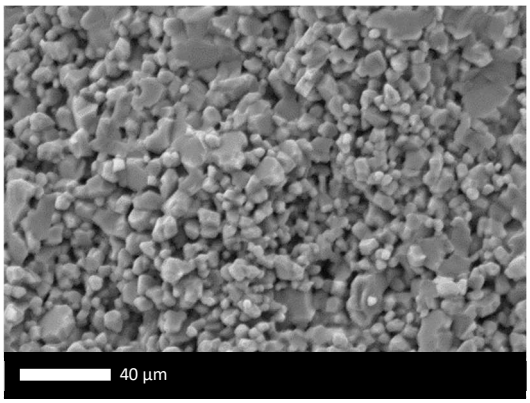
d)



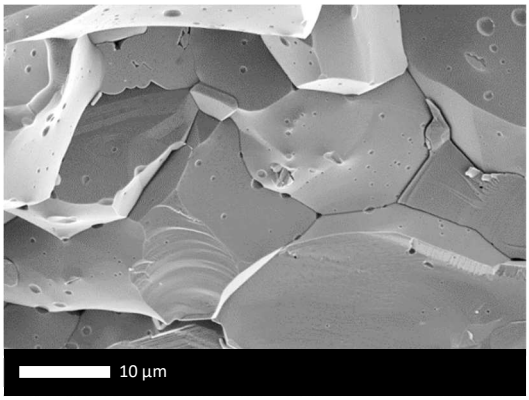
e)



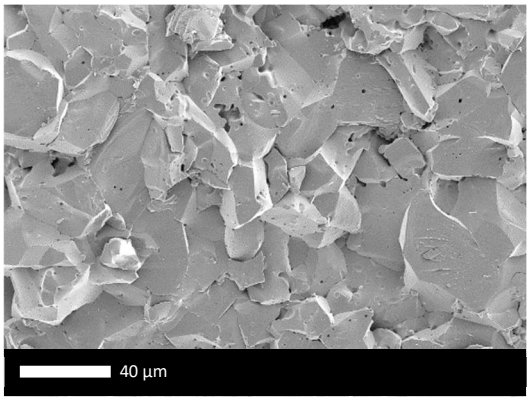
f)



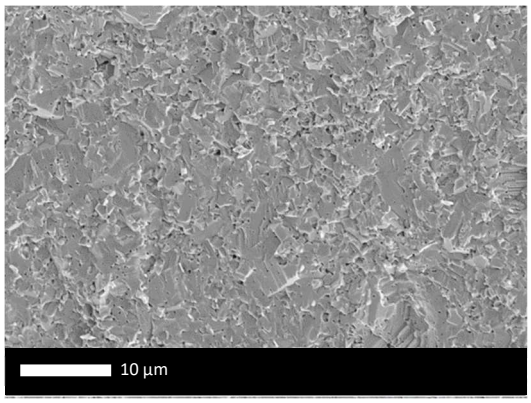
g)



h)



i)



j)

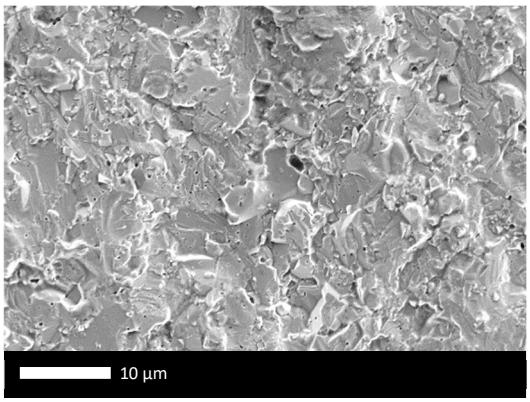


Figure 115: SEM images showing details of the fracture surface in samples fractured during 6.1.5, in a-b) Al_2O_3 sintered for 4 hours at 1400 ^{O}C and sintered for 4 hours at 1550 ^{O}C in c-d) Al_2O_3 e-f) Al_2O_3-1wt.%SiC g-h) Al_2O_3-500ppmY_2O_3 i-j) Al_2O_3-1wt.%SiC-100ppmY_2O_3.

Al_2O_3-1wt.%SiC-100ppmY_2O_3 resulted in a fracture surface with a distinct structure from that seen in the other 3 samples seen in Figure 115. Large areas of the fracture surface are smooth without the faceting seen in Figure 115.i. Therefore, this sample exhibits transgranular fracture similar to the crack behaviour seen in Figure 103. Microscopy was conducted along the fracture surface to attempt to locate the critical flaw that resulted in the overall sample failure however they could not be located.

6.2 DISCUSSION

The changes in grain boundary structure and segregation discussed in 5.3 have been shown to result in a notable change in fracture behaviour. The presence of Y_2O_3 results in a consistent transgranular fracture path regardless of the fracture method used to cause the failure; various examples of this change in failure mode from the experiments conducted in 6.1 can be seen in Figure 103, Figure 111 and Figure 115. In order to produce a shift in failure mode of this fashion the relative energy required to fracture along grain boundaries, when compared to fracturing through the grains themselves, must be sufficiently high to make transgranular fracture the preferential option. SEM-EDX suggests that negligible quantities of silicon or yttrium are present within the abnormal grains, and as such it is unlikely that the energy required for a crack to pass through the bulk alumina has changed from its value in unmodified alumina. In order to achieve the failure path seen in Al_2O_3-SiC-Y_2O_3, therefore, the grain boundaries seen on the borders of the abnormal grains in Al_2O_3-1wt.%SiC-Y_2O_3 must possess a force deflecting the crack away from the grain boundary into the grain itself. In alumina-silicon carbide nanocomposites, *Jiao et al.*, attributed the change in failure mode, and the formation of transgranular cracks, to the deflection of a crack from the grain boundary upon its collision with a silicon carbide particle lying on the same grain boundary [89]. This work also found that once the crack is within a grain, silicon carbide particles do not cause significant deflection of the crack direction as it already lies along the direction of average crack propagation. As the mullite particles created in this work possess a similar distribution along both grain boundaries and intragranularly to the silicon carbide nanocomposite in the work of *Jiao et al.* it is likely that the same mechanism is operating to cause the formation of transgranular cracks during failure. The shift in failure mode has been widely attributed as a cause of both strengthening and toughening in hot pressed Al_2O_3-SiC nanocomposites [6, 89, 102-104], even if it is not the sole strengthening method observed, and so it is likely a similar effect is present in the alumina-mullite composites studied here.

6.2.1 Hardness

Both macroscopic Vickers hardness and microhardness testing show a trend of increasing hardness and modulus with decreasing Y_2O_3 content. This may be due to the mean grain size of the composite decreasing. However, there is a flaw with this argument as the sole explanation for the increasing properties: the behaviour of the composite under nanoindentation. Indentations that took place entirely within abnormal grains showed a statistically significant increase in modulus from samples of Al_2O_3-1wt.%SiC-500ppmY_2O_3 to Al_2O_3-1wt.%SiC-100ppmY_2O_3 as is shown in Figure 107. These indentations should be under nearly identical conditions, as the grain boundaries affecting these indents possess the same composition and therefore properties for the reasons discussed in 5.3.1. This testing showed an increase in modulus for samples containing 100ppm Y_2O_3 under each indentation environment when compared to the equivalent condition in samples containing 500ppm Y_2O_3, as is shown in Figure 107. The increased modulus seen here may be due to a different resultant distribution of mullite grains within the abnormal grains. SEM-EDX mapping of silicon in samples containing 100ppm Y_2O_3 shows a distribution containing smaller mullite particles more finely spaced throughout the abnormal grains, 5.1.2.3.2, when compared to samples manufactured with 500 or 1000ppm Y_2O_3. In hot pressed Al_2O_3-SiC nanocomposites [80] and Al_2O_3-mullite composites [106, 107] the inability of dislocations to pass through the SiC particles prevent their movement through the material. It is likely that the same effect is manifesting, as the Al_2O_3-SiC-Y_2O_3 composites produced in this work have a similar structure of distinct grains within larger alumina grains. The maximum stress required for a dislocation to bow between 2 pinning particles is given by the Orowan stress in the form [239]:

$$\sigma_{orowan} = \frac{\alpha \mu b}{L}$$

where α is a numerical constant, μ is the shear modulus of the bulk material, b is the Burges vector of the bulk material and L is the particle spacing. As $\alpha\mu b$ is a constant for the alumina matrix, the stress required to overcome the pinning effect is inversely proportional to the particle spacing. For

indentations of known consistent depth produced in nanoindentation testing, this results in the measured modulus being inversely proportional to particle spacing. Using the quantities and sizes of mullite grains found in 5.1.2.4 and the formula for interparticle distances, τ [240]:

$$\tau = d\left(\left(\frac{\pi}{6\varphi_P}\right)^{\frac{1}{3}} - 1\right)$$

where d is the mean particle diameter and φ_p is the volume fraction of the material composed of the particles, it would be predicted that Al_2O_3-1wt.%SiC-100ppmY_2O_3 would have a modulus 70% higher than Al_2O_3-1wt.%SiC-500ppmY_2O_3. The actual increase is significantly lower than this, which suggests that the mullite particles do not completely pin the movement of dislocations but merely retard their progress.

6.2.1.1 The Effect of Indentation Load

A notable distinction between the hardness measurements taken under Vickers hardness measurements with a 5 kg load and nanoindentations conducted with loads of less than 400 mN can be easily seen. Samples of Al_2O_3-1wt.%SiC-100ppmY_2O_3 sintered for 4 hours at 1550^{O}C possessed a higher Vickers hardness than alumina when tested under loads of 5 kgf but a lower hardness when tested using nanoindentation. This comparison is shown in Figure 116. Under Vickers hardness indentations Al_2O_3-1wt.%SiC-100ppmY_2O_3 possessed a hardness 10% higher than pure alumina, however the inverse is the case under nanoindentation tests. While the discrepancy in average hardness value seen between the two

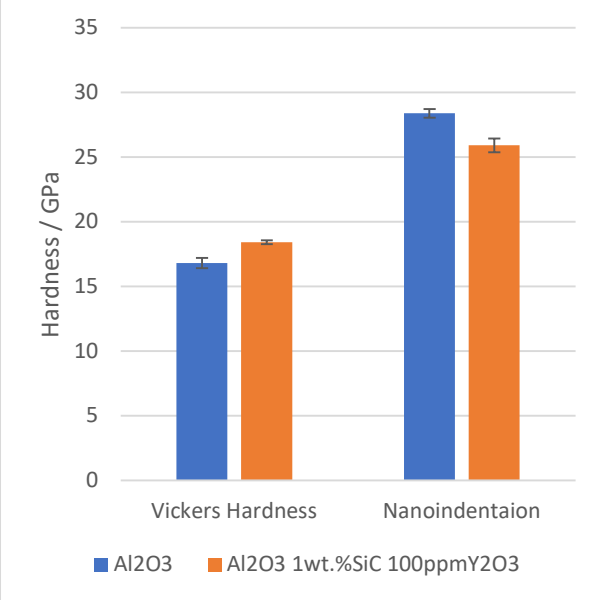


Figure 116: Graph showing the comparison between the measured hardness in both Al_2O_3 and Al_2O_3-1wt.%SiC-100ppmY_2O_3 sintered for 4 hours at 1550^{O}C under different hardness testing methodologies.

testing methods can be explained through the indentation size effect described in 2.7.1, the inversion in which material has the higher measured hardness cannot be explained in this fashion. This phenomenon can only be explained through a difference in material behaviour surrounding the indentations. Microscopy around the site of any nanoindentations made does not show any cracking. This suggests the indentation is made through purely plastic deformation of the ceramic. Deformation in this fashion is typically seen in ceramics under nanoindentation [158, 163]. Therefore, the pure alumina must possess a higher modulus when plasticly deforming prior to fracture. Conversely, the larger Vickers hardness indentation requires the formation of cracks surrounding the indentation to produce the required deformation. The shift in failure mode, from intergranular seen in Al_2O_3 to the transgranular failure seen in Al_2O_3-1wt.%SiC-100ppmY_2O_3, discussed above in 6.2, therefore causes a higher measured hardness than in pure alumina. This is due to the strengthening effect that results from the shift in failure mode increasing the energy required to form the cracks and thus the total force required to form an indentation of any given size if material cracking is required.

6.2.2 Toughness

As the mullite particles in Al_2O_3-SiC-Y_2O_3 are distributed at least partially throughout the large alumina grains, thermal expansion based toughening due to differences in expansion coefficient is present in a similar fashion to that discussed in 2.4.3.1. However, the final toughness value calculated in Al_2O_3-1wt.%SiC-100ppmY_2O_3, while higher than Al_2O_3, was not significantly different. The thermal expansion toughening effect must still be present, as Al_2O_3-SiC-Y_2O_3 results in a distribution of mullite grains within larger alumina grains and possesses a lower thermal expansion coefficient than alumina. This creates a stress field around the mullite grains which inhibits the progression of cracks through the material. Additionally, the deflection of cracks away from grain boundaries, as proposed by *Jiao et al.* [89], has been shown to increase overall toughness in similar composites, with the transition from intergranular fracture to transgranular fracture resulting in a 58% increase in fracture toughness in SiC-whisker reinforce alumina compared to pure alumina [103].

Therefore, this effect must be countered by a decrease in toughness from another source. Crack bridging and friction between the two crack surfaces likely increased fracture toughness in the intergranular failure of Al_2O_3 in a way not seen in the significantly less deflected crack path seen in Al_2O_3-SiC-Y_2O_3, however this effect must be present in the hot-pressed alumina-silicon carbide nanocomposites considered in the previous work in 6.2.

	Thermal Expansion Coefficient / 10^{-6} $^{O}C^{-1}$
Al_2O_3	8.4 [241]
SiC	4.0 [242]
Mullite	5.4 [243]

Table 5

A key distinction between silicon carbide and mullite are the thermal expansion coefficients seen. For comparison the thermal expansion coefficients are shown in Table 5. The difference between the expansion coefficients in alumina-silicon carbide is greater than in the alumina-mullite material produced in this work. This will result in a smaller generated stress field and therefore a smaller toughening effect, potentially explaining the measured toughness in Al_2O_3-1wt.%SiC-100ppmY_2O_3 being only slightly higher than unmodified Al_2O_3. Additionally, mullite [244] has a significantly lower Young's modulus than either alumina [66] or silicon carbide [244] and so likely has a negative effect on the overall toughness of the composite due to the proportional relationship between fracture toughness and the square root of Young's modulus.

6.2.3 Strength

In many ceramics, including Al_2O_3 [245], strength has been shown to be inversely proportional to the square root of the average grain size due to the Hall-Petch effect [246]. Plotting this relationship for the samples tested in 6.1.5.1, results in a plot which does not show this relationship, Figure 117. This appears to show a peak in the relationship when measured using the normal grain size suggesting the Hall-Petch effect is not valid in these materials. However, when abnormal grain size is measured in those materials that develop abnormal grains, and normal grain size in materials that do not grow abnormally, a trend that does follow the Hall-Petch effect can be seen, with materials displaying the highest strength possessing the smallest grain size. This suggests the abnormal grains dominate the

strength of the resultant macroscopic material and the change in failure mode seen in Al_2O_3-1wt.%SiC-100ppmY_2O_3 does not provide enough of a strengthening effect in this material to overcome the effect of the larger abnormal grains.

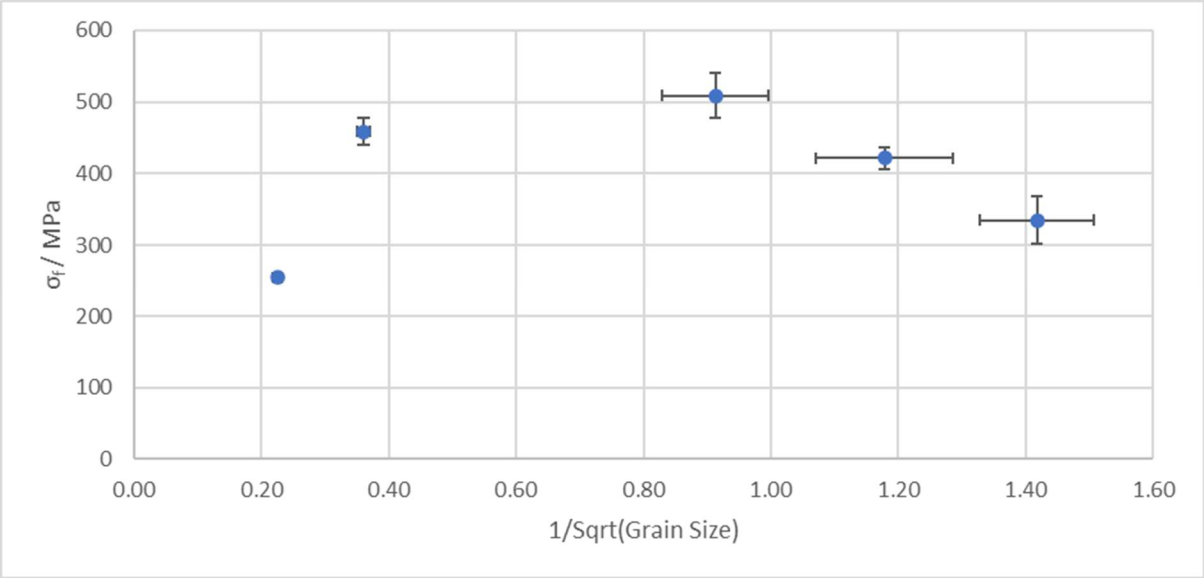


Figure 117: Graph showing the relationship between the strength of the materials tested under 3-point bend testing and the measured normal grain size in the same materials.

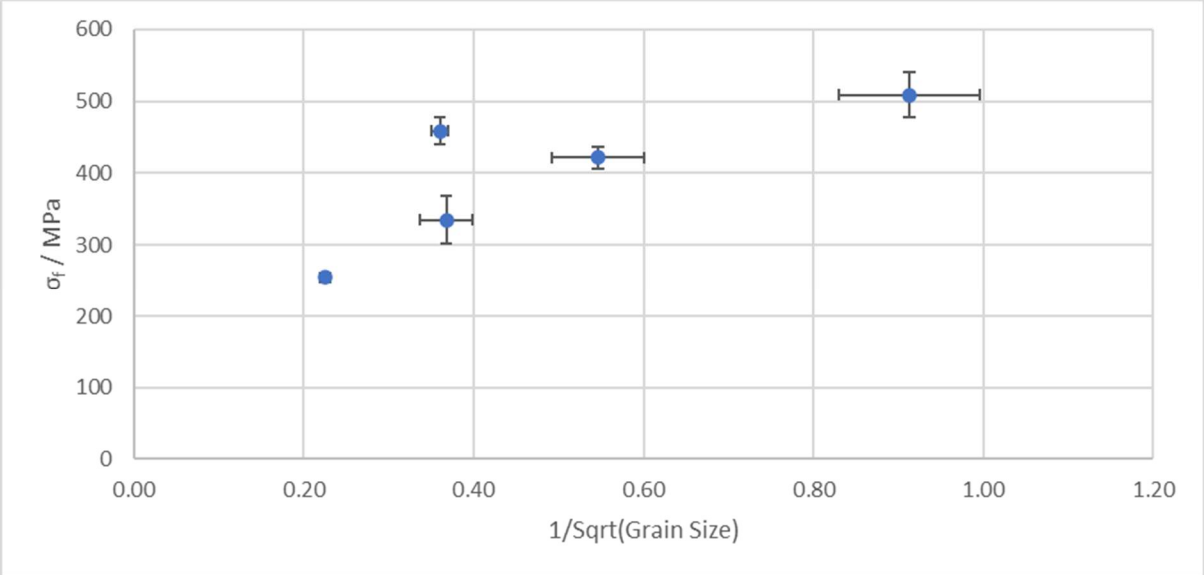


Figure 118: Graph showing the relationship between the strength of the materials tested under 3-point bend testing and the measured abnormal grain size in the same materials.

In Figure 118, 2 of the measured samples possess very similar grain sizes but notably different

strengths, these are Al_2O_3 and Al_2O_3-1wt.%SiC both sintered for 4 hours at 1550 ^{O}C. The lower strength seen in the sample containing silicon carbide is likely due to the higher porosity seen in this material [247, 248], as Al_2O_3-1wt.%SiC possessed a final density of only 95.0% compared to the density of over 99% achieved in pure Al_2O_3.

6.2.4 Weibull Modulus

There is a difference in Weibull modulus between Al_2O_3-SiC-Y_2O_3 and pure Al_2O_3. Therefore, failure in Al_2O_3-SiC-Y_2O_3 must behave in a more consistent fashion as it possesses a higher Weibull Modulus as discussed in 6.1.5.2. The most obvious manifestation of this is the change in failure mode noted above. Cracks in Al_2O_3 deflect significantly along grain boundaries resulting in a crack path with an inconsistent length and therefore local variations in toughness. Comparatively, failure in Al_2O_3-SiC-Y_2O_3 follows a far more consistent failure path owing to its transgranular nature. This is likely not the sole explanation for the improved Weibull modulus, as the lower density in Al_2O_3-SiC-Y_2O_3 samples was shown above to result in more visible fine porosity alongside the large pores. This results in a more even distribution of initial flaws and therefore a more consistent initial failure.

6.2.5 Wear Resistance

In hot-pressed alumina-silicon carbide composites, the transition from intergranular to transgranular failure resulted in a significant increase in wear resistance compared to unmodified alumina [249]. This is due to the difference in pullout formation upon encountering a grain boundary. When intergranular failure dominates, the crack path can extend around one or more grain boundaries leading to a large volume of material being pulled out. Conversely, in the case of transgranular failure, the effect of a grain boundary is far less prominent, and a small volume of material is removed regardless of the presence of a grain boundary. This is shown schematically in Figure 119.

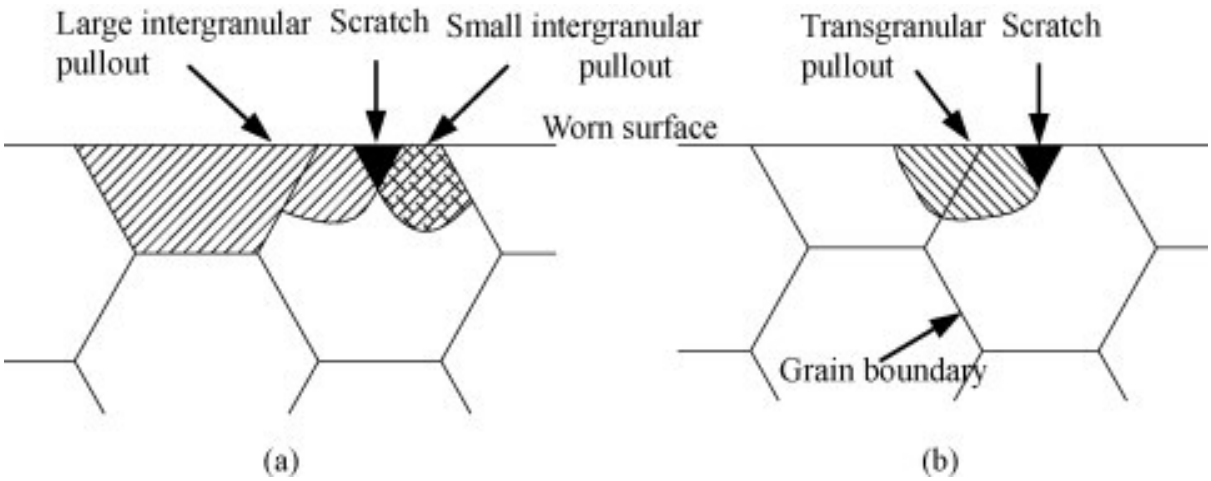


Figure 119: Schematic showing the effect of a) intergranular and b) transgranular failure mode on the volume of pullout during wear. [249]

The same change in failure mode has been seen in Al_2O_3-SiC-Y_2O_3 manufactured in this work and this is reflected in the wear scars shown in Figure 111. However, the accompanying wear resistance measurements do not display the expected improvements from the change in failure mode as seen in hot-pressed alumina-silicon carbide composites. This is potentially due to a combination of the large abnormal grains in the Al_2O_3-SiC-Y_2O_3 composite reducing the benefit seen due to the change in failure mode in this test environment and the lower overall strength seen in this composite. The lowest wear resistance measured in this work being measured in alumina-mullite composites follows this explanation as well as it displays the same abnormal grain growth as Al_2O_3-SiC-Y_2O_3 but a lower strength resulting in a lower overall wear resistance.

6.3 High Speed Impact Testing

6.3.1 Results

High speed impact testing was conducted on Al_2O_3-1wt.%SiC-100ppmY_2O_3 sintered at 1550^{O}C for 4 hours, Al_2O_3 sintered at 1550^{O}C for 4 hours and Al_2O_3 sintered at 1400^{O}C for 1 hour using the method described in 4.4.6. While testing was conducted using ball bearings of differing sizes all the following results are presented from experiments conducted using 2 mm projectile.

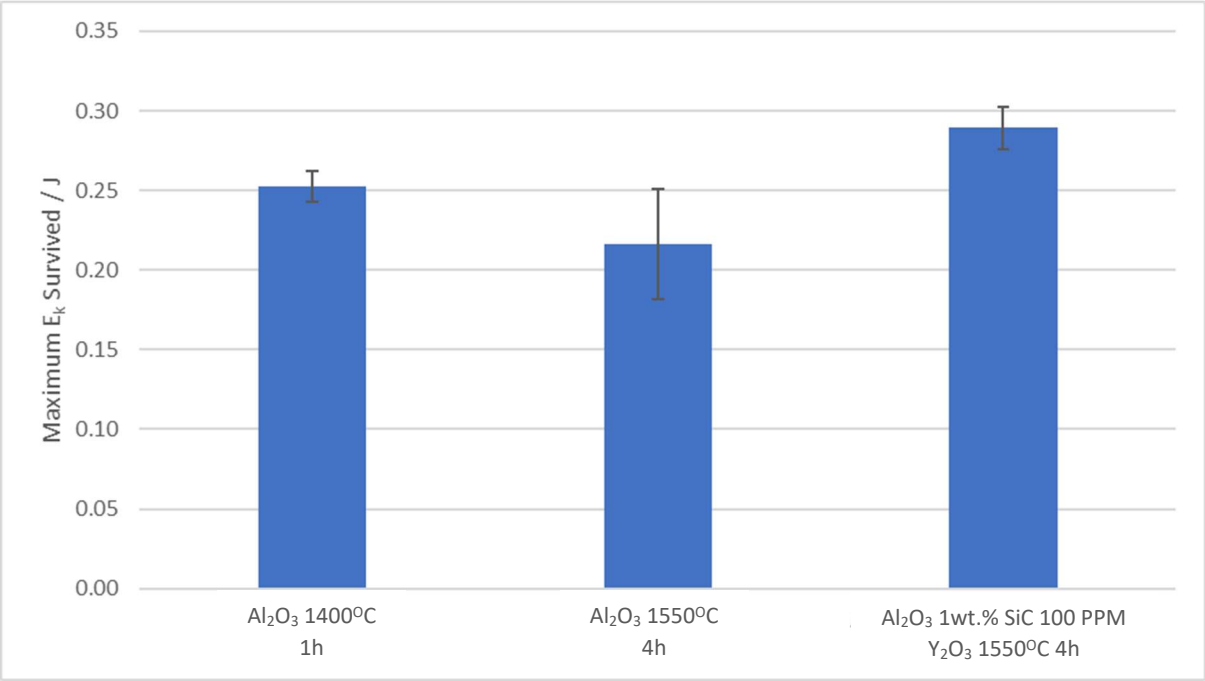


Figure 120: Graph showing the maximum particle kinetic energy survived in samples manufactured from Al_2O_3 sintered for 1h at 1400 ^{O}C, Al_2O_3 sintered for 4h at 1550 ^{O}C and Al_2O_3-1wt.%SiC-100ppmY_2O_3 sintered at 1550 ^{O}C for 4 hours.

Al_2O_3-1wt.%SiC-100ppmY_2O_3 sintered at 1550 ^{O}C for 4 hours showed an improvement of 14 % in the maximum energy survived compared to Al_2O_3 sintered at 1400^{O}C or 34 % compared to Al_2O_3 sintered at 1550^{O}C, as can be seen in Figure 120.

After complete failure, the difference in kinetic energy in the ball bearing was measured and consequently the amount of energy used in fracture calculated according to the calculation described

in 4.4.6. The results of this calculation are shown in Figure 121. Al_2O_3-1wt.%SiC-100ppmY_2O_3 sintered at 1550^{O}C for 4 hours showed an improvement of 7 % in the maximum energy survived compared to Al_2O_3 sintered at 1400 ^{O}C or 25 % compared to Al_2O_3 sintered at 1550 ^{O}C.

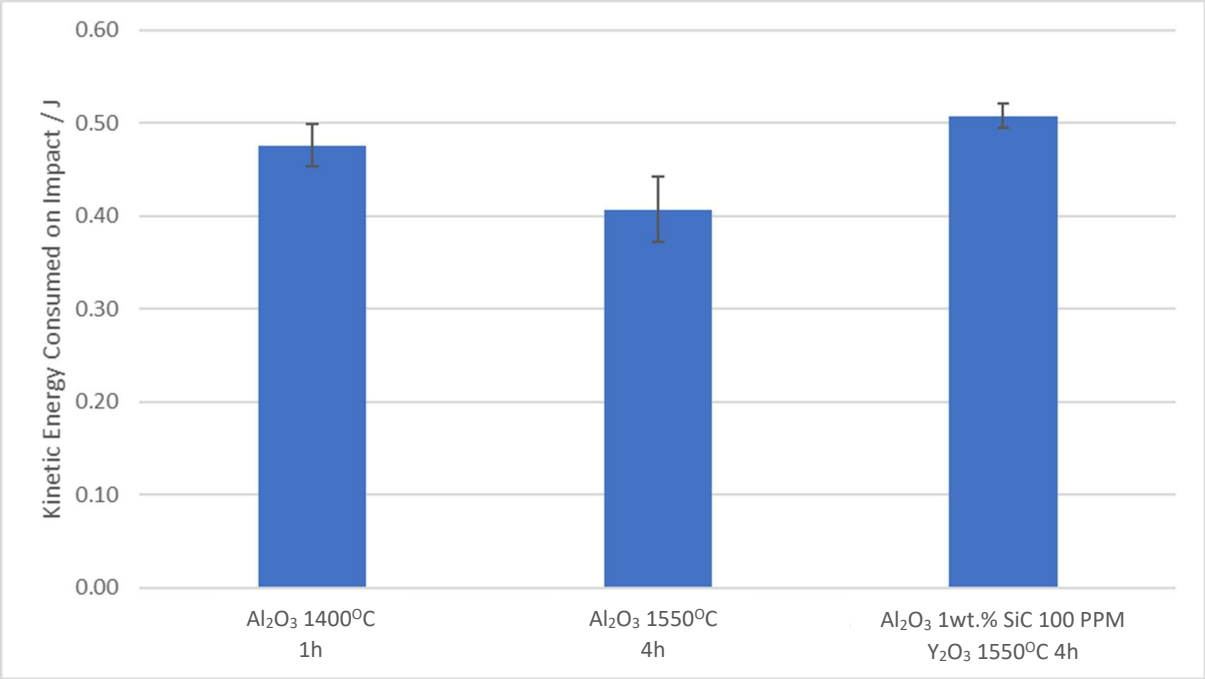


Figure 121: Graph showing the change in kinetic energy of the impacting ball bearing after fracture of samples manufactured from Al_2O_3 sintered for 1h at 1400 ^{O}C, Al_2O_3 sintered for 4h at 1550 ^{O}C and Al_2O_3-1wt.%SiC-100ppmY_2O_3 sintered at 1550 ^{O}C for 4 hours.



Figure 122: Photo showing a side angle of the cone crack formed after failure of Al_2O_3-1wt.%SiC-100ppmY_2O_3.

High speed videography of the impact shows a difference in failure pattern with failure. Al_2O_3-1wt.%SiC-100ppmY_2O_3 fails through a combination of radial cracking and the formation of a cone crack. Examples of the resultant cone are shown in Figure 122 and Figure 123. Measurements of the cone around the tip show

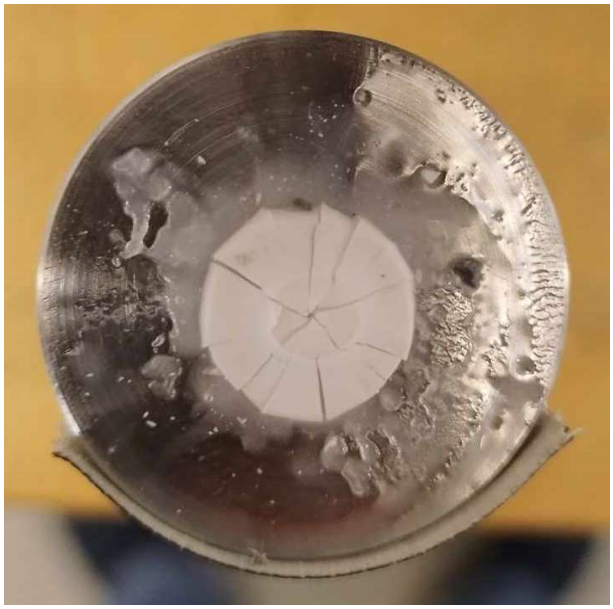


Figure 123: Photo showing the resultant cone after failure in Al_2O_3-1wt.%SiC-100ppmY_2O_3 once the surrounding section has been removed.

it fractured at angle of 41±1^{O} from the original surface of the sample. Comparatively, both alumina samples tested failed entirely through radial cracks. Al_2O_3-1wt.%SiC-100ppmY_2O_3 also showed a far higher quantity of radial cracks forming compared to pure alumina. These differences can both be seen in Figure 124.

Microscopy of the fracture surfaces produced in the impacts shown in Figure 124 show the same difference in structure seen in 6.1.5.3. Fracture surfaces produced along the radial cracks in Al_2O_3 show significant faceting regardless of sintering conditions indicative of intergranular fracture. The equivalent fracture surfaces in Al_2O_3-1wt.%SiC-100ppmY_2O_3 do not display faceting in the same fashion, and instead fail in a transgranular manner. This comparison is shown in Figure 125.

a) b)

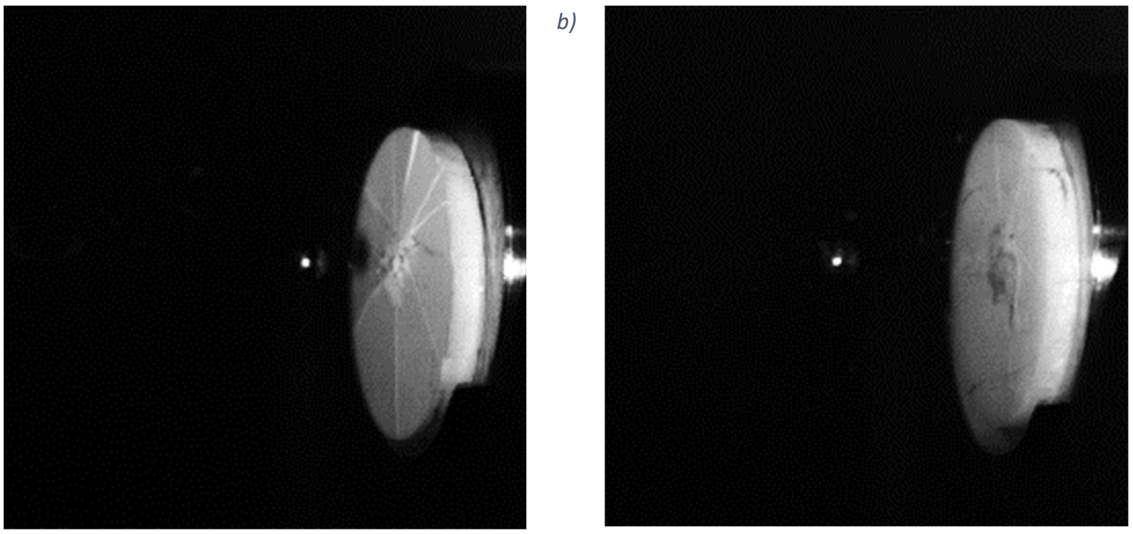


Figure 124: still frames from immediately after impact in high-speed testing showing the difference in radial cracking between a) Al_2O_3-1wt.%SiC-100ppmY_2O_3 sintered for 4 hours at 1550 ^{O}C and b) Al_2O_3 sintered for 4 hours at 1550 ^{O}C.

a) b)

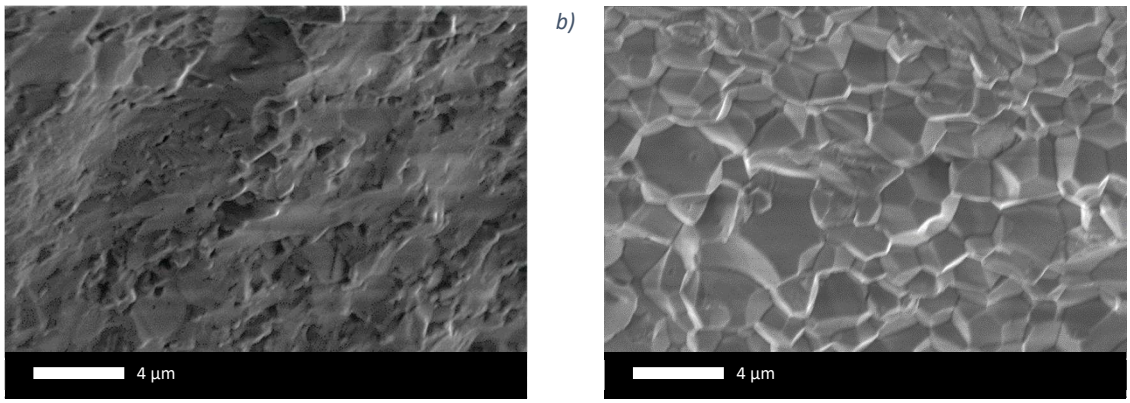


Figure 125: Micrographs showing the fracture surfaces in radial cracks created after failure in a) Al_2O_3-1wt.%SiC-100ppmY_2O_3 sintered for 4 hours at 1550 ^{O}C b) Al_2O_3 sintered for 4 hours at 1550 ^{O}C.

Microscopy of the surface of the cone cracks produced show the cracks are transgranular, similar to the radial cracks in Al_2O_3-1wt.%SiC-100ppmY_2O_3 shown in Figure 125. This trend continues regardless of location on the surface of the cone crack and an example of this surface is shown in Figure 126.

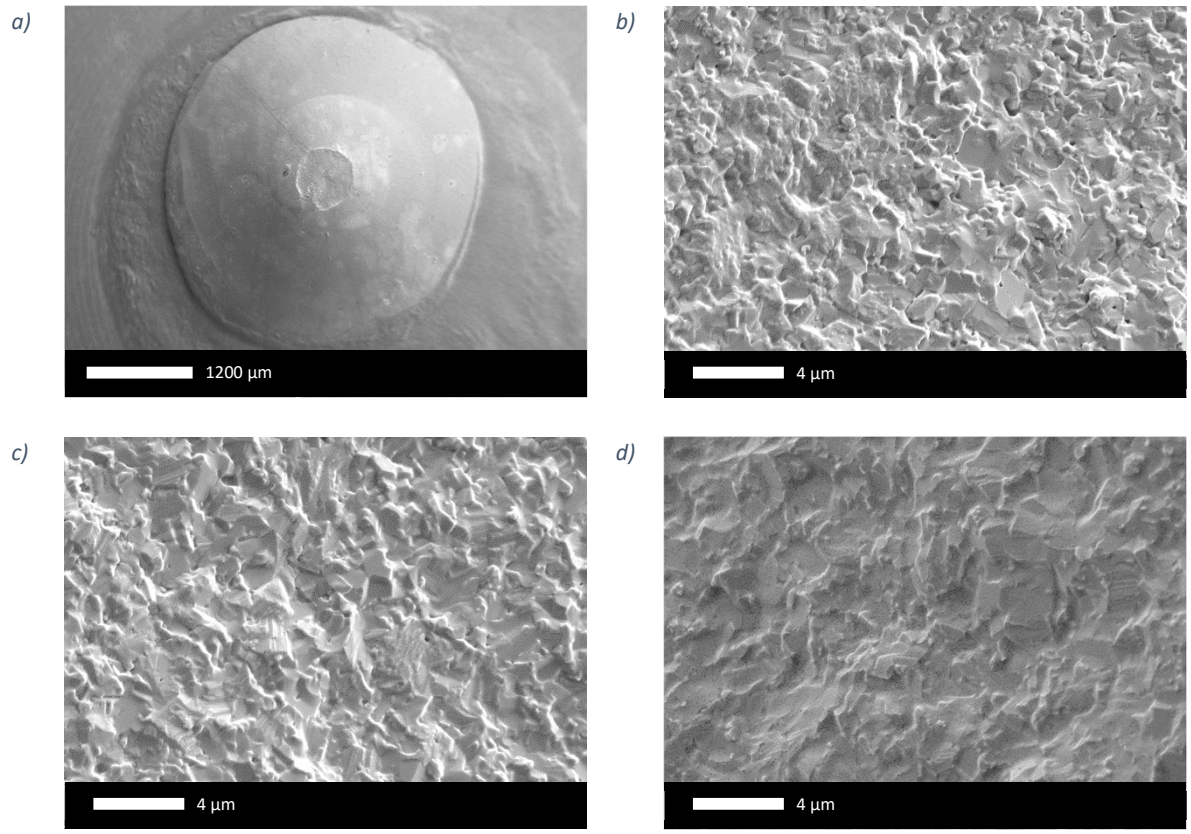


Figure 126: Micrographs showing the fracture surfaces in cone cracks created after failure in Al_2O_3-1wt.%SiC-100ppmY_2O_3 sintered for 4 hours at 1550 ^{O}C, showing a) the whole tip of the cone and b) a higher magnification detailed area above the halfway mark of the slope of the cone crack c) a higher magnification detailed area below the halfway mark of the cone cracks slope d) a higher magnification detailed area on the slope of the cone crack taken from a larger segment that broke away from the surface.

Microscopy of samples that have received an impact but not fractured show the formation of some surface cracking without total failure. These cracks have only been found in samples subjected to the highest impact velocities without failure. An example of these cracks are shown in Figure 127 alongside details of the interior fracture surface.

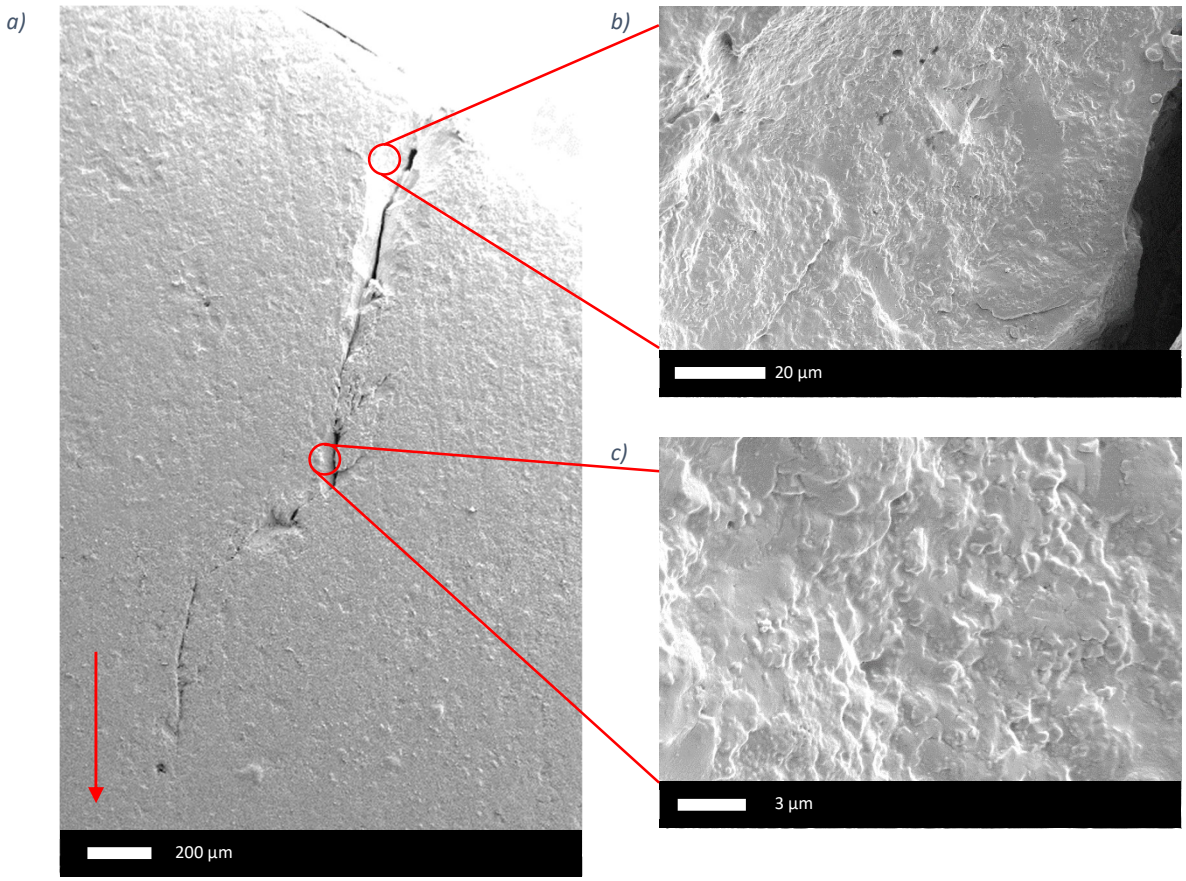


Figure 127: SEM images showing surface cracking in Al_2O_3-1wt.%SiC-100ppmY_2O_3 sintered for 4 hours at 1550 ^{O}C after high-speed impact without complete failure. The point of impact is below the micrograph in the direction of the red arrow in image a.

6.3.2 Discussion

High speed impact testing of Al_2O_3 and Al_2O_3-SiC-Y_2O_3 shows a notable difference in the failure patterns of the two materials: the presence, or absence, of cone cracks. Al_2O_3-SiC-Y_2O_3 clearly produces a cone crack upon failure, an example of which can be seen in Figure 122. Al_2O_3 fails by radial cracking in this testing. The formation, or lack thereof, of cone cracks is controlled by the balance between Hertzian fracture and plastic deformation [211, 250]. This plastic region tends to form in materials that fail in a fashion that produces some crack bridging or internal friction such as sliding grains or the presence of whiskers. Imaging of the cracks created by high-speed impacts clearly shows that for a given ceramic there is no difference in crack path between those created through quasi-static methods such as Vickers hardness testing and those created due to high-speed impacts. This suggests the crack deflection seen in pure Al_2O_3 has allowed for the formation of a plastic zone that dominates the failure under ballistic impact. *Dancer et al.* [211] showed that the relative strengths, and prevalence, of Hertzian failure and plastic deformation are linked to the angle of cone cracks formed. Previous work had shown that under purely brittle failure a very wide cone crack with an initial crack direction of between 22^O and 24^O is formed [251], an ideal, elastic cone crack. In the case of plastic deformation dominated failure, the initial crack forms at an angle of 90^O to the material surface and what appears as a radial cracks form without the central cone. This is what is seen in the failure of Al_2O_3. When the effects are balanced, however, a cone crack with an angle between the two extremes of 90^O and 22^O is formed. This is the case for the 41 ± 1^O angle seen in Al_2O_3-SiC-Y_2O_3 implying that, while brittle Hertzian failure is now present to such an extent as to cause a reasonably wide cone crack, the formation of a plastic zone prior to cracking has not been entirely eliminated. This is likely somewhat beneficial for the resultant properties of the Al_2O_3-SiC-Y_2O_3 material, as the properties of crack propagation that lead to the formation of the plastic zone tend to also result in macroscopic toughness. The formation of cone cracks also improves ballistic properties through 2 factors. The wider area encompassed on the back of the material by the cone crack acts to spread the impact force

out over a larger area. Secondly, the material within the cone crack erodes the projectile, as it breaks apart.

The increased energy consumed on failure by Al_2O_3-SiC-Y_2O_3 samples, when compared to Al_2O_3 samples sintered at either 1400^{O}C or 1550^{O}C, can be explained through the difference in failure behaviour under high-speed impacts described above. Al_2O_3-SiC-Y_2O_3 formed both a highly fractured cone crack, an example of which can be seen in Figure 123, and a high number of radial cracks, as can be seen in the frames taken from the video of the impact in Figure 124.a, which shows the formation of nine distinct radial cracks. Comparatively, pure alumina samples fractured without the formation of a cone crack at all and tended to fracture into either two or three segments upon failure due to impact. The example in Figure 124.b fractured into three pieces. As both Al_2O_3-SiC-Y_2O_3 and Al_2O_3 possess a similar fracture toughness when sintered for 4 hours at 1550^{O}C, the significantly larger area of fracture surface produced in Al_2O_3-SiC-Y_2O_3 under high-speed impact is the cause of the increased energy consumed during fracture. An interesting distinction between the failure modes is the number of segments samples fracture into. This may be due to the lower relative density of Al_2O_3-SiC-Y_2O_3 compared to either of the Al_2O_3 samples tested resulting in a higher density of flaws. In other materials this has been shown to activate multiple smaller flaws upon impact rather than a single large flaw [27] and this activation of multiple flaws simultaneously lead to a larger quantity of cracks spidering out radially from the point of impact and the forming cone crack.

The improved kinetic energy withstood before failure is caused by a combination of factors, as no single property offers an exclusive understanding of this testing environment. As was discussed in 2.1.6.1, material hardness can result in a significant improvement in ballistic properties due to projectile blunting and mass loss [4] and this effect likely plays a role in the improvement of the high-speed impact properties of Al_2O_3-1wt.%SiC-100ppmY_2O_3 over alumina, with both a fine grained microstructure, 1400^{O}C sintering, and alumina manufactured under the same sintering conditions. Additionally, it appears Al_2O_3-SiC-Y_2O_3 may possess a higher flaw density, and this has been shown to

result in an improvement in ballistic performance due to the greater area of new surface created during failure [39]. The higher density of flaws also results in a crack being more likely to be present to initiate the cone cracking seen above.

Actual ballistic loads will impact the ceramic at far faster velocities with a higher weight impacting particle. This results in a different impact condition to those studied during this section and the higher speed impact results in the generation of more shock in the sample. The higher speed also allows for the interaction between shockwaves reflected off the outer surface of the sample that have been generated during the first impact unless significantly larger samples are tested allowing for the impacting particle to be entirely defeated before the waves return from being reflected of the outer limits of the sample.

7 SUMMARY

1. Alumina mullite Composites

    - This work investigated the resultant mechanical properties of alumina-silicon carbide composites when sintered under atmospheric pressure in air.
    - This resulted in an alumina matrix composite with mechanical properties almost universally worse than alumina sintered under the same conditions.
    - Silicon carbide was shown to have oxidised at below the sintering temperatures used and reacted to form mullite particles when dispersed in alumina as is the case in this work.
    - The presence of mullite also served to significantly hinder sintering in a similar fashion to what is seen in alumina-silicon carbide nanocomposites. As a result of this, alumina-mullite composites possessed a maximum density of around 95%.

2. The Microstructure of Alumina-mullite-yttria Composites

    - The addition of yttria in quantities of 1000 ppm or lower, resulted in the alumina-mullite-yttria composite sintering to a density of 98%.
    - This increase in density is not seen at sintering temperatures below 1550^{O}C.
    - At these temperatures, abnormal grain growth consumes a significant percentage of the overall microstructure. The fraction of the overall microstructure consumed by abnormal grain growth was measured to be proportional to the quantity of yttria initially added.
    - SEM-EDX mapping of the materials sintered at these temperatures showed the abnormal grains contained mullite particles distinct from the surrounding alumina matrix. Transmission electron microscopy analysis of these particles through both

STEM-EDX and diffraction confirmed that they are formed of mullite with an estimated composition of $1.8Al_2O_3{\cdot}SiO_2$.

- Grain boundaries were analysed to compare the composition between the boundaries in the normal and abnormal grains. Both types of grain boundaries showed a silicon excess of 140 silicon atoms per square nanometer, but the boundaries of abnormal grains showed an additional excess of 0.9 yttrium atoms per square nanometer. Comparatively, the border in normal grains showed an excess of only 0.09 yttrium atoms per square nanometer.

3. Macroscopic and Mechanical Properties of Alumina-mullite-yttria Composites
    - Alumina-mullite-yttria composites showed transgranular failure through the abnormal grains. Comparatively, pure alumina samples that failed under similar testing showed failure exclusively along grain boundaries.
    - Testing of varying compositions showed that lower quantities of yttria additions, down to the lowest tested value of 100 ppm Y_2O_3, resulted in a higher measured Vickers hardness and modulus. This behaviour was linked to the finer distribution of mullite particles seen in samples containing lower quantities of yttrium additives.
    - The improvement in mechanical hardness is only seen when loads sufficient to cause cracking are used to make the hardness measurements.
    - Alumina-mullite-yttria composites did not display a significant improvement in fracture toughness over unmodified alumina. As mullite has a different thermal expansion coefficient to alumina, thermal expansion toughening is present. Therefore, the change in failure mode and relative increase in porosity must be reducing fracture toughness.
4. High Speed Impact Testing

- Under impacts, alumina fractures radially into a small number of segments. This is due to the deflection of cracks along grain boundaries leading to the formation of 'quasi-plastic' deformation.
- Alumina-mullite-yttria composites fractured under the same conditions produced a cone crack alongside the same radial cracks as seen in the pure alumina. Therefore, Hertzian failure has occurred in this material.
- As the cone crack has an angle of around 40^{O}, a combination of Hertzian failure and 'quasi-plastic' deformation has occurred.
- Alumina-mullite-yttria composites consumed more energy on failure and required more projectile energy before failure occurred than unmodified alumina.

8 CONCLUSIONS

The addition of mullite resulted in a significant reduction in density and grain size compared to alumina sintered under the same conditions. However, the addition of yttria to alumina-mullite composites resulted in a significant change in microstructure from the undoped material. Alumina-mullite-yttria composites comparatively produced a material with a relative density in excess of 98% alongside significant grain growth. This material also displayed abnormal grain growth, with the quantity of proportional to the quantity of yttria added. Alumina-mullite-yttria composites produced in this work had a microstructure consisting of mullite grains within the larger abnormal alumina grains along with some mullite grains located on alumina grain boundaries. This closely reflected the microstructure seen in hot-pressed alumina-SiC nanocomposites which has been reported to offer significant mechanical benefits [85, 88, 89]. The growth of abnormal grains was found to be facilitated by the presence of yttrium exclusively on the grain boundaries of abnormal grains, while equal quantities of silicon were found to decorate the boundaries of all the alumina grains studied.

The similarity in microstructure between the alumina-mullite-yttria composites produced in this thesis to that seen in alumina-SiC nanocomposites extended to their behaviour in mechanical testing. The best performing alumina-mullite-yttria composite possessed a hardness and modulus than alumina without any dopants when tested under Vickers hardness conditions. This was attributed to the shift in failure mode seen in alumina-mullite-yttria composites from intergranular to transgranular cracks as a similar shift had been shown to improve hardness in alumina-SiC composites [6, 102]. When testing was conducted under nanoindentation, these cracks did not form, and the test yielded a higher hardness in pure alumina than the produced composite.The improvements in mechanical properties seen during mechanical testing resulted in a similar improvement in performance during gas gun testing. Alumina-mullite-yttria composites required a larger amount of energy before failure and consumed a larger amount of energy on failure than undoped alumina. This was also reflected in the formation of a cone crack and the larger number of segments the material fractured into upon impact.

9 FUTURE WORK

1. Hertzian Testing
    - Hard sphere indentations can produce ring cracks around the point of indentation. This is the same crack nucleation as was seen in the high-speed impacts in Al_2O_3-SiC-Y_2O_3 prior to the formation of the cone cracks. Repeated indentations of this kind allow for the distribution of initial flaws to be determined. This flaw size distribution may be the cause of the higher Weibull modulus measured in alumina-mullite-yttria composites.
2. Residual Stress Measurements
    - The residual stresses of the alumina-mullite and alumina-mullite-yttria materials due to the differing thermal expansion coefficients of alumina and mullite can be measured through the use of Raman spectroscopy. This has been shown to have a significant effect on the final material properties and may explain the difference in properties measured in this work from other work conducted into the alumina-silicon carbide system.
3. Crack Distribution Controls
    - Investigations into methods to control the distribution of initial cracks within the composite produced could result in more favourable failure conditions and better toughness and ballistic properties. This may be achievable through the inclusion of further additives that are designed to combust and be removed during sintering, such as graphene, however investigation into this possibility would require significant further work.
4. High Resolution TEM
    - Further TEM work could allow for direct imaging of the grain boundary structure in the various complexions found in Al_2O_3-SiC-Y_2O_3. This could allow for more specific characterisation of the grain boundaries, including the relative positioning of silicon

and yttrium atoms along the boundary, between two abnormal Al_2O_3 grains, one abnormal and one normal Al_2O_3 grain, and one mullite and one Al_2O_3 grain. In order to achieve this, multiple TEM lamellae would likely need manufacturing in order to obtain a grain boundary with a favourable misorientation between the neighbouring grains to allow for both grains to have a zone axis parallel to each other.

- Additional STEM-EDX work on samples manufactured containing different levels of yttria doping would allow for measurements of the yttrium content on the abnormal grain boundaries to confirm if the concentration of yttrium on grain boundaries is independent of the overall yttria content.

5. Optimum Al_2O_3-SiC-Y_2O_3 Composition

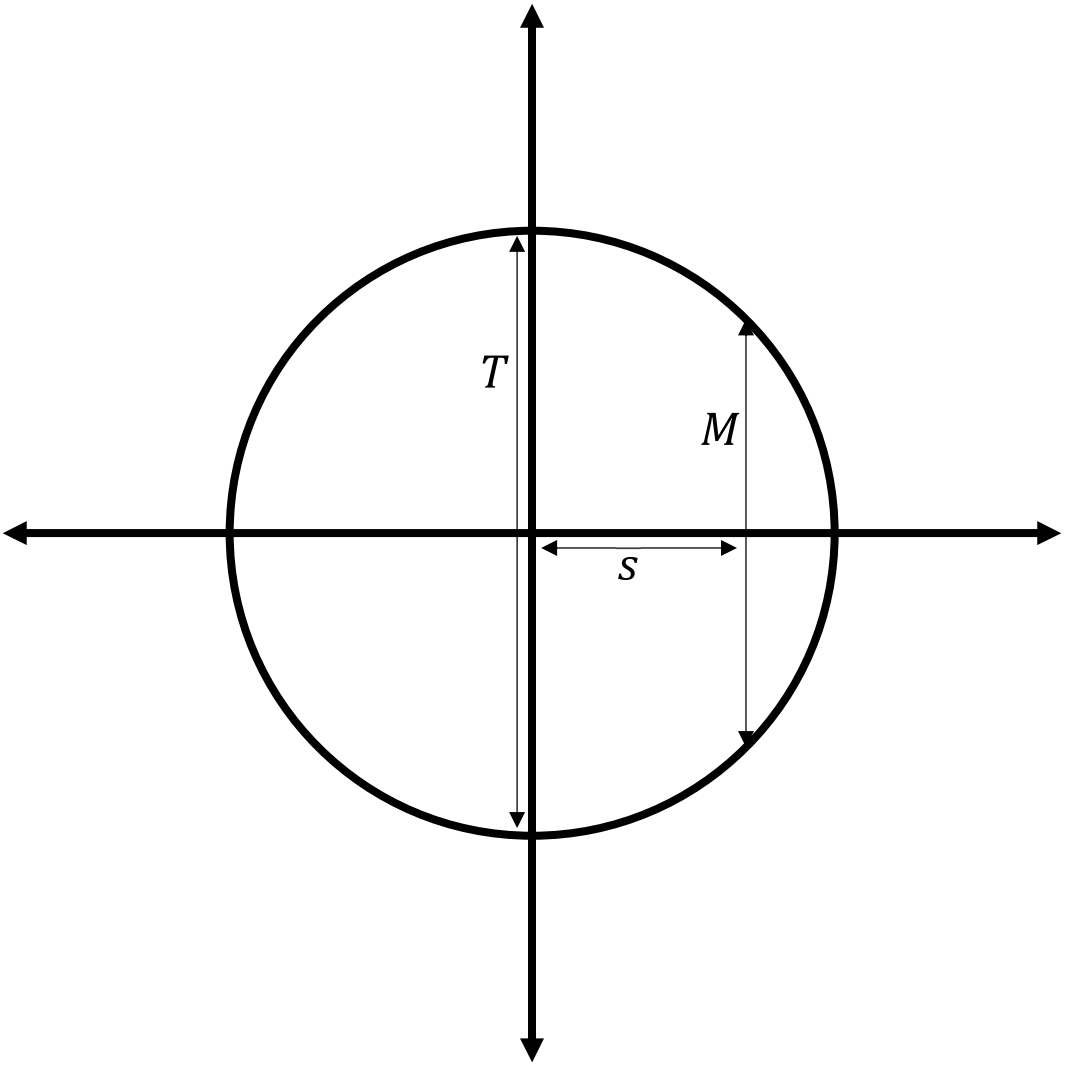
    - It has been shown that in metrics such as Vickers hardness, the lower this Y_2O_3 content added to Al_2O_3-SiC-Y_2O_3, the better the performance is measured. However, the performance of Al_2O_3-1wt.%SiC-100ppmY_2O_3 was better than the performance of either Al_2O_3 or Al_2O_3-1wt.%SiC. Therefore, there must exist an optimum composition of Al_2O_3-SiC-Y_2O_3 and sintering conditions to produce the best resultant performance. Further work would be required to identify this composition, but this project would be very time consuming due to the production time required in milling new powders and sintering large numbers of distinct samples.

6. Full Scale Ballistic Testing

    - Before any material investigated in this work can be considered for actual armour applications, full scale ballistic testing must be carried out. This work could not be carried out during this project as a sufficient number of samples of sufficient size for ballistic testing could not be manufactured. In order to perform ballistic testing, samples with a diameter of at least 8 cm are required. This requirement imposed two restrictions. The first of these is that investigations showed that without isostatic pressing during green body production the final composite produced had a

significantly lower density and worse mechanical properties. The CIP used in production had a diameter significantly smaller than this requirement, so samples could not be manufactured. The second restriction is due to the small-scale production of powder used. In order to manufacture sufficient samples to test in this fashion over 1 kg of material would be required per composition being tested. As production of powders was conducted in batches of 30 g and required multiple days this was not feasible within the timeframe of this project.

10 APPENDIX



The expected measured diameter, *M*, can be calculated as the integral of all diameters across the circle with diameter *T* multiplied by the probability of each individual slice taken.

$$\mathbb{E}[Measured\ Diameter]$$

$$= \int_{-\infty}^{\infty} \mathbb{E}[Measured\ Diameter | Cross\ Section\ at\ s] \mathbb{P}[Cross\ Section\ at\ s] ds$$

$$= \int_{-\frac{T}{2}}^{\frac{T}{2}} 2\sqrt{\left(\frac{T}{2}\right)^2 - s^2}\frac{1}{T} ds$$

$$= \int_{-\frac{T}{2}}^{\frac{T}{2}} 2\sqrt{\left(\frac{T}{2}\right)^2 - s^2} ds \frac{1}{T}$$

The integral here is equal to the area of a circle with diameter T which results in:

$$\mathbb{E}[Measured\ Diameter] = \pi\left(\frac{T}{2}\right)^2 \frac{1}{T} = \frac{\pi}{4}T$$

$$T = \frac{4}{\pi}M \approx 1.27M$$

Therefore, the true diameter is 1.27 times the average measured diameter.

11 BIBLIOGRAPHY

1. Vandiver, P., et al., *The Origins of Ceramic Technology at Dolni Vestonice, Czechoslovakia.* Science (New York, N.Y.), 1989. **246**: p. 1002-8.
2. Craig, O.E., et al., *Earliest evidence for the use of pottery.* Nature, 2013. **496**(7445): p. 351-354.
3. Shockey, D.A., et al., *Failure phenomenology of confined ceramic targets and impacting rods.* International Journal of Impact Engineering, 1990. **9**(3): p. 263-275.
4. Woodward, R.L. and B.J. Baxter, *Ballistic evaluation of ceramics: Influence of test conditions.* International Journal of Impact Engineering, 1994. **15**(2): p. 119-124.
5. Fakolujo, O.S., *Characterisation and properties improvement of armour ceramics*. 2016, Université d'Ottawa/University of Ottawa.
6. Borsa, C.E., et al., *Processing and properties of Al2O3/SiC nanocomposites.* Journal of Microscopy, 1995. **177**(3): p. 305-312.
7. Cantwell, P.R., et al., *Grain boundary complexions.* Acta Materialia, 2014. **62**: p. 1-48.
8. Dunstan, S., *Flak Jackets: 20th Century Military Body Armour*. 1984: Osprey Publishing.
9. Hazell, P.J., *Armour : materials, theory, and design*. 1st ed. 2015, Boca Raton: CRC Press.
10. Showalter, D.D., et al., *Ballistic testing of SSAB ultra-high-hardness steel for armor applications*. 2008, ARMY RESEARCH LAB ABERDEEN PROVING GROUND MD WEAPONS AND MATERIALS RESEARCH ….
11. Crouch, I.G., *Metallic Armor - form Cast Aluminum alloys to High-Strength Sheets.* Materials Forum, 1988. **12**: p. 31-37.
12. Yadav, R., et al., *Body armour materials: from steel to contemporary biomimetic systems.* RSC advances, 2016. **6**(116): p. 115145-115174.
13. Crouch, I., *The science of armour materials*. 2016: Woodhead Publishing.
14. Greaves, L.J., *Failure mechanisms in glass fibre reinforced plastic armour.* DRA Military Division Memorandum 12/92, 1992.

15. Crouch, I.G., *Do composites make good armour.* Composites Australia & the Composites CRC Annual Conference & Trade Show 2009, 2009.

16. Crouch, I.G., *Body armour – New materials, new systems.* Defence Technology, 2019. **15**(3): p. 241-253.

17. Rozenberg, Z. and Y. Yeshurun, *The relation between ballastic efficiency and compressive strength of ceramic tiles.* International Journal of Impact Engineering, 1988. **7**(3): p. 357-362.

18. Medvedovski, E., *Ballistic performance of armour ceramics: Influence of design and structure. Part 1.* Ceramics International, 2010. **36**(7): p. 2103-2115.

19. Medvedovski, E., *Ballistic performance of armour ceramics: Influence of design and structure. Part 2.* Ceramics International, 2010. **36**(7): p. 2117-2127.

20. LeGallic, C., et al. *A consideration of damage in the interaction between tungsten rod penetrators and ceramic materials*. in *16th International Symposium on Ballistics, San Francisco, CA, USA*. 1996.

21. Crouch, I. *Threat defeating mechanisms in body armour systems*. in *Next generation bosy armour conference*. 2009.

22. Domnich, V., et al., *Boron carbide: structure, properties, and stability under stress.* Journal of the American Ceramic Society, 2011. **94**(11): p. 3605-3628.

23. Subhash, G., et al., *Characterization of the 3-D amorphized zone beneath a Vickers indentation in boron carbide using Raman spectroscopy.* Acta Materialia, 2013. **61**(10): p. 3888-3896.

24. Chen, M., J.W. McCauley, and K.J. Hemker, *Shock-Induced Localized Amorphization in Boron Carbide.* Science, 2003. **299**(5612): p. 1563.

25. Ge, D., et al., *Structural damage in boron carbide under contact loading.* Acta Materialia, 2004. **52**(13): p. 3921-3927.

26. Roberson, C., et al. *The effective hardness of hot pressed boron carbide with increasing shock stress*. in *Advances in Ceramic Armor: A Collection of Papers Presented at the 29th*

International Conference on Advanced Ceramics and Composites, January 23-28, 2005, Cocoa Beach, Florida, Ceramic Engineering and Science Proceedings. 2005. Wiley Online Library.

27. Kaufmann, C., et al., *Influence of Material Properties on the Ballistic Performance of Ceramics for Personal Body Armour.* Shock and Vibration, 2003. **10**: p. 357637.
28. Hozer, L., J.-R. Lee, and Y.-M. Chiang, *Reaction-infiltrated, net-shape SiC composites.* Materials Science and Engineering: A, 1995. **195**: p. 131-143.
29. Leo, S., et al., *Near-net-shaping methods for ceramic elements of (body) armor systems.* Journal of the American Ceramic Society, 2014. **97**(10): p. 3013-3033.
30. Crouch, I.G., M. Kesharaju, and R. Nagarajah, *Characterisation, significance and detection of manufacturing defects in Reaction Sintered Silicon Carbide armour materials.* Ceramics International, 2015. **41**(9, Part B): p. 11581-11591.
31. Wilkins, M.L., *Mechanics of penetration and perforation.* International Journal of Engineering Science, 1978. **16**(11): p. 793-807.
32. Normandia, M., et al., *Protecting the future force: ceramics research leads to improved armor performance.* Amptiac Q, 2004. **8**(4): p. 21-7.
33. Anderson, C.E. and J.D. Walker, *An analytical model for dwell and interface defeat.* International Journal of Impact Engineering, 2005. **31**(9): p. 1119-1132.
34. Hazell, P.J. and M.J. Iremonger, *The numerical analysis of dynamically loaded ceramic: a crack softening approach.* International Journal for Numerical Methods in Engineering, 2000. **48**(7): p. 1037-1053.
35. Hazell, P.J. and M.J. Iremonger, *Crack softening damage model for ceramic impact and its application within a hydrocode.* Journal of Applied Physics, 1997. **82**(3): p. 1088-1092.
36. Knight, C.G., M.V. Swain, and M.M. Chaudhri, *Impact of small steel spheres on glass surfaces.* Journal of Materials Science, 1977. **12**(8): p. 1573-1586.
37. Holmquist, T.J. and G.R. Johnson, *Response of silicon carbide to high velocity impact.* Journal of Applied Physics, 2002. **91**(9): p. 5858-5866.

38. Chen, W.W., et al., *Dynamic Fracture of Ceramics in Armor Applications.* Journal of the American Ceramic Society, 2007. **90**(4): p. 1005-1018.

39. Curran, D.R., et al., *Micromechanical model for comminution and granular flow of brittle material under high strain rate application to penetration of ceramic targets.* International Journal of Impact Engineering, 1993. **13**(1): p. 53-83.

40. Woodward, R., et al. *Energy absorption in the failure of ceramic composite armours*. in *Materials forum (Rushcutters Bay)*. 1989.

41. Wilkins, M., C. Cline, and C. Honodel, *Fourth progress report of light armor program*. 1969, California Univ., Livermore. Lawrence Radiation Lab.

42. Chen, W. and G. Ravichandran, *Dynamic compressive failure of a glass ceramic under lateral confinement.* Journal of the Mechanics and Physics of Solids, 1997. **45**(8): p. 1303-1328.

43. Holmquist, T.J. and G.R. Johnson, *Modeling prestressed ceramic and its effect on ballistic performance.* International Journal of Impact Engineering, 2005. **31**(2): p. 113-127.

44. López-Puente, J., et al., *The effect of the thickness of the adhesive layer on the ballistic limit of ceramic/metal armours. An experimental and numerical study.* International journal of impact engineering, 2005. **32**(1-4): p. 321-336.

45. Hallam, D., et al., *The correlation of indentation behaviour with ballistic performance for spark plasma sintered armour ceramics.* Journal of the European Ceramic Society, 2015. **35**(8): p. 2243-2252.

46. Savio, S., V. Madhu, and A. Gogia, *Ballistic Performance of Alumina and Zirconia-toughened Alumina Against 7.62 Armour Piercing Projectile.* Defence Science Journal, 2014. **64**(5).

47. Savio, S.G., et al., *An experimental study on ballistic performance of boron carbide tiles.* International Journal of Impact Engineering, 2011. **38**(7): p. 535-541.

48. Padovan, O., *Failure of Armour Ceramics in Compression*, in *Department of Materials*, R. Todd, Editor. 2019, University of Oxford.

49. Lankford, J., *Mechanisms responsible for strain-rate-dependent compressive strength in ceramic materials.* Journal of the American Ceramic Society, 1981. **64**(2): p. C-33-C-34.

50. Auerkari, P., *Mechanical and physical properties of engineering alumina ceramics*. Vol. 23. 1996: Technical Research Centre of Finland Espoo.

51. Cleveland, J. and C. Fritsch, *Fine grain translucent alumina*. 1974, Google Patents.

52. Rohrer, G.S., *Structure and bonding in crystalline materials*. 2001: Cambridge University Press.

53. Wachtman, J.B., W.R. Cannon, and M.J. Matthewson, *Mechanical properties of ceramics*. 2009: John Wiley & Sons.

54. Kronberg, M., *Plastic deformation of single crystals of sapphire: basal slip and twinning.* Acta Metallurgica, 1957. **5**(9): p. 507-524.

55. Nettleship, I., R.J. McAfee, and W.S. Slaughter, *Evolution of the Grain Size Distribution during the Sintering of Alumina at 1350°C.* Journal of the American Ceramic Society, 2002. **85**(8): p. 1954-1960.

56. Coble, R.L., *Sintering Alumina: Effect of Atmospheres.* Journal of the American Ceramic Society, 1962. **45**(3): p. 123-127.

57. Cahoon, H.P. and C.J. Christensen, *Sintering and Grain Growth of Alpha-Alumina.* Journal of the American Ceramic Society, 1956. **39**(10): p. 337-344.

58. Olszyna, A.R., P. Marchlewski, and K.J. Kurzydłowski, *Sintering of high-density, high-purity alumina ceramics.* Ceramics International, 1997. **23**(4): p. 323-328.

59. Bae, I.-J. and S. Baik, *Abnormal Grain Growth of Alumina.* Journal of the American Ceramic Society, 1997. **80**(5): p. 1149-1156.

60. Bae, S.I. and S. Baik, *Sintering and grain growth of ultrapure alumina.* Journal of Materials Science, 1993. **28**(15): p. 4197-4204.

61. Park, C.W. and D.Y. Yoon, *Effects of SiO2, CaO2, and MgO additions on the grain growth of alumina.* Journal of the American ceramic society, 2000. **83**(10): p. 2605-2609.

62. Bennison, S.J. and M.P. Harmer, *Effect of MgO Solute on the Kinetics of Grain Growth in A12O3.* Journal of the American Ceramic Society, 1983. **66**(5): p. C-90-C-92.

63. Bae, S.I. and S. Baik, *Critical Concentration of MgO for the Prevention of Abnormal Grain Growth in Alumina.* Journal of the American Ceramic Society, 1994. **77**(10): p. 2499-2504.

64. Bennison, S.J. and M.P. Harmer, *Grain-Growth Kinetics for Alumina in the Absence of a Liquid Phase.* Journal of the American Ceramic Society, 1985. **68**(1): p. C-22-C-24.

65. Bateman, C.A., S.J. Bennison, and M.P. Harmer, *Mechanism for the Role of Magnesia in the Sintering of Alumina Containing Small Amounts of a liquid Phase.* Journal of the American Ceramic Society, 1989. **72**(7): p. 1241-1244.

66. Hardy, D. and D.J. Green, *Mechanical properties of a partially sintered alumina.* Journal of the European Ceramic Society, 1995. **15**(8): p. 769-775.

67. Ruys, A.J. and I.G. Crouch, *7 - Siliconized silicon carbide*, in *Metal-Reinforced Ceramics*, A.J. Ruys, Editor. 2021, Woodhead Publishing. p. 211-283.

68. Deshmukh, Y.V., *Industrial Heating: Principles, Techniques, Materials, Applications, and Design*. 2005: CRC Press.

69. Song, S.G., et al., *Stacking faults in sic particles and their effect on the fracture behavior of a 15 Vol Pct SiC/6061-AI matrix composite.* Metallurgical and Materials Transactions A, 1996. **27**(2): p. 459-465.

70. Ruff, O., *The Formation and Dissociation of Silicon Carbide.* Transactions of The Electrochemical Society, 1935. **68**(1): p. 87.

71. Fuad, A., et al., *Low-Temperature Synthesis of α-SiC (6H-SiC) Nanoparticles with Magnesium Catalyst.* Materials Today: Proceedings, 2019. **17**: p. 1451-1457.

72. Park, D.J., et al., *Oxidation behavior of silicon carbide at 1200°C in both air and water–vapor-rich environments.* Corrosion Science, 2014. **88**: p. 416-422.

73. Singhal, S.C., *Oxidation kinetics of hot-pressed silicon carbide.* Journal of Materials Science, 1976. **11**(7): p. 1246-1253.

74. Gulbransen, E.A. and S.A. Jansson, *The high-temperature oxidation, reduction, and volatilization reactions of silicon and silicon carbide.* Oxidation of Metals, 1972. **4**(3): p. 181-201.

75. Jorgensen, P.J., M.E. Wadsworth, and I.B. Culter, *Oxidation of Silicon Carbide.* Journal of the American Ceramic Society, 1959. **42**(12): p. 613-616.

76. Ervin JR., G., *Oxidation Behavior of Silicon Carbide.* Journal of the American Ceramic Society, 1958. **41**(9): p. 347-352.

77. Costello, J.A. and R.E. Tressler, *Oxidation Kinetics of Hot-Pressed and Sintered α-SiC.* Journal of the American Ceramic Society, 1981. **64**(6): p. 327-331.

78. Costello, J.A. and R.E. Tressler, *Oxidation Kinetics of Silicon Carbide Crystals and Ceramics: I, In Dry Oxygen.* Journal of the American Ceramic Society, 1986. **69**(9): p. 674-681.

79. Hijikata, Y., H. Yaguchi, and S. Yoshida, *A Kinetic Model of Silicon Carbide Oxidation Based on the Interfacial Silicon and Carbon Emission Phenomenon.* Applied Physics Express, 2009. **2**: p. 021203.

80. Limpichaipanit, A. and R.I. Todd, *The relationship between microstructure, fracture and abrasive wear in Al2O3/SiC nanocomposites and microcomposites containing 5 and 10% SiC.* Journal of the European Ceramic Society, 2009. **29**(13): p. 2841-2848.

81. Ortiz-Merino, J.L. and R.I. Todd, *Relationship between wear rate, surface pullout and microstructure during abrasive wear of alumina and alumina/SiC nanocomposites.* Acta Materialia, 2005. **53**(12): p. 3345-3357.

82. Davidge, R.W., P.C. Twigg, and F.L. Riley, *Effects of silicon carbide nano-phase on the wet erosive wear of polycrystalline alumina.* Journal of the European Ceramic Society, 1996. **16**(7): p. 799-802.

83. Rodríguez, J., et al., *Sliding Wear of Alumina/Silicon Carbide Nanocomposites.* Journal of the American Ceramic Society, 1999. **82**(8): p. 2252-2254.

84. Carroll, L., M. Sternitzke, and B. Derby, *Silicon carbide particle size effects in alumina-based nanocomposites.* Acta Materialia, 1996. **44**(11): p. 4543-4552.

85. Winn, A.J. and R.I. Todd, *Microstructural requirements for alumina–SiC nanocomposites.* British Ceramic Transactions, 1999. **98**(5): p. 219-224.

86. Chen, H.J., W.M. Rainforth, and W.E. Lee, *The wear behaviour of Al2O3-SiC ceramic nanocomposites.* Scripta Materialia, 2000. **42**(6): p. 555-560.

87. Stearns, L.C., J. Zhao, and M.P. Harmer, *Processing and microstructure development in Al2O3-SiC 'nanocomposites'.* Journal of the European Ceramic Society, 1992. **10**(6): p. 473-477.

88. Niihara, K., *New design concept of structural ceramics.* Journal of the Ceramic Society of Japan, 1991. **99**(1154): p. 974-982.

89. Jiao, S., M. Jenkins, and R. Davidge, *Electron microscopy of crack/particle interactions in Al2O3/SiC nanocomposites.* Journal of Microscopy, 1997. **185**(2): p. 259-264.

90. Schneider, H., K. Okada, and J.A. Pask, *Mullite and mullite ceramics*. 1994, Chichester: Wiley.

91. Liu, K.-C., et al., *Mullite formation in kaolinite-α-alumina.* Acta Metallurgica et Materialia, 1994. **42**(2): p. 489-495.

92. Aksay, I. and J. Pask, *Stable and metastable equilibria in the system SiO2-Al2O3.* J. Am. Ceram. Soc.;(United States), 1975. **58**(LBL-2747).

93. Klug, F.J., S. Prochazka, and R.H. Doremus, *Alumina-silica phase diagram in the mollite region.* Journal of the American Ceramic Society, 1987. **70**(10): p. 750-759.

94. Sato, T., M. Ishizuka, and M. Shimada, *Sintering and characterization of mullite—Alumina composites.* Ceramics International, 1986. **12**(2): p. 61-65.

95. Zhang, F., et al., *Stress state and fracture behavior of alumina–mullite intragranular particulate composites.* Composites Science and Technology, 2008. **68**(15-16): p. 3245-3250.

96. Luo, H., F. Zhang, and S. Roberts, *Wear resistance of reaction sintered alumina/mullite composites.* Materials Science and Engineering: A, 2008. **478**(1-2): p. 270-275.

97. Zhang, F., H. Luo, and S. Roberts, *Mechanical properties and microstructure of Al 2 O 3/mullite composite.* Journal of materials science, 2007. **42**(16): p. 6798-6802.

98. Limpichaipanit, A. and T. Tunkasiri, *Reaction sintering of alumina/mullite nanocomposites from nano-sized starting powders.* Advances in Applied Ceramics, 2016. **115**(6): p. 349-353.

99. Burgos-Montes, O., R. Moreno, and C. Baudín, *Effect of mullite additions on the fracture mode of alumina.* Journal of the European Ceramic Society, 2010. **30**(4): p. 857-863.

100. Zhao, J., et al., *Mechanical Behavior of Alumina–Silicon Carbide „Nanocomposites".* Journal of the American Ceramic Society, 1993. **76**(2): p. 503-510.

101. Sternitzke, M., *Structural ceramic nanocomposites.* Journal of the European Ceramic Society, 1997. **17**(9): p. 1061-1082.

102. Levin, I., et al., *Effect of SiC Submicrometer Particle Size and Content on Fracture Toughness of Alumina–SiC "Nanocomposites".* Journal of the American Ceramic Society, 1995. **78**(1): p. 254-256.

103. Hansson, T., R. Warren, and J. Wasén, *Fracture Toughness Anisotropy and Toughening Mechanisms of a Hot-pressed Alumina Reinforced with Silicon Carbide Whiskers.* Journal of the American Ceramic Society, 1993. **76**(4): p. 841-848.

104. Belmonte, M., et al., *Influence of the SiC grain size on the wear behaviour of Al2O3/SiC composites.* Journal of the European Ceramic Society, 2006. **26**(7): p. 1273-1279.

105. Medvedovski, E., *Alumina–mullite ceramics for structural applications.* Ceramics International, 2006. **32**(4): p. 369-375.

106. Todd, R.I., et al., *Neutron diffraction measurements of residual stresses in alumina/SiC nanocomposites.* Acta Materialia, 1997. **45**(4): p. 1791-1800.

107. Aksay, I.A., D.M. Dabbs, and M. Sarikaya, *Mullite for Structural, Electronic, and Optical Applications.* Journal of the American Ceramic Society, 1991. **74**(10): p. 2343-2358.

108. Taya, M., et al., *Toughening of a Particulate-Reinforced Ceramic-Matrix Composite by Thermal Residual Stress.* Journal of the American Ceramic Society, 1990. **73**(5): p. 1382-1391.

109. Hart, E.W., *Two-dimensional phase transformation in grain boundaries.* Scripta Metallurgica, 1968. **2**(3): p. 179-182.

110. Tang, M., W.C. Carter, and R.M. Cannon, *Diffuse interface model for structural transitions of grain boundaries.* Physical Review B, 2006. **73**(2): p. 024102.

111. Dillon, S.J. and M.P. Harmer, *Multiple grain boundary transitions in ceramics: a case study of alumina.* Acta Materialia, 2007. **55**(15): p. 5247-5254.

112. Dillon, S.J. and M.P. Harmer, *Relating Grain-Boundary Complexion to Grain-Boundary Kinetics I: Calcia-Doped Alumina.* Journal of the American Ceramic Society, 2008. **91**(7): p. 2304-2313.

113. Dillon, S.J. and M.P. Harmer, *Relating Grain Boundary Complexion to Grain Boundary Kinetics II: Silica-Doped Alumina.* Journal of the American Ceramic Society, 2008. **91**(7): p. 2314-2320.

114. Dillon, S.J., et al., *Complexion: a new concept for kinetic engineering in materials science.* Acta Materialia, 2007. **55**(18): p. 6208-6218.

115. Dillon, S.J., M.P. Harmer, and J. Luo, *Grain boundary complexions in ceramics and metals: An overview.* JOM, 2009. **61**(12): p. 38-44.

116. Kogtenkova, O., et al., *Grain Boundary Complexions and Phase Transformations in Al- and Cu-Based Alloys.* Metals, 2018. **9**(1): p. 10.

117. MacLaren, I., et al., *Abnormal Grain Growth in Alumina: Synergistic Effects of Yttria and Silica.* Journal of the American Ceramic Society, 2003. **86**(4): p. 650-59.

118. Krause, A.R., et al., *Review of grain boundary complexion engineering: Know your boundaries.* Journal of the American Ceramic Society, 2019. **102**(2): p. 778-800.

119. Brydson, R., et al., *Microstructure and Chemistry of Intergranular Glassy Films in Liquid-Phase-Sintered Alumina.* Journal of the American Ceramic Society, 1998. **81**(2): p. 369-379.

120. Brydson, R., et al., *Influence of CaO–SiO2 ratio on the chemistry of intergranular films in liquid-phase sintered alumina and implications for rate of erosive wear.* Journal of Materials Research, 2001. **16**(3): p. 652-665.

121. Blonski, S. and S.H. Garofalini, *Atomistic structure of calcium silicate intergranular films in alumina studied by molecular dynamics simulations.* Journal of the American Ceramic Society, 1997. **80**(8): p. 1997-2004.

122. Galusek, D., et al., *Wet erosive wear of alumina densified with magnesium silicate additions.* Journal of the American Ceramic Society, 2001. **84**(8): p. 1767-1776.

123. Kleebe, H.-J., et al., *Role of interface structure on mechanical properties of fluorine-doped Si3N4-SiC ceramics.* Journal of the Ceramic Society of Japan, 1998. **106**(1229): p. 17-24.

124. Feng, L., et al., *The influence of dopants and complexion transitions on grain boundary fracture in alumina.* Acta Materialia, 2018. **142**: p. 121-130.

125. Bokov, A., et al., *Energetic design of grain boundary networks for toughening of nanocrystalline oxides.* Journal of the European Ceramic Society, 2018. **38**(12): p. 4260-4267.

126. Cao, W., et al., *Direct correlations between fracture toughness and grain boundary segregation behavior in ytterbium-doped magnesium aluminate spinel.* Scripta Materialia, 2013. **69**(1): p. 81-84.

127. Wu, L., et al., *Thermodynamic Strengthening of Heterointerfaces in Nanoceramics.* Chemistry of Materials, 2016. **28**(9): p. 2897-2901.

128. Buban, J.P., et al., *Grain Boundary Strengthening in Alumina by Rare Earth Impurities.* Science, 2006. **311**(5758): p. 212-215.

129. Pan, Z. and T.J. Rupert, *Amorphous intergranular films as toughening structural features.* Acta Materialia, 2015. **89**: p. 205-214.

130. Daniel, R., et al., *Grain boundary design of thin films: Using tilted brittle interfaces for multiple crack deflection toughening.* Acta Materialia, 2017. **122**: p. 130-137.

131. Dillon, S.J., M.P. Harmer, and G.S. Rohrer, *The Relative Energies of Normally and Abnormally Growing Grain Boundaries in Alumina Displaying Different Complexions.* Journal of the American Ceramic Society, 2010. **93**(6): p. 1796-1802.

132. Fang, J., et al., *Effect of yttrium and lanthanum on the final-stage sintering behavior of ultrahigh-purity alumina.* Journal of the American Ceramic Society, 1997. **80**(8): p. 2005-2012.

133. Voytovych, R., et al., *The effect of yttrium on densification and grain growth in α-alumina.* Acta Materialia, 2002. **50**(13): p. 3453-3463.

134. Dillon, S.J. and M.P. Harmer, *Direct observation of multilayer adsorption on alumina grain boundaries.* Journal of the American Ceramic Society, 2007. **90**(3): p. 996-998.

135. Thompson, C.V., H.J. Frost, and F. Spaepen, *The relative rates of secondary and normal grain growth.* Acta Metallurgica, 1987. **35**(4): p. 887-890.

136. Kirch, D.M., et al., *Inclination dependence of grain boundary energy and its impact on the faceting and kinetics of tilt grain boundaries in aluminum.* Acta Materialia, 2008. **56**(18): p. 4998-5011.

137. Brandenburg, J.E., et al., *Motion of a grain boundary facet in aluminum.* Acta Materialia, 2013. **61**(14): p. 5518-5524.

138. Lee, S.B., et al., *Grain boundary faceting and abnormal grain growth in nickel.* Metallurgical and Materials Transactions A, 2000. **31**(3): p. 985-994.

139. Choi, J.S. and D.Y. Yoon, *The Temperature Dependence of Abnormal Grain Growth and Grain Boundary Faceting in 316L Stainless Steel.* ISIJ International, 2001. **41**(5): p. 478-483.

140. Cho, Y.K., S.-J.L. Kang, and D.Y. Yoon, *Dependence of Grain Growth and Grain-Boundary Structure on the Ba/Ti Ratio in BaTiO3.* Journal of the American Ceramic Society, 2004. **87**(1): p. 119-124.

141. Gleiter, H., *The mechanism of grain boundary migration.* Acta Metallurgica, 1969. **17**(5): p. 565-573.

142. Cahn, J.W., *Theory of crystal growth and interface motion in crystalline materials.* Acta Metallurgica, 1960. **8**(8): p. 554-562.

143. Fisher, J.G., S.-Y. Choi, and S.-J.L. Kang, *Abnormal Grain Growth in Barium Titanate Doped with Alumina.* Journal of the American Ceramic Society, 2006. **89**(7): p. 2206-2212.

144. Sun, R.C. and C.L. Bauer, *Tilt boundary migration in NaCl bicrystals.* Acta Metallurgica, 1970. **18**(6): p. 639-647.

145. Fiedler, H.C., *Grain oriented silicon- iron with a unique inhibition system for texture development.* Metallurgical Transactions A, 1977. **8**(8): p. 1307-1312.

146. Kim, M.J., Y.K. Cho, and D.Y. Yoon, *Facet–defacet transition of grain boundaries in alumina.* Journal of the American Ceramic Society, 2004. **87**(3): p. 455-460.

147. Blendell, J.E., W.C. Carter, and C.A. Handwerker, *Faceting and Wetting Transitions of Anisotropic Interfaces and Grain Boundaries.* Journal of the American Ceramic Society, 1999. **82**(7): p. 1889-1900.

148. Carter, C.B., D.L. Kohlsted, and S.L. Sass, *Electron Diffraction and Microscopy Studies of the Structure of Grain Boundaries in Al2O3.* Journal of the American Ceramic Society, 1980. **63**(11-12): p. 623-627.

149. Morrissey, K.J. and C.B. Carter, *Faceted grain boundaries in Al2O3.* Journal of the American Ceramic Society, 1984. **67**(4): p. 292-301.

150. Heuer, A., *Deformation twinning in corundum.* The Philosophical Magazine: A Journal of Theoretical Experimental and Applied Physics, 1966. **13**(122): p. 379-393.

151. Scott, W.D., *Rhombohedral Twinning in Aluminum Oxide*, in *Deformation of Ceramic Materials*, R.C. Bradt and R.E. Tressler, Editors. 1975, Springer US: Boston, MA. p. 151-166.

152. Marvel, C.J., et al., *Linking grain boundary structure and composition to microstructure in commercial-grade-doped specialty Aluminas.* Journal of the American Ceramic Society, 2022. **105**(1): p. 626-638.

153. Yu, Z., et al., *Atomic-resolution observation of Hf-doped alumina grain boundaries.* Scripta Materialia, 2013. **68**(9): p. 703-706.

154. Gülgün, M.A., V. Putlayev, and M. Rühle, *Effects of Yttrium Doping α-Alumina: I, Microstructure and Microchemistry.* Journal of the American Ceramic Society, 1999. **82**(7): p. 1849-1856.

155. Kundu, A., et al., *Identification of a bilayer grain boundary complexion in Bi-doped Cu.* Scripta Materialia, 2013. **68**(2): p. 146-149.

156. Clinton, D.J. and R. Morrell, *Hardness testing of ceramic materials.* Materials Chemistry and Physics, 1987. **17**(5): p. 461-473.

157. Quinn, G.D. and R.C. Bradt, *On the Vickers Indentation Fracture Toughness Test.* Journal of the American Ceramic Society, 2007. **90**(3): p. 673-680.

158. Bull, S.J., T.F. Page, and E.H. Yoffe, *An explanation of the indentation size effect in ceramics.* Philosophical Magazine Letters, 1989. **59**(6): p. 281-288.

159. Barick, P. and B.P. Saha, *Mixed Particle Size Effect on Improvement of Mechanical Properties of Reaction Bonded B4C.* Transactions of the Indian Ceramic Society, 2023. **82**(1): p. 56-64.

160. Peng, Z., J. Gong, and H. Miao, *On the description of indentation size effect in hardness testing for ceramics: Analysis of the nanoindentation data.* Journal of the European Ceramic Society, 2004. **24**(8): p. 2193-2201.

161. Meyer, E., *Untersuchungen über härteprüfung und härte.* Zeitschrift des Vereines Deutscher Ingenieure, 1908. **52**(17): p. 645-654.

162. Sangwal, K., A. Kothari, and S.K. Arora, *Formation of indentation cracks and origin of indentation size effect in cadmium tartrate pentahydrate single crystals.* Surface Science, 2006. **600**(7): p. 1475-1486.

163. Tarkanian, M., J. Neumann, and L. Raymond, *Determination of the temperature dependence of {100} and {112} slip in tungsten from Knoop hardness measurements.* Westbrook, J. & Conrad, H. The science of hardness testing and its research applications. American Society for Metals, Ohio, USA, 1973: p. 187-198.

164. Mukhopadhyay, N.K. and P. Paufler, *Micro- and nanoindentation techniques for mechanical characterisation of materials.* International Materials Reviews, 2006. **51**(4): p. 209-245.

165. Oliver, W.C. and G.M. Pharr, *An improved technique for determining hardness and elastic modulus using load and displacement sensing indentation experiments.* Journal of Materials Research, 1992. **7**(6): p. 1564-1583.

166. Yan, W., C.L. Pun, and G.P. Simon, *Conditions of applying Oliver–Pharr method to the nanoindentation of particles in composites.* Composites Science and Technology, 2012. **72**(10): p. 1147-1152.

167. Min, L. and C. Weimin, *Factors Resulting in Micron Indentation Hardness Descending in Indentation Tests.* Chinese Journal of Aeronautics, 2009. **22**(1): p. 43-48.

168. Gee, M. and S. Owen-Jones, *Wear testing methods and their relevance to industrial wear problems.* 1998.

169. Zu, J.B., I.M. Hutchings, and G.T. Burstein, *Design of a slurry erosion test rig.* Wear, 1990. **140**(2): p. 331-344.

170. Vuorinen, E., et al., *Erosive and abrasive wear performance of carbide free bainitic steels–comparison of field and laboratory experiments.* Tribology International, 2016. **98**: p. 108-115.

171. Ma, L., et al., *Modeling of erodent particle trajectories in slurry flow.* Wear, 2015. **334**: p. 49-55.

172. International, A., *Standard Test Method for Resistance of Transparent Plastics to Surface Abrasion by the Taber Abraser*. 2019. p. 8.

173. Barceinas-Sánchez, J.D.O. and W.M. Rainforth, *On the role of plastic deformation during the mild wear of alumina.* Acta Materialia, 1998. **46**(18): p. 6475-6483.

174. Leyland, A. and A. Matthews, *Design criteria for wear-resistant nanostructured and glassy-metal coatings.* Surface and Coatings Technology, 2004. **177-178**: p. 317-324.

175. Rutherford, K. and I. Hutchings, *Theory and application of a micro-scale abrasive wear test.* Journal of Testing and Evaluation, 1997. **25**(2): p. 250-260.

176. Zorzi, J.E., C.A. Perottoni, and J.A.H. da Jornada, *Hardness and wear resistance of B4C ceramics prepared with several additives.* Materials Letters, 2005. **59**(23): p. 2932-2935.

177. Moshtaghioun, B.M., et al., *Abrasive wear rate of boron carbide ceramics: Influence of microstructural and mechanical aspects on their tribological response.* Journal of the European Ceramic Society, 2016. **36**(16): p. 3925-3928.

178. Medvedovski, E., *Wear-resistant engineering ceramics.* Wear, 2001. **249**(9): p. 821-828.

179. Gogotsi, G.A. and V.I. Galenko, *Comparative analysis of fracture toughness test methods for ceramics and crystals at room and lower temperatures.* Strength of Materials, 1997. **29**(3): p. 287-297.

180. Gogotsi, G.A., *Fracture toughness of ceramics and ceramic composites.* Ceramics International, 2003. **29**(7): p. 777-784.

181. Cesar, P.F., et al., *ADM guidance—Ceramics: Fracture toughness testing and method selection.* Dental Materials, 2017. **33**(6): p. 575-584.

182. Quinn, J.B. and I.K. Lloyd, *Comparison of Methods to Determine the Fracture Toughness of Three Glass-Ceramics at Elevated Temperatures.* Journal of the American Ceramic Society, 2000. **83**(12): p. 3070-3076.

183. Creager, M. and P.C. Paris, *Elastic field equations for blunt cracks with reference to stress corrosion cracking.* International Journal of Fracture Mechanics, 1967. **3**(4): p. 247-252.

184. Schellenberger, A., *On the robustness of the Single-Edge-Precracked-Beam (SEPB) method for fracture toughness testing of ceramic materials.* Engineering Fracture Mechanics, 2023: p. 109527.

185. Nose, T. and T. Fujii, *Evaluation of Fracture Toughness for Ceramic Materials by a Single-Edge-Precracked-Beam Method.* Journal of the American Ceramic Society, 1988. **71**(5): p. 328-333.

186. Quinn, G., et al. *The New Astm Fracture Toughness of Advanced Ceramics Standard: PS 070-97*. in *22nd Annual Conference on Composites, Advanced Ceramics, Materials, and Structures: A: Ceramic Engineering and Science Proceedings*. 1988. Wiley Online Library.

187. Scherrer, S., et al., *Fracture toughness (KIc) of a dental porcelain determined by fractographic analysis.* Dental Materials, 1999. **15**(5): p. 342-348.

188. Wang, H., et al., *Influence of Test Methods on Fracture Toughness of a Dental Porcelain and a Soda Lime Glass.* Journal of the American Ceramic Society, 2005. **88**(10): p. 2868-2873.

189. Torres, Y., et al., *Fracture toughness evaluation of hardmetals: influence of testing procedure.* International Journal of Refractory Metals and Hard Materials, 2001. **19**(1): p. 27-34.

190. Bertolotti, R.L., *Fracture Toughness of Polycrystalline Al2O3.* Journal of the American Ceramic Society, 1973. **56**(2): p. 107-107.

191. Scherrer, S.S., I.L. Denry, and H.A. Wiskott, *Comparison of three fracture toughness testing techniques using a dental glass and a dental ceramic.* Dental Materials, 1998. **14**(4): p. 246-255.

192. Kubler, J., *Fracture toughness of ceramics using the SEVNB method: round robin*. 1999, Citeseer.

193. Kübler, J., *Fracture Toughness of Ceramics Using the Sevnb Method: Preliminary Results*, in *Proceedings of the 21st Annual Conference on Composites, Advanced Ceramics, Materials, and Structures—B: Ceramic Engineering and Science Proceedings*. 1997. p. 155-162.

194. Quinn, G.D., et al., *Fracture toughness of advanced ceramics at room temperature.* Journal of research of the National Institute of Standards and Technology, 1992. **97**(5): p. 579.

195. Fischer, H., A. Waindich, and R. Telle, *Influence of preparation of ceramic SEVNB specimens on fracture toughness testing results.* Dental Materials, 2008. **24**(5): p. 618-622.

196. Damani, R., R. Gstrein, and R. Danzer, *Critical notch-root radius effect in SENB-S fracture toughness testing.* Journal of the European Ceramic Society, 1996. **16**(7): p. 695-702.

197. Fett, T., *Notch effects in determination of fracture toughness and compliance.* International Journal of Fracture, 1995. **72**(2): p. R27-R30.

198. *High Purity Alumina Beads Product Info*. 2008 [cited 2022 12 21]; Available from: https://www.taimei-chem.co.jp/product/english/02.html.

199. *Silicon Carbide Powder*. 2022 [cited 2022 12 21]; Available from: https://us.store.logitech.uk.com/index.php?route=product/product&product_id=56.

200. *Calcium nitrate tetrahydrate, ACS, 99.0-103.0%, Product Specification*. 2022 [cited 2022 12 21]; Available from: https://alfaaesar.com/en/prodspec/012364.

201. *Neodymium(III) nitrate hexahydrate, 99.9% (REO), Product Specification*. 2022 [cited 2022 12 21]; Available from: https://alfaaesar.com/en/prodspec/012912.

202. *Magnesium nitrate hexahydrate, Product Specification*. 2022 [cited 2022 12 21]; Available from: https://www.sigmaaldrich.com/GB/en/product/sigald/237175.

203. *Yttrium(III) oxide, REacton , 99.99% (REO), Product Specification*. 2022 [cited 2022 12 21]; Available from: https://alfaaesar.com/en/prodspec/011181.

204. MENDELSON, M.I., *Average Grain Size in Polycrystalline Ceramics.* Journal of the American Ceramic Society, 1969. **52**(8): p. 443-446.

205. Cliff, G. and G.W. Lorimer, *The quantitative analysis of thin specimens.* Journal of Microscopy, 1975. **103**(2): p. 203-207.

206. Gu, H., R.M. Cannon, and M. Rühle, *Composition and chemical width of ultrathin amorphous films at grain boundaries in silicon nitride.* Journal of Materials Research, 1998. **13**(2): p. 376-387.

207. Reed, S.J.B., *The single-scattering model and spatial resolution in X-ray analysis of thin foils.* Ultramicroscopy, 1982. **7**(4): p. 405-409.

208. Rutherford, K.L. and I.M. Hutchings, *A micro-abrasive wear test, with particular application to coated systems.* Surface and Coatings Technology, 1996. **79**(1): p. 231-239.

209. Bažant, Z.P., *Fracture mechanics of concrete structures*. Proceedings (International Conference on Fracture Mechanics of Concrete Structures). 1992, London: Elsevier Applied Science.

210. Fett, T., *Mixed-mode stress intensity factors for three-point bending bars.* International Journal of Fracture, 1991. **48**(4): p. R67-R74.

211. Dancer, C.E.J., et al., *High strain rate indentation-induced deformation in alumina ceramics measured by Cr3+ fluorescence mapping.* Journal of the European Ceramic Society, 2011. **31**(13): p. 2177-2187.

212. Cho, Y.J. and K. Lu, *High temperature oxidation behaviors of bulk SiC with low partial pressures of air and water vapor in argon.* Corrosion Science, 2020. **174**: p. 108795.

213. Gadalla, A., M. Elmasry, and P. Kongkachuichay, *High temperature reactions within SiC–Al2O3 composites.* Journal of materials research, 1992. **7**(9): p. 2585-2592.

214. Baud, S., et al., *High temperature sintering of SiC with oxide additives: I. Analysis in the SiC–Al2O3 and SiC–Al2O3–Y2O3 systems.* Journal of the European Ceramic Society, 2003. **23**(1): p. 1-8.

215. Valentine, J.D. and A.E. Rana, *Centroid and full-width at half maximum uncertainties of histogrammed data with an underlying Gaussian distribution-the moments method.* IEEE Transactions on Nuclear Science, 1996. **43**(5): p. 2501-2508.

216. Shirley, B. and E. Jarochowska, *Chemical characterisation is rough: the impact of topography and measurement parameters on energy-dispersive X-ray spectroscopy in biominerals.* Facies, 2022. **68**(2): p. 7.

217. Angel, R.J. and C.T. Prewitt, *Crystal structure of mullite: A re-examination of the average structure.* American Mineralogist, 1986. **71**(11-12): p. 1476-1482.

218. Jeong, Y.-K. and K. Niihara, *Microstructure and properties of alumina-silicon carbide nanocomposites fabricated by pressureless sintering and post hot-isostatic pressing.* Transactions of Nonferrous Metals Society of China, 2011. **21**: p. s1-s6.

219. Baron, B., et al., *Comparison of different alumina powders for the aqueous processing and pressureless sintering of Al2O3–SiC nanocomposites.* Journal of the European Ceramic Society, 2002. **22**(9-10): p. 1543-1552.

220. Elmer, P. *Thermogravimetric Analysis*. 2010 01/01/2024]; Available from: https://resources.perkinelmer.com/lab-solutions/resources/docs/gde_tgabeginnersguide.pdf.

221. EDAX. *Optimizing Spatial Resolution for EDS Analysis*. [cited 2023 22 Nov]; Available from: https://www.edax.com/-/media/ametekedax/files/resources/tips_tricks/optimizingspatialresolutionforedsanalysis.pdf?la=en&revision=f141f61a-b1cc-4235-bab0-56ccd91cbec4.

222. Cock, A.M., et al., *Effects of Yttrium on the Sintering and Microstructure of Alumina–Silicon Carbide "Nanocomposites".* Journal of the American Ceramic Society, 2005. **88**(9): p. 2354-2361.

223. Brosnan, D.A., *Alumina-silica brick.* MECHANICAL ENGINEERING-NEW YORK AND BASEL-MARCEL DEKKER THEN CRC PRESS/TAYLOR AND FRANCIS, 2004. **178**: p. 79.

224. Dana, K., et al., *Refractories of Alumina-Silica System.* Transactions of the Indian Ceramic Society, 2014. **73**(1): p. 1-13.

225. Aramaki, S. and R. Roy, *Revised Phase Diagram for the System Al2O3—SiO2.* Journal of the American Ceramic Society, 1962. **45**(5): p. 229-242.

226. Aksay, I.A. and J.A. Pask, *The Silica-Alumina System: Stable and Metastable Equilibria at 1.0 Atmosphere.* Science, 1974. **183**(4120): p. 69-71.

227. Zhou, N., et al., *Calculation and validation of a grain boundary complexion diagram for Bi-doped Ni.* Scripta Materialia, 2017. **130**: p. 165-169.

228. Luo, J. and X. Shi, *Grain boundary disordering in binary alloys.* Applied Physics Letters, 2008. **92**(10).

229. Reed-Hill, R.E. and R. Abbaschian, *Physical metallurgy principles*. 3rd. ed. ed. The PWS-Kent Series in Engineering. 1992, Boston, Mass: PWS-Kent Publishing Co.

230. Kokhanchik, G.I., A.V. Serebryakov, and Y.A. Shiyanov, *Diffusion movement of particles in solids.* physica status solidi (a), 1974. **23**(1): p. 99-103.

231. Serebryakov, A.V., T.M. Redkova, and V.I. Lobanov, *On recrystallization of dispersion-hardened alloys.* physica status solidi (a), 1972. **14**(1): p. 77-81.

232. Gruber, E.E., *Calculated Size Distributions for Gas Bubble Migration and Coalescence in Solids.* Journal of Applied Physics, 2004. **38**(1): p. 243-250.

233. Gottstein, G. and L.S. Shvindlerman, *Theory of grain boundary motion in the presence of mobile particles.* Acta Metallurgica et Materialia, 1993. **41**(11): p. 3267-3275.

234. Schneider, H., R.X. Fischer, and J. Schreuer, *Mullite: Crystal Structure and Related Properties.* Journal of the American Ceramic Society, 2015. **98**(10): p. 2948-2967.

235. Saalfeld, H. and W. Guse, *STRUCTURE REFINEMENT OF 3: 2-MULLITE (3AL2O32SIO2).* 1981.

236. Angel, R.J., R.K. McMullan, and C.T. Prewitt, *Substructure and superstructure of mullite by neutron diffraction.* American Mineralogist, 1991. **76**(3-4): p. 332-342.

237. Whittemore, O.J. and J.J. Sipe, *Pore growth during the initial stages of sintering ceramics.* Powder Technology, 1974. **9**(4): p. 159-164.

238. Watanabe, R., K. Tada, and Y. Masuda, *Ostwald Ripening of Residual Pores in Sintered Copper.* International Journal of Materials Research, 1976. **67**(9): p. 619-624.

239. Smallman, R.E. and A.H.W. Ngan, *Chapter 13 - Precipitation Hardening*, in *Modern Physical Metallurgy (Eighth Edition)*, R.E. Smallman and A.H.W. Ngan, Editors. 2014, Butterworth-Heinemann: Oxford. p. 499-527.

240. Zhang, H., et al., *Property improvements of in situ epoxy nanocomposites with reduced interparticle distance at high nanosilica content.* Acta Materialia, 2006. **54**(7): p. 1833-1842.

241. Corporation, A.C. *99.5% Alumina Material Properties*. n.d. 29/12/2023]; Available from: https://accuratus.com/pdf/995aluminaprops.pdf.

242. Corporation, A.C. *Silicon Carbide Material Properties*. n.d. 29/12/2023]; Available from: https://accuratus.com/pdf/sicprops.pdf.

243. Corporation, A.C. *Mullite Material Properties*. n.d. 29/12/2023]; Available from: https://accuratus.com/pdf/Mulliteprops.pdf.

244. Bauccio, M., *ASM engineered materials reference book*. 1994, ASM International Materials Park, OH: Materials Park, OH.

245. Teng, X., H. Liu, and C. Huang, *Effect of Al2O3 particle size on the mechanical properties of alumina-based ceramics.* Materials Science and Engineering: A, 2007. **452-453**: p. 545-551.

246. Kambale, K.R., A. Mahajan, and S.P. Butee, *Effect of grain size on the properties of ceramics.* Metal Powder Report, 2019. **74**(3): p. 130-136.

247. Jiang, C., et al., *Effect of Porosity on Dynamic Mechanical Properties and Impact Response Characteristics of High Aluminum Content PTFE/Al Energetic Materials.* Materials (Basel), 2019. **13**(1).

248. Al-Maharma, A.Y., S.P. Patil, and B. Markert, *Effects of porosity on the mechanical properties of additively manufactured components: a critical review.* Materials Research Express, 2020. **7**(12): p. 122001.

249. Zhang, F.C., et al., *Influence factors on wear resistance of two alumina matrix composites.* Wear, 2008. **265**(1): p. 27-33.

250. Lawn, B.R., *Indentation of Ceramics with Spheres: A Century after Hertz.* Journal of the American Ceramic Society, 1998. **81**(8): p. 1977-1994.

251. Fischer-Cripps, A.C., *Predicting Hertzian fracture.* Journal of Materials Science, 1997. **32**(5): p. 1277-1285.